Shear Velocity Structure of the Mantle Beneath the North American Plate

Thesis by

Stephen Pierre Grand

In Partial Fulfillment of the Requirements
for the Degree of
Doctor of Philosophy

California Institute of Technology
Pasadena, California

1986
(Submitted April 14, 1986)

Acknowledgements

It is a pleasure to thank the people who have made my stay at the Seismo Lab both rewarding and enjoyable. Don Helmberger has been an excellent advisor, providing both great support and guidance while allowing me all the freedom I could ask for. I would also like to thank Hiroo Kanamori, Don Anderson, and Rob Clayton, who have freely shared their time, ideas and enthusiasm with me.

The students of the Seismo Lab, as well as the faculty, have been an important part of my learning experience here. Jeff Given and Larry Ruff were especially patient and helpful with my many questions as a new student. Special thanks go also to my office mates, Steve Cohn, Hsui-Lin Liu, John Cipar, Vicki Lefevre, Luciana Astiz, and John Louie, for their encouragement over the years. I would also like to thank Gene Humphreys, Chris Creaven, Holly Eissler and Ronan Lebras for being such good classmates and friends. Finally, I would like to thank my wife, Zonia, for her love and patience during the completion of this thesis.

Cindy Arveson and Lazlo Lenches deserve my gratitude for their expert drafting of most of the figures in this work. Cindy also spent many hours digitizing the data I have used and without her help I would probably still be working on the final chapter.

Support for the research in this thesis came from NSF grants EAR-8116023, EAR-8306411 and EAR-8507788.

Abstract

The long-period tangential components of seismograms recorded by the WWSS network over the last 20 years are used to constrain the shear velocity variations in the mantle beneath the North American plate. The first two chapters derive vertical shear velocity profiles beneath three tectonic provinces: the East Pacific Rise, the Canadian shield and the old northwest Atlantic ocean. The SH motion seismograms were interpreted as multi-bounce shear bodywaves and use was made of Cagniard-de Hoop and WKBJ synthetic seismogram techniques to model the data with the assumption that the structure within each province was laterally homogeneous. The three models were constructed such that the S-waves and up to 4 minutes of later arrivals in the data were fit in terms of travel-time, phase and amplitude. The most useful arrival in the study was the SS phase.

The three regions studied were found to have very similar structure below 400 km depth. Anomalously large increases in velocity of about 6.5% from 375 to 425 km depth and 11% from 625 to 700 km depth were found beneath each tectonic area with no indication of lateral variations in the structures. These high gradient zones were modeled as discontinuities of 4.5% at 405 km depth and 7.5% at 660 km depth. Other common features of the models are a high gradient from 425 to 625 km depth and an anomalously high gradient beneath the discontinuity at 660 km depth to about 750 km depth. Above 400 km depth, large lateral differences in structure exist beneath the three provinces. Velocities beneath the shield were found to be about 10% higher at 100 km depth, 5% higher at 200 km depth and 3% higher at 300 km depth, relative to the Rise model. The old Atlantic has high velocities to about 100 km depth, but below 150 km the structure is similar to that beneath the East Pacific Rise. The shield model has a very low gradient and high velocity in the upper 175 km. The velocity decreases by about 3% at 200 km depth with a low gradient below to 400 km depth. Beneath the Atlantic and East Pacific, very low velocities occur near 200 km depth. The Rise model has the lowest velocities (4.3 km/sec) near 100 km depth. Both models have very high gradients (about .035%/km) from 175 to 375 km suggesting a partial melt or dislocation relaxation explanation for the low velocities near 200 km depth.

Chapter 3 is an attempt to develop a fully three-dimensional model of mantle shear velocity beneath the entire North American plate to 1700 km depth. S and SS arrival time anomalies were measured relative to a simple starting model. The raypaths of the different measured phases were found using the experience gained in Chapters 1 and 2. The travel-time anomalies were then used as the input for a tomographic back projection inversion for velocity fluctuations within blocks on the order of 500 by 500 by 100 kms. A high velocity root to 400 km depth is found directly beneath almost all of the shield and platform of North America. Eastern North America was found to have similar structure to the old Atlantic with high velocities to 140 km depth and average to low velocities to 400 km depth. The Basin and Range, Carribean, Mid-Atlantic Ridge and the East Pacific have the lowest velocities in the upper 400 km. From the southwest Carribean to the northern United States, a major high velocity feature is observed to exist from 700 to 1700 km depth with about a 1% increase in velocity over an 800 km width in an east-west direction. The structure has a slab-like shape and dips to the east. It is hypothesized that the anomalous high velocities are due to remnants of the subducted Farallon plate going

back to 100 Ma.

Table of Contents

Chapter 1: Upper Mantle Shear Structure of North America from S and SS Phases

Chapter 2: Upper Mantle Shear Structure Beneath the Northwest Atlantic

Chapter 3: Tomographic Inversion for Mantle Shear Velocity Beneath the North American Plate

Introduction

From the earliest days of seismology, determining the elastic velocities in the interior of the earth has been a primary goal of the science. An early model of P and S velocity in the mantle was developed by Jeffreys (1939) and it is still used as a standard today, especially for the lower mantle. The model was constructed by measuring the arrival times of P and S waves with increasing distance and thus increasing depth. Jeffreys' model was constructed to be as smooth as possible consistent with the first arrival data. He found, however, an increase in amplitude and a change in the slope of the time-distance curve near 20^o distance. This was reflected in the model by a region of high gradient from about 400 to 800 km depth. Gutenburg (1948) presented evidence of a more complicated structure with a decrease in velocity in the shallow mantle and a higher gradient below 200 km depth. Birch (1952) used these early seismic models to deduce that the mantle was formed of ferro-magnesium silicates. Below 800 km depth he found the velocities could be explained by the self-compression of a uniform mineral assemblage. Above 800 km, the gradients were too high to explain this way and he postulated that either the mantle silicates undergo phase transformations to closer packed oxide structures or there is a chemical difference between the upper and lower mantles. The work in these early studies of structure and composition are considered correct to first order today.

More recent studies of mantle velocity structure have followed two separate paths. Following Jeffreys' approach, bodywaves have been examined more closely. By measuring the arrival times of secondary arrivals and using arrays of stations to get accurate values of $\frac{dT}{d\Delta}$, more detailed models were derived. Early examples of these techniques using P-waves are given in Niazi and Anderson (1965), Kanamori (1967) and Johnson (1967). Early studies of shear velocity structure were done by Ibrahim and Nuttli (1967) and Anderson and Julian (1969). These studies found evidence for discontinuities or regions of very high gradient near 400 and 650 km depth. In some cases the increases in velocity were up to 10% in magnitude. Anderson (1967) explained these regions as the location of phase changes in a primarily olivine mantle. The different studies, however, produced very different models, particularly in the case of shear structure. In fact, discontinuities have also been proposed to occur at 200, 300 and 530 km depth. Several others have been proposed deeper than 700 km depth as well (see Datt, 1981, for one of the more complicated models). It is of great interest to know the mantle structure in some detail since each discontinuity or change in gradient implies there is a fundamental change in the properties of the mantle at that depth.

Improvements were made in our knowledge of mantle structure with the application of synthetic seismogram modeling. As well as using the information above, models can be tested by predicting the waveforms for a particular model and comparing them directly to the data. Early modeling of upper mantle P-waves was done by Helmberger and Wiggins (1971) and Wiggins and Helmberger (1973) using short-period data. Burdick and Helmberger (1978) and Given and Helmberger (1981) applied the technique to more stable long-period data. One of the very few studies of shear structure using this technique was done by Helmberger and Engen (1974). They found a smoother shear structure with more subdued discontinuities than many of the previous models had shown.

A second approach taken to discover the elastic velocity structure in the mantle has been to measure the dispersion of surface waves. Fundamental mode surface waves sample the upper few hundred kilometers of the mantle along their entire paths. The amplitudes are generally large to great distances and thus, they provide a means of investigating the upper mantle over the entire earth as opposed to the more regional bodywave studies discussed above. To sample below 100 km depth one must examine long-period modes with long wavelengths, thus, the surface wave data can not resolve the finer structure of the mantle. The great value of surface waves, however, is that by measuring the dispersion of many surface waves over great distances one can investigate the lateral variations in shear velocity over the earth in an average sense. Early important papers by Toksoz and Anderson (1966) and Kanamori (1970) divided the earth into oceanic, tectonic and shield provinces. They showed that there are fundamental differences in shear structure between the provinces to at least 200 km depth and maybe deeper. Many similar studies have been performed since then with finer regionalizations. An ambitious recent study by Woodhouse and Dziewonski (1984) has given maps of shear velocity variation for the whole earth to 600 km depth. Determining the lateral variations in velocity is just as important as determining the vertical structure. The dependence on temperature of shear velocity can be used to interpret the lateral velocity variations in terms of the convection patterns in the earth. These studies are also relevant to understanding the chemical composition of the earth.

This thesis is a continuation of the attempt to find the elastic velocity structure in the earth. In particular, the shear velocity distribution beneath the North American plate and some adjacent regions from just below the crust to about 1700 km depth is studied. The goal has been to determine more detailed shear velocity profiles beneath different tectonic provinces including the size of the gradients in the upper mantle and the position and size of any discontinuities which may exist. A second goal has been to determine the nature of the lateral heterogeneity within the mantle for the region of study. This includes the depth to which there are differences in structure correlated with the surface tectonics and also, to determine the nature of any other lateral heterogeneity which may exist.

Chapter 1 is a comparison study of the upper mantle shear structure beneath the tectonically active western part of North America and the stable Canadian shield. Models are derived for shear velocity as a function of depth to 800 km beneath the two regions. The technique used combines some features from both the bodywave and surface wave approaches. As in surface wave studies, the later arriving energy, relative to the S-wave, is modeled so that areas which can only be sampled by event-station geometries of great distance can be investigated. The later arrivals generally travel at more shallow depths and thus, even if the S-wave is sampling below the upper mantle, these later arrivals can sample the upper mantle along their ray paths. In surface wave studies, these later phases are considered as the interference of higher modes. This thesis, however, uses bodywave theory to model them as multiply-reflected shear waves. Synthetic seismograms are used to model these arrivals and derive compatible structures which predict the waveforms. Bodywave concepts such as travel-time and triplications are employed to understand the waveforms and allow one to intuitively adjust structures to predict the data.

Chapter 2 is a study of the upper mantle beneath the northwest Atlantic ocean. The techniques developed in Chapter 1 are used in this chapter also. The thin oceanic crust produces arrivals not encountered in the continental regions and there is some discussion of the difference between continental and oceanic wave propagation. The region of this study comprises an area of old oceanic crust and thus with Chapter 1, models are derived for representitive areas of the old earth regionalization schemes: shield, tectonic and ocean (Toksoz and Anderson, 1966). Significant differences are seen to at least 350 km depth for the three regions.

Chapter 3 is an attempt to determine a fully three-dimensional model of the shear velocity beneath the North American plate. The experience gained in Chapters 1 and 2 allowed us to understand the ray paths followed by phases observed in seismograms. The arrival times of the phases were measured relative to a starting model for many paths crisscrossing the North American plate. With known travel-time delays for known ray paths, we used a tomographic inversion technique discussed by Comer and Clayton (1986) and Humphreys (1985) to derive a laterally varying model of shear velocity to 1700 km depth. Variations were observed at all depths, though the largest variations occur above 320 km depth. An interesting pattern seen below 700 km depth may be related to past subduction of the Farallon plate.

Finally, the conclusion discusses the relation of the work in this thesis to other mantle studies. Some general implications for the earth's upper mantle are also discussed.

Chapter 1

Upper Mantle Shear Structure of North America from S and SS Phases

Introduction

Upper mantle shear velocity structure and lateral heterogeneity have important consequences for geochemical and geodynamic modelling of the earth. Past efforts at looking at this problem have generally used the dispersion of surface waves or the travel times of teleseismic bodywaves. Recently, Nakanishi (1981) regionalized the earth according to tectonic provinces and inverted great circle phase velocities to derive regional upper mantle shear models. Cara (1979) used Rayleigh wave overtones, to increase resolution, and derived Pacific, western United States and eastern United States upper mantle shear models. Both studies found very large differences in velocity in the upper 200 km from region to region, but much less heterogeneity at greater depths. Unfortunately, the resolution in these studies decreased with depth and heterogeneity of a few per cent below 200 km may not have been resolvable. Furthermore, due to the long wavelengths used, surface wave studies provide little information on the fine structure of the upper mantle, such as the position and size of discontinuities and the gradients in between.

In another approach Sipkin and Jordan (1975, 1976, 1980) and Okal and Anderson (1975) have used the travel times of multiple ScS waves to investigate mantle shear heterogeneity. These studies all found travel-time anomalies but their interpretation has remained ambiguous. Okal and Anderson (1975) claimed that the surface wave and ScS data could be satisfied with heterogeneity above about 200 km whereas Sipkin and Jordan (1980) need differences between oceans and continents extending to at least 400 km. At present it is agreed that there are large differences in shear velocity above 200 km associated with surface tectonic features, but the shear structure and its lateral variation below that depth is still being debated.

Bodywave studies in the distance range 10–30° offer better resolution of upper mantle structure due to the fact that seismic energy, at these ranges, is bottoming between 150 and 800 km and the wavelengths are short relative to surface waves sampling these depths. There have been numerous studies using the travel-times and $\frac{dT}{d\Delta}$ measurements of short period P-waves in this distance range. Several examples are listed in the introduction. Due to greater attenuation, however, short-period S-waves from shallow earthquakes are rarely observed. Recently, a technique of matching synthetic seismograms to P-waves recorded on long-period WWSSN instruments has proved very fruitful (Burdick and Helmberger, 1978; Given and Helmberger, 1981). The waveforms between 10° and 30° have been found to be stable yet sensitive to upper mantle velocity structure. Helmberger and Engen (1974) used the same procedure to explore the shear velocity structure of the United States and southern Canada. Well-located west coast earthquakes were used in that study to determine accurate travel-times which provided constraints on the modelling process. They found it was necessary to use only SH motion as shear coupled PL-waves produced large spurious secondary arrivals on seismograms with appreciable SV energy (for a discussion of shear-coupled PL see Baag and Langston, 1985). This greatly decreased the available data, yet the method proved successful in modeling the 400 km discontinuity. A limitation of these studies is that sources and receivers must be within 30° of each other. For that reason, at present there are few areas that can be studied with this technique alone.

In this chapter, we follow the approach of using synthetic seismograms to model long-period SH waveforms to investigate the upper mantle shear structure under North America. To extend the data set, SS phases between 30° and 60° as well as S-waves from 10° to 30° are used. The SS phase, in this distance range, travels almost entirely in the upper mantle and passes through two major triplications in the same way as S-waves between 10° and 30°. Since the SS travel time is double that of S for a similar raypath, the SS triplication branches are separated in time by twice as much as the S branches and thus, they are easier to identify. Heterogeneities in the upper mantle also produce large changes in SS due to the long time spent in the upper mantle.

In Fig. 1.1, synthetic S- and SS-waves predicted for two upper mantle models of roughly the same area are compared. Both models were derived from data which propagated through western North America. Model SHR14 (Helmberger and Engen, 1974) was derived from SH bodywaves and has three first-order discontinuities. WUS was derived from Rayleigh wave overtones (Cara, 1979) and has a much smoother variation of velocity with depth. The models are displayed in Fig. 1.2. The S-waves are aligned at zero time and the amplitudes are normalized so that the S-waves are of equal amplitude. At these distances, S has a simple waveform. SS is the following phase. Note that the SS waveforms are very different at almost every distance, and that the SS-S times between 30° and 40° differ by nearly 30 sec. The SHR14 model predicts very clear interference patterns due to its large jumps in velocity near 400

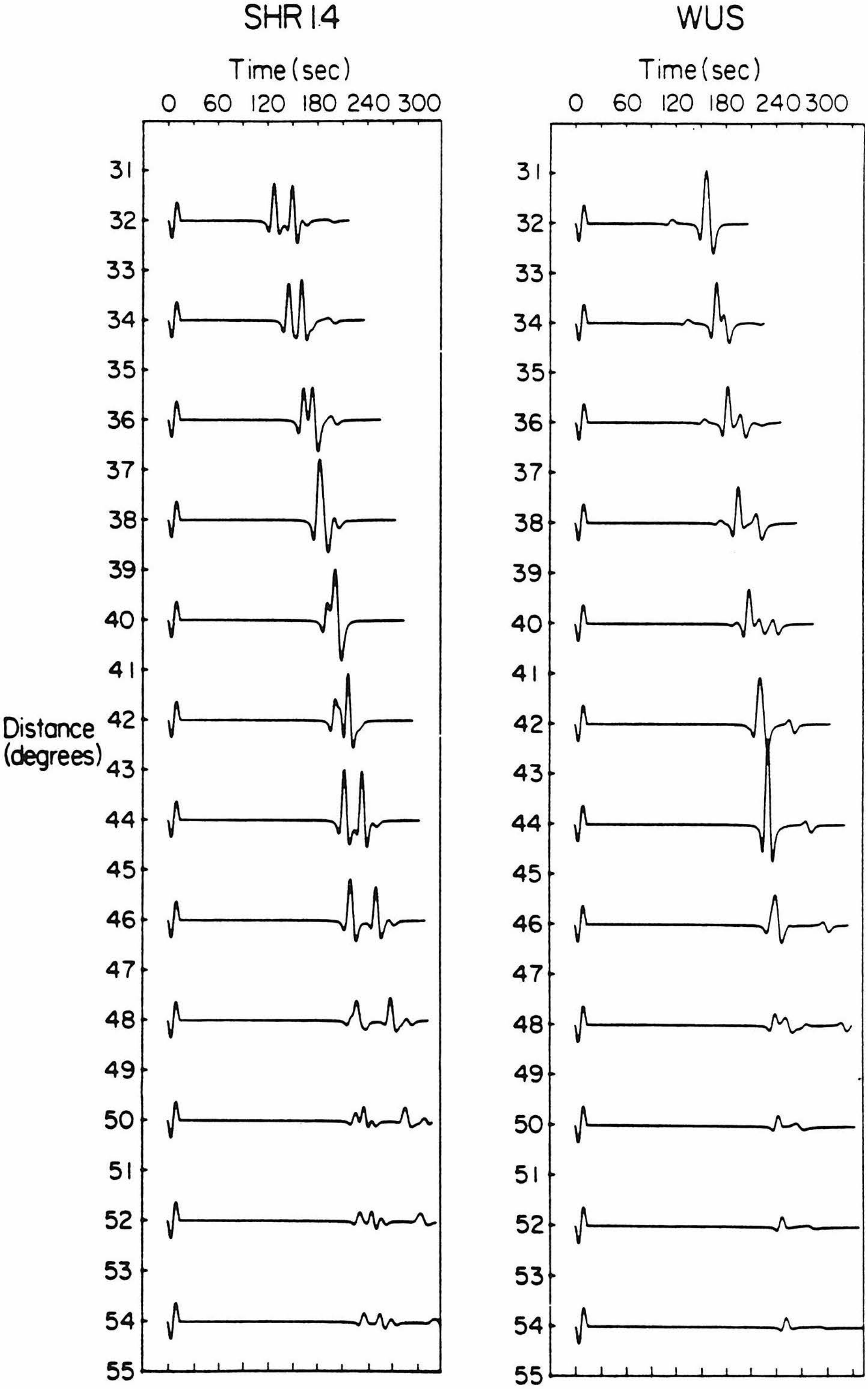

Figure 1.1 S and SS synthetics for two models of the western United States, SHR14 (Helmberger and Engen, 1974) and WUS (Cara, 1979). The S-waves are aligned at zero time and normalized to equal amplitude.

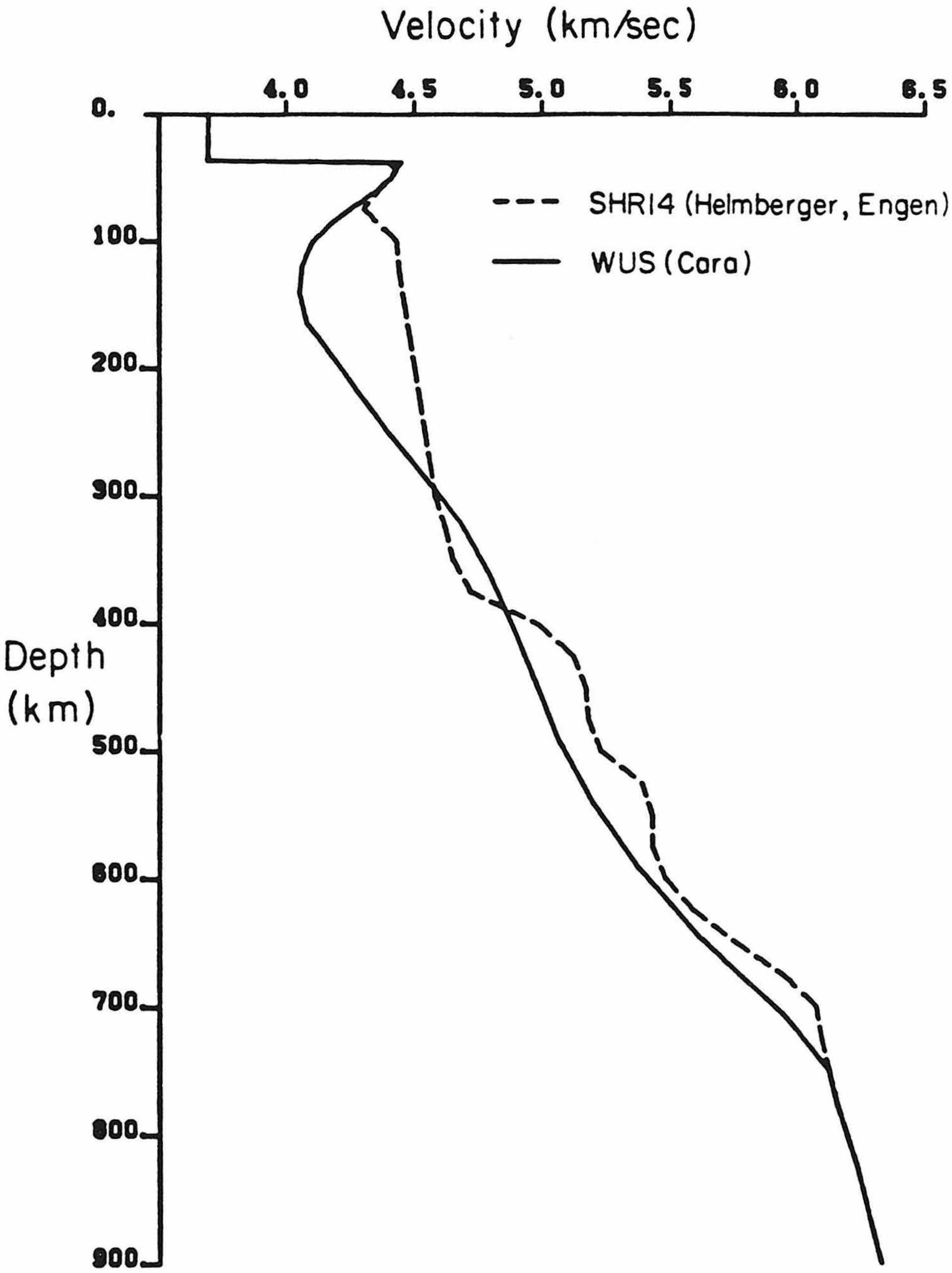

Figure 1.2 Velocity structure of models SHR14 and WUS.

and 660 km. These high gradient zones produce large secondary arrivals. Interference patterns, as predicted by SHR14, can be clearly seen in data such as is shown in Fig. 1.3. The data shown in this figure are typical of the seismograms produced by the many events that occur along the transform faults located in Southern California and the Gulf of California recorded in eastern North America. Note the similarity between the SHR14 synthetics near 36^o and the data near that range. The ray-paths of the arrivals producing this waveform are shown schematically in Fig. 1.4. As the distance increases the SS ray associated with the 400 km discontinuity overtakes the slower double bounce from near 200 km and a large single pulse is produced. This constructive interference occurs at 38^o in the SHR14 synthetics; whereas in the data, it occurs near 41^o. It should also be noted that the SS-S travel-times of the synthetics are too slow at distances less than 38^o. It is relatively easy to adjust the model to produce synthetics that fit these features by increasing the velocity in the upper 300 km. However, the travel-times and waveforms of the single bounce S-waves were fit well by SHR14. Thus it becomes apparent what the difficulty is: the velocity in the upper part of the mantle varies from west to east in North America, with increased velocities in the east. The upper part of SHR14 is based on the slower western velocity structure, and the faster SS arrivals observed in the east are due to much higher upper mantle velocities in the east.

To solve the problem of lateral velocity changes will require mapping out asymmetric paths, such as those in Fig. 1.3. To separate vertical from horizontal velocity structure in this fashion is a difficult problem. For this reason, we will begin this work by studying data we believe to have traveled mostly through laterally homogenous structure. This chapter will focus on paths beneath the East Pacific Rise and the

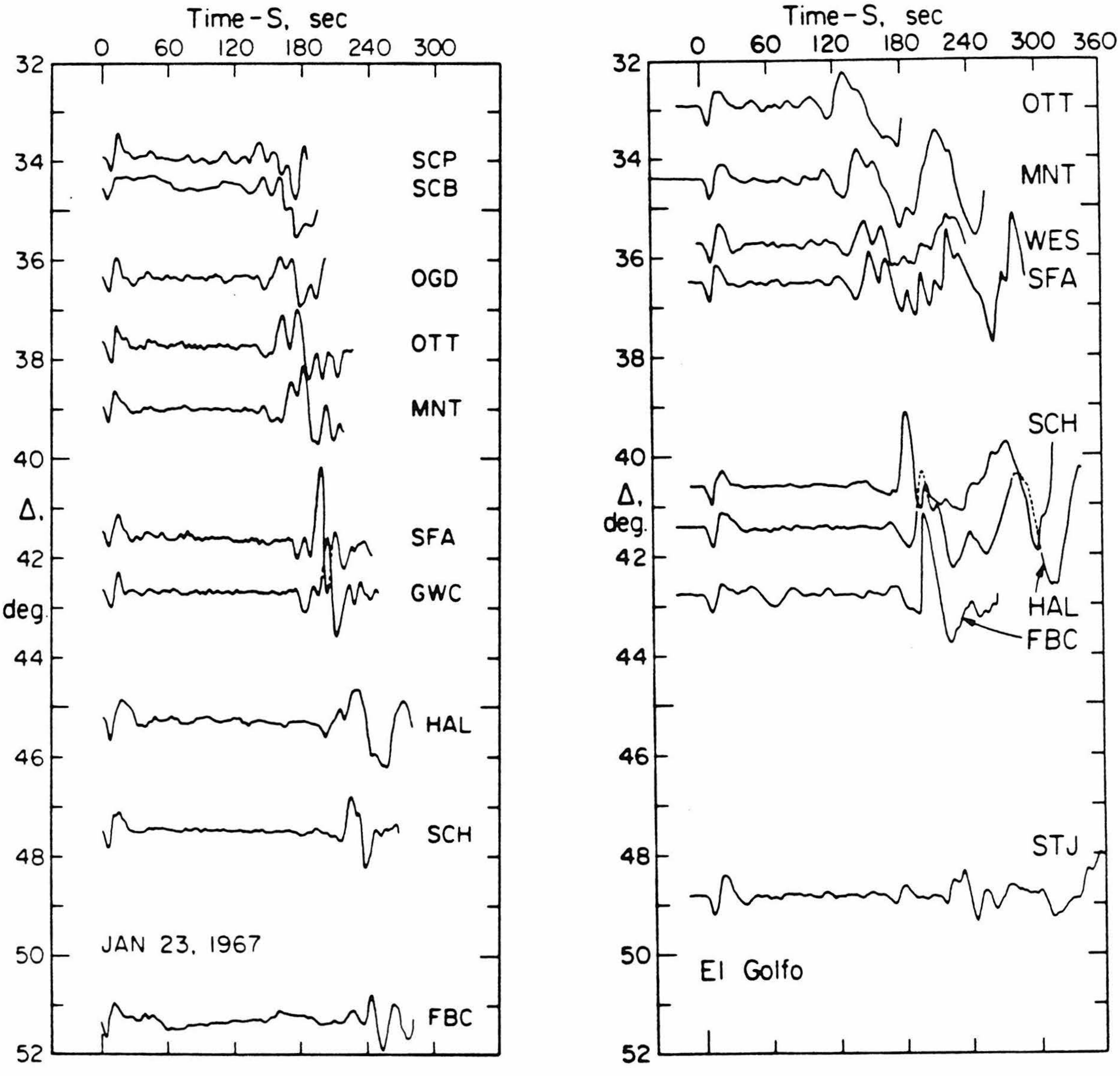

Figure 1.3 S and SS data from two earthquakes in the southwest of North America. El Golfo was at the north end of the Gulf of California. The event in 1967 was off the southern coast of Mexico. The locations of these events are given in table 1.2.

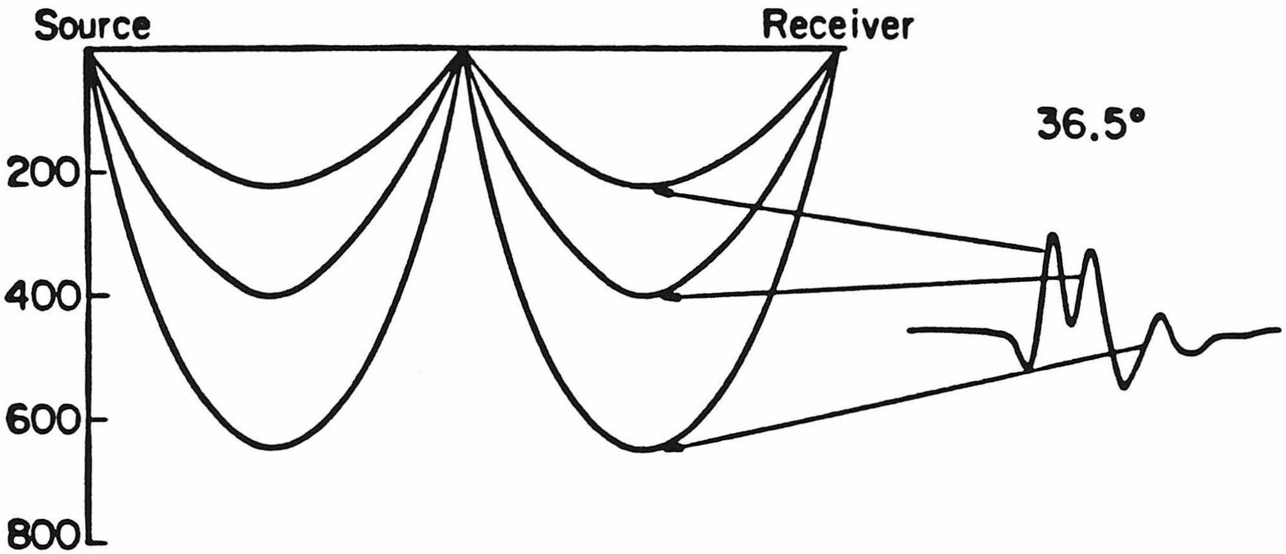

Figure 1.4 Schematic illustration of the arrivals producing an SS waveform at about 36^o.

Canadian shield. Vertical profiles can then be derived for the particular areas. Chapter 3 will deal with data as in Fig. 1.3 and a full three-dimensional model will be presented there. The results of modeling pure-path shield and rise data will be presented next, followed by a detailed documentation.

Results

A large data set with paths mainly in the stable Canadian shield or the more active western part of North America including the northern part of the East Pacific Rise was collected. In this chapter the two data sets are modeled separately to determine average vertical shear velocity profiles for the two areas assuming lateral homogeneity within the two data sets. The profiles are determined to 800 km depth with the deeper structure assumed to be given by the Jeffreys-Bullen model.

Fig. 1.5 shows a comparison of S and SS data which have propagated mostly in the Canadian shield with data from events on the East Pacific Rise recorded in western North America. The S-waves are normalized and aligned at zero time and pairs of seismograms at nearly the same distance are plotted together. For SH propagation the phase following S is SS until about 46^o, after which ScS arrives before SS. ScS can be best seen at MSO in this figure, about 3 min after the S-wave. The radiation patterns for these events are such that ScS is usually small relative to S and SS, and thus does not interfere significantly with SS near 46^o.

Fig. 1.5 illustrates most of the features of the two SS data sets we used. The obvious systematic differences between the two areas provided the motivation for looking at SS in more detail. Between 35^o and 39^o, in the tectonic data, SS is up to 5 times larger than the S-wave and is very simple in waveform. A small arrow indicates

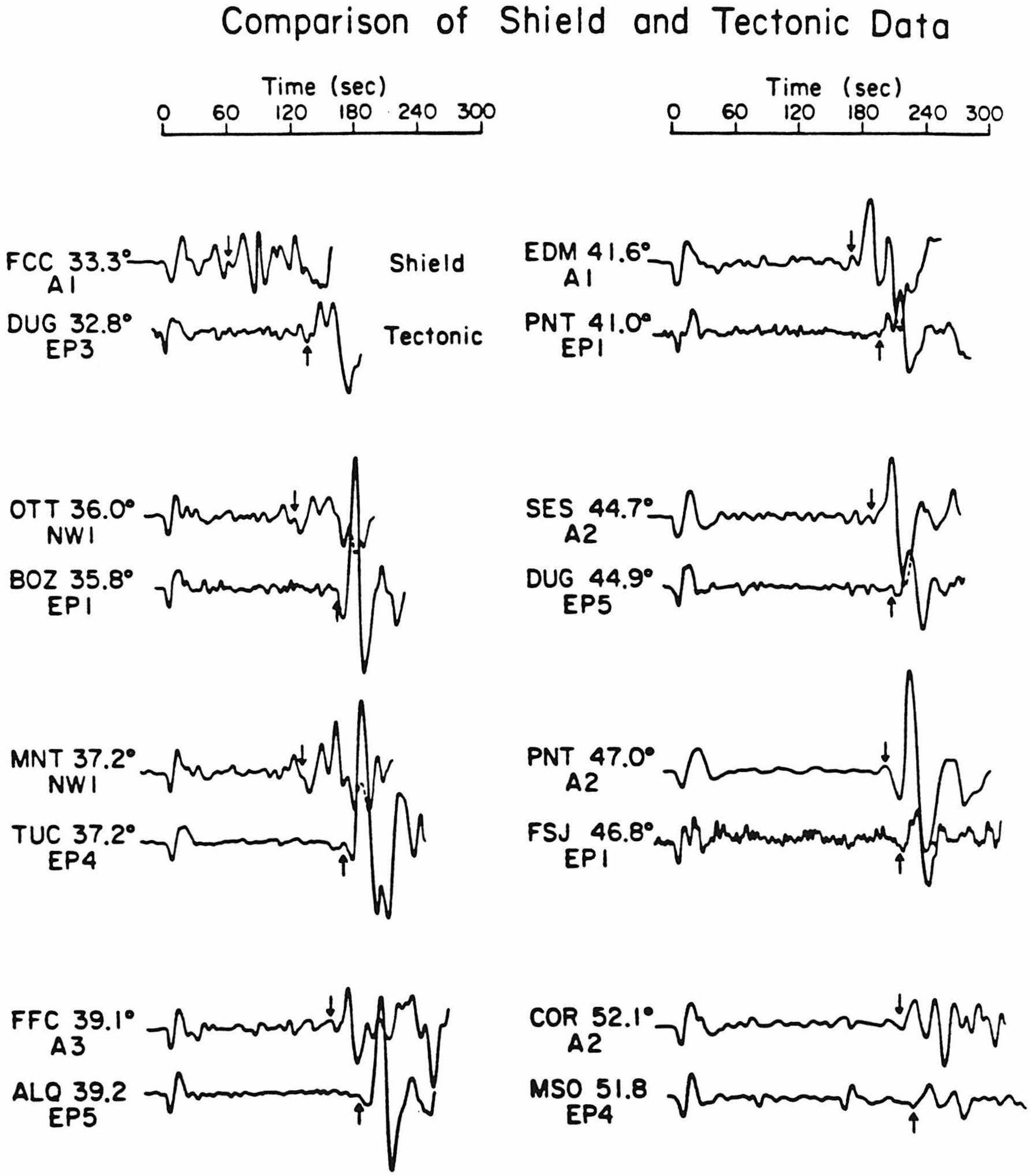

Figure 1.5 Comparison of S and SS data from the Canadian shield and tectonic western North America. The arrows mark arrivals discussed in the text.

the approximate onset of the phase. Notice the absence of any arrivals between S and the SS onset in the tectonic seismograms. In the shield data, however, there is no large single arrival which can be identified as SS at these distances. At OTT and MNT there is some very low amplitude energy followed by a double arrival, marked by an arrow, of about the same amplitude as the S-wave. At FFC, this arrival is clearer and simpler in shape but the amplitude is still on the order of the S-wave amplitude. Note that at all three distances, the clear arrivals marked by arrows in the shield data have SS-S times 30s less than in the tectonic data. Near 33°, both the tectonic and shield records are complicated without any amplification of SS, but the shield record has clear arrivals after S more than 1 min before any arrival on the tectonic record. Beyond 40° the SS phase becomes more separated from the following Love wave and is thus easier to identify. In the tectonic data the SS amplitude decreases around 41° and the waveform undergoes changes with distance. At 41° SS has a double arrival appearance, at DUG it is very simple, but from FSJ to MSO two SS arrivals clearly separate out again. The shield SS also goes through changes in waveform, at 41° there are two clear arrivals, the phase becomes simple at 44.7° and 47° but at 52.1° there are again two clear arrivals. Note, also, the large amplification of SS at 47°. This is seen in all the SS data from the shield region between 45° and 48°. The travel-time anomalies change through these distances also. At 41° the SS-S time for the shield seismogram is still 30 sec less than for the tectonic one. Beyond 44° this difference decreases to about 12 sec and remains the same to 60°.

The features of the SS data mentioned above, for the two areas, are consistent with a large body of data. This chapter derives two relatively simple upper mantle shear models (Fig. 1.6) which predict the properties given above. The mantle

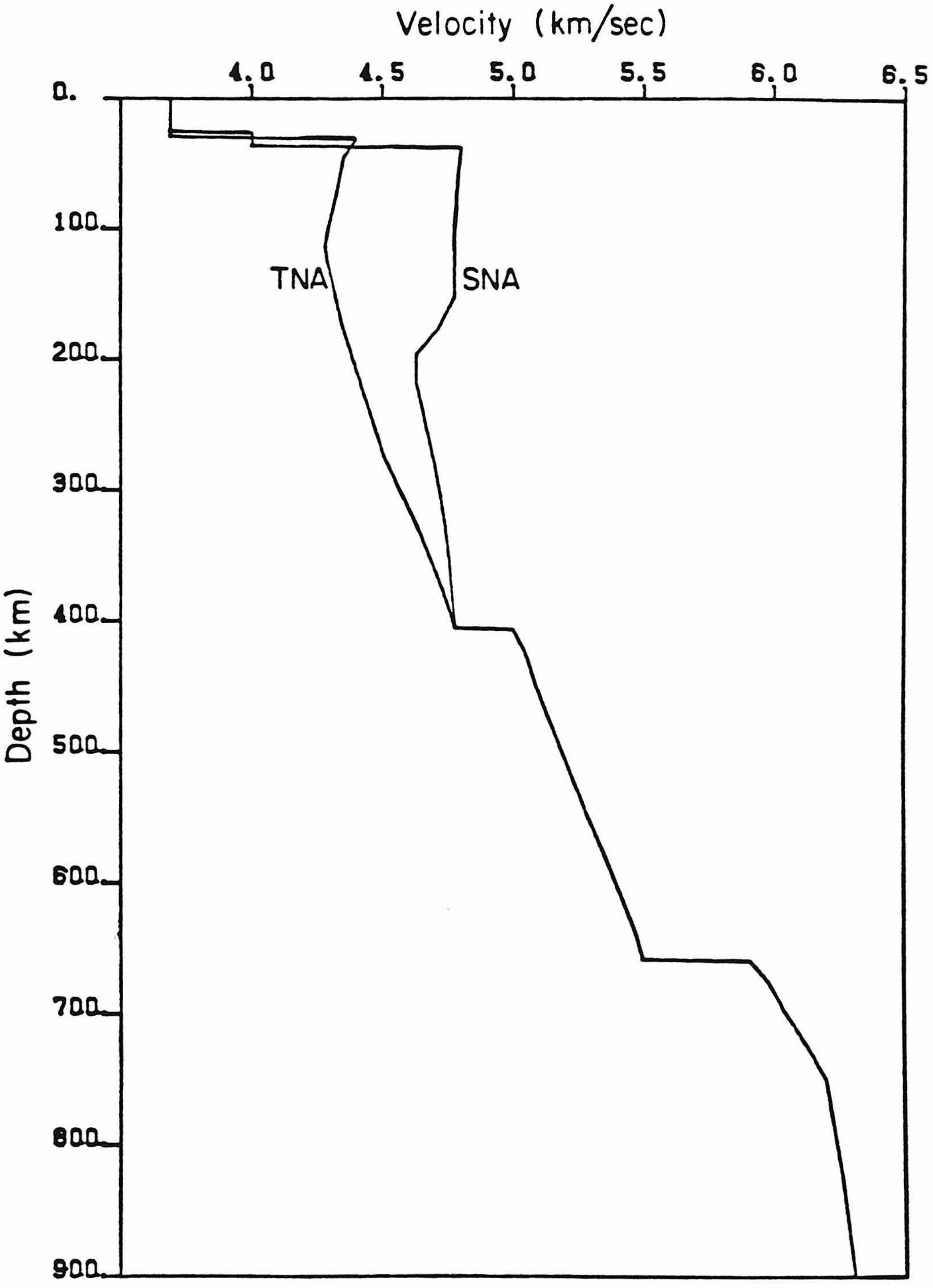

Figure 1.6 Tectonic (TNA) and shield (SNA) models.

Table 1.1 : Velocity Models TNA and SNA

Depth km	TNA km/sec	SNA km/sec	Depth km	TNA km/sec	SNA km/sec
38.0	4.400	4.800	550.0	5.290	5.290
50.0	4.350	4.790	575.0	5.345	5.345
75.0	4.320	4.775	600.0	5.395	5.395
100.0	4.290	4.775	625.0	5.445	5.445
125.0	4.290	4.775	658.0	5.500	5.500
150.0	4.320	4.775	660.0	5.910	5.910
175.0	4.350	4.710	675.0	5.980	5.980
200.0	4.390	4.630	700.0	6.050	6.050
225.0	4.430	4.640	725.0	6.130	6.130
250.0	4.470	4.670	750.0	6.200	6.200
275.0	4.510	4.695	775.0	6.220	6.220
300.0	4.570	4.720	800.0	6.240	6.240
325.0	4.630	4.740	825.0	6.260	6.260
350.0	4.680	4.755	850.0	6.275	6.275
375.0	4.730	4.765	875.0	6.290	6.290
404.0	4.780	4.780	900.0	6.305	6.305
406.0	5.000	5.000	925.0	6.320	6.320
425.0	5.050	5.050	950.0	6.335	6.335
450.0	5.090	5.090	975.0	6.350	6.350
475.0	5.140	5.140	1000.0	6.365	6.365
500.0	5.190	5.190	1025.0	6.385	6.385
525.0	5.240	5.240	1050.0	6.405	6.405

velocities are given in Table 1.1. The variations in SS waveforms can be explained by two first-order jumps in velocity of 4.5% at 405 km and 7.5% at 659 km. The differences in the data from the two tectonic provinces are due to the large heterogeneity above 400 km. These models differ by 10% in the upper 170 km and by about 5% at 250 km with the difference progressively becoming less below. No resolvable heterogeneity was found below 400 km. In the following sections the data and methods will be discussed in more detail.

Technique

The approach of this study is essentially the same as that of Helmberger and Engen, (1974). As they have shown, it is necessary to use only SH energy when modelling shear waveforms for upper mantle structure due to shear-coupled PL contamination. With this in mind, data were selected from recordings at WWSSN (World Wide Standard Seismic Network) and CSN (Canadian Seismic Network) stations from strike-slip earthquakes only at azimuths which were near P, SV nodes and SH maxima. Further, most of the seismograms used are very nearly naturally rotated into radial and tangential components. Visual inspection of the radial component enabled detection of data with strong SV signals. Unless otherwise mentioned, all the data shown will be the instrument component nearest the tangential direction.

The models were constructed using two sets of information. First, S and SS-S travel-times were used as a first-order constraint on the structure. The SS-S travel-time has a couple of advantages over traditional S-wave travel-times. Localized source area anomalies will affect S and SS nearly the same. Since most earthquakes are in tectonic areas, this is an advantage when one wants to isolate the structure of a stable region like the Canadian shield. Secondly, when looking for lateral heterogeneity with SS-S times, source location errors are less important since $\frac{dT}{d\Delta}$ is much less for SS-S than for S times. Since SS is a maximum time phase (Choy and Richards, 1975) it is usually emergent. For this reason the SS-S times were found by a visual correlation of data with synthetic seismograms. This was first done by Butler (1979) to look at SS times for SS waves with midpoints beneath the Canadian shield. The second set of information used were the waveforms and amplitudes of S and SS. The structure of the upper mantle causes complicated SS waveforms between 30° and 60°. To understand these features, we used synthetic seismograms computed for many possible models. By trial and error, models were found that fit the waveforms within the travel-time constraints.

As in past studies using waveform analysis, synthetic seismograms were constructed by convolving linear operators representing the different factors in the makeup of a seismogram (Helmberger and Burdick, 1979). We can write a synthetic, Y(t), as

$$Y(t) = S(t) * I(t) * A(t) * M(t) \tag{1.1}$$

where S(t) is the source, I(t) is the instrument response, A(t) is an attenuation operator and M(t) is the Green's function for elastic wave propagation through the mantle.

The source for SH propagation consists of the earthquake time function and the S-sS surface interaction. For shallow strike-slip events, the relative strength of S and sS does not change significantly with distance and the separation in time changes only slightly in the distance range we are using (Helmberger and Engen, 1974). Also the polarity of S and sS is the same at all distances. With this in mind, when constructing synthetic S or SS for a particular earthquake, we used a typical teleseismic S-wave from that event as both the source and the instrument response. This assumes the elastic propagation effect for a teleseism is essentially a delta function. The S-wave source then contains the earthquake time function and any complexity in it, the S-sS interaction, the instrument response and, to first order, any local source or receiver effects. The S-wave also contains the effect of attenuation which will be discussed next. Some instruments had a different response from the majority of the others. In these cases we used an S-wave at that station as the source for SS.

The anelasticity of the earth is not known well and therefore we used the constant t^* approximation from previous studies to account for it (Helmberger and Engen, 1974; Burdick and Helmberger, 1978). This assumes Q is lower in the upper part of the mantle so that t^*, the travel-time divided by the average Q along the ray-path, remains constant with distance. Thus for synthetic S-waves the source wavelet, taken as a teleseismic S-wave, also contains the attenuation operator A(t). The SS-waves travel twice through the upper part of the mantle and therefore should be attenuated more than the S-waves. To model this effect a Futterman Q operator (Futterman, 1962; Carpenter, 1966) was convolved with the source when making synthetic SS. We used a t^* of 3.0 sec for SS in the tectonic region and a t^* of 1.5 sec for the shield synthetics. These values were derived by fitting the synthetic S to SS amplitude ratio to the best quality data. Since the interference pattern mapping is only weakly sensitive to Q, these assumptions appear reasonable although a joint inversion at a later time should be conducted.

The S(t), A(t) and I(t) operators are assumed known and we are left with the effect of elastic wave propagation through the mantle as the only variable. Two well-documented methods were used to construct Green's functions for mantle propagation. Most of the trial and error modeling was done using the WKBJ technique of Chapman (1976, 1978) and Wiggins (1976). These seismograms are most accurate for high frequencies and structures with smooth gradients. The velocity model was interpolated using the Mohorovicic law, $V(r)=ar^b$ (Dey-Sarkar and Chapman, 1978), between given depth-velocity points. The discontinuities are modelled as regions of very high gradient over 3 km. The vertical radiation pattern of a strike-slip event was used. The SS phase is easy to compute using the WKBJ method. Essentially, one computes an S-wave at half the distance and doubles the time spacing between the points. The phase shift due to the SS caustic (Choy and Richards, 1975) is accounted for by applying a Hilbert transform to the S waveform. No interaction between the discontinuities is computed, that is, there are no rays reflected from the 400 km discontinuity, the free surface and then off the 660 km discontinuity.

As a test of the WKBJ method for SS, synthetics were also computed by a Cagniard-de Hoop technique (Helmberger, 1973) for the two models derived in this chapter. In this technique the earth is approximated by layers of constant velocity. No external Hilbert transform is needed for SS rays. To construct SS, we summed all generalized rays which had a free surface reflection and two reflections within the depth range of interest for the phase. The large number of rays needed make this method impractical for modelling the SS phase. The travel-time curves for the two models are shown in Fig. 1.7. We will generally refer to branches by single letters. They will denote the two arrivals forming the cusp designated by the letter. With long-period data the two geometric arrivals forming a branch usually cannot be distinguished. When there is the possibility of confusion in the branch names the full

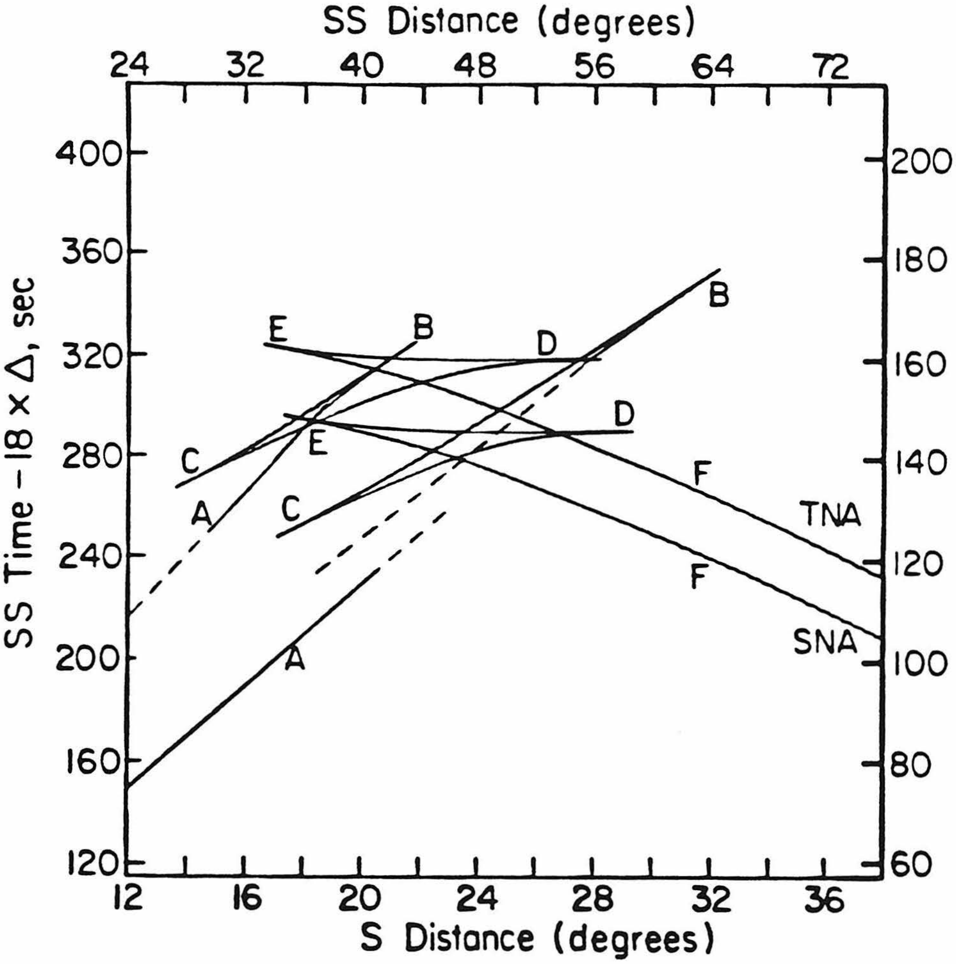

Figure 1.7 Travel-time distance curves for models TNA and SNA. The branches for both models are labelled the same and are referred to extensively in the text. The axes show both the S times and distances and the SS times and distances. The SS travel-time curve is just double the S travel-time curve.

designation will be given. In Fig. 1.8, synthetics computed using both the Cagniard-de Hoop and WKBJ methods are compared with the tectonic model as the structure. Both S and SS are computed and the S-waves are normalized to equal amplitude. The comparison for this model is excellent, the only major discrepancies being at 30° and 55°. At 30° the largest arrival in the generalized ray synthetic is much smaller in the WKBJ synthetic. This arrival is branch A of the SS phase and at 30° it is still in the shadow of the thin lid. The WKBJ method does not model the tunnelling of long-period energy through the lid while the Cagniard-de Hoop method does, and this is probably the reason for the difference in amplitude. Between 50° and 55°, the SS phase consists of two arrivals, branches D and F. The amplitude decay of arrivals from branch D beyond the end of the triplication occurs more rapidly in the Cagniard-de Hoop synthetics. This is actually true off the ends of all the triplication branches though the differences are not very large. Note, however, that in general the waveforms are very similar, indicating that the Hilbert transform is an accurate approximation for the phase shift of SS. Also the relative amplitudes of SS to S are close using the two techniques while the amplitudes change drastically with distance due to the structure.

The comparison for the shield model (Fig. 1.9) is not as good as for the tectonic model although the reasons for the differences are the same. The first large phase after S at 35° can be traced to near 45° with progressively decreasing amplitude. This is actually not the SS phase but is the B branch of the S-wave triplication which ends 12° earlier in the tectonic model. As in the tectonic synthetics, the decay of arrivals off the ends of triplication branches is faster for Cagniard-de Hoop synthetics than for WKBJ synthetics. The shield B branch of the S-wave is a good example of

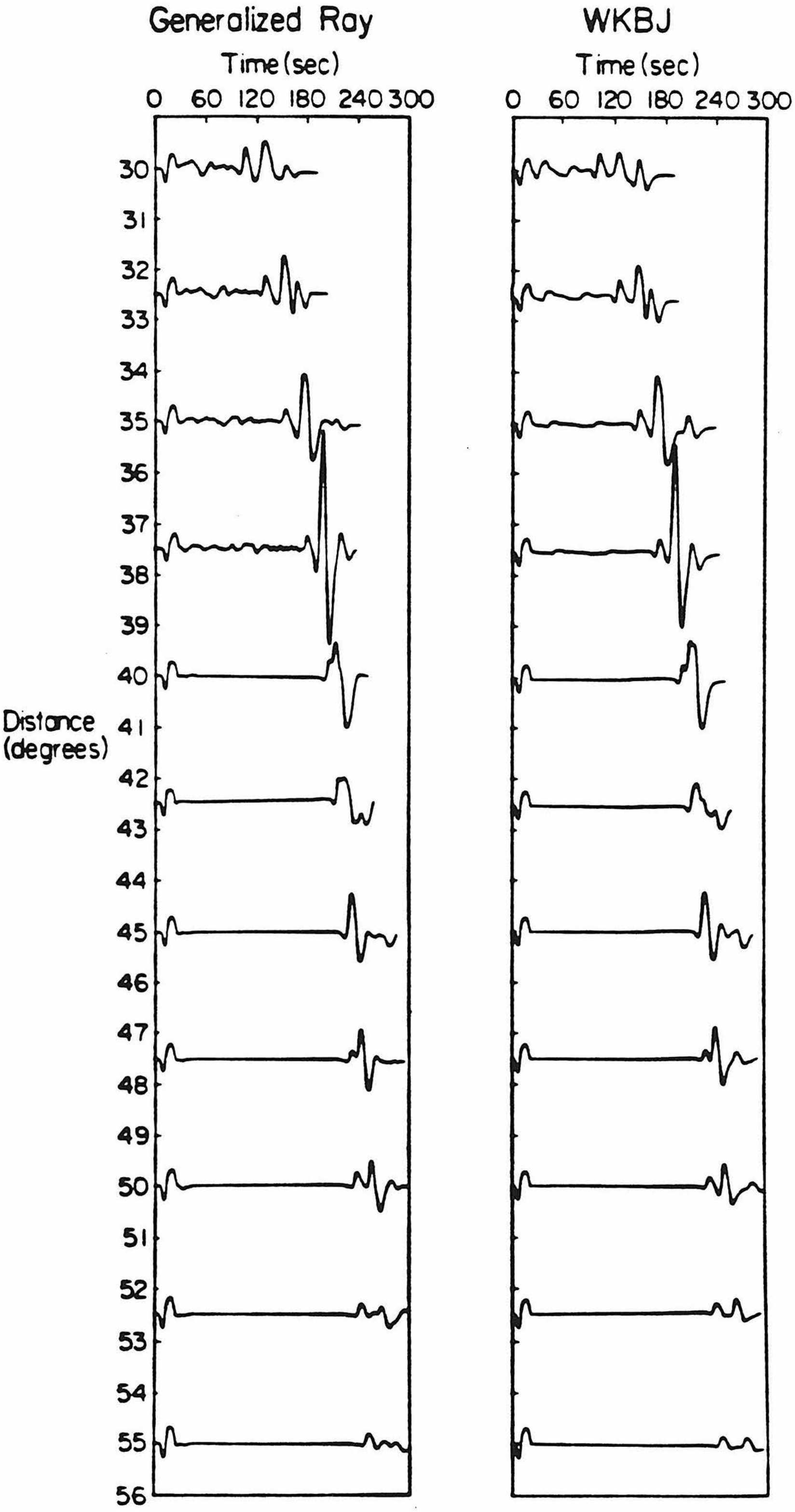

Figure 1.8 Comparison of generalized ray and WKBJ S and SS synthetics for the tectonic model.

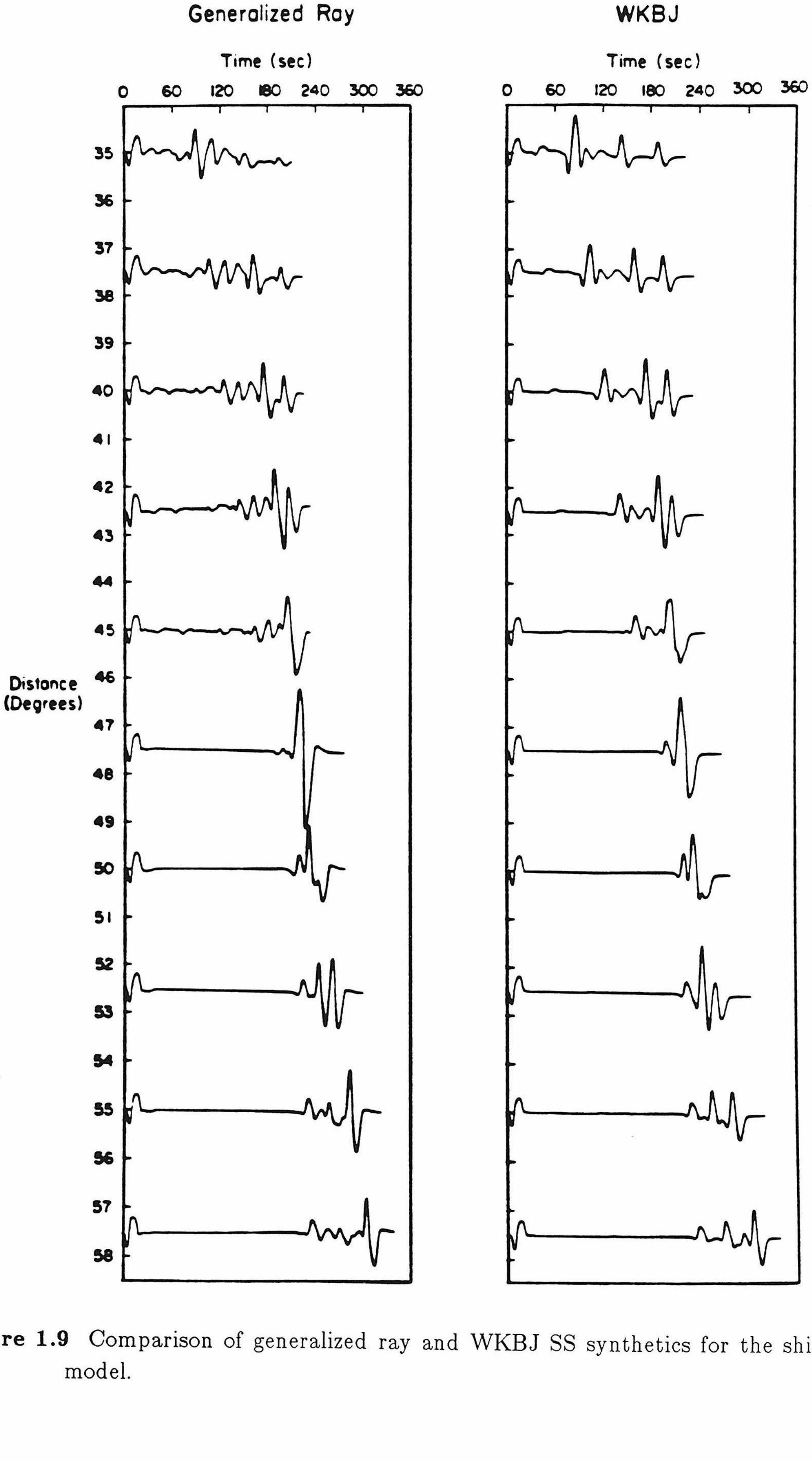

Figure 1.9 Comparison of generalized ray and WKBJ SS synthetics for the shield model.

this. Between 52° and 58° the synthetics also show some disagreement. There are three arrivals in SS at these distances, branches B, D and F. The second arrival, branch D, decreases faster in the Cagniard-de Hoop case as one goes off the end of the triplication, as mentioned before. The third arrival, branch B, is much larger in the Cagniard-de Hoop synthetic however. This is probably due to the lack of tunneling with the WKBJ technique. Part of branch B for SS between 50° and 55°, as can be seen in the triplication curve, is still in the shadow of the thick lid. By 57.5° the amplitudes of these arrivals are about the same. This comparison also shows that interaction between the discontinuities is very small. For instance, at 40° and 42.5° the two largest SS arrivals are the C and E branches, which are reflections from the 405 km and 660 km discontinuities respectively. There is no apparent arrival between them in the Cagniard-de Hoop synthetics, indicating that the rays from the 405 km discontinuity to the surface and back to the 660 km discontinuity are of very low energy.

As stated before, the models were derived by trial and error using the WKBJ method. The discrepancies between the techniques, however, are large at some distances. Since the Cagniard-de Hoop method has been compared favorably with the reflectivity method (Burdick and Orcutt, 1978), the final models were adjusted slightly so that the generalized ray synthetics fit the data better. In the figures, at distances where the WKBJ-Cagniard-de Hoop comparison is poor we used the Cagniard-de Hoop technique. More work needs to be done on the validity of the two methods for constructing SS, but the differences we have found should not significantly alter the conclusions of this paper.

A potential problem with using the SS phase is a possible precursory arrival from a reflection off the underside of the Moho at the midpoint. To check its significance, a Cagniard-de Hoop synthetic was calculated including all the rays which reflect at the Moho as well as the free surface reflections for model SNA. The Moho was taken as a sharp jump in velocity from 3.7 to 4.78 km/sec. Fig. 1.10 shows a comparison at 46^o with and without these Moho reflections. The seismograms are only slightly different in the front, with no clear precursor in spite of the extreme model used for the Moho. This small effect was not considered in the modelling process.

Tectonic Model

The first problem encountered in a study like this is how to regionalize the data. The SS data appropriate for western North America and the East Pacific Rise is taken from the events shown in Fig. 1.11. All the events used in this study are listed in Table 1.2. Even within this data set there is obvious lateral heterogeneity. Fig. 1.12 shows the S and SS records at LUB and DAL for two events to the south of these stations. The distances are almost identical and the azimuths are close so location errors will not change this fact, but in both cases the DAL SS-S time is about 5 sec less than the time at LUB. This heterogeneity is probably close to the stations since the raypaths are nearly identical in the source region. Teleseismic S-waves also show a decrease in travel-time from stations such as GSC, TUC and DUG to LUB, JCT and DAL (Lay, 1983), although the differences are small. Similarly, in the north, travel-time studies such as that by Wickens and Buchbinder (1980) show a large horizontal gradient in velocity from west to east with stations FSJ and PHC slower than SES,

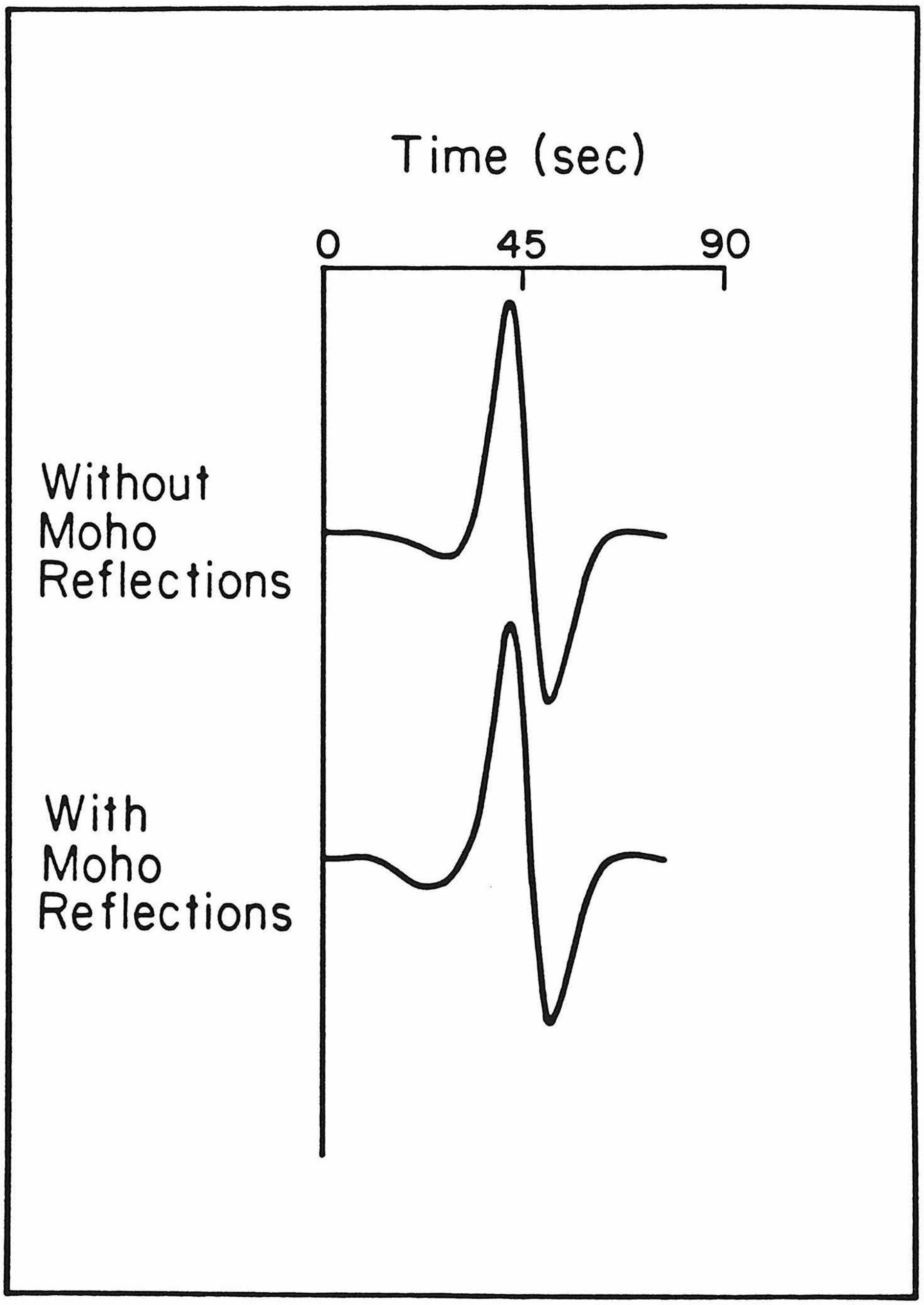

Figure 1.10 Comparison of an SS waveform with and without underside Moho reflections at the midpoint.

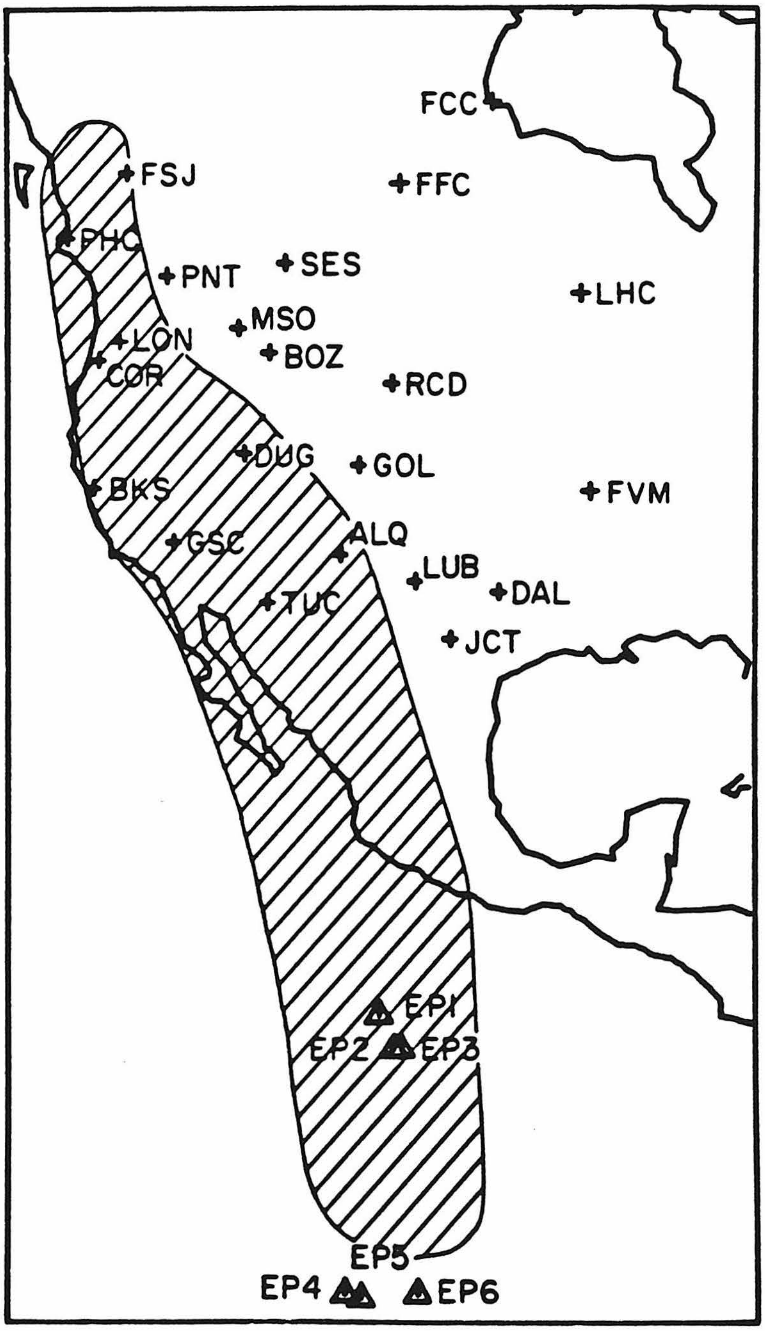

Figure 1.11 Map of events and stations used to construct model TNA. The shaded area is approximately the region of validity for the model. Great circle paths are straight lines in this projection.

Table 1.2 : Event Locations

Event	Date	Location	Origin Time
EP1	Sep 3, 1966	10.3° N, 104.1° W	1624:20.4
EP2	Jul 7, 1968	8.5° N, 103.3° W	2305:18.2
EP3	Oct 15, 1965	8.5° N, 102.9° W	0034:8.9
EP4	Jul 11, 1975	4.6° S, 105.0° W	0708:39.4
EP5	Sep 9, 1969	4.4° S, 105.9° W	1523:10.8
EP6	Sep 21, 1973	4.3° S, 102.1° W	0731:34.0
NW1	Mar 13, 1971	50.6° N, 130.0° W	2331:35.5
NW2	Dec 5, 1971	49.6° N, 129.5° W	0550:5.8
NW3	Feb 23, 1976	51.5° N, 130.4° W	1515:16.0
A1	Nov 23, 1967	80.2° N, 1.0° W	1342:1.6
A2	Oct 18, 1967	79.8° N, 2.4° E	0111:44.8
A3	Oct 26, 1971	79.8° N, 2.7° E	2053:32.4
B	Sep 4, 1963	71.3° N, 73.0° W	1332:8.0
ELG	Aug 7, 1966	31.7° N, 114.4° W	1736:22.8
BOR	Apr 9, 1968	33.2° N, 116.1° W	0228:59.0
HSV	Mar 15, 1979	34.3° N, 116.4° W	2107:16.5
TR	Sep 12, 1966	39.4° N, 120.2° W	1641:2.6
M	Jan 23, 1967	19.9^0 N, 109.3° W	2025:38.0

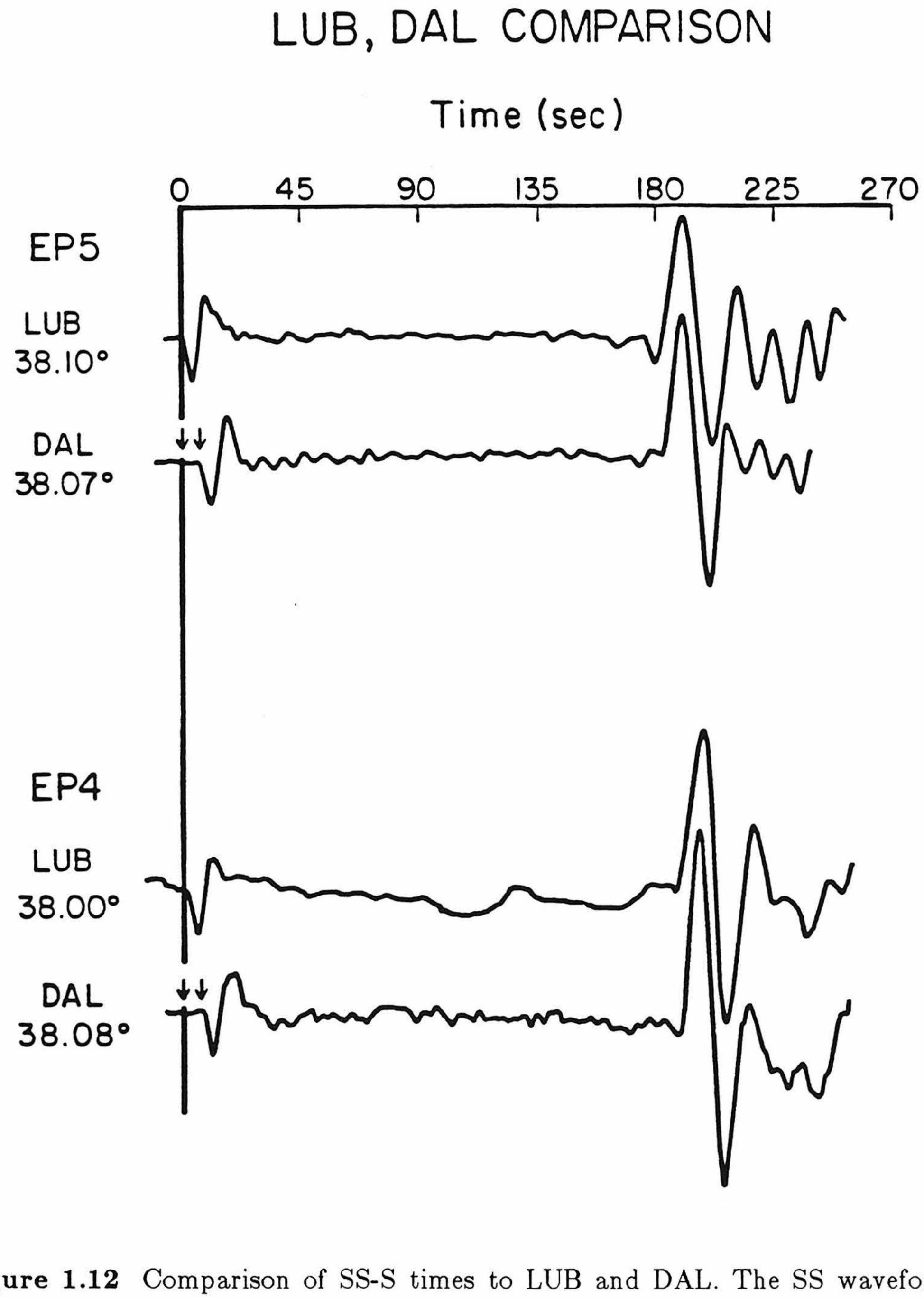

Figure 1.12 Comparison of SS-S times to LUB and DAL. The SS waveforms are aligned and the discrepancy in time becomes obvious as a relative shift in the onset of the S-wave.

for instance. We have made the assumption that the slowest areas in western North America and the region near the East Pacific Rise are of a uniform structure, aside from the crust. In situations where the East Pacific Rise SS data are double the distance of S-waves in western North America, the SS travel-times are twice the S travel-times to within a couple of seconds. Thus the tectonic model is derived from the slowest S and SS data and is appropriate for the shaded region in Fig. 1.11.

The crustal structure for western North America is taken as a 30 km thick layer with a velocity of 3.7 km/sec. For SS phases with midpoints beneath the ocean, a 6 km thick crust was used. A thin lid with a velocity of 4.4 km/sec was taken as an average for the area. This is close to results from Stewart and Pakiser (1962) using Sn data from the Gnome explosion. The lid thickness is arbitrarily set at about 35 km which is consistent with the thickness of the lid in Cara's western United States model (1979) and that of Priestly et al. (1979) for the basin and range. The S and SS waves used here are not very sensitive to the very shallow structure. The velocity below the lid and above 200 km has been determined using the absolute travel-times and waveforms of well-located events in Southern California. Fig. 1.13 shows the data on a map of the area used for this part of the study. At these distances the first arrival S energy is travelling above 200 km depth and thus the travel-times are very sensitive to the velocity there. The synthetics were computed using the Cagniard-de Hoop technique. All primary S rays to 600 km depth and also SS and SSS rays above 300 km depth were included. The effect of the SS rays is to broaden the first downward swing. The reflection from the 405 km discontinuity is most visible at FSJ as a secondary arrival. At LON it is interfering with the first arrival to produce a broad waveform but it is not visible as a distinct arrival. The structure proposed here for

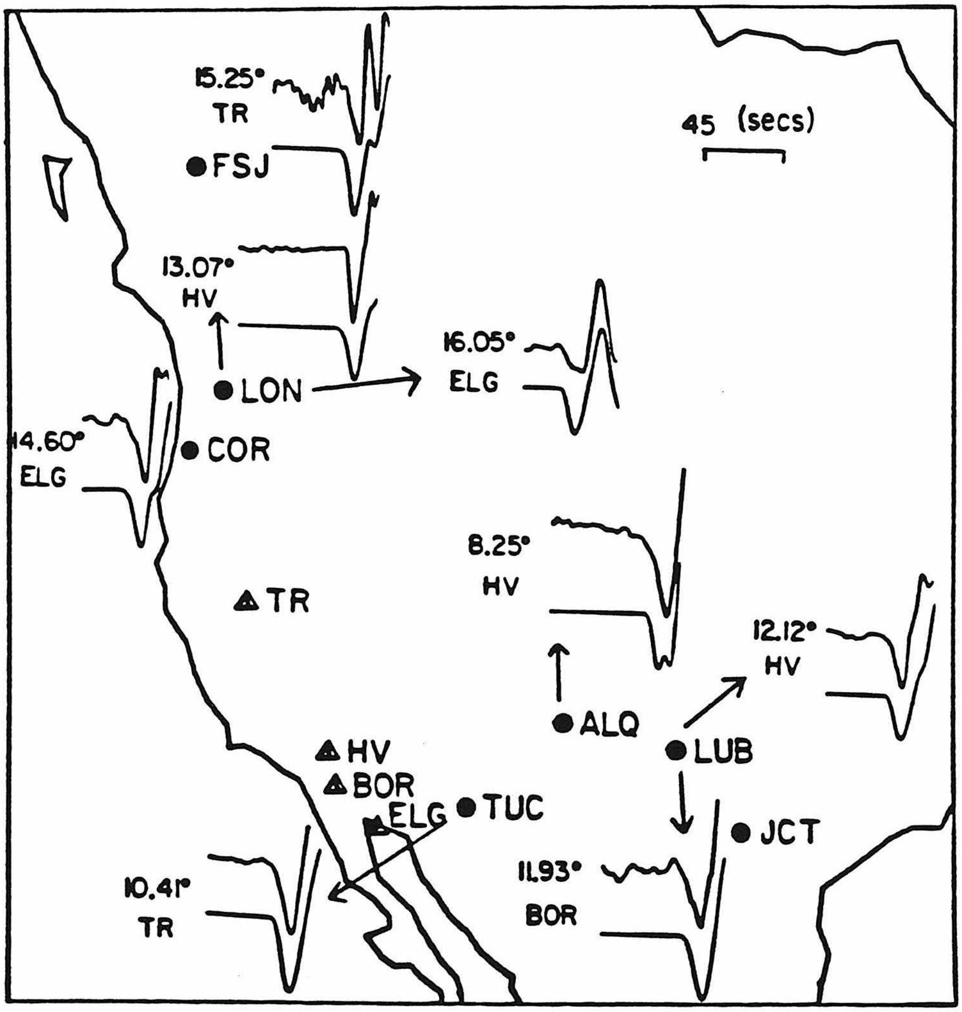

Figure 1.13 Data and synthetics used to derive the upper part of the tectonic model. The synthetics are beneath the data near the corresponding station on the map. The synthetic and data times are absolute.

the upper 200 km is given as an average. The data presented here do not have the resolving power to investigate the fine structure of the lid and low-velocity zone but the overall travel-time fits will not allow large velocity perturbations in this depth range.

The structure from 200 km to 400 km depth was derived from the data shown in Fig. 1.14. As can be seen in the triplication curve (Fig. 1.7), for the tectonic model, the SS phase from 30° to 36° should consist of two arrivals, the A branch turning at 200 km to 300 km depth and the C branch from the 405 km discontinuity moving progressively closer together with distance. These two arrivals are labelled in the synthetics to 32.8° and can also be seen in the data. The two arrivals cross near 36°. Between 30.8° and 32.8°, shallow generalized SSS rays were included in the synthetics. They cause the broadening of the first SS pulse at 30.8° and by 32.8° SSS constructively interferes with the arrival of the SS branch C. Beyond 33° the SSS rays and higher multiple arrivals are behind the SS phase and no longer interfere with the upper mantle SS arrivals. Therefore they are not included in the synthetics. They do contribute to the energy following SS at these distances. The small precursor to the SS branch A arrival from 30° to 37° is due to diffracted lid energy and a partially trapped wave in the low-velocity zone. Its appearance in the data is variable and we have not attempted to model it though it could provide information on the finer structure of the lid in this area. The very large SS amplitudes from 35.8° to 39° are due, not only to the constructive interference of branches A and C, but also because the branch A arrival is bottoming below 250 km and the gradient becomes very high there. It is interesting to note that a structure with a large discontinuity near 200 km depth and low gradients above and below it would produce a large arrival much

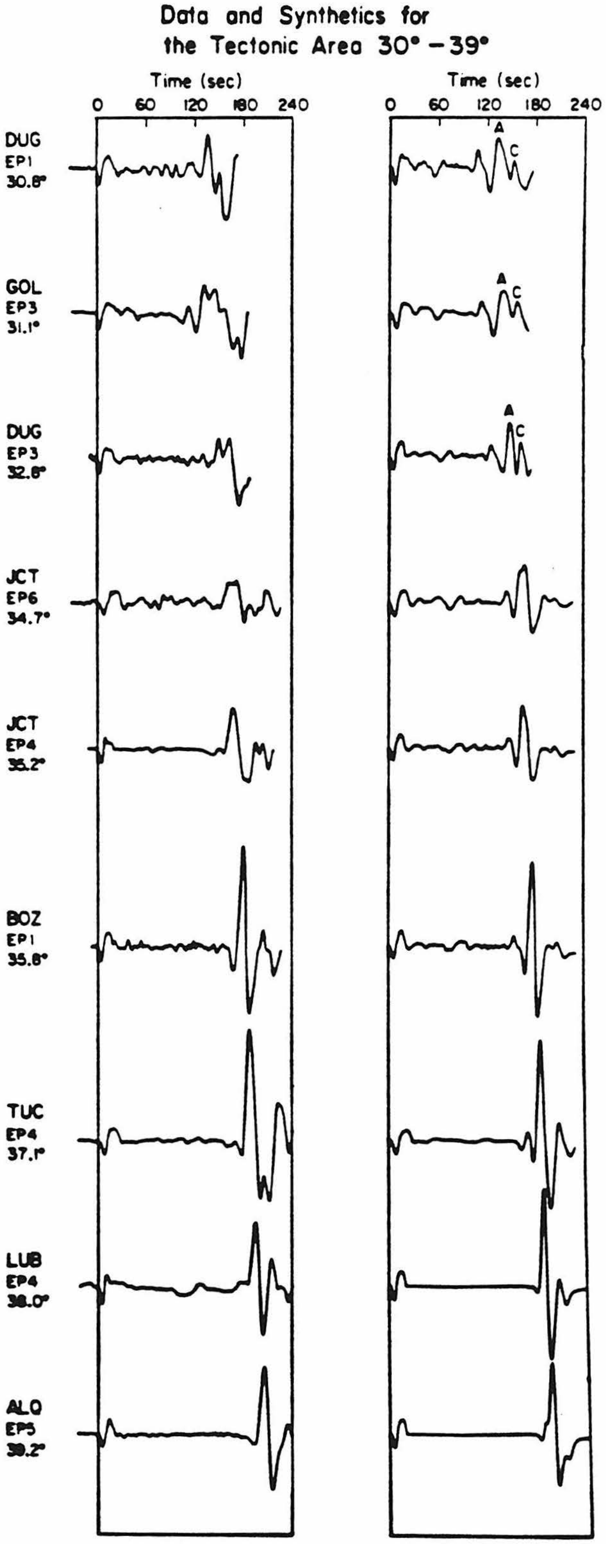

Figure 1.14 Comparison of tectonic S and SS data and synthetics using the TNA model. The synthetics are on the right and show the crossing of the A and C branches (Fig. 1.7).

earlier, between 28° and 32°, and would not predict the amplification observed near 37°. The amplitude at LUB is not fit well but this path is along the boundary of our tectonic province and perhaps lateral heterogeneity has affected the SS amplitude. Note that the SS-S times are fit to within a couple of seconds over the whole range. With the upper 200 km fixed these data give good resolution of the structure to 400 km depth. The identification of the C branch from 30° to 33° constrains the depth of the discontinuity to be near 405 km depth. An arrival from the 659 km jump (branch E) can be seen in the back of the synthetics, however, its presence in the data is unclear.

Fig. 1.15 shows the S and SS data from 41° to 45°. In this range the SS waveforms are dominated by the crossing of the EF and CD branches. These two arrivals cause the interference between 41° and 42.3°, by 42.9° they cannot be distinguished and near 44.9° they are crossing. Note that there is no evidence of branch B moving out of the SS waveform beyond 42°. At nearer distances this branch may be masked by the CD branch but by 42° the 400 km branch of the triplication is definitely of very low amplitude. The rapid decay of this branch is further evidence of the very high gradient from 250 km to 400 km depth. The separation of the EF and CD branches is unusual in long-period data. The S-waves from 20° to 21° in the western United States do not show separate arrivals as the time separation is too small (Helmberger and Engen, 1974). Since branch CD at these distances bottoms just below 400 km, these data put a tight constraint on the size of the discontinuity at 405 km depth. TNA has about a 4.5% jump in velocity there.

Fig. 1.16 shows the S and SS data from 46° to 55°. At these distances SS consists of two arrivals, the F and D branches. The separation begins near 46° and the

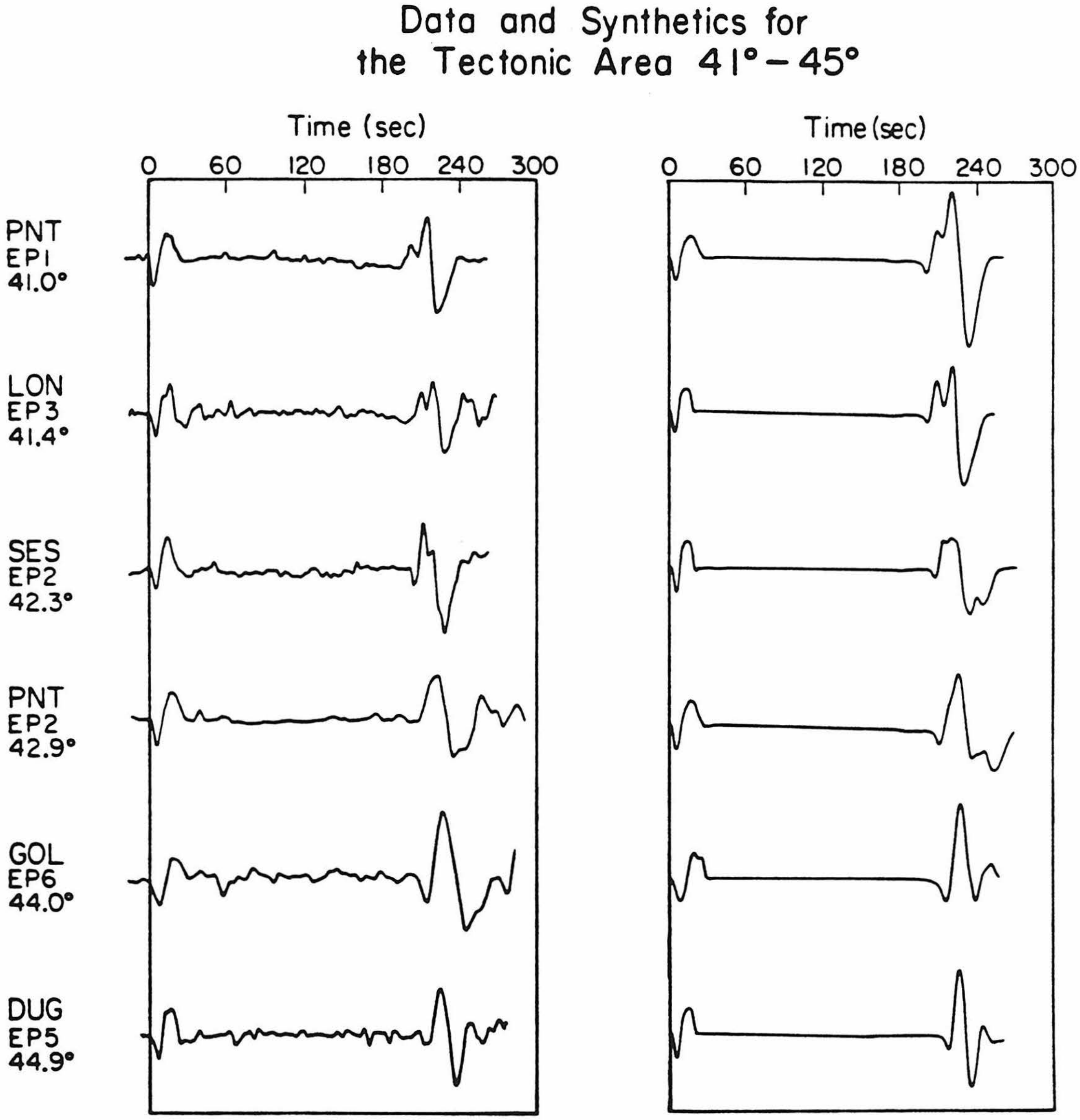

Figure 1.15 Comparison of tectonic S and SS data with synthetics using model TNA. The data illustrate the crossing of the EF and CD branches near 44.5^o .

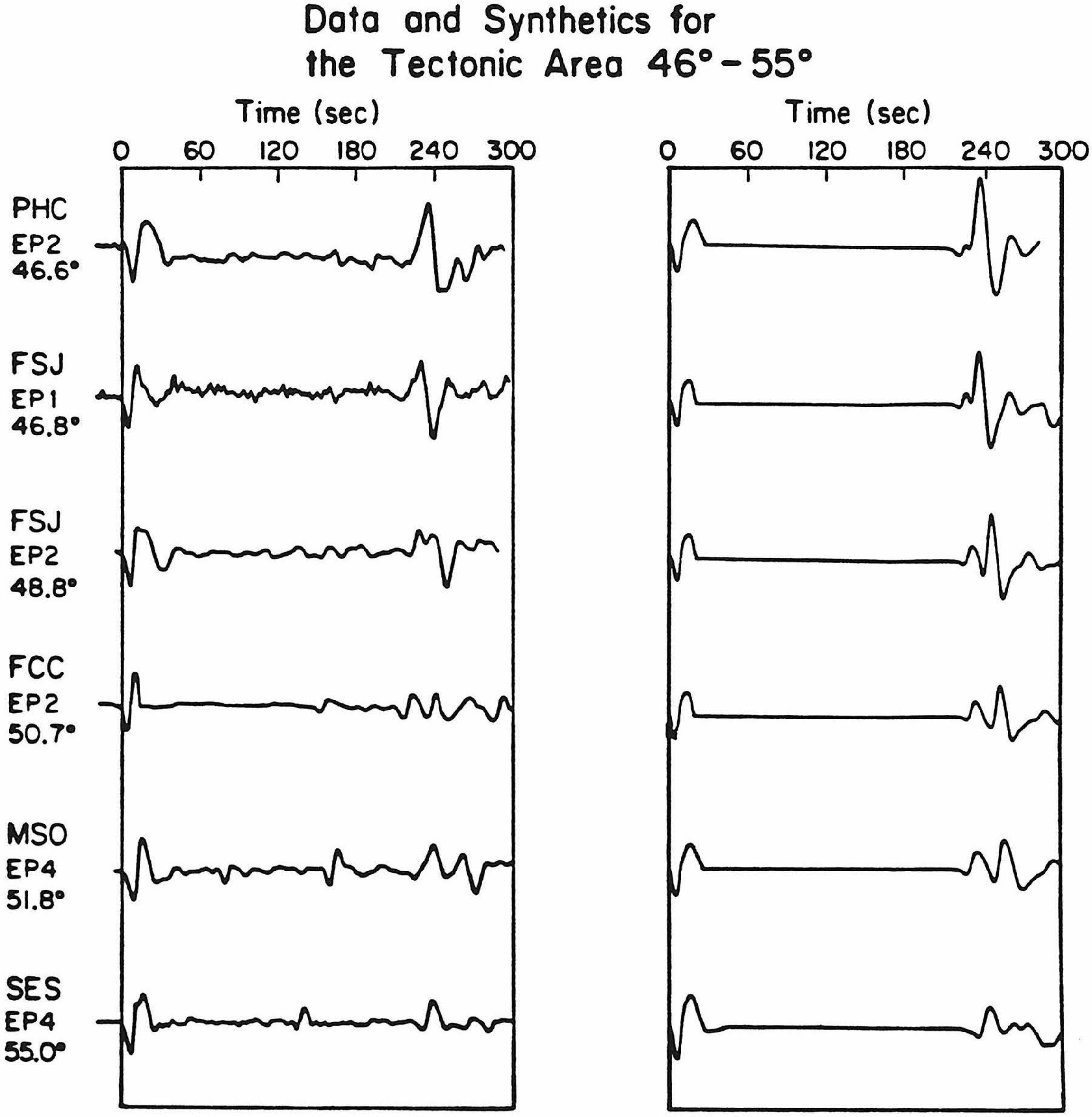

Figure 1.16 Comparison of tectonic S and SS data with synthetics using TNA. The separation of the F and D branches begins near 47°. From 50.7° to 55° ScS is visible between S and SS.

two arrivals become clear between 48° and 52°. By 55° the D branch has almost disappeared in both the data and the synthetics. The quality of the data in the range 46-48.8° is poor due to the stations being off the SH maximum and perhaps this is the reason for some of the misfit in amplitude. Note also that the SS-S time at FCC is fast, though the waveform is fit. This is expected as the midpoint for this path is east of the shaded region in Fig. 1.11. It was included here due to the scarcity of SS data in this range. Though the data set is small, it provides several constraints on the model. The gradient between 400 and 650 km must be, on average, high to model the decay of the D branch near 55°. Also the fast separation of the D and F branches, which are arrivals bottoming just above and below the 659 km discontinuity, indicate that the size of the discontinuity must be quite large. Finally the SS-S timing of the F branch constrains the absolute velocity below the discontinuity. Model TNA has a 7.5% jump in velocity there. The depth of the jump is constrained to be near 660 km by the observations at 41–43° of the E branch, a narrow angle reflection from this discontinuity. There has been some suggestion that between 400 and 600 km there is a further discontinuity near 530 km (Fukao et al., 1982). Using long-period S data, a small feature such as a 2% jump at this depth can not be resolved; however, a larger discontinuity should produce triplication branches separated enough from the arrivals from the 660 km discontinuity to be visible. No separate arrivals besides the D branch are observed. The mismatch in amplitude of the D branch in these data could be due to small-scale structure at these depths but there is no evidence of any large feature there. Just below 660 km the gradient is high relative to the gradient below 900 km, this was needed to match the SS-S times of the F branch and assumes the S times are correctly predicted by the structure below 900 km.

TNA was derived using SS data but there also exists a good S-wave data set from 22° to 30° which should show the D and F branches. Fig. 1.17 shows this data set with synthetics computed using TNA. These S-waves were taken from Given's study of shear structure (1984). The two branches begin to separate just beyond 24°, at 26.5° the two arrivals are well separated and both are large. By 29°, the D branch is a low amplitude long-period later arrival. The model derived from SS predicts the amplitude, moveout and decay of the D branch in the S data very well and confirms the identification of the arrivals in the SS data.

Shield Model

The shield model, SNA, was derived from two sets of S- and SS-waves. Figs. 1.18 and 1.19 show sources and receivers for the two areas. The midpoints of almost all the paths are within the Canadian shield. However, the events on the west coast of North America are probably within the tectonic region and some of the observations of the events in the Arctic were recorded at stations in the tectonic region.

There are very few shield S-waves at upper mantle distances, so SNA is derived almost entirely from SS data. There have been many observations of short-period Sn propagated to beyond 20° in shield areas (Brune and Dorman, 1963; Bath, 1966), indicating a thick, high Q lid. Surface wave studies have also found thick lids in shield regions (Brune and Dorman, 1963). Our model also has a lid about 170 km thick with a very high velocity of 4.78 km/sec. This feature completely changes the mode of propagation of S-waves. In Fig. 1.20 the synthetic construction of an S-wave at 18.8°, for model SNA, is illustrated. The Cagniard-de Hoop technique is used and, by adding successive groups of rays, one can see where the energy of visible arrivals

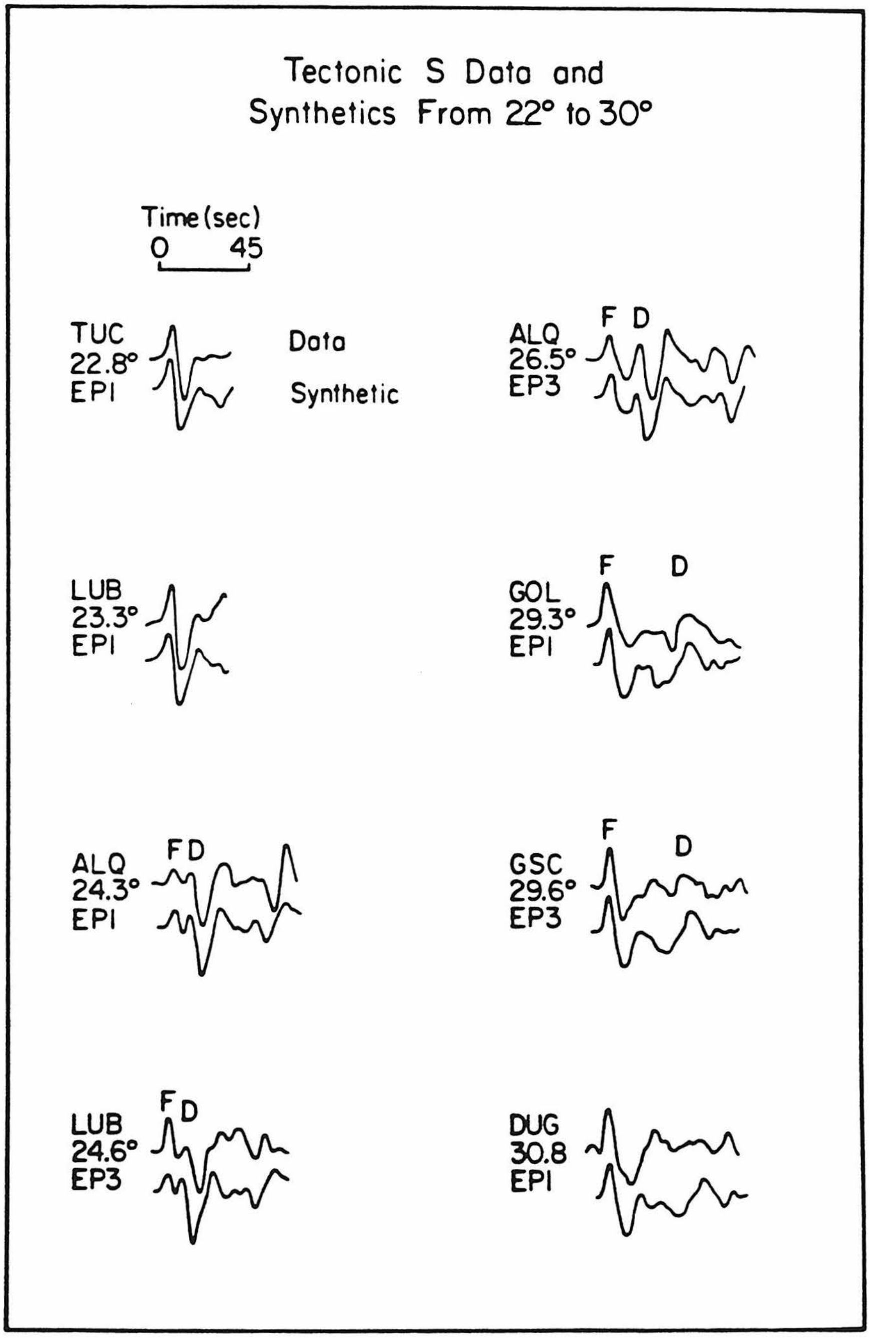

Figure 1.17 Comparison of S data with TNA synthetics. The data illustrate the same separation of the F and D branches as in Fig. 1.16.

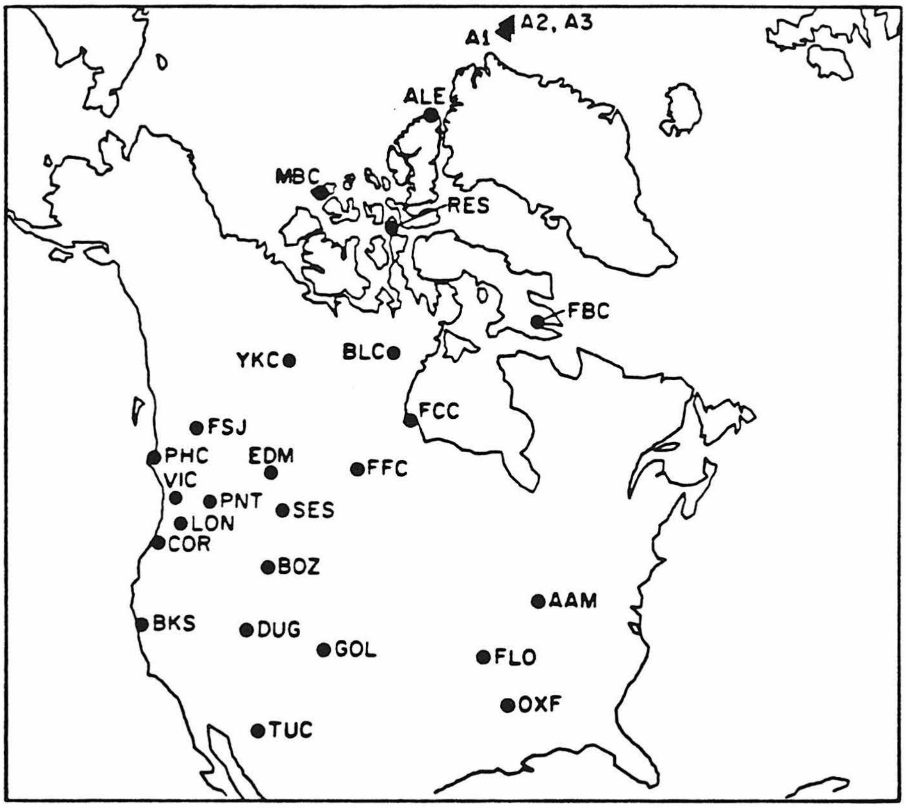

Figure 1.18 Map of events and stations used to derive the shield model (SNA). Great circles are straight lines from the events.

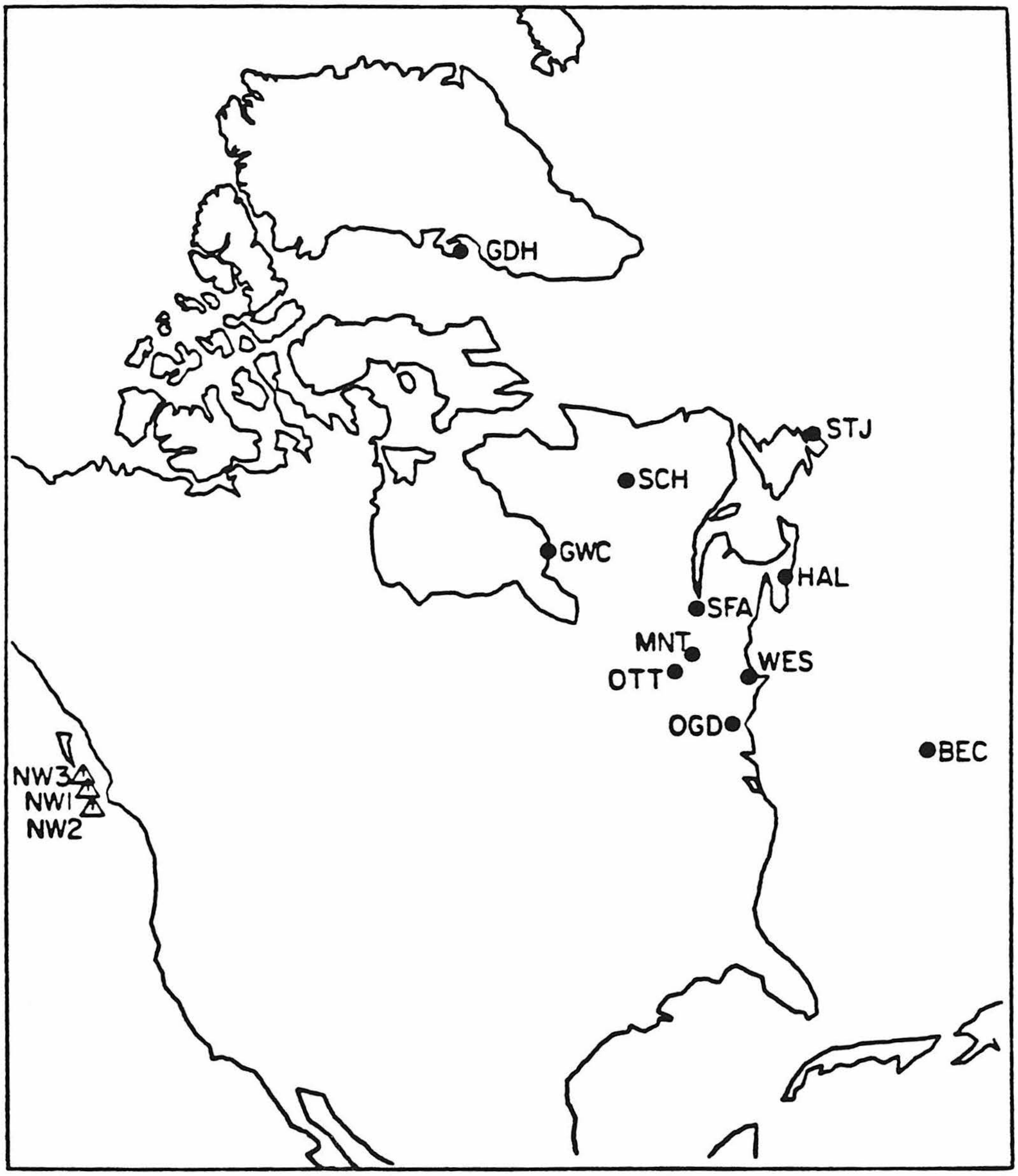

Figure 1.19 Map of western events and stations used to derive the SNA model.

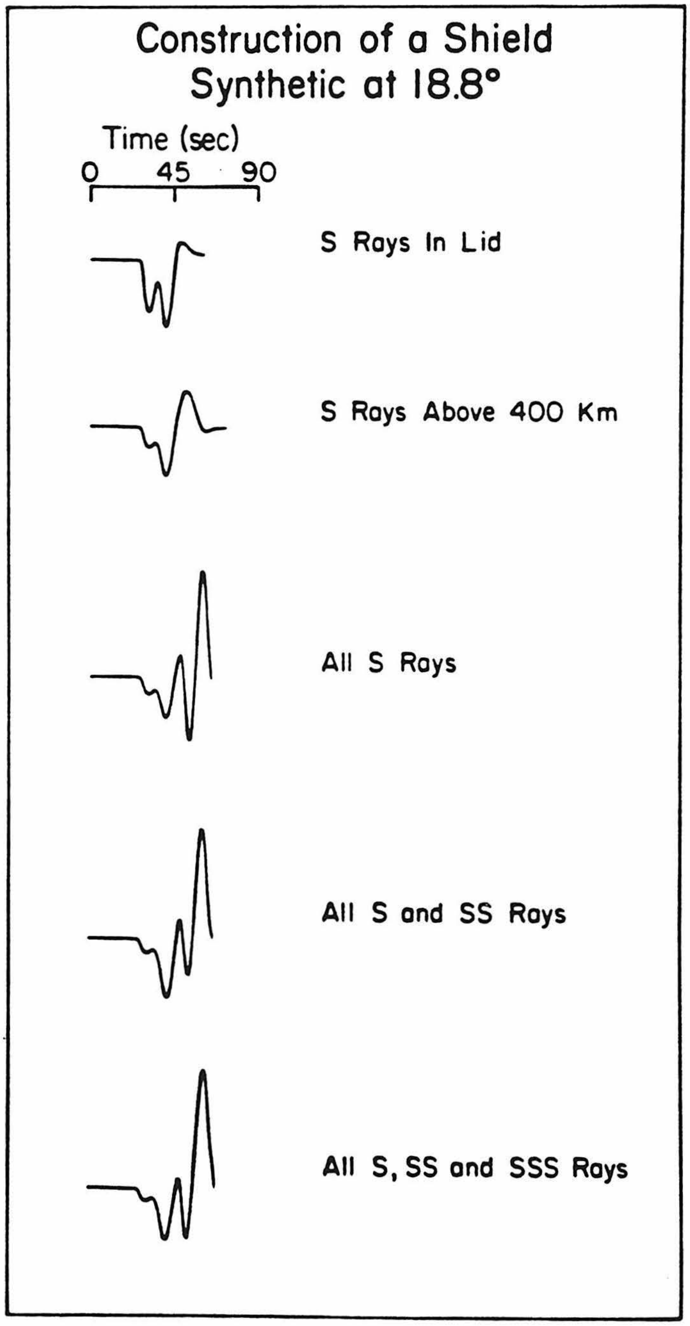

Figure 1.20 Illustration of the contribution of different groups of generalized rays to a synthetic at 18.8° for model SNA. Each progressive seismogram shows the effect of adding a new group of rays to the previous record.

comes from. This is very important in the modeling process. The first seismogram in Fig. 1.20 is due to S rays turning in the lid (branch A in Fig. 1.7). There is some tunnelling however, which adds a second arrival about 10 sec later, from below the lid. Rays below the lid but above 400 km depth are added in the second seismogram. The third seismogram contains the reflection from the 405 km discontinuity. As can be seen, it is larger than the other arrivals but is about 20 sec later than the first arrival. If we add in the SS rays, we find that SS in the lid arrives at the same time as the tunnelling S energy and well before the S reflection from the 405 km jump (the fourth seismogram). Finally SSS rays in the lid arrive at about the same time as the 405 km arrival. This complicated waveform contrasts with S-waves at 18^o in a tectonic regime as shown in Helmberger and Engen (1974). There the waveform is very large and simple, as the 405 km reflection is crossing with a diving ray from a gradient near 200 km depth. This also indicates that SS-waves will be very complicated at distances less than 38^o with many multiple bounce lid arrivals arriving before the SS mantle arrivals from below 200 km depth. This can be readily seen in the data.

With this in mind, a small data set of shield S-waves from 9^o to 19^o were modeled. The crust is taken as two layers with velocities of 3.7 km/sec and 4.0 km/sec. The overall thickness is 37 km. This is an average for the area (Berry, 1973), but its structure is not crucial to investigating the mantle. The data and synthetics are shown in Fig. 1.21. The absolute time of the first arrivals from 9^o to 19^o give the velocity in the lid. The mislocation of these events is unlikely to be more than 15 km which implies resolution of the lid velocity to about 1%. The waveforms are also fit to the extent of matching peaks by the technique used in Fig. 1.20. The 405 km reflection is identified with the help of SS data from 37^o to 44^o shown later. Note

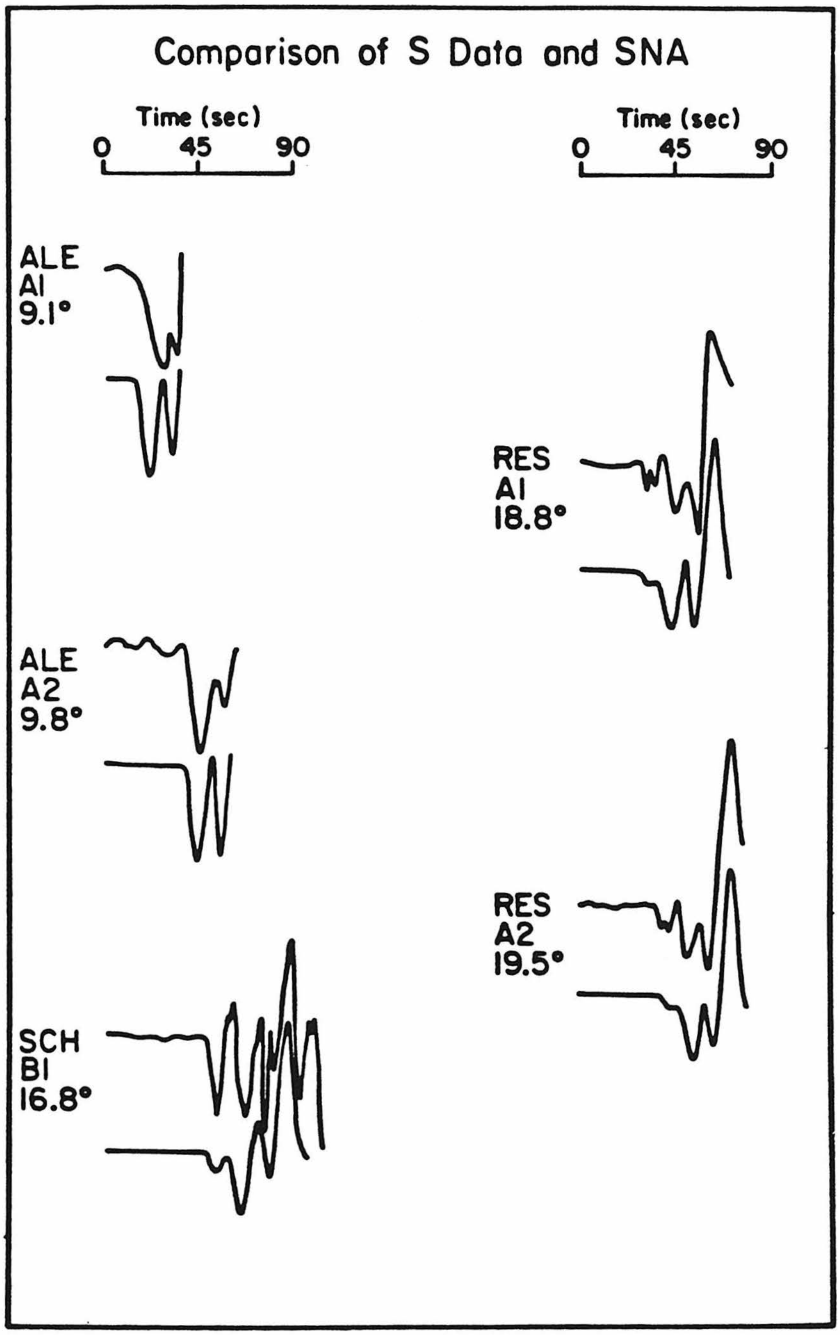

Figure 1.21 Comparison of S data from the Arctic events with synthetics computed using SNA. The timings are absolute between the data and synthetics assuming the sources are at 10 km depth.

that if the 4.78 km/sec velocity is extended to a depth of 400 km, the arrival from the discontinuity there would be much too early. Some decrease in velocity is necessary but this data set clearly does not resolve the depth and size of the low velocity region at all. A further problem with these synthetics is that the Q operator is assumed the same for all rays. This is probably not true since short-period arrivals are seen from the lid but not from energy diving below it (Brune and Dorman 1963). Including a more realistic Q structure may help fit these records better, for instance, by increasing the amplitude and frequency content of the first arrival at 18° and 19°.

The upper 400 km of the shield region was also modeled using SS data with the lid velocity and thickness of the lid assumed from the S-waves. Fig. 1.22 shows the shield data from 30° to 40°. The seismograms are much more complicated than the tectonic data at similar distances because of the lid. The branches in the synthetics are labelled with respect to the triplication curve in Fig. 1.7. Note the largest arrival at GWC, labelled Bs, can be followed out to 40°. This is the B branch from the S-wave triplication and corresponds to energy bottoming from 250 km to 400 km depth. Since this phase is part of the S waveform, it has not been attenuated in the synthetics. However, this arrival has spent almost as much time in the upper mantle as the following SS arrivals and probably should be attenuated as much as SS. This could be the reason for it being larger in the synthetics than in the data at FFC and GDH. In any case, Bs is clear in the data at shorter distances and this constrains the velocity between 200 km and 400 km fairly closely. Note that branch B ended more than 12° earlier in the tectonic region for S-waves. The Bs branch at GWC and SCH is slow by about 2 sec. This is most likely due to the fact that the first part of their paths is in the slower, tectonic part of western Canada.

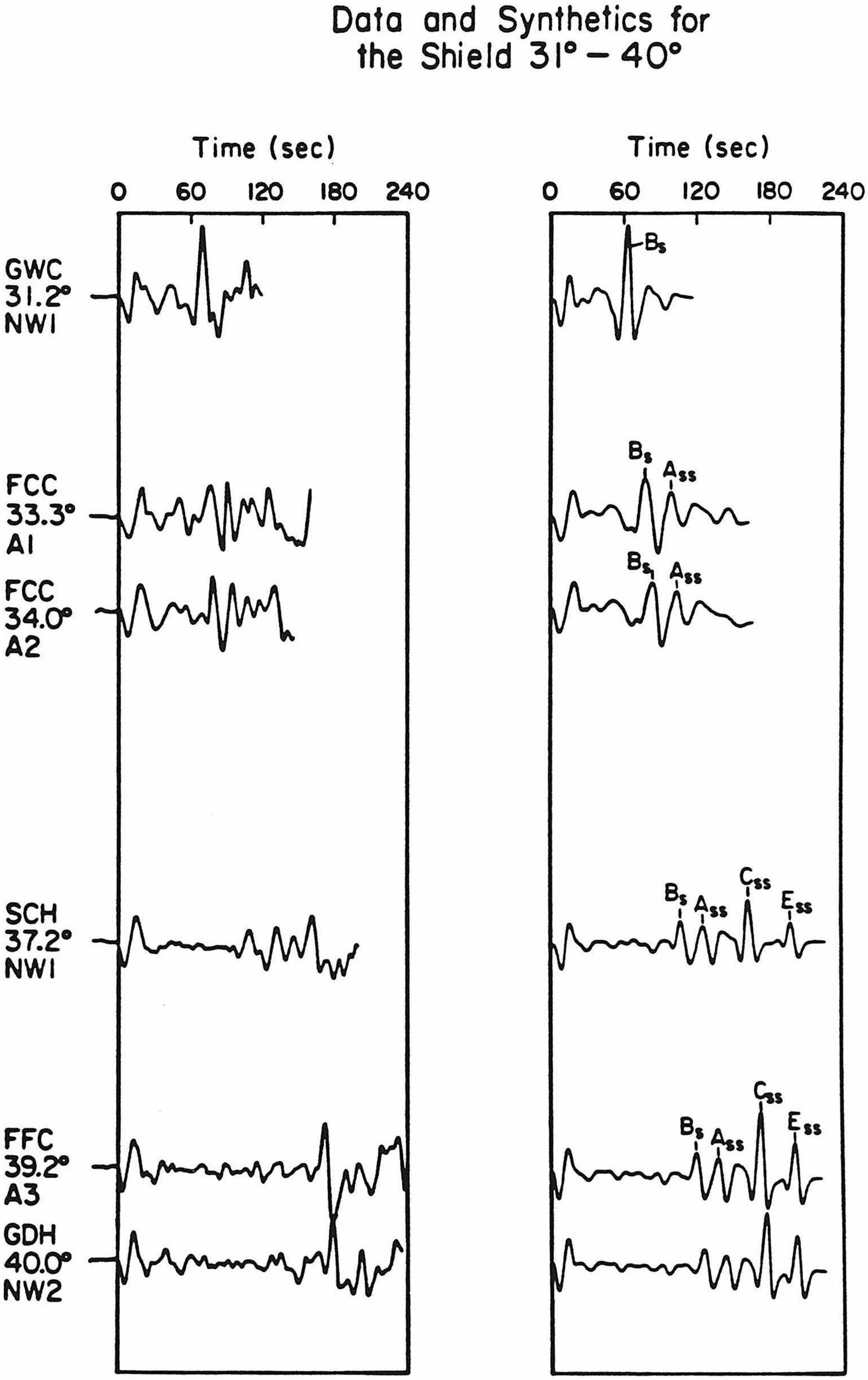

Figure 1.22 Comparison of S and SS data in the shield with synthetics computed using SNA. The arrivals are labelled in the synthetics with respect to Fig. 1.7. Subscript s stands for an S-wave branch and ss for an SS-wave branch.

Changing lid thickness would modify the velocities from 200 to 300 km. Surface wave studies have found thinner lids than in SNA (Brune and Dorman, 1963). If a thinner lid is assumed, the velocities below would have to be increased slightly. However, if one assumes the lid to be thinner by more than about 25 km, the S-wave synthetic first arrivals at 18° and 19° would be much too small. The exact depth of the low-velocity zone is very uncertain, probably to near 30 km, but the overall picture of a thick lid with a decrease in velocity to near 4.65 km/sec is well constrained.

The SS 405 km reflection, branch C, becomes clear near 37° at SCH, and can be followed to 40° . With the upper 400 km fixed this constrains the depth of the discontinuity to be at 405 km, the same as the tectonic region to within the accuracy of the method. This timing of the C branch agrees with what was picked in the S-wave data. Branch E, at 40° , can also be identified. This is the narrow angle reflection from the 659 km discontinuity. Note that between branches A and C of the SS-waves there are many other low amplitude arrivals in the data. According to model SNA, these are multiply-reflected rays within the lid. No attempt has been made to model these arrivals as they are of low amplitude and vary from record to record though they certainly contain significant information about the structure of the lid and crust. In any case, these arrivals do not interfere with the identification and timing of the S B branch from 30° to 35° and the SS C branch beyond 37° .

Fig. 1.23 shows further SS data in the 30° to 40° range from an event on the west coast of North America with paths slightly to the south of the previous data. The C branch of the SS phase can be followed easily from 36° to 40° . SNA models this well; however, the B branch of the S-wave is not obvious in the data, at least at the time SNA would predict. Part of the problem could be that the source is in a

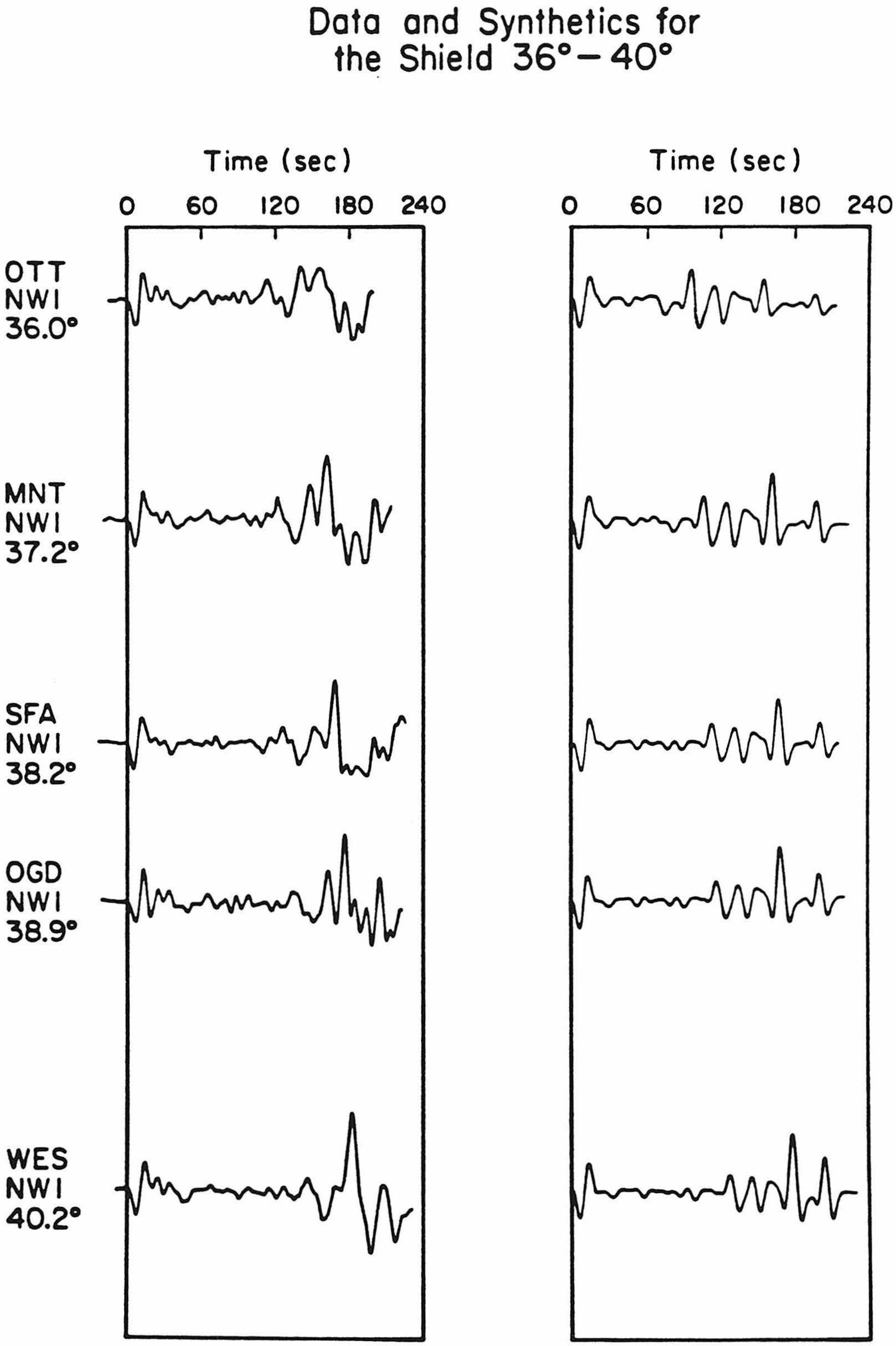

Figure 1.23 Comparison of S and SS data from the southern shield with synthetics computed using SNA. The distance range is the same as in the previous figure but the B branch of the S-wave is much later and smaller. The SS C branch is fit well though.

tectonic region. This would tend to shift the triplication forward, though for paths from the same event to SCH and GWC the fits are much better. A thinner lid with slightly lower velocities in the upper 300 km will cause branch B to end earlier. It is likely that a change to thinner lid structure and lower velocities from north to south is the cause of this discrepancy.

Fig. 1.24 shows the S and SS data from 41° to 47°, all from the Arctic region. In this range the two major arrivals in SS are the C and E branches, near critical reflections from the two major discontinuities. SnSn from the lid and the tunnelling SS from below the lid are precursory to the large SS arrivals but they are of very low amplitude. This helps constrain the thickness of the lid. If the lid were much thicker SnSn would be larger. A trace of these arrivals may be seen in the data but the C and E branches are much clearer. The SS data map the crossing of these two branches very well. Notice the difference at SES for two events shifted by only .7°. The crossing occurs near 46° and produces the very large amplitude common to SS in that range in the shield. The SS-S travel times are again fit well in this region. While the 405 km reflection is the first arrival, these SS-S times are about 25 sec less than those for the tectonic region. Below 400 km SNA has the same structure as TNA and it fits the shield E branch very well. The fit of the timing and amplitude of this branch indicate that the structure of the 659 km discontinuity is very similar from the East Pacific Rise to the Canadian shield. These waveforms provide unambiguous measurements of the two near critical reflections from the two upper mantle discontinuities helping to constrain their depths.

Fig. 1.25 shows the data between 48° and 55° for the shield. In Fig. 1.7 one can see that in this range three arrivals should become apparent in the SS-wave, the F, D

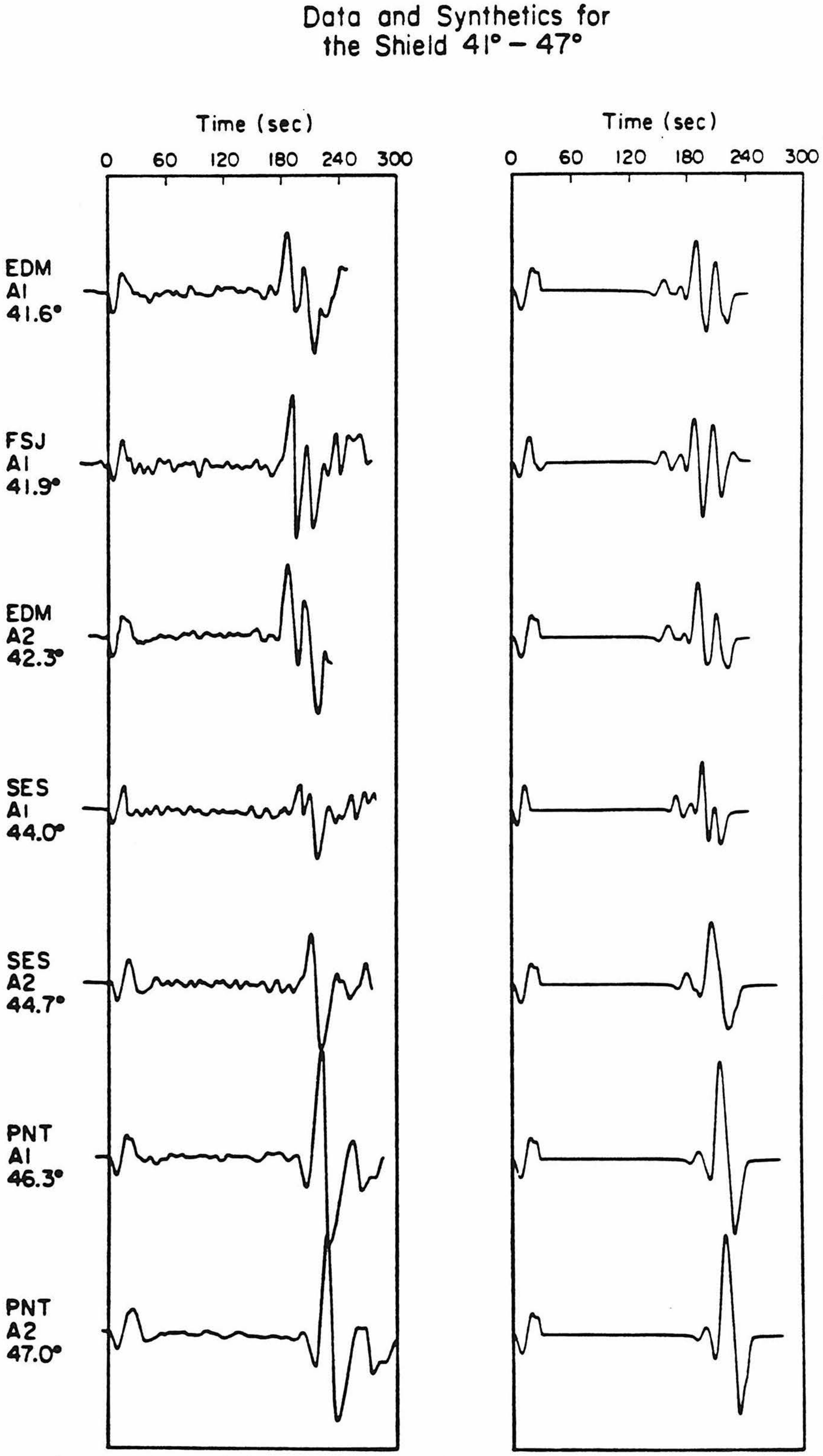

Figure 1.24 Comparison of S and SS data from the shield with synthetics computed using the SNA model. This figure illustrates the crossing of the C and E branches. Small precursory SS arrivals are from the lid and tunnelled energy from below it, they are shown as dashed lines in Fig. 1.7.

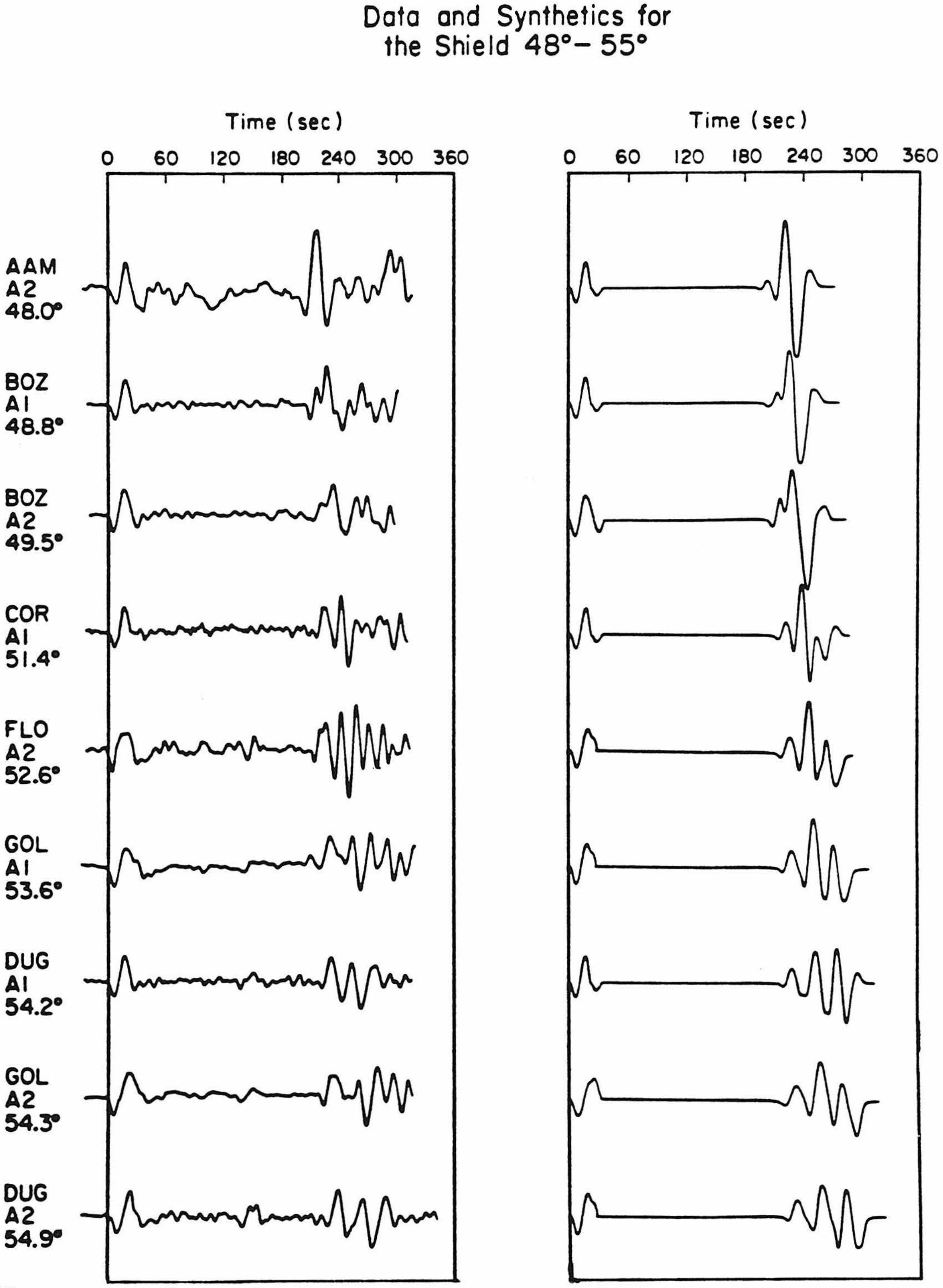

Figure 1.25 Comparison of S and SS data from the shield with synthetics using model SNA. This data shows the separation of branches F, D and B. Arrivals after branch B, the last SS arrival, are probably SSS rays in the lid which are not included in the synthetics. The small arrival between S and SS is the ScS phase.

and B branches. At 48° they are still together, at 48.8° and 49.5°, branch F can be seen separating from the other two branches. This is energy bottoming just below the 659 km discontinuity. Beyond 53° all three branches are clear separate arrivals and produce complicated waveforms. The absolute time from SS-S and the moveout of branch D from F is modeled very well, but the amplitude of the D branch is large in the synthetics compared to the data. Branch B at COR and DUG is predicted to be larger than the data show. At these stations we are getting well into the tectonic region. Branch B is travelling in the upper 400 km, where the heterogeneity is large, and one would expect this branch to die off very quickly upon entering a tectonic zone. Another effect of entering the tectonic area would be to slow down branch B relative to the other branches. Fig. 1.26 shows data from Arctic events to stations VIC, LON and COR. About 10° of these paths are tectonic. VIC shows a clear second arrival in SS, this is probably the B branch slowed by about 5 sec relative to the SNA model. This branch may be followed to LON and at COR it is probably absent. This mixing of the paths would also shift the D triplication forward a little and this could be the reason for the amplitude mismatch of the D branch. In spite of these problems, the model derived for the tectonic region below 405 km does a very good job of fitting the shield data at these distances. The moveout of the F and D branches is the same for the two regions if one takes into account the different structure above 405 km. The shallow structural differences between the shield and tectonic areas produce about a 3° shift in the SS 660 km triplication. These observations indicate there is little or no heterogeneity between the shield and rise regions at transition zone depths.

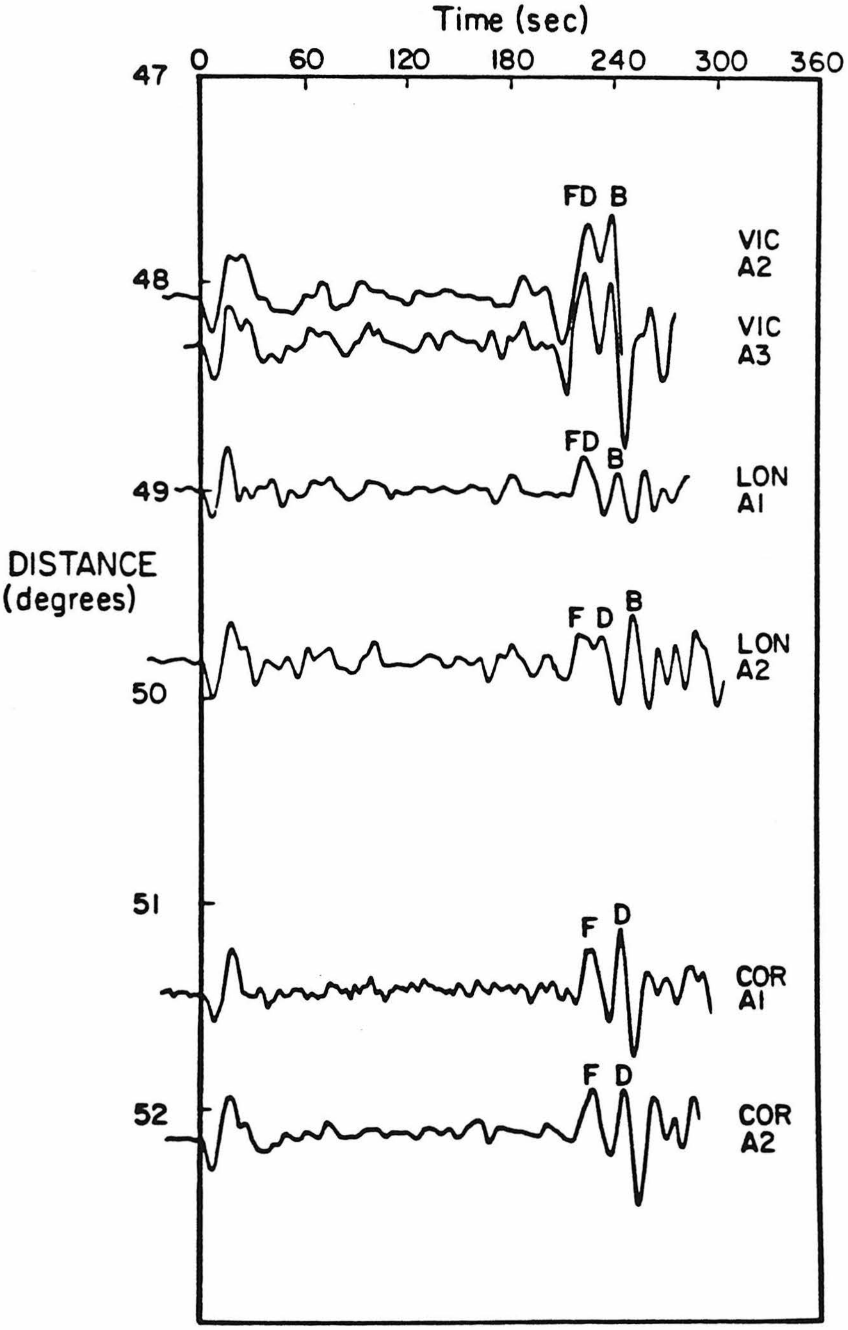

Figure 1.26 Profile of data from the Arctic which has propagated through a substantial portion of a tectonic region. The arrivals marked are with respect to Fig. 1.7. Note that branch B arrives considerably later relative to the data in the previous figure.

Fig. 1.27 shows data from 58° to 62° from the Arctic events to stations well into the tectonic region. Due to the receiver location there is no indication of the B branch but since the midpoints are well within the shield we would expect SNA to predict the SS-S travel-times well. The SS arrival is bottoming at about 800 km depth and the fits of the travel-times are a consistency check on the velocities at these depths which were considered as known originally. A long-period trace of the D branch is also visible though it is not very consistent in the data from station to station.

In the range 20°–30° very few shield S waves were found. Fig. 1.28 shows three seismograms from the Arctic events to FBC and BLC compared with synthetics. The fits are adequate, though by themselves they do not provide new information. The large secondary arrival at BLC should be the 405 km B branch but there is a lot of PL interference at this station and it is not certain that this is truly a triplication arrival. The S-waves, however, do not contradict the shield model derived from SS data.

Comparison of the Models

The two models presented here provide a good opportunity to investigate the depth of lateral heterogeneity since the same method was used to model both profiles. Figs. 1.29-1.32 summarize the data from the events used most in this study. Synthetics for the model appropriate for the event are also present with the travel-time lines. In Figs. 1.31 and 1.32 the shield travel-time line from the previous figure is also on the data illustrating the consistency of the large differences in time. The travel-time curves beyond 15° were derived entirely from SS-S times. This assumes the S

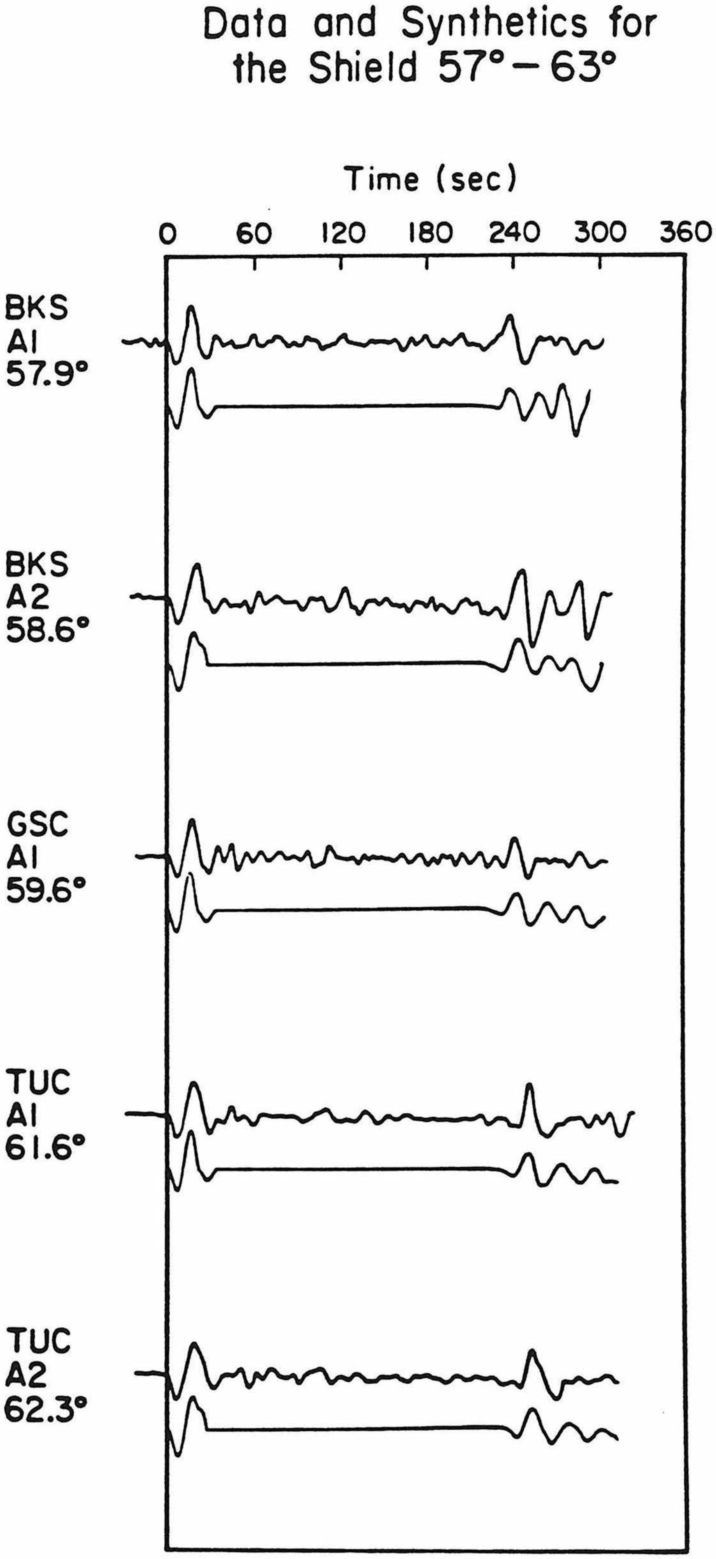

Figure 1.27 Comparison of S and SS data, with midpoints within the shield, with synthetics computed using SNA.

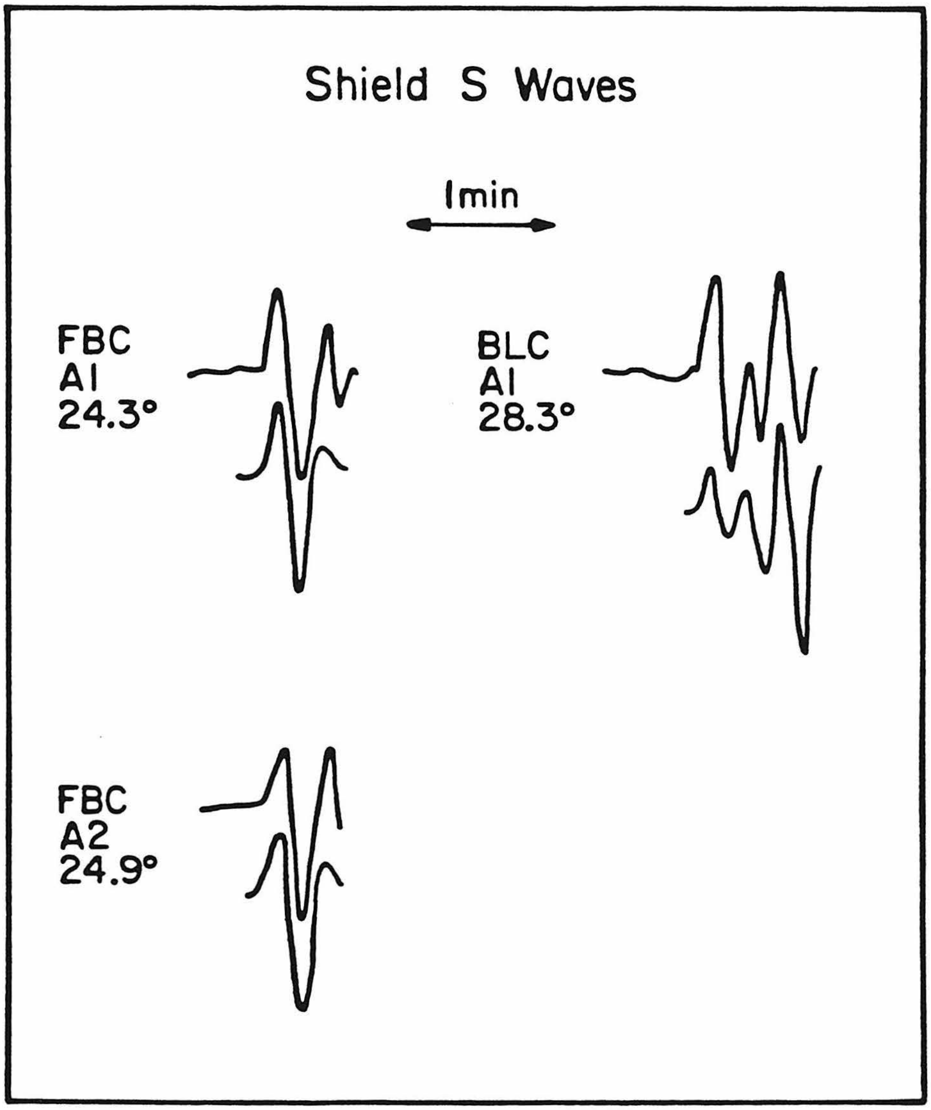

Figure 1.28 Comparison of S-wave data from the shield with synthetics computed using SNA. The timing is arbitrarily set to match the waveforms.

travel-times are correctly predicted by our models. The S and SS data from 58° to 62° support this assumption, but not conclusively. The travel-times of S-waves from 30° to 60° are determined mostly by the velocities from 800 to 1200 km depth. We have used the Jeffreys-Bullen model at these depths since this has proved to be a reliable standard in the past. Fig. 1.33 shows the S residuals for events for which SS data were used in this study. The residuals are plotted by station and a 10 km depth was assumed for all sources. The residual line corresponds to using a path half tectonic and half shield. The line labeled TNA is wholly tectonic and the East Pacific events to tectonic stations lie very near the TNA line. The same events to stations like FCC and FFC are nearer the zero residual line, as expected. The data used for the shield study are also plotted. The events labelled NW are from the north-west coast of North America, probably in a tectonic structure, the stations for the most part are within stable areas and thus, one would expect the data to fall near the zero residual line. The data seem to scatter closer to +2 sec. Similarly the Arctic events should lie near the SNA line for shield stations and the zero line for tectonic stations. There is quite a bit of scatter from this area but the expected pattern is matched to within a couple of seconds.

There is no evidence for a large bias in the S travel-times between the two regions when the difference in the upper 400 km is accounted for. At any one station there can be a 2-3 sec difference from the expected result, this could be the result of source mislocation or of structural differences near the station or source. These causes will effect the SS-waves by nearly the same amount and the SS-S times would be largely unaffected. We feel the SS-S time measurements provide a stable measure of the upper-mantle travel-time curves. The differences of 2-3 sec are on the same order

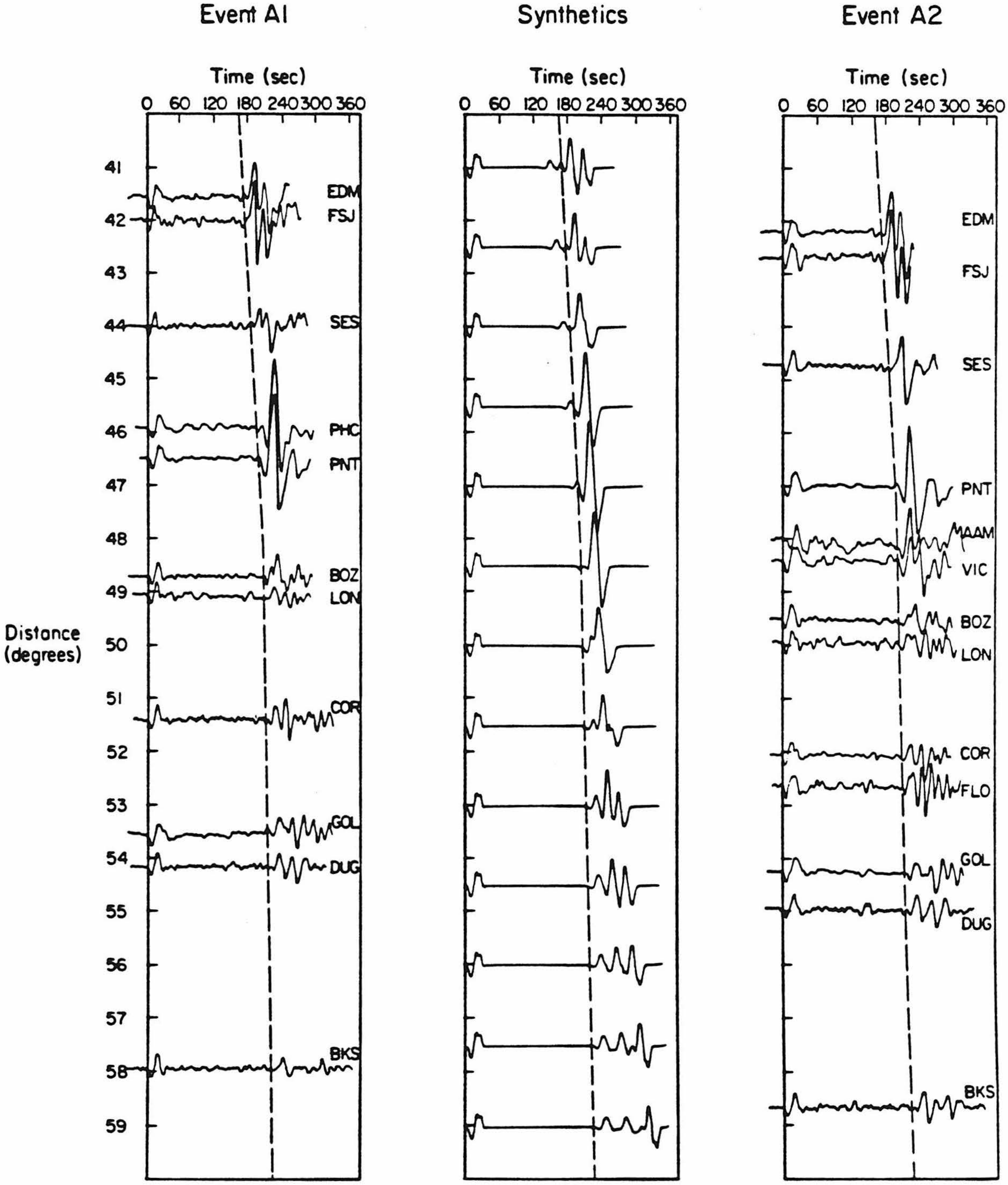

Figure 1.29 Complete data set for events A1 and A2 with synthetics using SNA. The travel-time line on the synthetics is reproduced on the data. Some of the waveform mismatch is due to the use of a single source and instrument response for the synthetics.

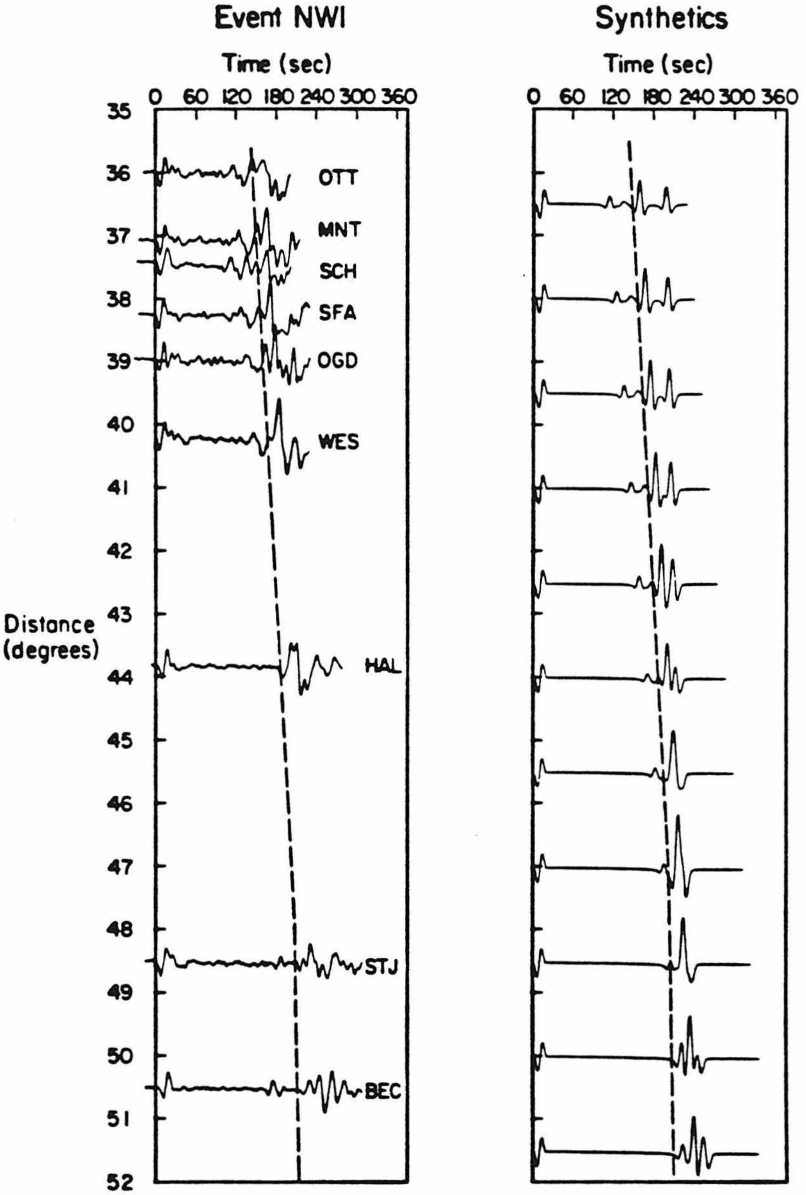

Figure 1.30 Complete data from event NW1 with synthetics computed using the SNA model. The travel-time line follows branch B (the 405 km reflection) at distances less than 42°. Arrivals before branch B are from the upper 200 km.

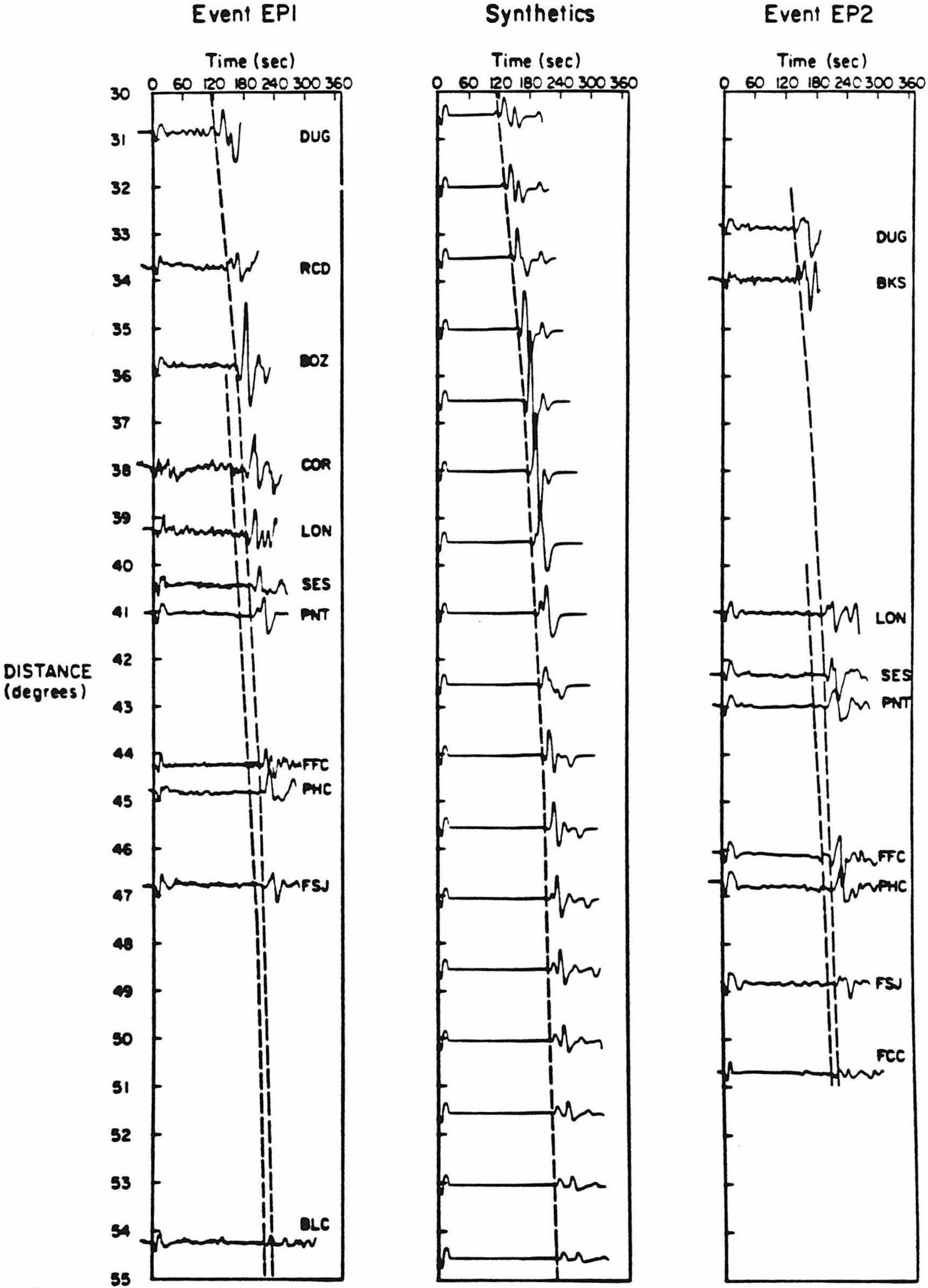

Figure 1.31 Complete data set for events EP1 and EP2 with synthetics computed using TNA. The early travel-time line on the data profiles is the same as shown in the previous figure indicating the shield SS onset. Note that BLC and FCC are fast. These stations have midpoints to east of the tectonic province, see Fig. 1.11.

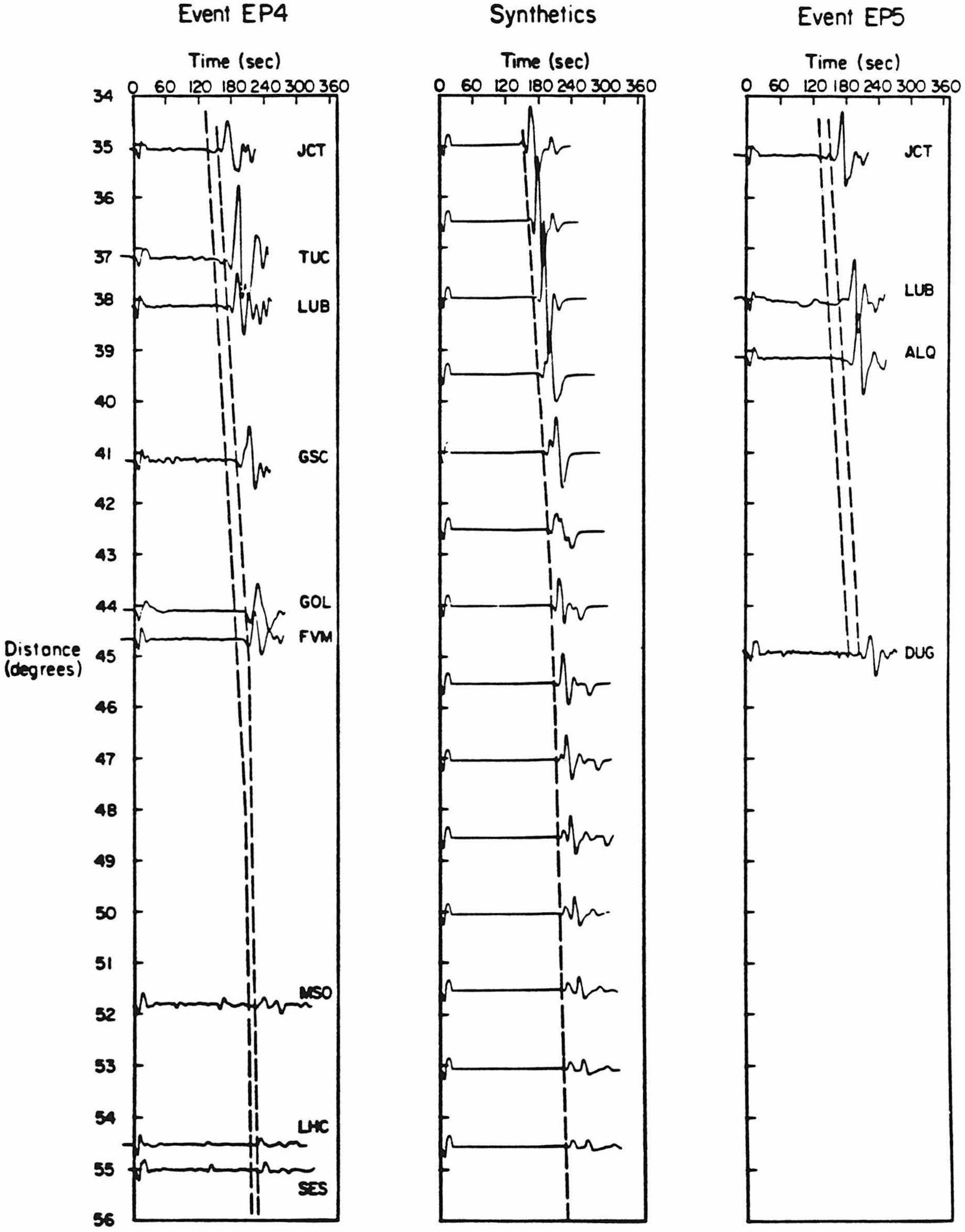

Figure 1.32 Complete data set for events EP4 and EP5 with synthetics computed using TNA. The early travel-time line is again the same as that in Fig. 1.30.

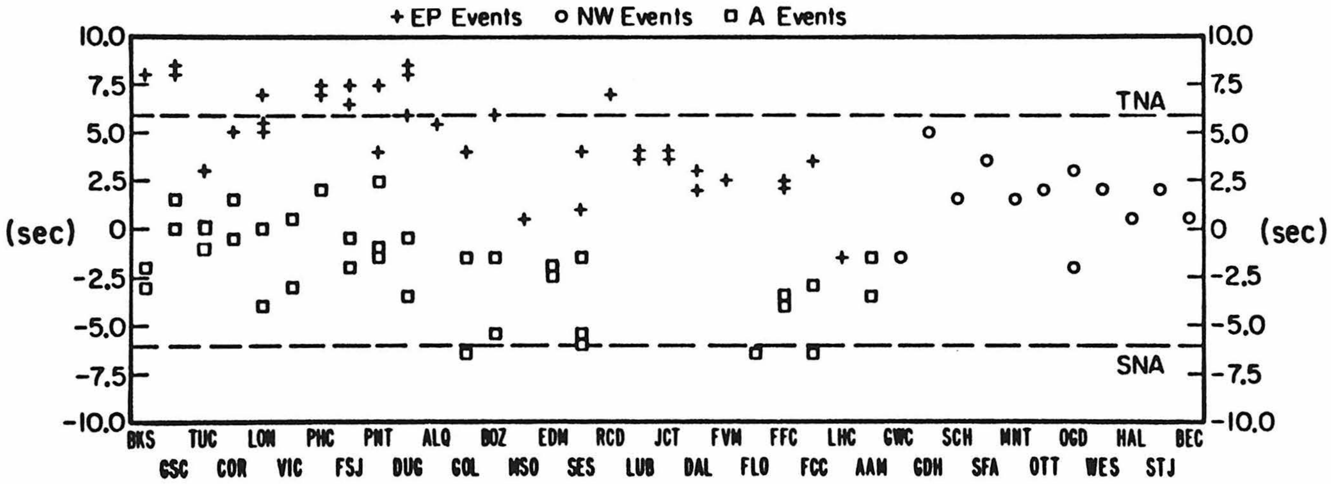

Figure 1.33 Relative teleseismic S-wave residuals for the data used to measure the SS-S times. The values appropriate for TNA and SNA are given as dashed lines. The events are assumed to be 10 km deep.

as the fits of the SS-S times by the models. This uncertainty is much lower than the 30 sec differences in SS-S times found in the two regions. In Chapter 3 we will return to these measurements and try to find out the significance of the variations from our models discussed above.

Given that the travel-time curves for SS are accurate to within 3 sec the models should be well constrained. As shown in the previous sections, every triplication branch in both areas is visible and the two models fit the times closely. There are misfits in the amplitudes of certain arrivals, such as the D branch from the 659 km discontinuity near 50°. These misfits could be caused by errors in the model on a local scale. For instance, a lower gradient to 530 km, a small jump in velocity and again a lower gradient below could decrease the amplitude of the D branch. We cannot resolve small features such as jumps of 2% or less but the relative timing of the arrivals will not allow appreciable differences over an extended depth range. A variation of 1% over about 100 km is probably close to the resolution of this study. Given (1984) presented an inversion of uppermantle S data sampling the TNA region of this study. His results agree with model TNA very well with the largest discrepancies ocurring near the discontinuities. His approach found the smoothest model which would fit the data while we have arbitrarily made regions causing triplications to be sharp discontinuities. This is just a matter of taste when modelling long-period S data since synthetics are identical for sharp jumps in velocity and gradients over about 50 km depth with the same velocity increase. Given's results near the discontinuities appear to be just the spreading of the velocity increase we find, over about 100 km. With this in mind, his results give us confidence in our estimate of the resolution of the data.

Within the estimated resolution discussed above, we feel there is definitely heterogeneity to 350 km depth between the shield, in particular just west of Hudson Bay where most of our data sampled, and near the Gulf of California. The difference in gradient from 200 to 400 km is strongly indicated by the extension of the B branch in the shield by at least 10^o . Similar gradients for both models below 250 km would not be able to match this difference. The uncertainty in the shield lid thickness also does not invalidate this conclusion. If it were thinner, the velocity would be slightly higher from 200 to 400 km depth. If it were much thicker, SnSn would be much larger beyond 40^o . Within that constraint thicker lids would not modify the structure below 200 km by much. TNA and SNA are different from 350 to 400 km but this is not well resolved. There could equally well be a small amount of heterogeneity below 400 km for 50 km or so. On the other hand, the data will not permit a 1% difference in velocity from 400 to 650 km for instance. This would change the timing of the D branch beyond 48^o by more than 5 sec which would be easily noted in the data.

As mentioned above, the discontinuities were made arbitrarily sharp. The refracted long-period arrivals used in this study can not determine the sharpness of these regions; however, short-period vertical reflections have been observed from depths of around 400 and particularly 650 km indicating there are sharp boundaries near these depths (for example Whitcomb and Anderson, 1970 and Adams, 1971). Assuming the discontinuities are sharp, the depths are probably constrained to within 10 km with some tradeoff with the structure above and below the discontinuity. The overall increase in velocity at these depths is even better constrained due to the timing of arrivals from just above and just below the jumps. There does not appear to be any large difference in the structure of the discontinuities beneath the Canadian shield and the East Pacific Rise. This may have serious implications for the idea of a chemical tectosphere extending to even 400 km depth (Jordan, 1981a).

The models presented here are consistent with other data. Teleseismic S-wave travel-time studies (Doyle and Hales, 1967; Lay, 1983; Wickens and Buchbinder, 1980) have found 5-7 sec variations across North America, which is consistent with the 6 sec difference in vertical one-way travel-time between our models. The study of Cara (1979) found a thick lid with a high velocity in the eastern United States compared to a western United States model with a large low-velocity zone and a high gradient below it. These models are qualitatively the same as TNA and SNA, though the absolute velocities in the Cara models are lower by about 3.5% near 200 km depth relative to the corresponding models we have found. This is perhaps due to a combination of dispersion and anisotropy.

A natural question is how does the compressional velocity compare to the shear velocity in these regions. P travel-times are known to be more stable than S times (Lay, 1983), though they show variations across the United States tracking the S-times. Burdick (1981) found data from an event near Bermuda to eastern North American stations required a higher velocity mantle than data within the Western United States. Walck (1984) studied upper mantle data from the Gulf of California to the southern California array. She finds that the B branch from the 400 km discontinuity ends near 20^o. This is earlier than any other P models published but agrees with the shear data observed in this study. Similarly, Given and Helmberger (1981) found the end of the B branch to vary by several degrees for different paths from Soviet nuclear explosions. Data near the center of the Russian platform had an extended B branch relative to data nearer the Arctic Ocean. This may be an indication of variations in the upper 400 km similar to those observed in this study. England et al. (1977) also found variations in P velocity to great depths between the Russian platform and southern Europe. How these variations compare with the shear heterogeneity will be an important area for future research.

Conclusion

The SS phase has proved to be a valuable tool in the modelling of upper mantle shear structure and heterogeneity. As shown in the previous sections, all the triplication branches from the two major discontinuities are clearly visible. The long time spent in the upper mantle causes the various arrivals to be well separated and the crossing points of the arrivals can be accurately mapped due to this feature. The greatest advantage to using SS, though, is that it can be used to map many areas of the world which cannot be investigated with the usual body-wave techniques.

Shear velocity vertical profiles were determined for two different tectonic regimes, the Canadian shield and the tectonic part of western North America. Very large lateral heterogeneity was obvious in the data. The derived models differ in velocity to a depth of 400 km, substantially above 350 km. The shield has a thick high-velocity lid with a low-velocity gradient below it to 400 km depth. The tectonic area has a thin lid and a large low-velocity zone. Also, the tectonic region has a very high gradient from 200 km to 400 km depth. Below 405 km the models are identical with two major discontinuities: a 4.5% jump in shear velocity at 405 km and a 7.5% jump at 659 km.

Chapter 2

Upper Mantle Shear Structure Beneath the Northwest Atlantic

Introduction

The results of Chapter 1 show slower velocities in the upper 400 km of the mantle beneath the East Pacific relative to the Canadian shield. This result is significant but leaves open the question of which of the two provinces is anomalous and which normal. Jordan (1981a) has proposed that old continents have chemical roots to great depths in the upper mantle. The results of Chapter 1 support this idea, however, one could interpret the heterogeneity equally well as anomalously hot material beneath young spreading centers with the continent more typical of the earth. In most tectonic regionalizations, such as in Nakanishi (1981), Kanamori (1970), Sipkin and Jordan (1976), etc., there are young oceanic, old continent and old oceanic provinces. Oceanic areas with crustal ages greater than 50 Ma represent the largest portion of the earth. Thus, before generalizing the results of Chapter 1 with respect to theories such as proposed by Jordan (1981a), it is necessary to develop an upper mantle model for old oceanic areas.

In Chapter 1 the travel-times and waveforms of S and SS phases from 10^o to 60^o were used to derive upper mantle shear structures. This study showed that using the travel-times and waveforms of S and SS one could constrain the shear structure to 800 km depth with a resolution of about 1% over 100 km. This technique provides better resolution, at depth, than conventional surface wave dispersion studies due to the fact that the wavelengths of energy sampling deeper structure do not increase substantially. In this chapter the western part of the North Atlantic ocean is studied using essentially the same technique of modeling S and SS phases. The area studied has oceanic crust ranging in age from 0 to 150 Ma (Sclater and Parsons, 1981). Thus, a comparison of an active spreading center, old ocean, tectonic continent and a stable craton can be made using a single method. The data from the Atlantic ocean show features very similar to the data from the East Pacific Rise and the Canadian shield. Discontinuities near 400 km and 660 km produce triplication branches which are visible in both the S and SS waves. Using the times from these branches we have derived an average model for the older part of the Atlantic (70 to 150 Ma) near North America. The model, listed in Table 2.1, and shown in Fig. 2.1 with the previously derived models from Chapter 1, has a high velocity lid about 100 km thick. Below the lid, the velocity decreases to 200 km depth at which depth it has the same velocity as that derived for the East Pacific Rise in Chapter 1. Below 200 km we find no difference in structure between the old Atlantic and the young East Pacific regions.

Technique

To determine the upper mantle shear velocity beneath the Atlantic, we modeled the SH motion from Atlantic earthquakes recorded on long-period WWSSN (World Wide Standard Seismic Network) and CSN (Canadian Seismic Network) stations in eastern North America. The approach is to match the travel-times and waveforms of regional data from 10^o to 16^o, using synthetic seismograms, to constrain the shallow structure. As one looks at seismograms at further distances, deeper structure is

Table 2.1 : Atlantic Model

Depth km	Velocity km/sec	Depth km	Velocity km/sec
0.0	3.700	475.0	5.135
9.0	3.700	500.0	5.190
10.0	4.750	525.0	5.240
25.0	4.750	550.0	5.290
50.0	4.750	575.0	5.345
75.0	4.750	600.0	5.395
100.0	4.750	625.0	5.445
125.0	4.540	658.0	5.500
150.0	4.490	660.0	5.910
175.0	4.470	675.0	5.980
200.0	4.460	700.0	6.050
225.0	4.460	725.0	6.130
250.0	4.480	750.0	6.200
275.0	4.510	775.0	6.220
300.0	4.570	800.0	6.240
325.0	4.630	825.0	6.260
350.0	4.680	850.0	6.275
375.0	4.730	875.0	6.290
404.0	4.780	900.0	6.305
406.0	5.000	925.0	6.320
425.0	5.050	950.0	6.335
450.0	5.090	975.0	6.350

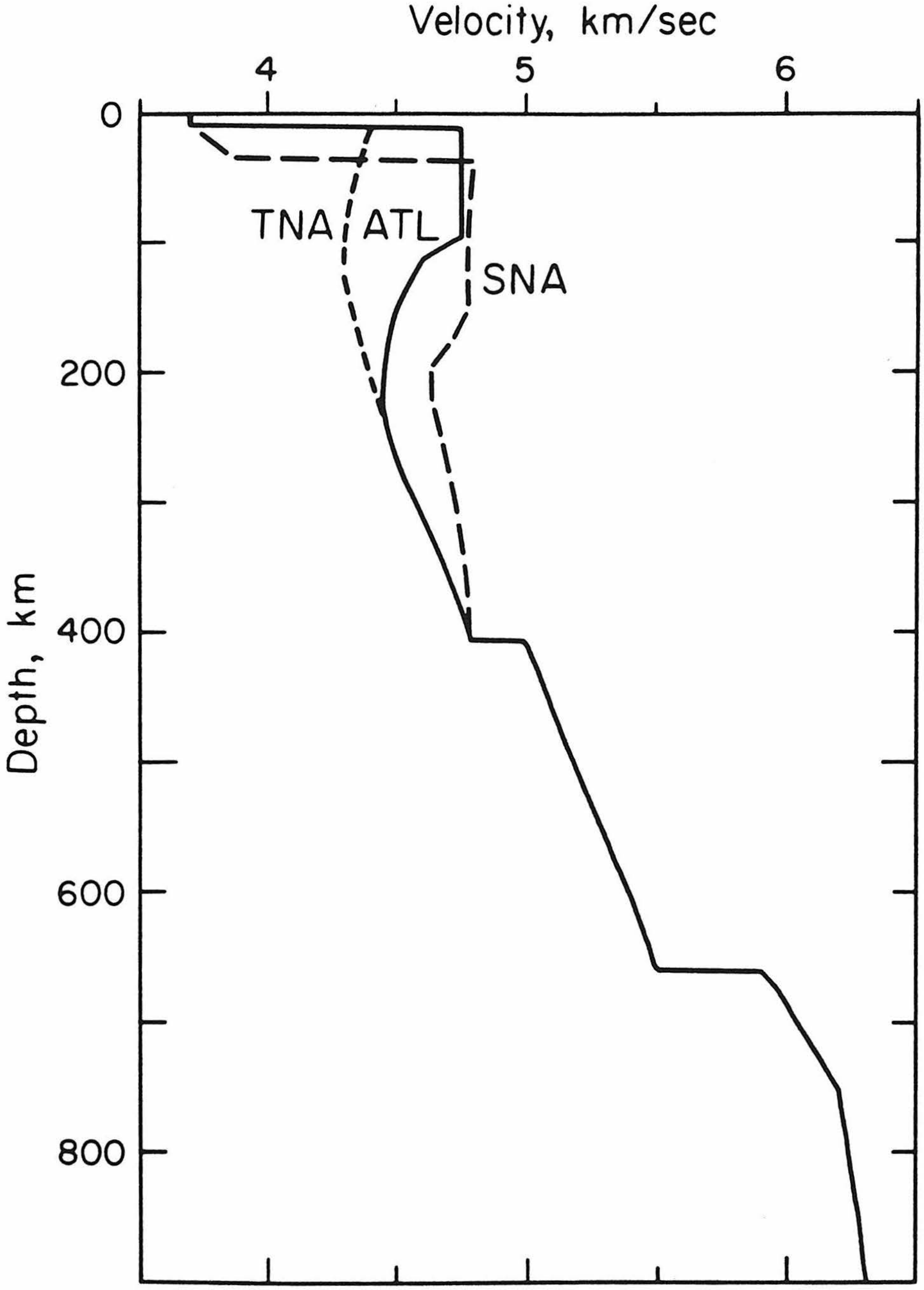

Figure 2.1 Velocity model ATL derived in this chapter compared to models of the Canadian shield (SNA) and tectonic western North America.

sampled. Using synthetic seismograms we can analyze from what depth individual arrivals come and thus adjust the model appropriately when discrepancies between the synthetics and data appear. The starting model was taken as the East Pacific Rise model (TNA) found in Chapter 1. Changes to it were made from the top downward until the Atlantic data were satisfied. The resolution of this trial and error approach was investigated by Given (1984). He developed a formal inversion for structure, using S wave travel-times and waveforms, and applied it to data from the East Pacific Rise and western North America. The resulting model was very similar to TNA, which was derived by a trial and error technique; thus, we feel confident in the conclusions of our modelling.

The earthquakes used are listed in Table 2.2. Fig. 2.2 shows the locations of the events and stations relative to oceanic crustal age (Jordan, 1981b). The events were selected on the basis of the quality of the SH signals from them. The stations used were nearly naturally rotated and thus data with strong SV energy was apparent. Due to the problem of shear-coupled PL interference, discussed in Helmberger and Engen (1974), any data which had a high SV to SH ratio at the arrival time of S or SS was rejected. The events on the Mid-Atlantic Ridge had teleseismic SH waves similar to those from strike-slip earthquakes, thus, the mechanisms were assumed to be strike-slip for them. Event 1, near Bermuda, was studied by Stewart and Helmberger (1981), and Event 2, by Molnar and Sykes (1969). The focal mechanisms of the two Events were thrust but they still produced simple SH waves to some stations.

The data fall in the range 11^{o} to 52^{o} and sample ocean of varying age. From 11^{o} to 30^{o}, the S waves travel wholly in the upper mantle and the triplications are obvious in the data. Data at these distances came from events 1 and 2, and, as can

Table 2.2 : Event Locations

Event	Date	Location	Origin Time
1	March 24, 1978	29.9° N, 67.3° W	0042:37.7
2	Nov 3, 1966	19.2° N, 67.9° W	1624:31.3
3	Nov 18, 1970	35.2° N, 35.7° W	1223:18.0
4	May 17, 1964	35.2° N, 35.9° W	1926:20.6
5	March 28, 1976	33.8° N, 38.6° W	2019:45.6
6	March 26, 1980	23.9° N, 45.6° W	2043:37.9
7	Oct 20, 1972	20.6° N, 29.7° W	0433:48.9
8	June 2, 1965	15.9° N, 46.7° W	2340:23.5
9	June 19, 1970	15.4° N, 45.9° W	1425:18.4

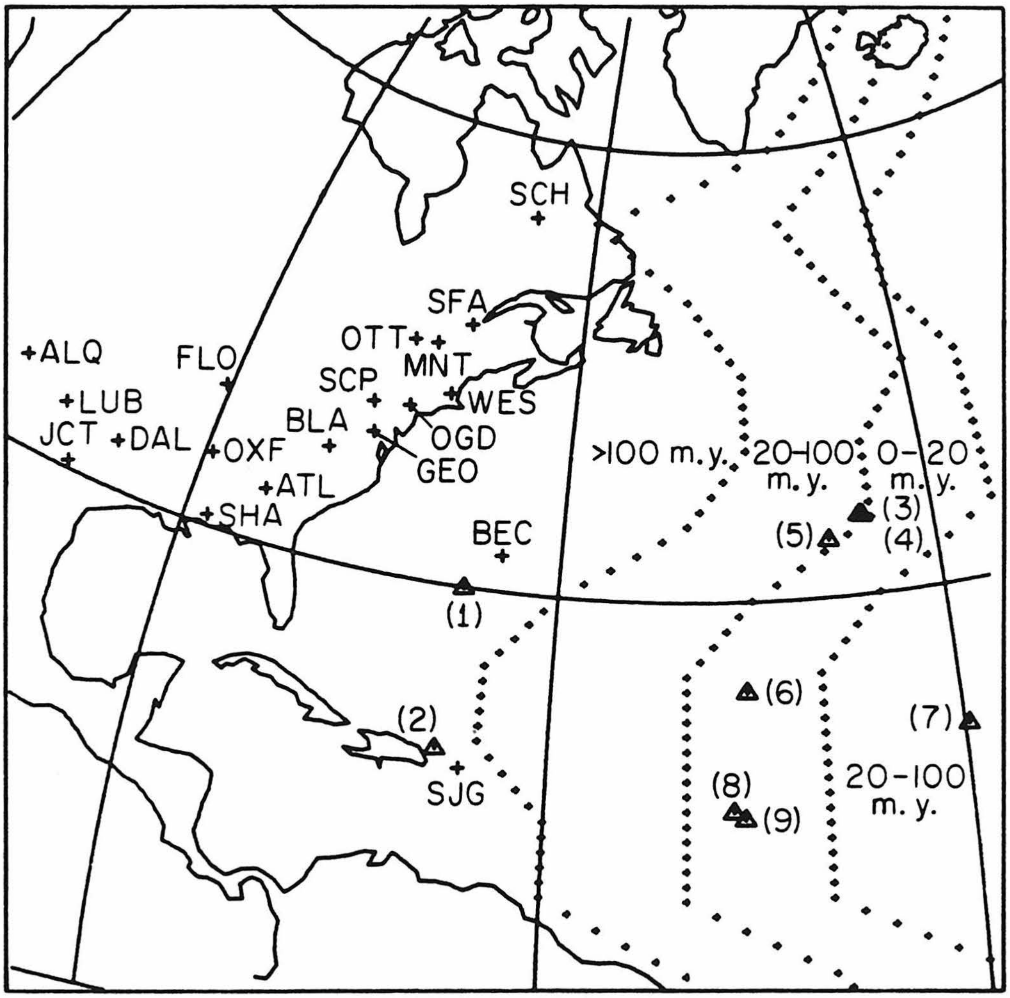

Figure 2.2 Stations and events used to determine the Atlantic structure. The age of the oceanic crust in the region is also indicated.

be seen on the map, their paths were totally beneath ocean older than 100 Ma. Data from 27° to 52° came from the events near the Mid-Atlantic Ridge. We used the SS waveforms and SS-S times at these ranges to determine the structure. SS goes through the same triplication as S at nearer distances as discussed in Chapter 1. These earthquakes are beneath much younger ocean than those used for S; however, their midpoints are within ocean older than 100 Ma. Using SS-S times should decrease the contamination of the data by the initial propagation through younger structure.

To derive an upper mantle structure which would reproduce the relatively complicated seismograms used, we constructed synthetic seismograms. Synthetics enable one to model interfering signals and, also, to intuitively understand them. The procedure used to calculate the synthetics is well established. One assumes a seismogram consists of a series of linear operators representing the different factors in a record (Helmberger and Burdick, 1979). We can write a seismogram Y(t) as

$$Y(t)=S(t)*I(t)*A(t)*M(t), \tag{2.1}$$

where S(t) is the source, I(t) is the instrument response, A(t) is an attenuation operator and M(t) is the Green's function for wave propagation through the mantle.

The source function was constructed by fitting the teleseismic S waveforms. A trapezoidal time function was convolved with an operator representing the S, sS interaction, dependant on focal mechanism (Langston and Helmberger, 1975). The depth and time function are adjusted to fit the teleseismic data. All the events used in this study are shallow and produced simple teleseismic SH waves. The details of the source are not too important as the arrivals we modeled are generally well separated.

The attenuation operator was taken from Futterman (1962) and Carpenter (1966). The amount of attenuation is parameterized by the value of t^*, the travel-time divided by the average Q along the ray path. It is generally believed that Q is lower in the upper few hundred km than below. For this reason, SS arrivals were attenuated more than S arrivals. A t^* of 4 sec was used for S and a t^* of 7 sec for SS waves. These values are rather arbitrary but are fairly close to values computed from published Q models such as PREM (Dziewonski and Anderson, 1981). Improvements in Q structure will help the synthetic to data amplitude fits but should not affect the relative timings of different arrivals significantly.

The Green's functions, for upper mantle propagation, were computed using two techniques. Preliminary modeling was done using the WKBJ method of Chapman (1978) and Wiggins (1976). This method is very inexpensive and useful in the modeling process. There are situations, however, where it does a poor job, such as energy from shadow zones and interactions with sharp discontinuities. Therefore, after deriving a model fitting the travel-times of the most obvious arrivals with the WKBJ synthetics, we used a Cagniard-de Hoop code (Helmberger, 1973) to model, in more detail, our data. Comparisons of synthetics by the two methods are given in Chapter 1 for two upper mantle models.

The Cagniard-de Hoop synthetic is generated by adding the responses of generalized rays through a stack of homogeneous layers. A limitation of the technique is that for SS, or other multiple bounce phases, a large number of rays are needed to compute the response. At different distances, which rays were necessary was found by progressively adding more rays until the synthetics did not change appreciably. The rays used in different situations will be mentioned in the following. Comparisons of Cagniard-de Hoop with the reflectivity method (Burdick and Orcutt, 1978) have been positive and thus it is felt this approach is valid.

Lid Structure

To investigate the upper mantle below 200 km a good estimate of the upper 200 km is necessary since all the data used to look at deeper structure will be contaminated by the more shallow structure. The upper part of the model was found by fitting travel-times and waveforms of the SH motion at close-in distances (11° to 16°). For a continental structure, at these ranges, there are well separated arrivals from the mantle. Depending on the structure, they can be from above or below the lid. These separate arrivals (S, SS, SSS etc.) were modeled in Chapter 1 to determine the average shallow structure beneath the Canadian shield and western North America. The reason the arrivals are well separated at these ranges is due to the thick crust above the mantle. Each time a phase comes to the surface it must travel through the much slower crust and thus multiple bounce phases, such as SS and SSS, fall rapidly behind the direct arrival S wave. In an oceanic structure the crust is much thinner and thus the separation of multiple bounce arrivals is much less in time. Fig. 2.3 illustrates this effect using the Cagniard-de Hoop generalized ray technique. The effect of adding successive multi-bounce arrivals is shown for two simple structures. To represent an oceanic structure, we used a 7 km thick layer of velocity 3.7 km/sec, over a half-space with velocity 4.75 km/sec. The continental synthetics are for a 30 km layer, of velocity 3.7 km/sec over the same half-space. The rays used are shown to the left of the synthetic step responses. The seismograms are calculated at a distance of 8°. The front of the records are due to multiple bounce head waves while the high

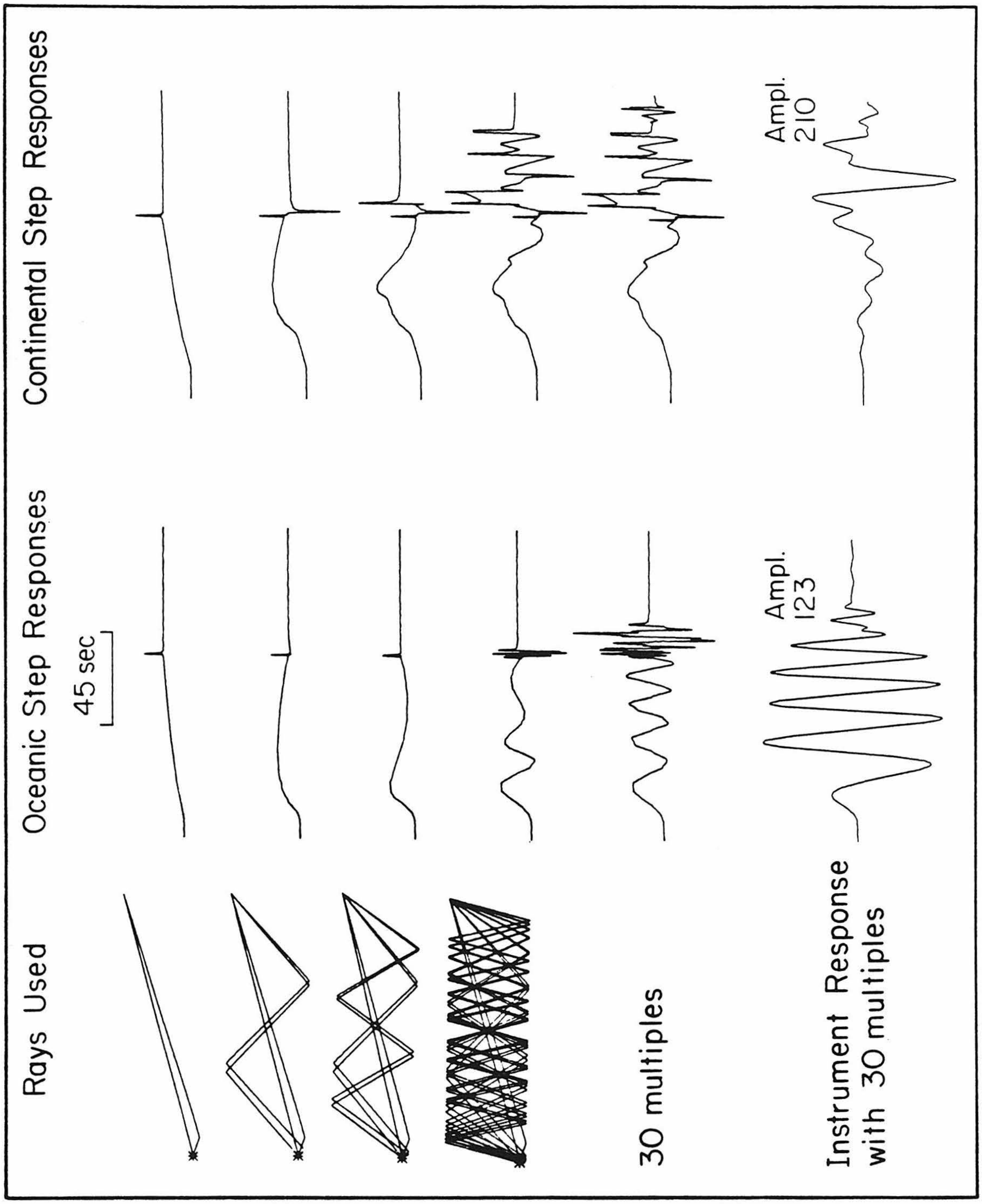

Figure 2.3 The step responses after summing various sets of rays in two simple structures. The final panel is the response of a long-period WWSSN instrument to the Green's function above it.

frequency later arrivals are reflections. Each multiple bounce ray is very similar in the two structures; however, the difference in crustal thickness changes the time separation of the arrivals and thus the interference. This produces the vastly different dispersion in the two structures. The final panel is the response after convolving with a long-period WWSSN instrument and a 6 sec trapezoidal time function. Obviously, the oceanic data, at regional distances, will have a very different appearance than the continental data just due to the crust. Large sets of multiply reflected crustal rays must be used to model oceanic records at upper mantle distances. In terms of modes, this can be understood by the fact that the fundamental Love mode, from 20 to 60 sec travels at mantle velocities and not crustal velocities, as in the continent. This phenomena was pointed out by Thatcher and Brune (1969) in their discussion of the interference of higher mode Love waves with the fundamental mode at periods less than 60 sec for oceans.

In spite of the fact that we cannot model regional data as distinct mantle arrivals, the waveforms still contain much information. Fig. 2.4 illustrates how we might use data at regional distances, say 12°. Fig. 2.4a shows the effect of changing crustal thickness. The synthetics were computed summing rays with up to 40 multiples in the crustal layer. A strike-slip source is at 5 km depth. With changing crustal thickness the arrival time of the first downswing stays the same. This is basically headwave energy with only a few free surface reflections. The later swings, in the waveform, change dramatically with crustal thickness differences of only a few kilometers. The signal contains higher frequencies with thinner crust due to the fact that the later arrivals in the wavetrain have bounced many times in the crust. Changing the crustal thickness changes the time separation of the multiply-reflected arrivals

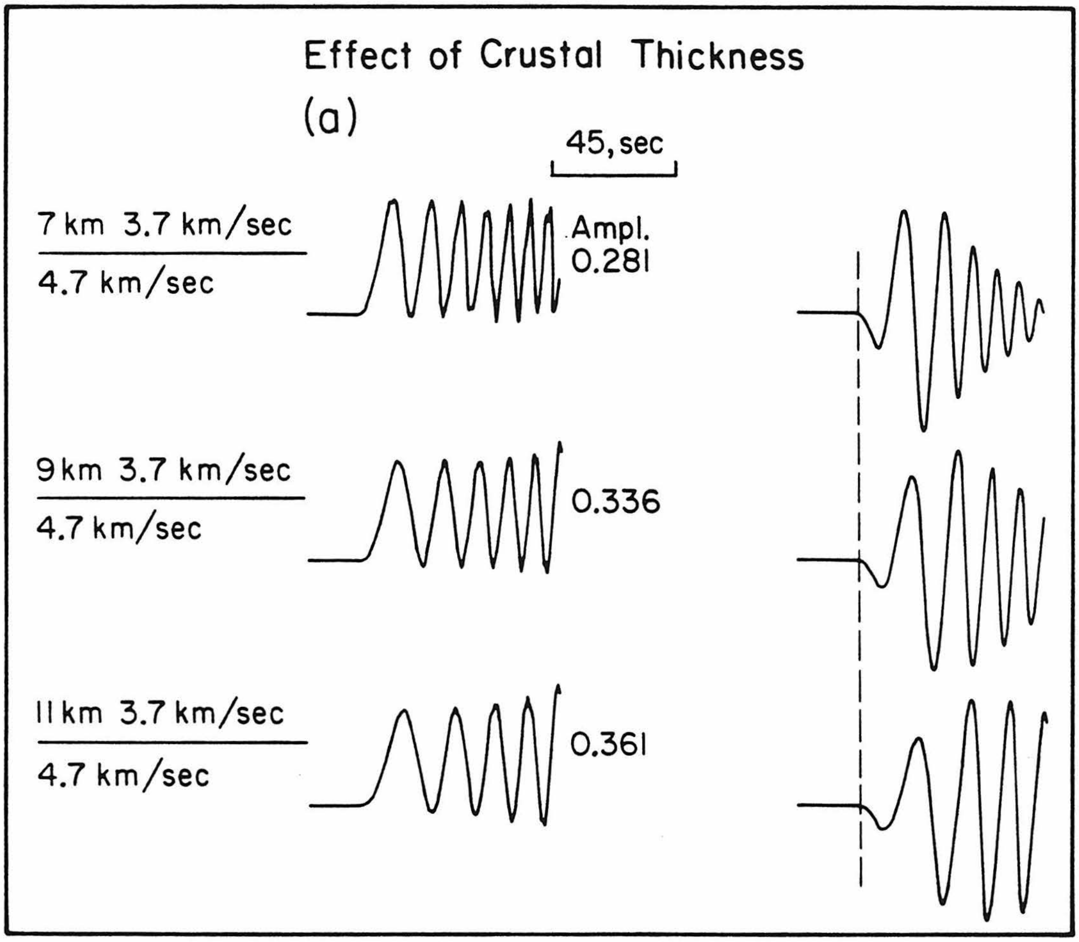

Figure 2.4a Step response at 12° for varying crustal thicknesses. The structure used is at the left, the step response in the middle and at the right is the response of a long-period WWSSN instrument to the step response. The dashed line indicates the same reference time.

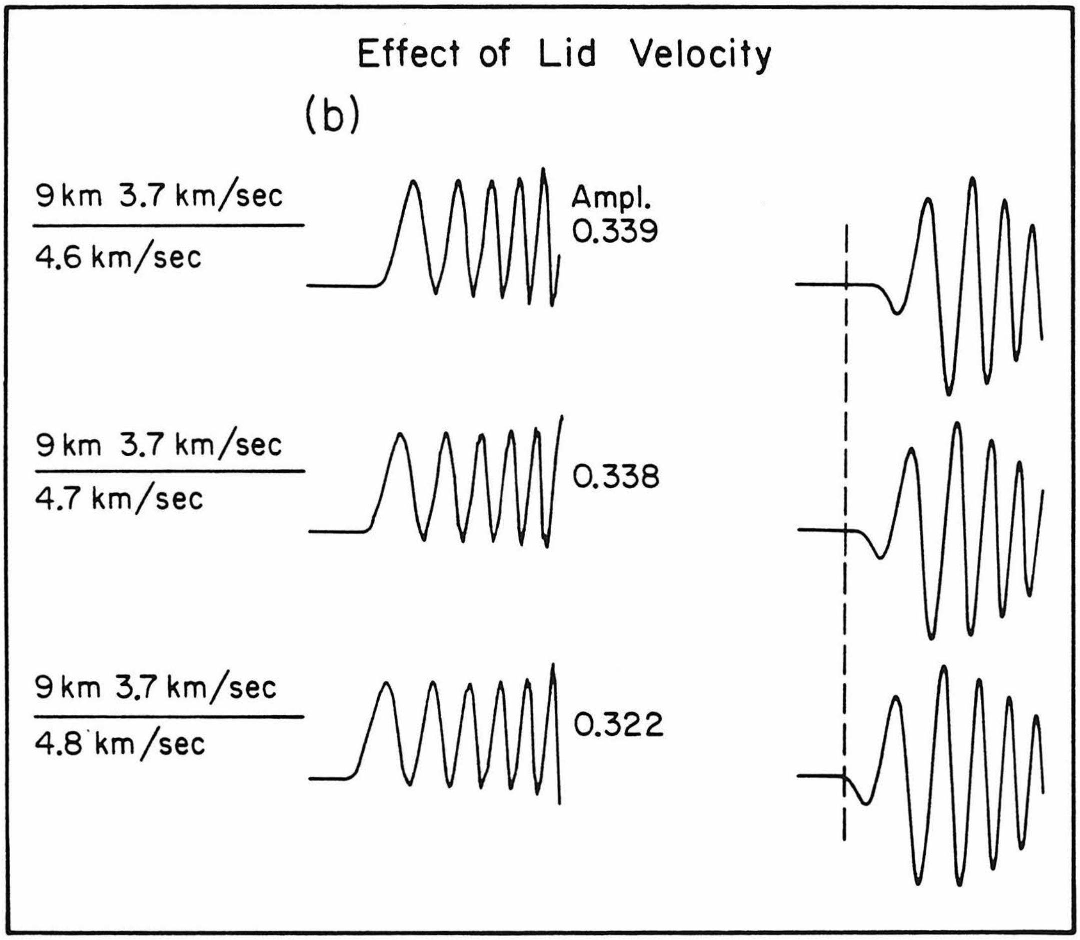

Figure 2.4b Step response at 12° for varying lid velocities. The columns are the same as in the previous figure.

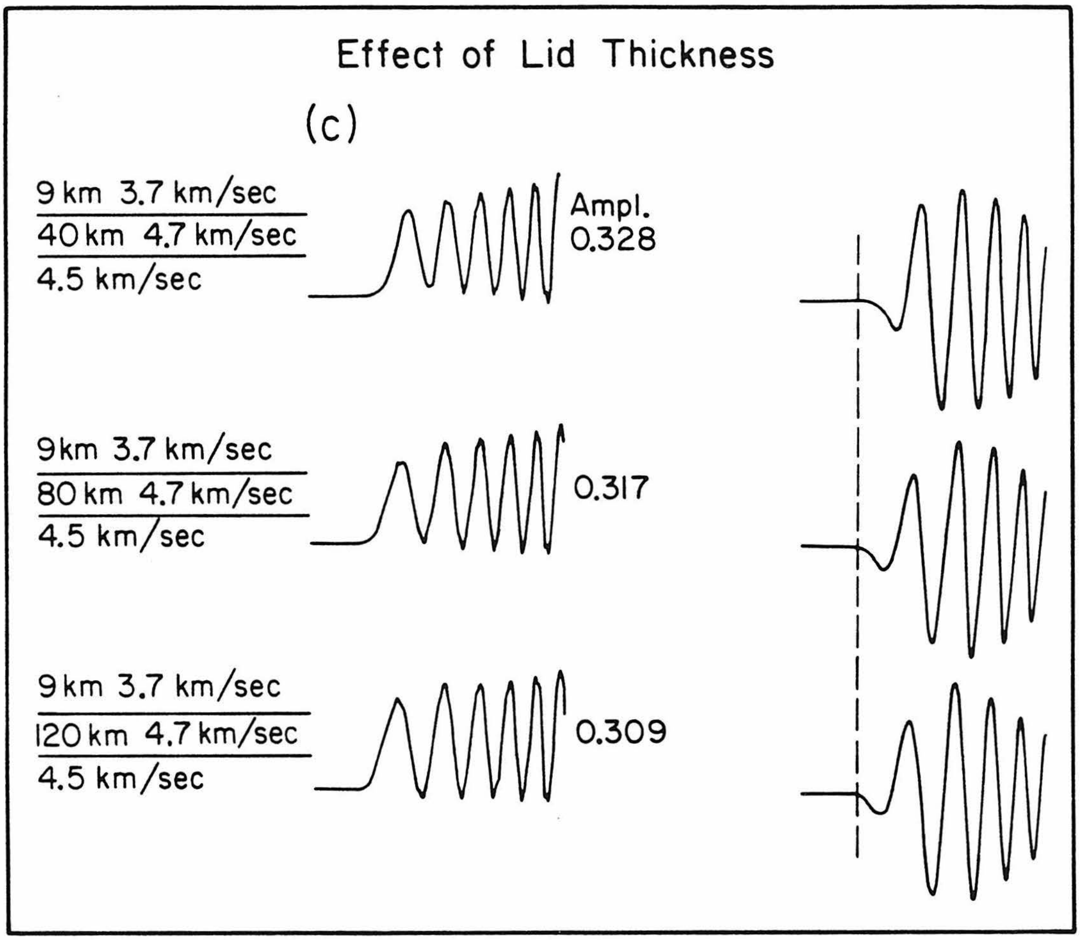

Figure 2.4c Step responses at 12° for different lid dimensions. The columns are the same as in Fig. 2.4a.

and this becomes more important in the back of the waveform where the reflections are more numerous. Changing crustal velocity will have the same effect. A slower crust would be equivalent to a thicker crust.

Fig. 2.4b shows the effect of changing lid velocity but keeping the crust constant. The waveforms are not changed significantly but the absolute travel-time changes by 12 sec with a change in lid velocity from 4.6 km/sec to 4.8 km/sec. In Fig. 2.4c we have added a further variation by putting a lower velocity half-space below the lid. In this case, all the crustal reverberations were used along with rays which have reflected from the bottom of the lid up to 4 times. The reflection coefficient at the lid half-space boundary is the opposite sign of that at the crust lid boundary. Thus, for a thin lid, the lid rays cancel the front of the waveform. The thicker lids have little effect at 12^o because the rays arriving at the station from deeper depths are steeper and thus the reflection coefficients are fairly small. The thicker lids will affect the Love wave at further distances.

We approached the data at regional distances in the following way. First, the crustal thickness was adjusted to match in time the successive peaks and troughs in the wavetrain. The crustal velocity was kept fixed at 3.7 km/sec. Next the lid velocity was modified to match the absolute travel-time of the first downswing. There is some tradeoff here between the lid thickness and the lid velocity. However, as can be seen in Fig. 2.4, there is a difference between a high velocity thin lid and a low velocity thicker lid. The separation of the first two downswings is different in the two cases since lid velocity basically shifts the whole waveform but lid thickness controls only the front of the signal. The lid models found in this way are obviously very crude but they should constrain the main features of the very shallow mantle and allow us to investigate deeper structure.

Fig. 2.5 shows the two nearest seismograms used in the study. The later arrivals at BEC were too large to recover. These seismograms both recorded almost pure SH motion with paths totally in ocean older than 100 Ma. The dispersion of the signal at SJG required a crustal thickness of 9.5 km. This is thicker than normal oceanic crust, though it could be that we used too high a crustal velocity. A low velocity, low Q layer at the surface would decrease the amplitude of the back of the wavegroup, since the signal there is due to more surface reflections than the front. It would also decrease the average crustal velocity. Officer et al. (1952) report an average 2 km thick sediment layer south of Bermuda from a refraction survey. Another cause of this could be that we used the wrong depth for the source. The source depth for the synthetics is 5 km but the event could be deeper. For the long periods this will have no effect but the shorter periods could be changed slightly. To match the timing of the first arrival a lid velocity of 4.75 km/sec was needed. The separation of the first downswings requires a lid thickness of at least 80 km. At these distances a thicker lid would appear about the same. Primary rays from below the lid are not noticeable.

In Fig. 2.6 we show further data at regional distances. These stations are within continents and the transition from oceanic to continental crust has an obvious affect on the waveforms. The overall period of these signals is much longer than the SJG record from the same event. From the previous discussion, this is what one would expect for an increase in crustal thickness. We used a crust of 19.5 km, with the same velocity as before, to model these records. This was found empirically to fit the overall dispersion of the data. How the actual ocean-continent transition affects the Love wave is not clear but since the crustal thickness does not change the arrival

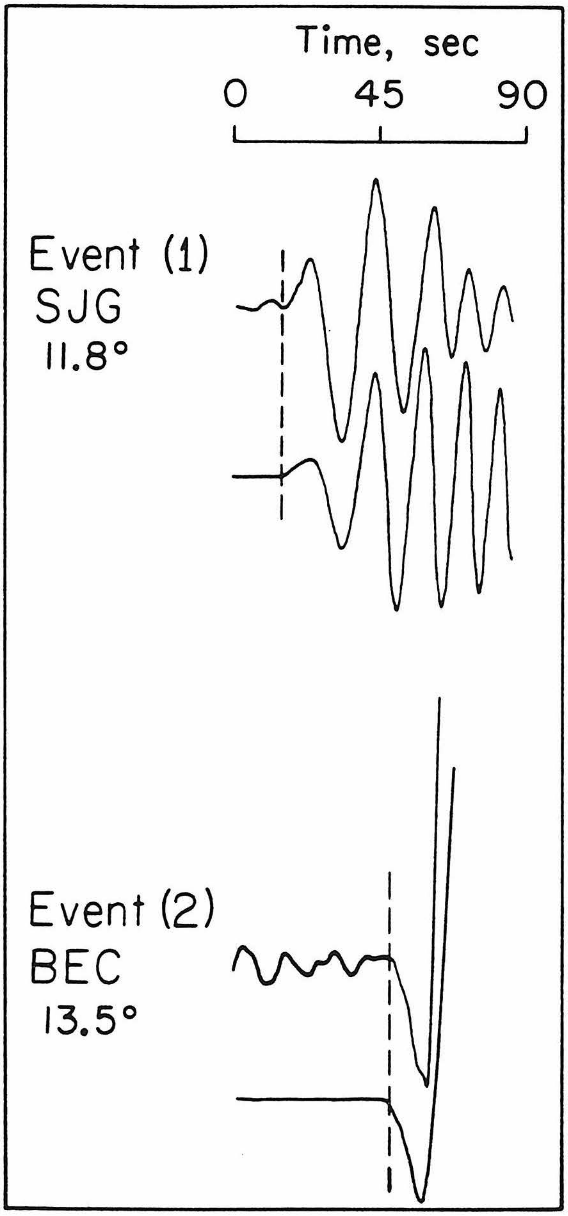

Figure 2.5 Data and synthetics for two oceanic paths at stations at regional distances. The timing is absolute. The data are shown above the appropriate synthetic.

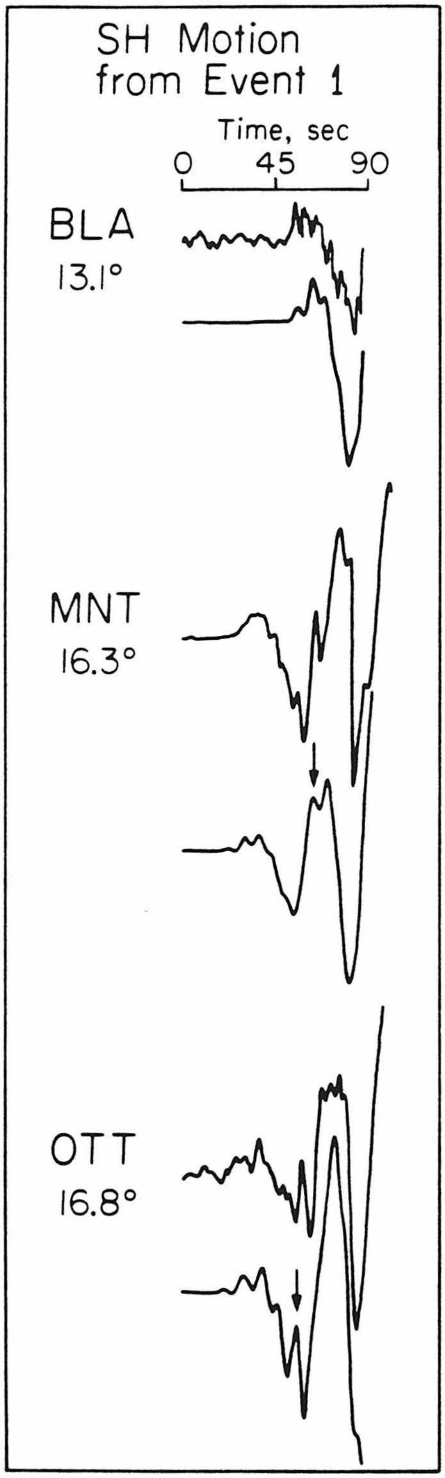

Figure 2.6 Data and synthetics for the Bermuda event to continental stations. The 405 km reflection is marked by an arrow. The timing is absolute.

time by much, using an average thickness for the crust is probably sufficient. Note that the arrival times are well fit for this data set using the same model as in the previous figure. Since the data is fit for three azimuths, from the same event, with the same model, it appears the event was not greatly mislocated, nor is there a large directional anisotropy. The arrows, in the figure, indicate the reflected arrival from the 405 km discontinuity. It can also be seen in the data at about the right time. The data, in the previous figures, constrain the lid to have a high velocity (4.75 km/sec) and a thickness of at least 80 km. The timing of the 400 km reflection indicates the velocities below the lid must be significantly lower than those found beneath the shield in Chapter 1. Further evidence for the thick lid will be presented later in relation to the SS data.

Structure Below the Lid

Fig. 2.7 shows the travel-time curve for the Atlantic model. The previous data basically established the AB branch to 16°, this is energy from the lid. The two seismograms at 16.3 and 16.8° showed an arrival corresponding to the cusp labelled C, a reflection from the 405 km discontinuity. The dashed lines refer to diffracted energy or tunnelled energy through the lid. There are several more seismograms from Events 1 and 2 which sample deeper than the lid. Fig. 2.8 shows a small profile to the north of these events. Again, most of the paths are through old ocean but the receivers are on continental crust. In the synthetics, an average crust of 19.5 km thickness is again used. The crustal arrivals, or Love waves, arrive just after the branch labelled B. Errors in the crustal approximation should not affect the measurements of the mantle arrivals which determine the triplication curve. The mechanism

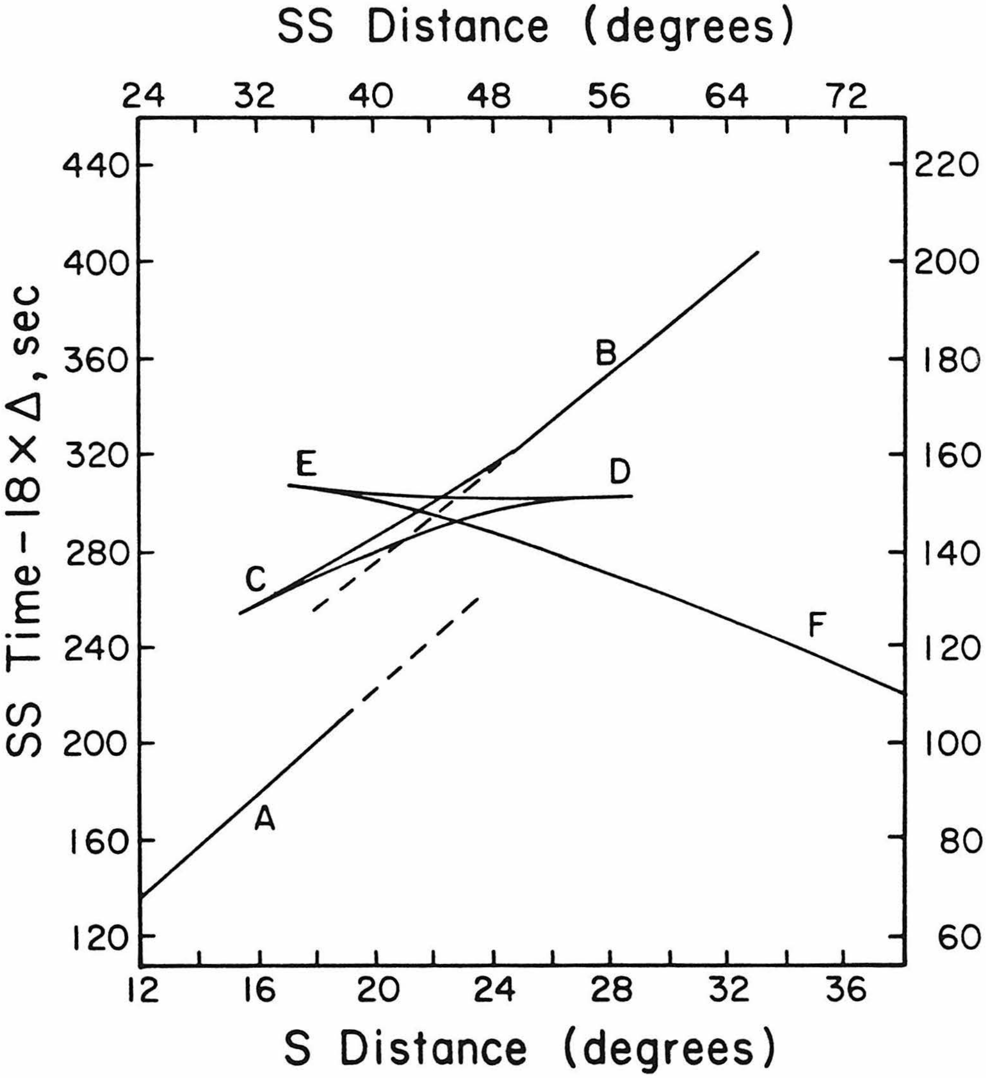

Figure 2.7 Triplication curve for the Atlantic model. Dashed lines represent diffracted or tunnelled energy.

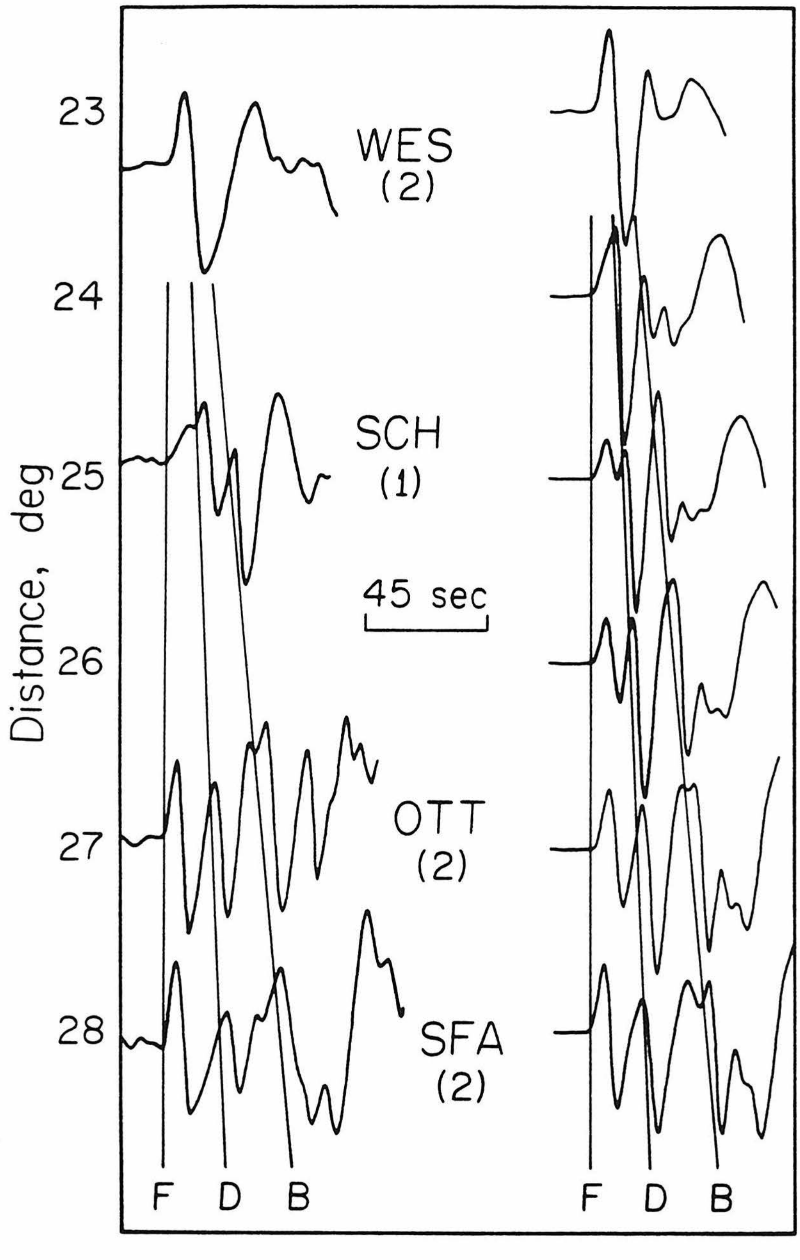

Figure 2.8 A short profile of S-waves beneath the old Atlantic with a synthetic profile to the right. The triplication branches corresponding to Fig. 2.7 are indicated.

appropriate for Event 2 was used in the synthetics. This is inappropriate for the record at SCH from Event 1 causing some of the misfit there, though there are obvious arrivals in the record corresponding to those in the synthetic at the right time. With respect to Fig. 2.7, one can follow three branches over several degrees. Branch F is from below the 660 km discontinuity, branch D is a wide angle reflection from the 660 km discontinuity and branch B is the wide angle reflection from the 405 km discontinuity. The model derived from East Pacific Rise data, in Chapter 1, which was used below 200 km, fits the timing of all the branches very well. Differences of 1% over 200 km at any depth range would be noticeable in the relative timings of these phases.

In Fig. 2.9, two records from this profile are shown compared to synthetics computed from the Atlantic model and a modified Atlantic model. The modified model is the same as the Atlantic model except from 225 to 400 km depth, where we have substituted the velocities found beneath the Canadian shield at those depths. The SCH synthetics were done using the appropriate source for Event 1, also the Love wave was not included as this station is much further inland than the others and the Love wave arrives later. This figure illustrates the sensitivity of the arrival time of branch B to the structure from 200 to 400 km. The arrows indicate the arrival from the 405 km discontinuity in the data and synthetics. The modified model is too fast by about 5 sec. The velocity could be decreased from 100 to 200 km to compensate for this but the observations of branch C at 16° and in the SS data (shown later) limit the amount one can modify the structure. Note that the 660 km triplication is hardly changed at all by the modification.

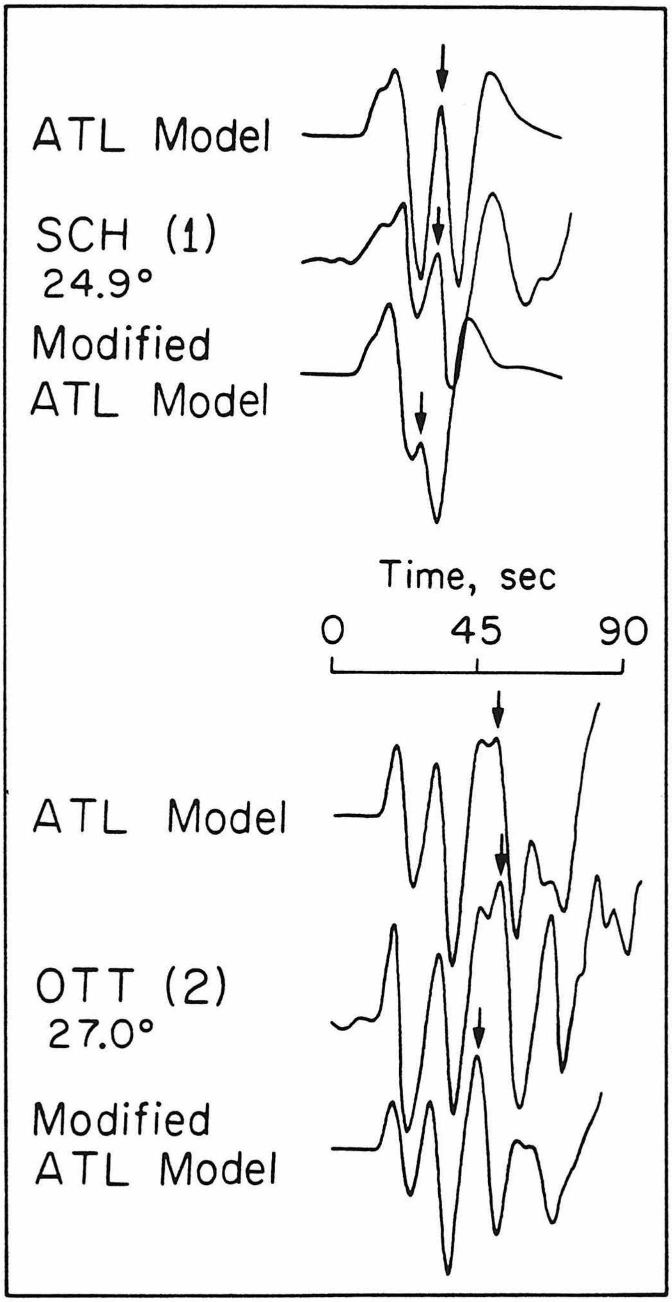

Figure 2.9 A comparison of the Atlantic model with a modified Atlantic model. The modified Atlantic model has shield velocities from 225 to 400 km and this changes the 405 km backbranch significantly, as indicated by the arrows.

From this small data set we can conclude several things. With the constraint of a high velocity lid, the velocity from 200 to 400 km must be substantially the same as beneath the East Pacific Rise. Also, the structure below 400 km appears to be the same as beneath the Canadian shield and the East Pacific Rise.

Observations of SS

Events 3 through 9 are further from the stations than the previous data, but they can still be used for studying the upper mantle. Events 3, 4 and 5, in particular, have paths to east coast stations through ocean mostly older than 100 Ma. These events produced data in the range 27° to 53°, thus the SS phases from these earthquakes are going through the same triplications as S waves from 13.5° to 26.5°. As discussed in Chapter 1, SS data in this range can be very useful in modelling the mantle. The S wave bottoms below 800 km where the structure is thought to be fairly uniform. The source and receiver structure is the same for both S and SS, thus the S wave serves as a useful absolute time marker for the SS phase which travels through the heterogeneous upper mantle.

Fig. 2.10 illustrates the synthetic construction of seismograms in this range. These seismograms were computed using the Cagniard-de Hoop technique. The first column shows the results of just adding in primary S rays. The triplication branches are labeled on the diagram. The backbranch due to the 660 km discontinuity can be followed to near 32°. The backbranch from the 405 km discontinuity is seen to about 30° but there is a small arrival continuing to greater distances. This more distant phase is not actually from the 400 km discontinuity but is due to rays coming just out of the shadow zone, bottoming near 250 km depth, which travel to large

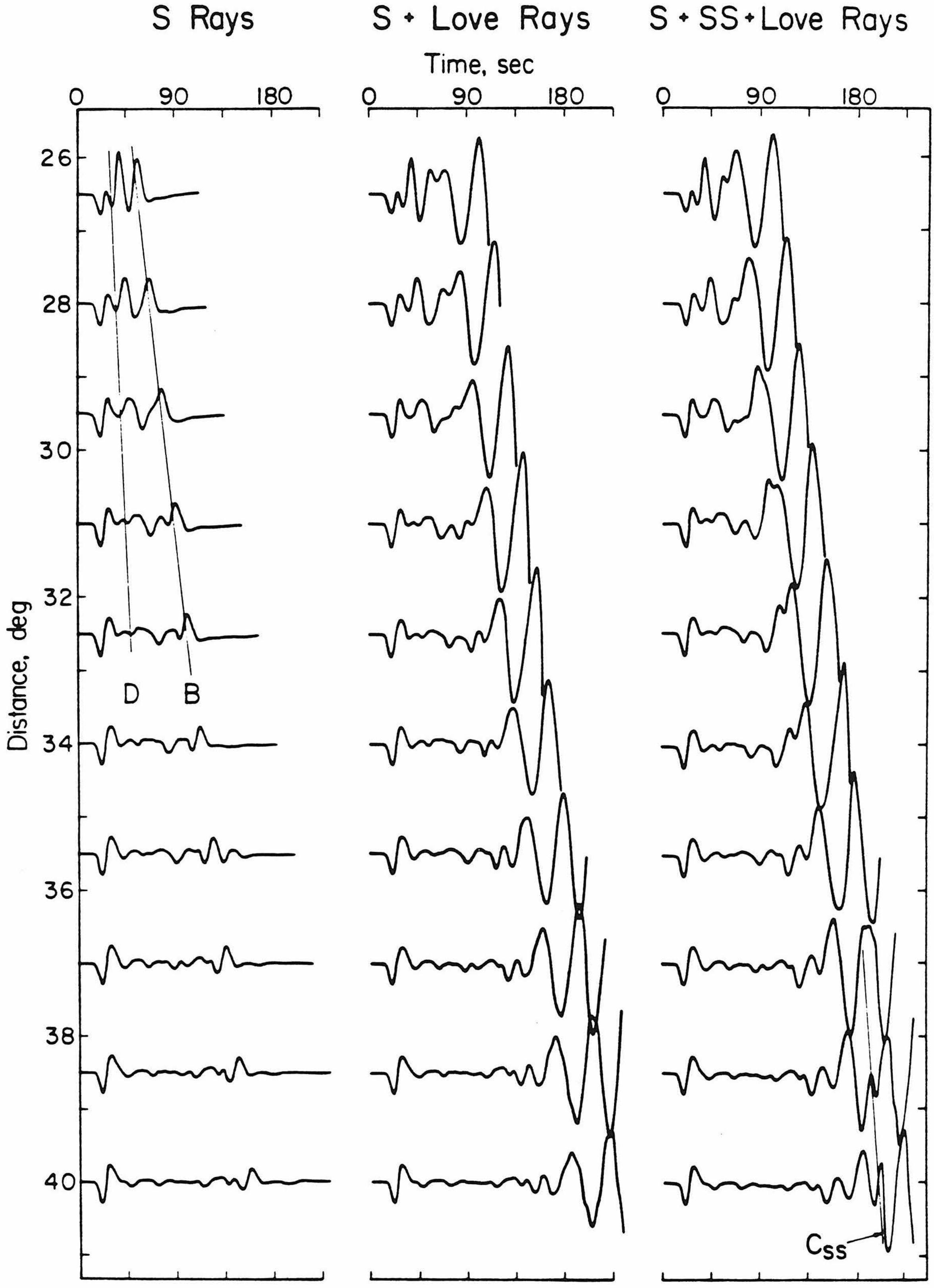

Figure 2.10 The construction of synthetic seismograms from 26° to 40° . The first column shows the effect of just S rays, the middle has crustal and lid multiples added and the right column has deeper SS rays added.

distances because of the high velocity thick lid. If there is a low Q layer below the lid this arrival could be more attenuated. In the second column we have added what we call the Love rays. These are multiples in the lid and crust. For this example, a 19.5 km crust was used, as the following data are all from continental stations. Rays with 25 reflections in the crust and up to 4 reflections from the bottom of the lid were used. One multiple within the lid was also found to be necessary. One can see that this energy drastically changes the appearence of the seismograms near the 405 km backbranch time. As stated before, this arrival does not interfere with upper mantle arrivals in continental areas. Finally, in the third column, we have added SS rays from below the lid. The major effect of these rays is seen from 37 to 40°. The SS B branch from the 400 km discontinuity can be seen clearly. Even at 40° it is well behind the Love wave.

The Love wave, at these distances, again provides information on the thickness of the lid. In Fig. 2.11 we have computed just the Love rays at a distance of 40°. The crust is fixed at 19.5 km and the lid velocity is 4.75 km/sec, as was found before. The lid thickness is varied from 50 to 110 km. Again, the rays reflecting from the bottom of the lid are negative relative to those of the crustal rays. The thinner lids have stronger reflections from this boundary and thus there is more destructive interference of the front of the Love wave. Fig. 2.11 shows the response of a WWSS instrument, convolved with a 5 sec trapezoidal time function, to the Love rays. The arrival time of the first large upswing is very sensitive to the lid thickness. The front of the Love wave from 27° to 40° should, then, put constraints on the lid. The other arrivals, at these distances, will constrain the deeper structure.

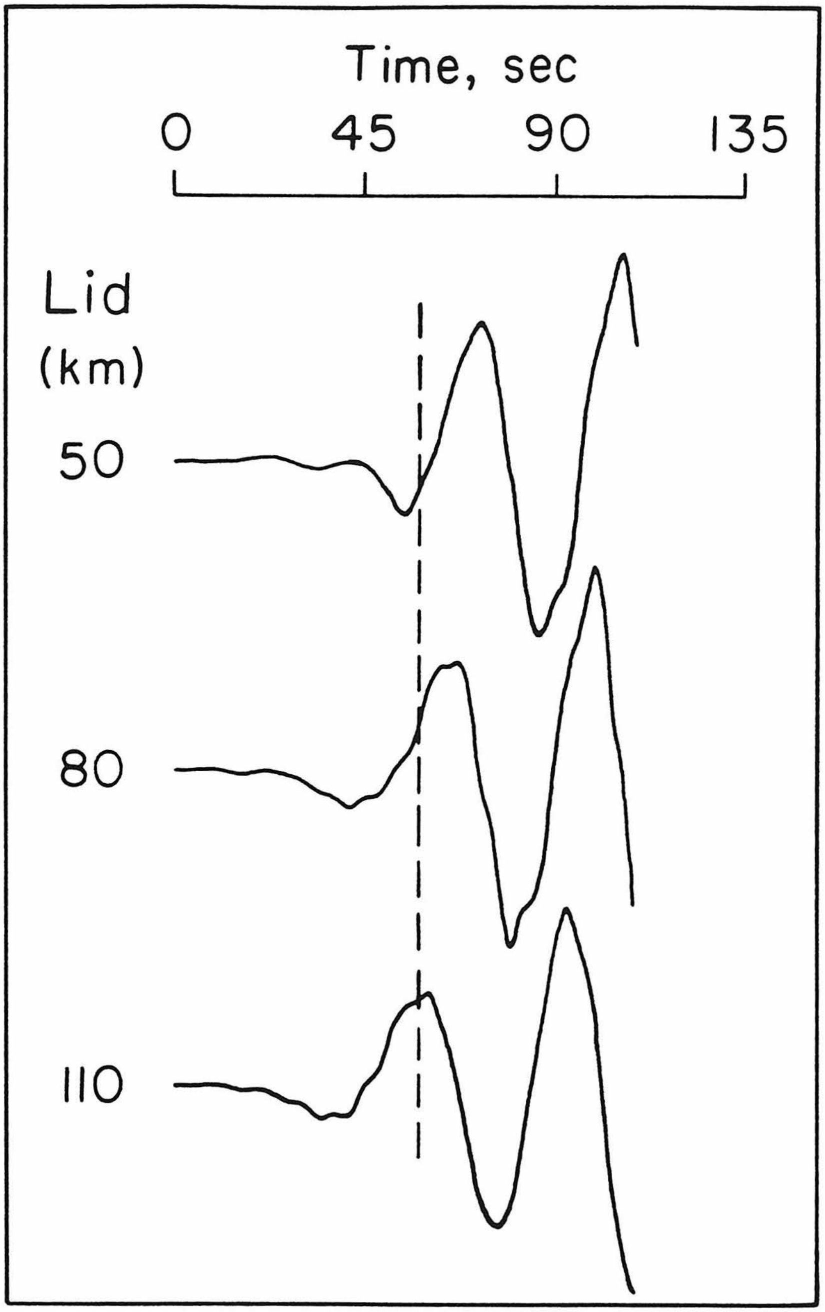

Figure 2.11 A sensitivity study on the effect of lid thickness on the front of the fundamental Love wave. Just crustal and lid multiples are computed for various lid thicknesses.

Fig. 2.12 shows the data in the range discussed above with the same synthetics as were derived in Fig. 2.10. The travel-time lines in Fig. 2.10 are reproduced in this figure on the data and synthetics. The stations, listed next to the seismograms recorded by them, are of varying distances from the ocean. A 19.5 km thick crust was used as an approximation to the actually more complicated situation. This thickness seems to satisfy the dispersion of the later part of the Love waves recorded at these stations and should not affect the mantle arrivals too much. All the arrivals pointed out in the previous discussion of the synthetics can be seen in the data. The arrival time and amplitude decay of the 660 km discontinuity, branch D, is modeled extremely well. The structure near 600 km was derived from a totally different area so that this fit is quite surprising. This indicates that heterogeneity below 400 km from the East Pacific Rise to the Canadian shield to the old northwest Atlantic is extremely small. Velocity differences of 1% from 400 to 600 km would change the synthetics significantly at these ranges.

From 38° to 40° the B branch of the 405 km discontinuity is visible in the data, as an SS arrival. It can be identified by the higher frequency content than the preceding Love wave pulse and its moveout from the S wave. Data beyond 40° confirm our identification of the SS B branch. Note, also, that the timing is consistent with the arrival at 16°, Fig. 2.6, which was modeled as the 405 km reflection. The midpoints of these paths are in ocean older than 100 Ma.

The part of this section showing the most variability in the data is indicated by the line labeled B. The arrivals just following this line are due to rays from several depths as was illustrated in Fig. 2.10. The front part of this waveform is due to S rays, and crustal multiples of them, coming from below the lid. This arrival is most

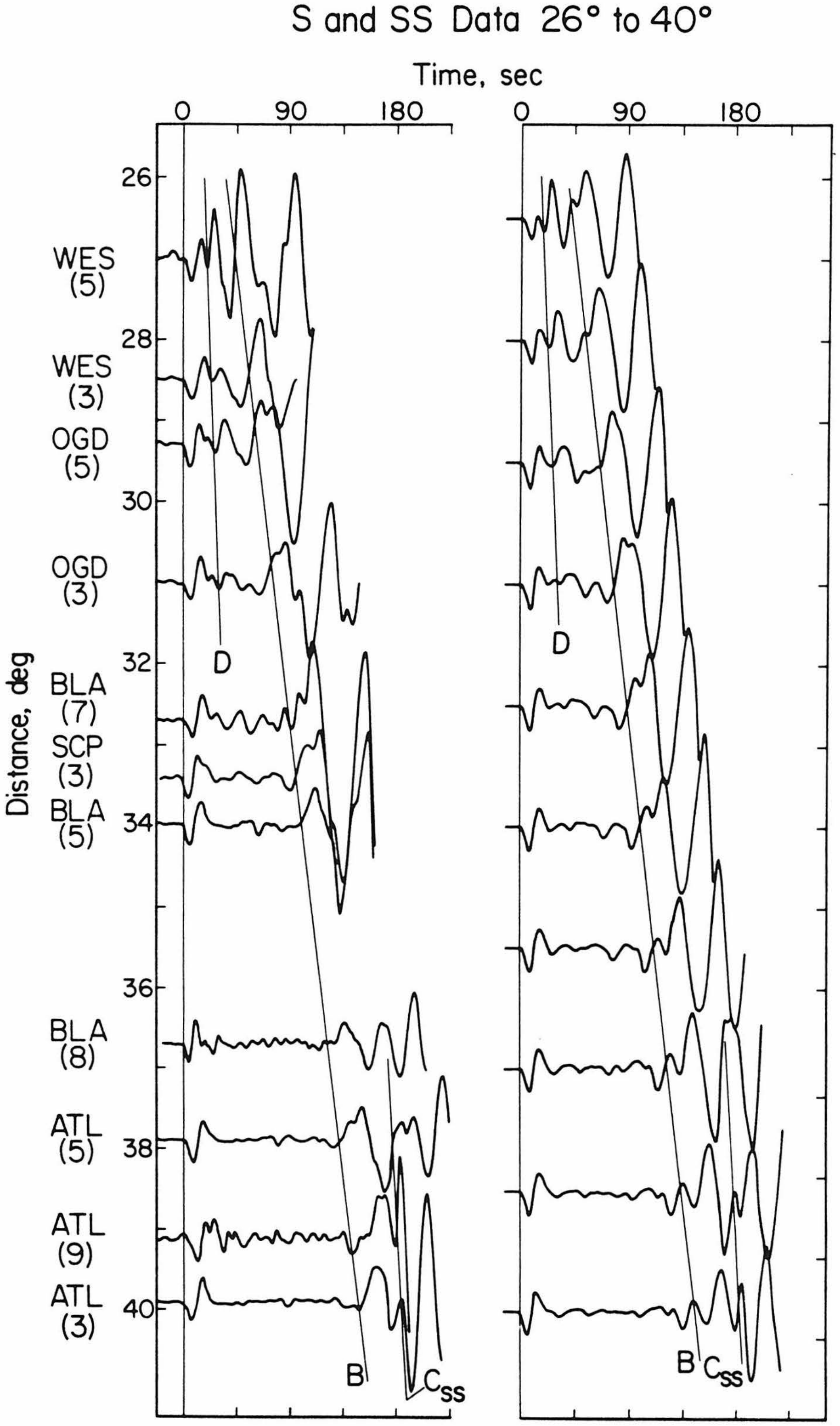

Figure 2.12 Data and synthetic comparison from 26° to 40°. The synthetics are from Fig. 2.10; several triplication branches from Fig. 2.7 are indicated.

sensitive to the velocity from 150 to 350 km. The late time of this phase, in the data, indicate low velocities at this depth range. Just following this energy is the start of the Love wave which travels at near the lid velocity. The time of this wave group indicates a thick, fast lid as discussed earlier. This energy, however, varies by several seconds from station to station but in an understandable way. Comparing the records at ATL from Events 3 and 9 one can see that the Love pulse is faster from Event 3. From the map in Fig. 2.2, it is seen that the path from Event 3 is 3/4 ocean older than 100 Ma whereas the path from event 9 is only about 1/2 ocean that old. Past studies, such as that by Mitchell and Yu (1980), have documented the growth in thickness and velocity of the lid with age in the Pacific. We are probably seeing this phenomenon here. The Atlantic model is an average of a varying lid in the older Atlantic. Event 3, at ATL, has a faster Love wave than the model predicts indicating the lid is probably even thicker than 100 km in the older ocean, while the first part of the paths from these events are probably through a thinner, lower velocity lid. However, a 100 km, 4.75 km/sec lid does a fair job over these paths, as it did for the data at regional distances.

In Fig. 2.13 further SS data is presented from distances beyond 40^o. The stations used for this profile are well inland, but again, the midpoints are within old ocean. The large distances used here and the fact that the stations are so far inland eliminate contamination by the Love wave. At SHA, long period Love wave energy is apparent but it is behind the SS wave and does not present a problem. Since the Love wave is not important here, and the SS phase at these distances is dominated by structure well below the lid, we computed the synthetics in this figure using the more efficient WKBJ technique. No Love wave is computed. In this range, SS passes

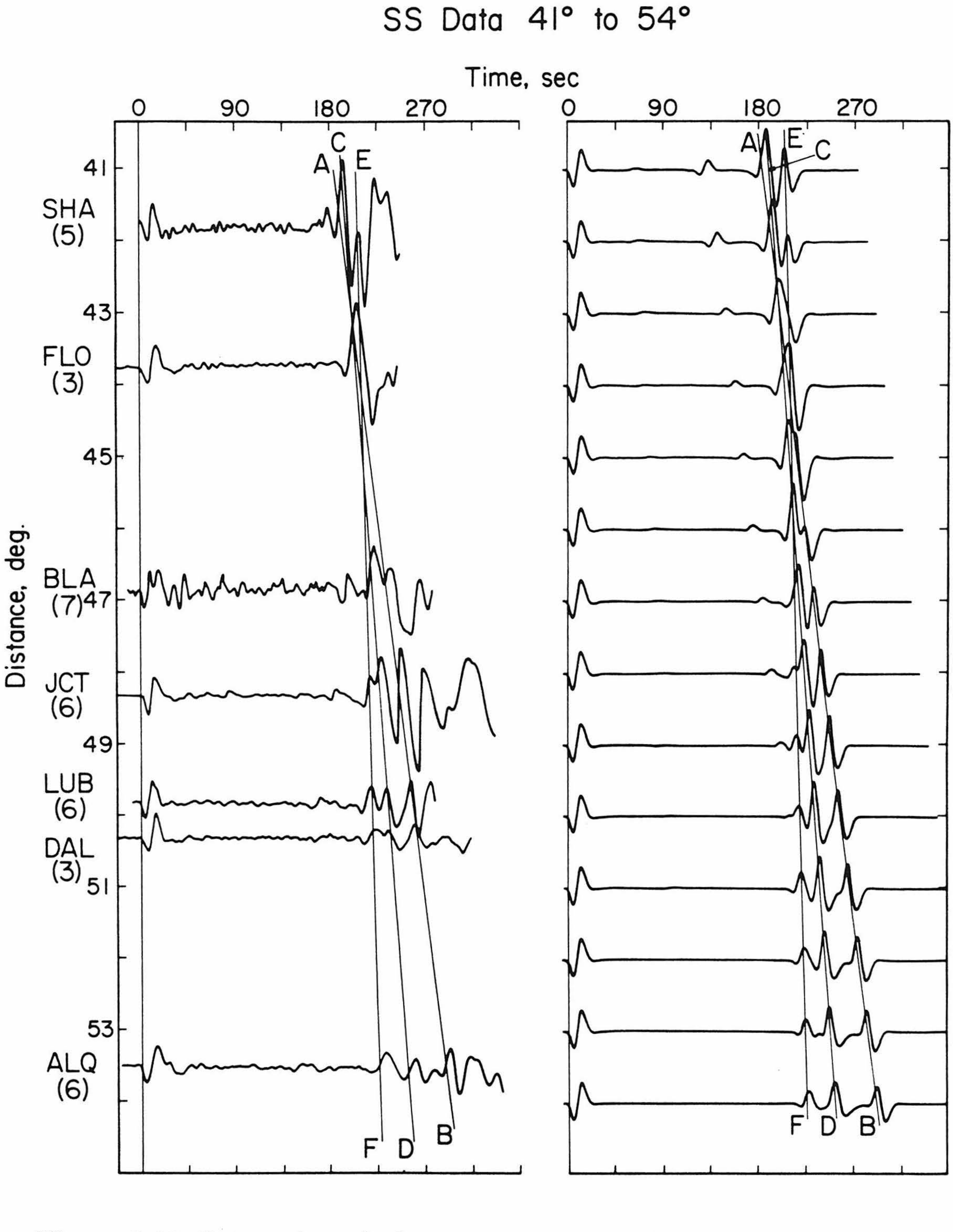

Figure 2.13 Data and synthetic comparison from 41° to 53°. The SS phase is passing through two triplications as indicated by the travel-time lines.

through the same triplications as S from 20° to 26°. The branches from the travel-time curve in Fig. 2.7 are labeled on the synthetics and the data. The data at 41° and 43° are reproduced many times from other events and at other stations. At 41° two arrivals are present, the first is from the 405 km discontinuity (branch C), the second from the 660 km discontinuity (branch E). At 43° they are crossing, producing a large simple SS wave. Near 46° the back branch of the 400 km discontinuity begins to separate out and can be followed to 53°. The 660 km back branch begins to separate from energy below 660 km near 48° and it too can be followed to 53°. This data just confirms the previous conclusions but also illustrates the compatiblity of S and SS wave modeling. Many regions which are inaccessible to an S wave upper mantle study can be sampled with SS.

Discussion

The model derived in this study was based on several assumptions. The lid was assumed to be a homogeneous high velocity layer. Structure in the lid is certainly possible but our technique of calculating synthetics prohibited using more than a couple of layers due to the number of rays needed. We have concentrated on fitting long period data, greater than 20 sec, which should not be too sensitive to the fine structure of the lid. A high gradient in the lid would necessitate a thicker lid as the shadow would be moved to nearer distances. Thus, the lid model is just an approximation to a more complicated structure which could be thicker.

The velocities just below the lid are difficult to determine due to the extensive shadow zone caused by the lid. The same structure was used below 200 km as was found beneath the East Pacific Rise in Chapter 1, but there is some tradeoff between the velocity from 100 to 200 km and the velocity from 200 to 400 km. On the other hand, decreasing the velocity in the Atlantic model just below the lid to values found beneath the East Pacific Rise at the same depths, would allow only a slight increase in velocity from 200 to 400 km. Models, such as PREM (Dziewonski and Anderson, 1981), with large velocity jumps near 200 km and corresponding low gradients to 400 km, cannot satisfy our data. The back branch from the 405 km discontinuity is too fast in these models. Thus, we feel confident in the conclusion that shear velocity from 200 to 400 km beneath the old Atlantic is far closer to the velocities beneath the East Pacific Rise than beneath the Canadian shield.

It is interesting to compare the results presented here to other studies of the upper mantle. Sipkin and Jordan (1975, 1976, 1980) have measured ScS and multiple ScS times, attributing their variations to upper mantle heterogeneity. For the shield model (SNA), with a 35 km thick crust, ScS is 4 sec faster than that predicted by the Jeffreys-Bullen model. The tectonic model, TNA, is 6.2 seconds slower and the Atlantic model is just about the same as the Jeffreys-Bullen prediction. For the two oceanic models a 9 km crust was used. The shield model fits the mean of the measurements by Sipkin and Jordan (1976) for Precambrian shields, though they have a 2 sec scatter for those measurements. Their oceanic data fall between -1 and 8 second residuals. These are mostly measurements in the Pacific ocean with varying oceanic crustal age. The two oceanic models, TNA and ATL, bracket their data fairly well. Thus, the two techniques seem compatible as far as generalizing the results of Chapters 1 and 2 to similar tectonic provinces on other parts of the earth.

A more widespread method for investigating the shear structure of the upper mantle, is the measurement of the dispersion of long-period surface waves. In Figs.

2.14 and 2.15, the dispersion curves of fundamental Rayleigh and Love waves are presented for the three models derived in Chapters 1 and 2. Corrections due to anelasticity were included assuming that the models are appropriate for a period of 10 sec. The Q structure was taken from PREM (Dziewonski and Anderson, 1981) with the exception that Q was kept high throughout the different lid portions of the models. The P velocity for the shield was taken from Given and Helmberger (1981) and for the East Pacific Rise from Walck (1984). The Atlantic P model used has the same P velocity in the lid as the shield model and velocities below the lid the same as in Walck's model. A crust of 35 km was used for the shield and a crust of 9 km for the two oceanic models. For Rayleigh waves, there are large differences in phase velocity at shorter periods (about 5% at 120 sec), which decrease rapidly with increasing period (to about 1.5% at 270 sec). The Love waves have a wide spread in phase velocity at all periods (6% at 120 sec to 5% at 270 sec).

Several authors have looked at great circle long-period surface waves to derive global dispersion curves. Recently, Nakanishi and Anderson (1983) have used new, high-quality long-period data to map the phase velocities of Rayleigh and Love waves over the earth. They give regionalized phase velocities for different age oceans and these are plotted on the dispersion curves for the models derived here. The regionalization is given on the figures. At periods greater than 150 sec, the regionalized Rayleigh wave phase velocities fall between the models ATL and TNA, with the exception of Region A. Region A is essentially the oldest region of the western Pacific, and perhaps the regionalization was unstable for that relatively small area. If Region A does have these high phase velocities, the models derived here, including the shield structure, are significantly too slow at great depths in the upper mantle in that area.

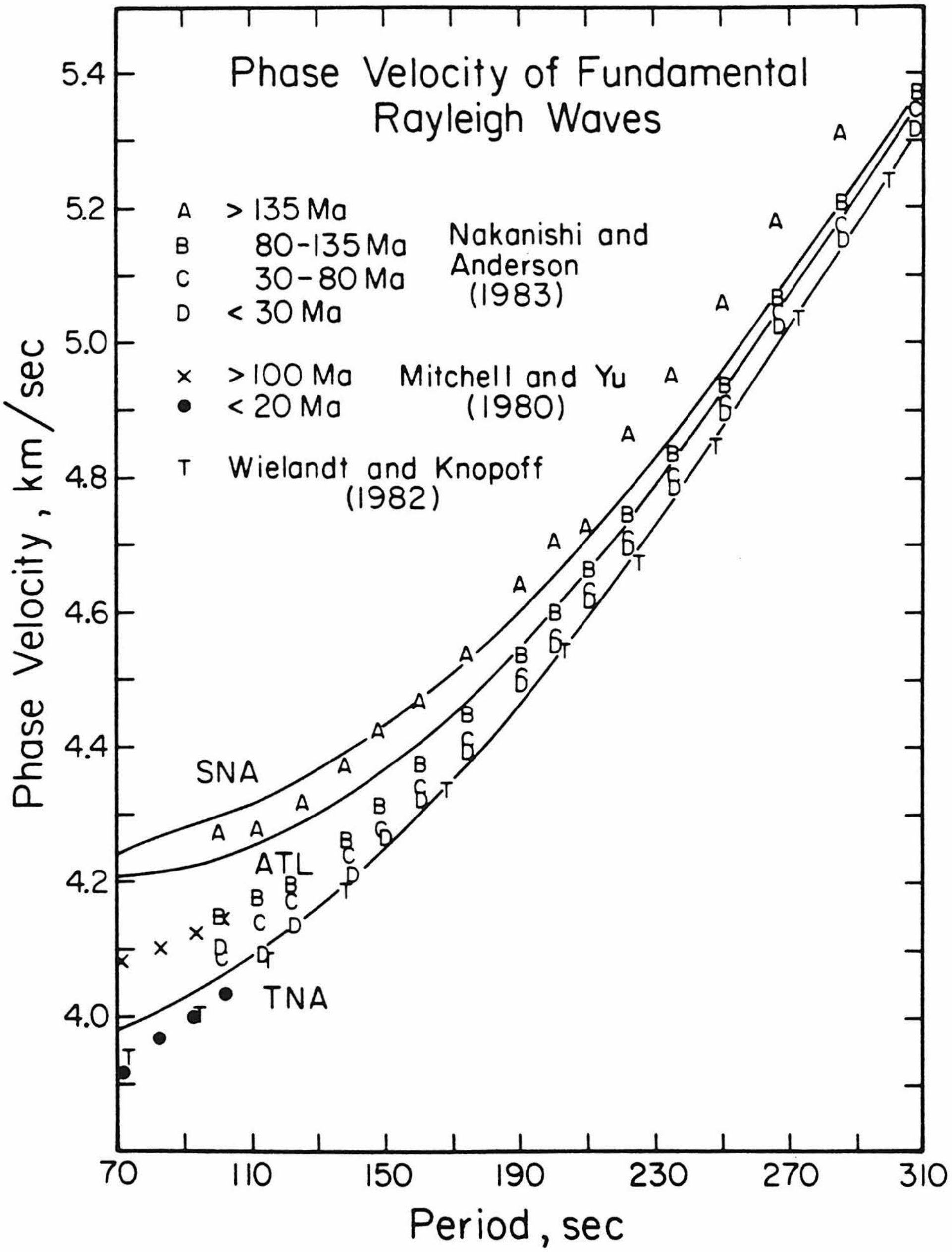

Figure 2.14 Fundamental Rayleigh wave dispersion curves appropriate for models SNA, TNA and ATL are compared with data obtained from the literature.

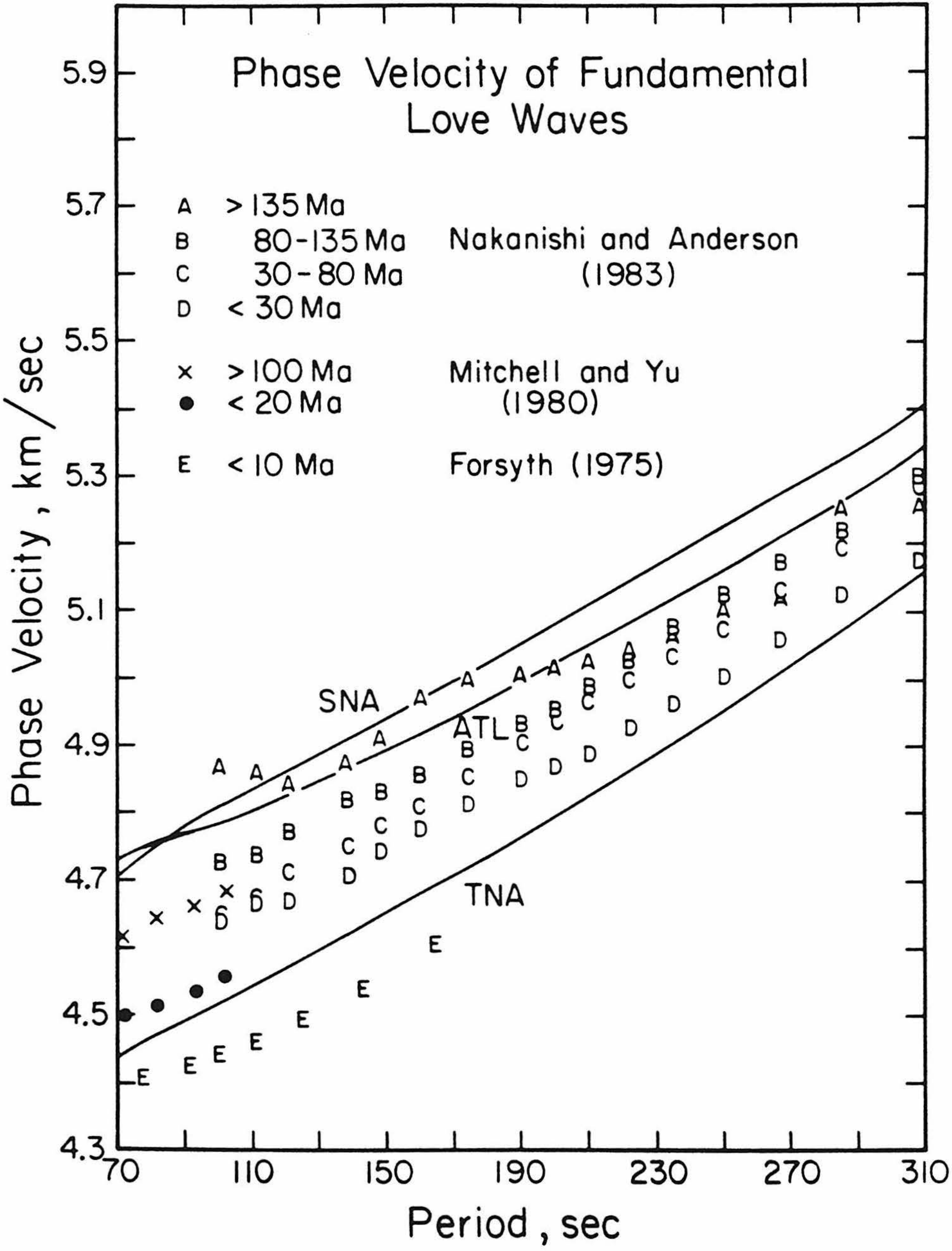

Figure 2.15 Fundamental Love wave dispersion curves for models SNA, TNA and ATL are compared with data from several other studies.

In all other oceanic areas, the deeper structure looks very similar to what is proposed here. Wielandt and Knopoff (1982) looked at long-period Rayleigh waves which propagated near the East Pacific Rise and one would expect TNA to agree with their results. In fact, from 100 to 310 sec, the agreement is excellent, indicating that TNA is probably a good model for most of the East Pacific Rise. This also indicates that there is little transverse anisotropy beneath this region. The long-period Love waves measured by Nakanishi and Anderson (1983) all fall between the TNA and ATL model predictions. Since the areas studied to derive TNA and ATL are the two extremes in terms of oceanic age, this is probably not too surprising. The Love waves, at these periods, sample shallow structure, and thus it appears that the lid of ATL is thicker or higher velocity than average oceanic lid beneath crust older than 80 Ma.

At shorter periods, there is a general discrepancy between Rayleigh wave measurements and our models. At periods less than 150 sec, Nakanishi and Anderson found significantly lower phase velocities than ATL predicts except for Region A. Mitchell and Yu (1980) studied Rayleigh waves in the Pacific at these periods and also found lower phase velocities for old the old Pacific than ATL predicts. The Love wave measurements of Mitchell and Yu are also seen to be slower than ATL, but the discrepancy is not as large as for the Rayleigh waves. For younger oceans, the discrepancy appears to be much less. Nakanishi and Anderson's Rayleigh wave dispersion for young ocean agrees well with TNA, as do the curves derived by Mitchell and Yu for young ocean and Wielandt and Knopoff for the East Pacific Rise. For Love waves, Mitchell and Yu also found phase velocities near those of TNA for young ocean, as did Forsyth (1975) in his study of the East Pacific Rise region. A possible cause of the discrepancy for older oceanic regions could be anisotropy in the lid, as proposed by Anderson and Regan (1983). However, since the Love wave phase velocities for old ocean in the Pacific are also lower than in model ATL, there may be structural differences between the old Atlantic and the old Pacific in the upper 100 km of the mantle.

In conclusion, the long-period Rayleigh wave dispersion predicted by the bodywave models presented here agree well with measurements from other areas with the exception of the oldest western Pacific from Nakanishi and Anderson (1983). This indicates good agreement of the deep structure (below about 250 km) between our models and global average models of the earth derived from surface waves. The shorter period Rayleigh waves and the Love waves show large variations which could be due to differences in the structure of the upper 100 km or to anisotropy at those depths.

Conclusion

We have modeled the waveforms and travel-times of SH wave motion in the older portions of the northwest Atlantic to investigate the upper mantle shear structure there. The old Atlantic has a thick, high velocity lid beneath which the structure is very similar to that found near the East Pacific Rise in Chapter 1. Using the same technique, the Canadian shield was found to have significantly higher velocity than both oceanic areas to about 400 km depth. The bottom of the lid does not appear to be the depth at which the craton and oceans become indistinct.

Below 400 km the model derived for the Canadian shield and East Pacific Rise fit the Atlantic data quite well. Thus, it is felt heterogeneity at these depths is very small throughout North America and its surrounding oceans. The agreement with very long period surface wave studies elsewhere suggest the model below 400 km is a good average for the earth.

Chapter 3

Tomographic Inversion for Mantle Shear Velocity Beneath the North American Plate

Introduction

The development of three-dimensional models of elastic velocities in the earth is in its infancy. On a global scale there has been remarkable progress, however, during the last two years. Global models of shear velocity in the upper mantle, to 600 km depth, have been presented by Woodhouse and Dziewonski (1984), Nataf, Nakanishi and Anderson (1984) and Tanimoto and Anderson (1985). These studies inverted the phase and group velocities of long-period surface waves to derive a spherical harmonic expansion of the shear velocity field of the shallow earth. No apriori regionalization was assumed in these studies, but the results showed a clear correlation of shear velocity with tectonic province in the upper 200 km or so. Below 200 km, the magnitude of lateral heterogeneity decreased and the pattern of velocity variation less closely followed the surface tectonics, although the Woodhouse and Dziewonski model shows faster than normal velocities beneath old, stable continental regions to 400 km depth. Using long-period data has proved very useful and produced interesting results, however, there are some drawbacks with the technique. Due to the wavelengths of the data and the limit of the spherical harmonic coefficients inverted for, one can only hope for a very broad view of the earth's structure, both laterally and vertically. Station residuals for S-waves show very abrupt changes in travel-times (for example, Doyle and Hales, 1967), indicating sharp boundaries in mantle structure. Information on the nature of sharp transitions cannot be found using the approach discussed above. Also, the use of surface waves, as is well known, has decreasing resolution of structure with depth and in fact, no large scale model of the variations in shear structure below 600 km has been published.

Though there are problems with finding laterally varying models of shear velocity in the deeper mantle on a large scale, there have been exciting breakthroughs in determining the three-dimensional P-wave structure in the lower mantle. Sengupta and Toksoz (1976) and Dziewonski, Hager and O'Connell (1977) published early models of laterally varying P velocity structure in the lower mantle. Recently, Dziewonski (1984) presented an improved model for the lower mantle. His solution is for the long-period variations in P-velocity expressed in spherical harmonics and was derived using ISC P-wave residuals as the data base. Clayton and Comer (1983) used an iterative back projection scheme (Comer and Clayton, 1986), using similar data as Dziewonski used, to derive another model for the lower mantle below 600 km. The inversion technique allowed the authors to resolve velocity variations on the order of 500 km in length. The amazing correlation of the long-period gravity field of the earth with that predicted by Clayton and Comer's model assuming a linear relation between velocity variation and density variation (Hager et al., 1985) gives support to the accuracy of their model at long periods. The shorter wavelength features are still uncertain. All of the above P-velocity studies used data beyond 25^o distance to avoid the complications associated with upper mantle triplications. This has limited the resolution of structure above 700 km depth.

In Chapters 1 and 2, vertical profiles of shear velocity were determined for three tectonic areas beneath the North American plate. The shield, old ocean and recently tectonically active regions of the plate were found to have large differences in shear velocity above about 350 km depth. Below 400 km depth, no systematic variations were found for the three study areas although scatter in the data sampling below 400 km indicates there could be velocity variations at these depths. The models were derived by modeling the consistent pulses seen in S and SS phases which form interference patterns depending on their relative arrival times. The pulses in complicated seismograms were readily explained by simple models of the upper mantle shear structure with two first order discontinuities near 400 km and 660 km depth. The large differences seen in these waveforms, at similar distances but different areas, could be explained by the presence or absence of a thick high-velocity layer near the top of the mantle. Large variations in the discontinuity structures or complicated gradients in the deeper mantle are not necessary to explain the data.

Two assumptions were made in the previous chapters with respect to the modelling process. First, we assumed that the data sets for particular areas studied propagated entirely through a laterally homogenous structure. The second assumption was that the mantle below 700 km was laterally homogeneous and correctly given by the Jeffreys-Bullen model. These assumptions were justified but probably only to first order. Also, the first assumption forced us to ignore a large body of data which clearly propagated through significant portions of two or more tectonic provinces. No information is given, in the previous studies, on the transition from shield to tectonic structure or the uniformity within provinces. In this chapter, we will drop the two assumptions discussed above and attempt to derive a continuous laterally varying model for shear velocity beneath the North American plate using the large body of data crossing the tectonic boundaries. The goal is to utilize body-wave synthetic techniques developed for local studies of upper mantle structure and to take advantage of the methods developed by workers studying whole earth structure (discussed above). We hope to bridge the gap between the long-period global surface wave studies of the upper mantle and the studies using P waves to determine lower mantle structure, on a scale large enough to make conclusions on global processes.

The following section will be a general discussion of the inversion technique used to derive the model. We used essentially the same tomographic method as Humphreys (1985) in his study of Southern California mantle structure and Comer and Clayton (1986). The discussion of the technique will follow their work closely. The next section will discuss the data and the details of the actual inversion. This will be followed by the results and discussion of the errors and significance of the work.

Inversion Technique

The data we will be working with (discussed in detail in the next section) consist of S and SS phases recorded at distances from 8^o to 85^o. These phases bottom from about 50 km depth to over 2000 km depth with many intersecting paths. The first question which arises is how does one go about determining a model which will fit all the data. Forward modeling of seismic data for structure is fairly straightforward when one assumes lateral homogeneity. The vertical structure can be parameterized with enough simplicity to be handled easily, that is, most reasonable models whose differences are significant can be tested by computing synthetic seismograms and comparing them to data. If one allows heterogeneity in all three dimensions the problem rapidly becomes too difficult to handle by a trial and error approach and thus, some inversion technique must be used. The best inversion would be one which fit the waveforms and travel-times of the raw data directly. This approach has been used by Woodhouse and Dziewonski (1984) and Lerner-Lam and Jordan (1983) with long-period mode data. Given (1984) did the same for body-wave data similar to what we are using, but he assumed lateral homogeneity and only inverted for a vertical structure. Unfortunately, efficient and accurate body-wave synthetic codes for three-dimensional structure have not been developed yet and we feel the direct inversion of the mantle waveforms in this study for lateral as well as vertical structure is not possible at this time.

The approach we take is to determine a set of travel-time delays from the waveform data. Each clear arrival, in the S and SS waveforms, is assigned a residual which is the measured time of the arrival minus the predicted arrival time for a particular starting model. From the work in the previous chapters, we can assign a raypath which is at least approximately correct for the arrivals in the data. Individual shear phases interacting with the upper mantle can have up to four clear arrivals due to the discontinuities in the structure and thus a single phase can produce four residuals and raypaths. Determining the raypaths and residuals is the most difficult part of this study and will be discussed in the next section. At this point, assume the bodywave data set can be reduced to a set of residuals relative to some starting model and a set of raypaths through the mantle associated with the residuals. Finding a model to satisfy a set of residuals with known raypaths has been done in many seismological studies. The problem can be made discrete by dividing the volume under study into blocks within which one assumes a constant slowness variation relative to the initial model. Assuming one knows the raypaths correctly, the problem can be reduced to

$$t_r = \sum_b l_{rb}\, s_b\,, \tag{3.1}$$

where t_r is the time delay of ray r, l_{rb} is the ray length of ray r through block b and s_b is the slowness perturbation of the b^{th} block (the notation is taken from Humphreys, 1985). In matrix form the set of r equations can be written

$$t = \mathbf{L}s. \tag{3.2}$$

Aki et al. (1977) rewrite equation (3.2) as

$$\mathbf{L}^T t = (\ \mathbf{L}^T\mathbf{L}\ )s\,, \tag{3.3}$$

and solve the problem by computing $(L^T L)^{-1}$. The solution s is only approximate in that contributions to t due to path length changes, which come from errors in the initial raypaths due to model error, are neglected. Aki et al. (1977) show that according to Fermat's principle this contribution to t is of second order relative to the terms Ls. In any case, it is important to use raypaths which are close to the actual raypaths in the inversion.

For large model spaces, that is, if one wants to determine a model with short wavelength variations, the matrix $L^T L$ can be very large and computing the inverse becomes a difficult problem. Comer and Clayton (1986) adapted an approach used in medicine called the Simultaneous Iterative Reconstruction Technique (SIRT), to determine a high-frequency slowness solution for the mantle from ISC P travel-time picks. The method uses an approximate solution to (3.1) which can be computed by sequentially using each row of L to process a single residual. We will use a slightly modified form of Comer and Clayton's algorithm given by

$$s_b^{\,1} = \frac{\sum\limits_r \frac{t_r^{\,o}}{L_r} l_{rb}\, w_r}{\sum\limits_r l_{rb}\, w_r \ + \mu}, \tag{3.4}$$

where $s_b^{\,1}$ is the estimate of the slowness perturbation for block b, l_{rb} is the path-length through block b of ray r, $t_r^{\,o}$ is the initial residual for ray r, L_r is the total path length of ray r, w_r is a weight assigned to ray r, and μ is a damping parameter. The solution, using this algorithm, is just an approximation to the solution of equation (3.1). By an iteration process, a better solution may be found. Comer and Clayton (1986) show that with increasing iterations the solution should converge to the generalized inverse solution to equation (3.3). We iterate by computing $t_r^{\,1}$ as

$$t_r^{\,1} = t_r^{\,o} - \sum_b l_{rb}\, s_b^{\,1}, \tag{3.5}$$

and then applying (3.4) using $t_r^{\,1}$ in place of $t_r^{\,o}$. The new solution would be $s_b^{\,1}+s_b^{\,2}$. Disregarding the damping factor μ, equation (3.4) has a simple intuitive meaning. The $\frac{t_r}{L_r}$ term in the numerator is just the slowness needed along the whole raypath to produce the residual t_r. The terms $l_{rb}\, w_r$, in the numerator and denominator, can be considered weighting terms. Thus the algorithm assumes a particular residual is produced by a slowness anomaly which is spread along the whole ray-path. The estimate of the slowness in a particular block is then just the weighted average of the slowness estimate from each ray passing through the block with the weight given by $l_{rb}\, w_r$.

The weight, w_r, has been used for two reasons. First, if several events located in the same place are used, the ray set will be given a large azimuthal bias which can cause streaking of the solution (Humphreys, 1985). Therefore, for sources within 100 km of other sources used in the study, the weight for each ray was decreased by a factor of two. The weights were also varied for individual rays by a qualitative estimate of the accuracy of the travel-time pick. The sharpness of S-wave onsets varies considerably and it was felt this should be recognized by the inversion. The weights were varied by negative powers of 2 from 0 to 5, thus the range in weight is from 1 to 1/32. The damping factor μ was set at 100 km. This value was chosen to allow rapid convergence (about 20 iterations) without allowing the solution to oscillate rapidly with each iteration. The exact value is arbitrary and 100 km was decided on by trying just a few values from 500 km to 0 km and observing the results.

The application of equations (3.4) and (3.5) is straightforward and rapid. The starting rayparameter for a particular ray was found in the measuring process to determine the residual of a particular arrival. This process is discussed in the next section. The residual, rayparameter, station location and source location were entered in a file. This file was then the input for a raytracing code. The code traced the rays in 5 km vertical steps. The velocity model was also given every 5 km in depth and between the given velocities the Mohorivic law was assumed for the gradient. With each 5 km step the depth, latitude and longitude were determined at the midpoint of the step. The pathlength was also determined and was then added to the length l_{rb} in the volume b within which the midpoint was located. The raylengths for each volume b for each ray form the matrix L in equation (3.2). To apply equation (3.4), two matrices of the order of the model space are computed. The first contains the numerator, the second the denominator of equation (3.4). These matrices are computed by processing a single ray at a time, and thus, a single row of the L matrix at a time. The model is calculated by just the quotient of the two computed matrices. New residuals can be computed from the solution by equation (3.5) and the process repeated to the desired convergence.

Data

Fig. 3.1 shows a map of the events and stations used in this study. The stations form part of the World Wide Standard Seismic Network (WWSSN) and the Canadian Seismic Network (CSN) and are labelled by their code names. The events occurred over the period from 1963 to 1983 and range in magnitude from m_b values of 5.0 to 6.3. These events produced 3923 arrivals used in the inversion. The distribution of earthquakes and stations give an idea of the model area we will be interested in. Just about all the data used were recorded on the long-period components of the seismographs. The exceptions to this were measurements of short-period Sn arrivals from the small events occurring in the central and eastern part of North America. The short-period arrivals were assumed to travel in the lid and were used only to constrain velocities in the shallowest part of the mantle, ie. the topmost layer in the inversion. The long-period arrivals were measured off the component nearest the tangential direction. If the separation of SV and SH was not clear the seismograms were digitized and rotated in order to measure the SH onset times. We tried to use only SH seismograms to avoid mispicking Sp phases or shear-coupled PL waves. Data with complicated teleseismic S or strong SV and weak SH signals were not used.

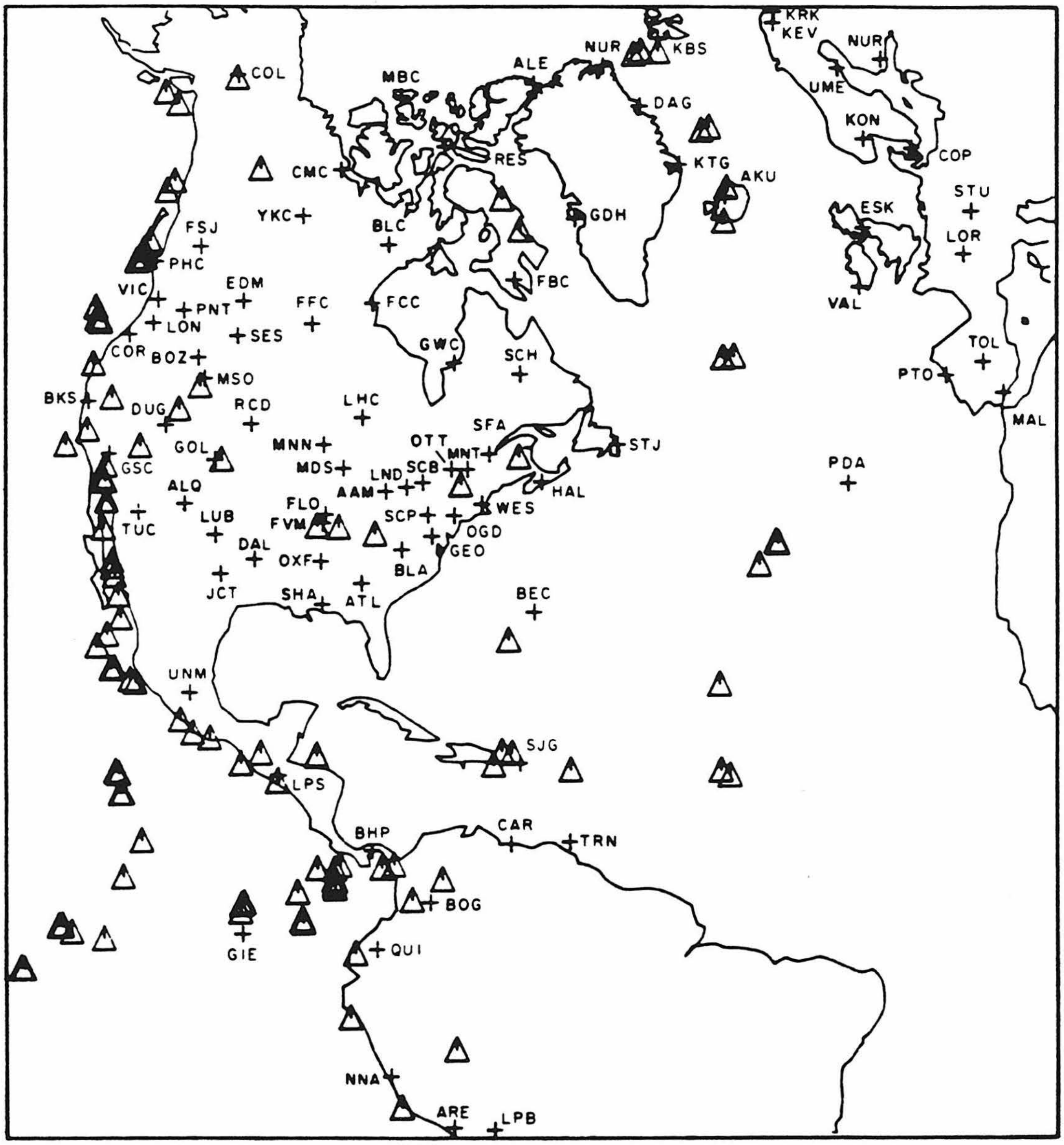

Figure 3.1 Distribution of events and stations used in the tomographic inversion.

The data can be classified into two groups. The first group consists of first-arrival S-wave times beyond 25^o. The second group consists of S-waves at less than 25^o and all secondary arrivals such as SS or S wave reflections from upper mantle discontinuities. The teleseimic S-waves (Group 1) are the most straightforward to measure. These phases bottom below 700 km depth and are essentially unaffected by the upper mantle discontinuities. They are the first arrivals on the tangential components of seismograms and are easy to identify. This set of data, in its sampling of the mantle, is equivalent to the P data used by Dziewonski (1984) and Clayton and Comer (1983). With measurements from 25^o to 85^o we sample the mantle from about 700 km to 2400 km depth although, due to the distribution of stations and events, there are little data sampling below 2000 km. Below 1000 km the model is determined completely by S-wave absolute times.

The measuring technique used in determining the teleseimic S residuals is simple. The ISC epicenters were used for the sources. ISC depths can be in error by many tens of kilometers due to the fact that for events with no local station coverage, the depth trades off with the origin time strongly. If one uses P times for lower mantle structure, this does not present a large problem. However, since the location is done with P times and we want absolute S times, there is not the same tradeoff between origin time and depth. We used only simple earthquakes such that the teleseismic S-waves were easily interpretable. The S-waves were assumed to consist of S and sS pulses convolved with a trapezoid. Using synthetic seismograms, the depth can be estimated by the S-wave waveform to within a few kilometers with the above assumptions. Each event was modeled to the extent of determining its depth to within a few kilometers. Most of the events are very shallow. The origin time was then adjusted assuming the Jeffreys-Bullen structure and a 60^o distance for the P time measurements which determined the ISC location. The S-wave travel-times were found by measuring the onset of S at its first break and using the depth corrected origin time for the event. The accuracy of the picks is generally within +1 and -1 seconds. Larger errors could come from mislocation of epicenters and this is a problem which has not been tackled in this study. A more severe systematic error is possible when there is an S-wave node and one picks sS instead of S. This could cause a systematic 2 to 3 sec azimuthal anomaly for shallow events. For this reason, synthetics were computed to locate the lower hemisphere SH nodes to help in determining the S onset and avoid confusion with sS. The mechanisms were taken from a host of studies. Chandra (1974) studied the northwest coast of North America, Molnar and Sykes (1969), the Carribean and middle America region, Stauder (1975), the northwest coast of South America, Eissler and McNally (1984), the Rivera plate and part of Baja and Anderson et al. (1974), the East Pacific Rise. More localized studies by Stewart and Helmberger (1981), Sykes (1970), Burdick and Mellman (1976), Weidner (1974), Bungum (1977), Bungum and Husebye (1977), Husebye et al. (1975) and Ebel et al. (1978) were also used. These studies not only helped in determining the S onset but were also very helpful in finding earthquakes with good shear data. Events occuring after the studies mentioned above were generally very close to a previous event studied and the mechanism was assumed to be the same as that published if the S data looked similar. The residual associated with an S-wave pick was found by computing the arrival time at the appropriate distance with the source at the depth we determined for the event, and comparing the result with the measured value. The model used in the computation was laterally heterogeneous and will be discussed next. The teleseimic residuals varied from -10 sec to +7 sec.

The teleseismic S data, though the most straightforward to measure, have several severe weaknesses. First, beyond 25° the S waves only sample the upper 600 km of the mantle at near vertical incidence and thus cannot resolve structure well at these depths. The second weakness is that with the distribution of stations and events (Fig. 3.1) that we used, there are many areas below 600 km which are not well sampled. To sample depths around 800 km well, it is necessary to have an event and station within 15° of the area under question. Thus the teleseismic S data is not going to resolve structure down to 800 km in the central and eastern portions of North America. For this reason, we have included S data from 8° to 25° as well as SS data from 30° to 85° in the inversion. The S data to 25° and SS to 50° provide good resolution of structure in the upper 600 km and the SS from 50° to 85° helps in determining the structure in inaccessible areas to 850 km depth.

The inclusion of upper mantle data creates many problems not encountered in Clayton and Comer's (1983) study or with the teleseismic S data. In Chapter 1, shear profiles were derived for western and eastern North America. Fig. 3.2 shows the rays predicted by these models at a distance of 18.2° . The dashed lines are rays produced by the shield model (SNA) and the solid lines are rays for the tectonic model (TNA). At this distance both models produce three arrivals, reflections from near 400 and 660 km and a turning ray in the upper 400 km. The turning ray in the shield is within the lithosphere and that for the tectonic region is from well below 200 km depth. The problem which arises immediately is that the rays at a particular distance follow very different raypaths and the inversion technique assumes the raypaths are correct. The 660 km reflection is similar enough for our purpose but both arrivals above 400 km are quite different for the two models. In particular, the shallowest arrivals in the two structures are sampling completely different depth ranges. Thus, no single laterally homogeneous model will predict raypaths even roughly correct for both areas above 400 km depth.

There is a second difficulty regarding rays in the upper 400 km of the mantle. Both SNA and TNA have velocity reversals in the upper mantle. This produces shadow zones in both models indicated by dashed lines on the triplication curves in Fig. 1.7. However, the data used in this study has wavelengths of up to 100 km and consequently, there is a great deal of tunnelled energy penetrating the lids. The tunnelled energy in the shield structure would produce a pulse which has sampled structure near 250 km depth in the case illustrated in Fig. 3.2. For pure Canadian shield paths, S at 18° or SS at 36°, show little evidence of this arrival. However, for many paths sampling south of the shield or for shield paths which have also sampled part of a tectonic area, these tunneled arrivals are prominent and contain a lot of information on shear velocity in the 150 to 300 km depth range. An illustration of this phase is shown in Fig. 3.3 taken from a study by Helmberger et al. (1985a) which attempted to model SS uppermantle waveforms from California earthquakes to stations on the east coast of North America. The synthetics are from their model for this particular cross section. Of interest here is the arrival whose onset is marked by a dashed line from 34° to 40°. These arrivals, more prominent beyond 37°, are tunnelled through the lid and are predicted by the synthetics as such but with low amplitude. The problem which arises from this phase is that tunnelled energy has no geometric raypath associated with it and thus cannot be used in the tomographic inversion if a model close to SNA is used as the starting structure. The situation in the upper 400 km of the mantle is then very complicated. For S from 16° to 20° and SS from 32°

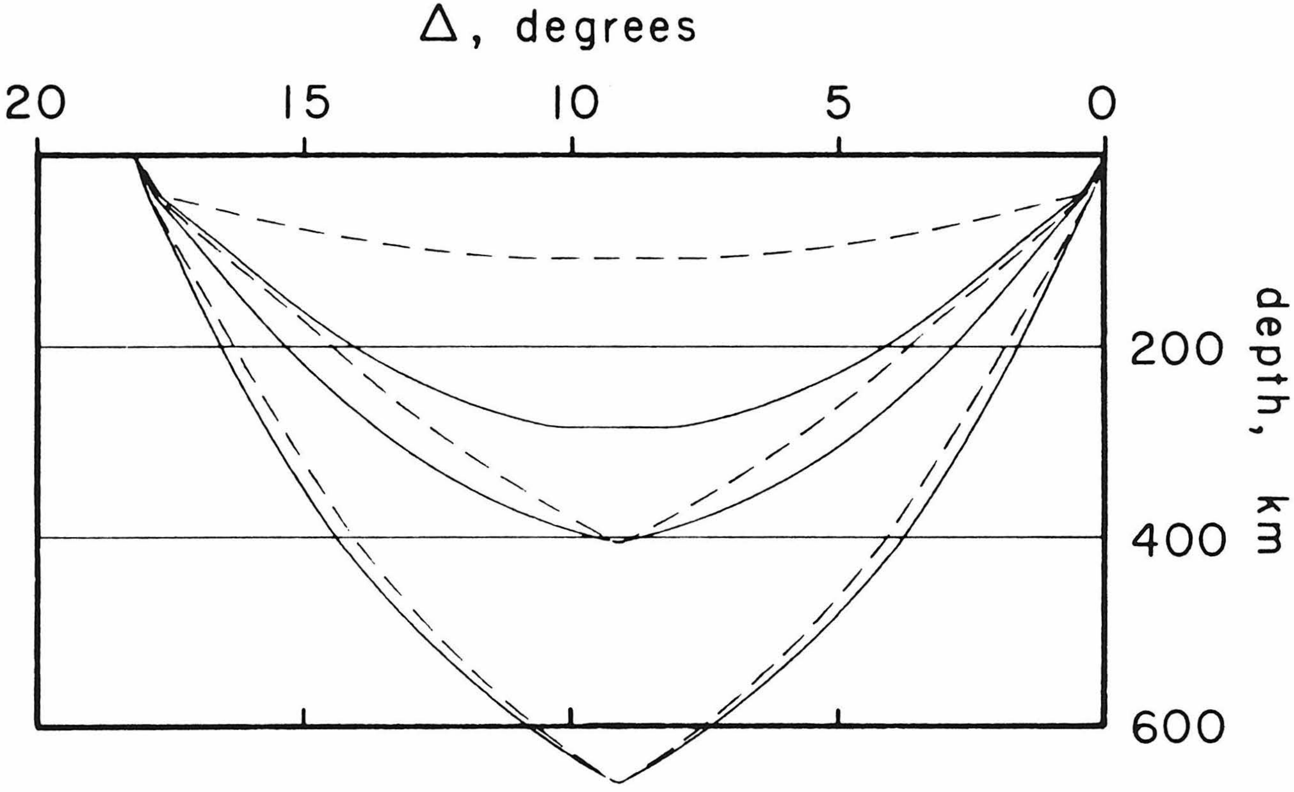

Figure 3.2 Raypaths at 18.2^o for models SNA and TNA. The dashed lines are the rays predicted by SNA.

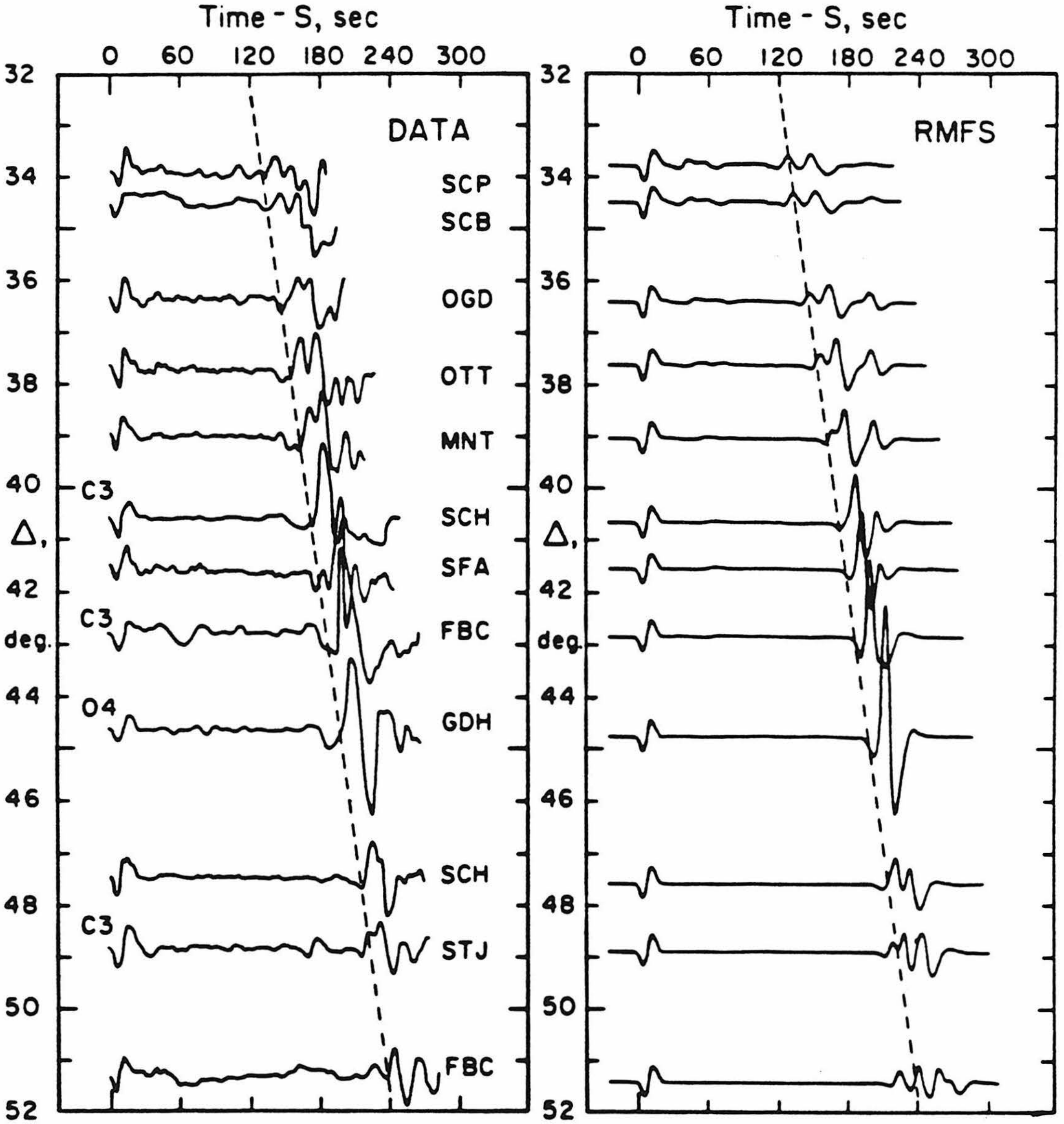

Figure 3.3 Profile of data from southwest North America to northeast North America. The dashed line from 34° to 40° indicates the tunnelled SS arrival bottoming near 250 km depth (taken from Helmberger et al., 1985).

to 40°, there is the possibility of three distinct arrivals from above 400 km depth which may or may not be present in a particular seismogram. It is the relative timing of these three phases and a means of assigning a raypath to each arrival which is of interest to us.

Before discussing the approach taken with this data, we show another example of data illustrating the discussion above. Fig. 3.4 shows a suite of seismograms all of which are near 39° distance. The S-waves are aligned at zero time and the stations are labelled by their code names. The events correspond to the numbers by each record and Fig. 3.5 shows both the event locations and stations. Above the OGD seismogram, the three arrivals from above 400 km are labelled by letters. L is the lid arrival, T is the tunnelled arrival and F is the reflection from the 405 km discontinuity. The record at FFC is for an almost pure shield path. Low amplitude energy can be seen arriving near the lid arrival time at OGD but no tunnelled phase is apparent in this record. The largest SS phase is the reflection from the 405 km discontinuity; note that it is about 5 sec faster relative to S than the reflection recorded at OGD. Below OGD there are two seismograms produced by an earthquake off the coast of Mexico recorded at stations near OGD. The three arrivals seen at OGD are all seen at these stations also, but they are all significantly later. It is particularly interesting to see large differences in time between MNT and WES from the same event. The tunnelled arrival from about 250 km depth is about 9 sec later to WES than to MNT though the paths are relatively similar. Note, the tunnelled arrival at WES is arriving just before the 405 km reflection and the two phases are not clearly separated though the SS waveform obviously shows the interference of the two arrivals. The last two seismograms are for oceanic paths and if the thin crust at

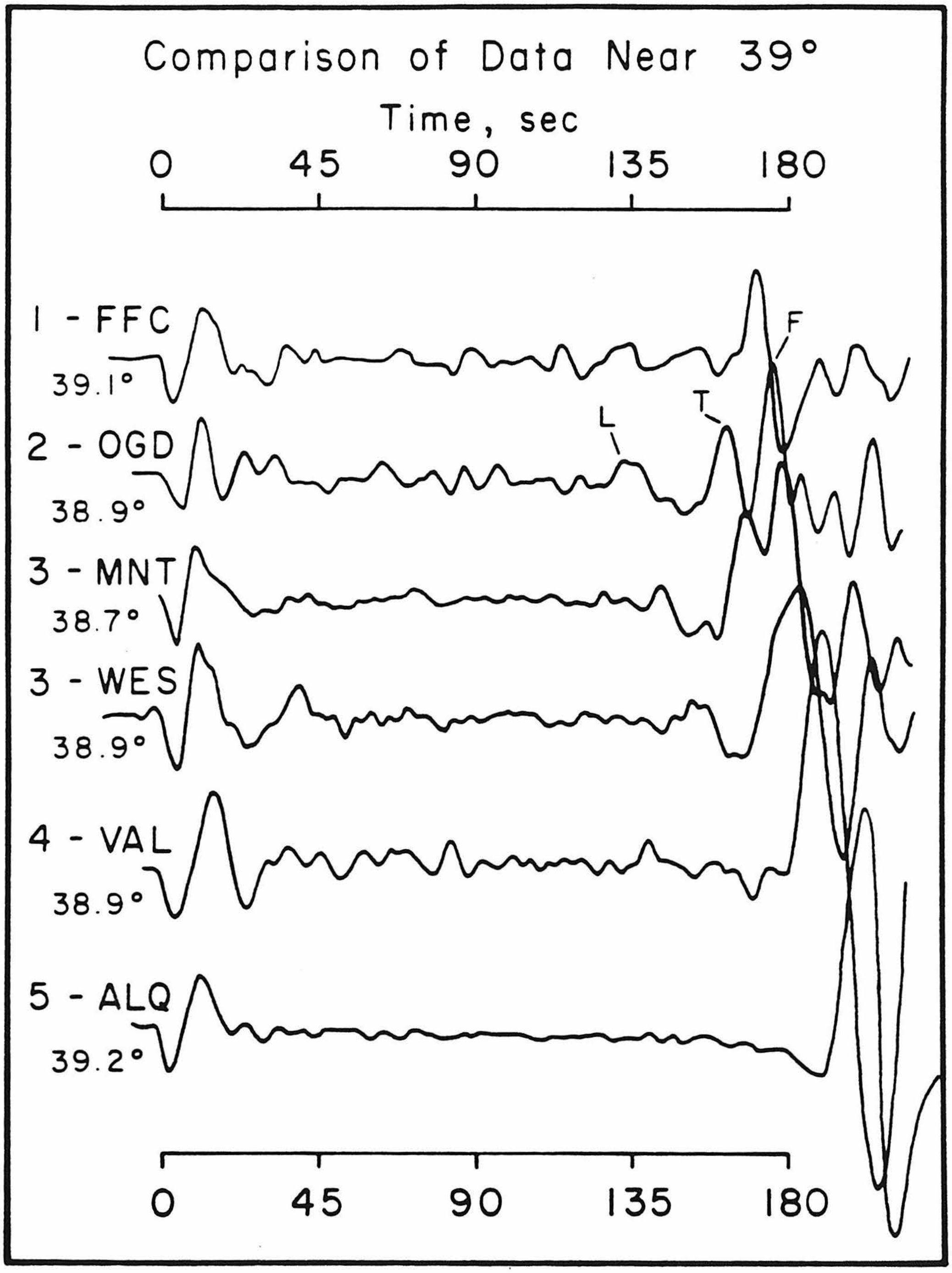

Figure 3.4 Comparison of data at 39° for various paths within and near North America. Note the progressively slower SS arrivals relative to S. The paths are shown in the next figure.

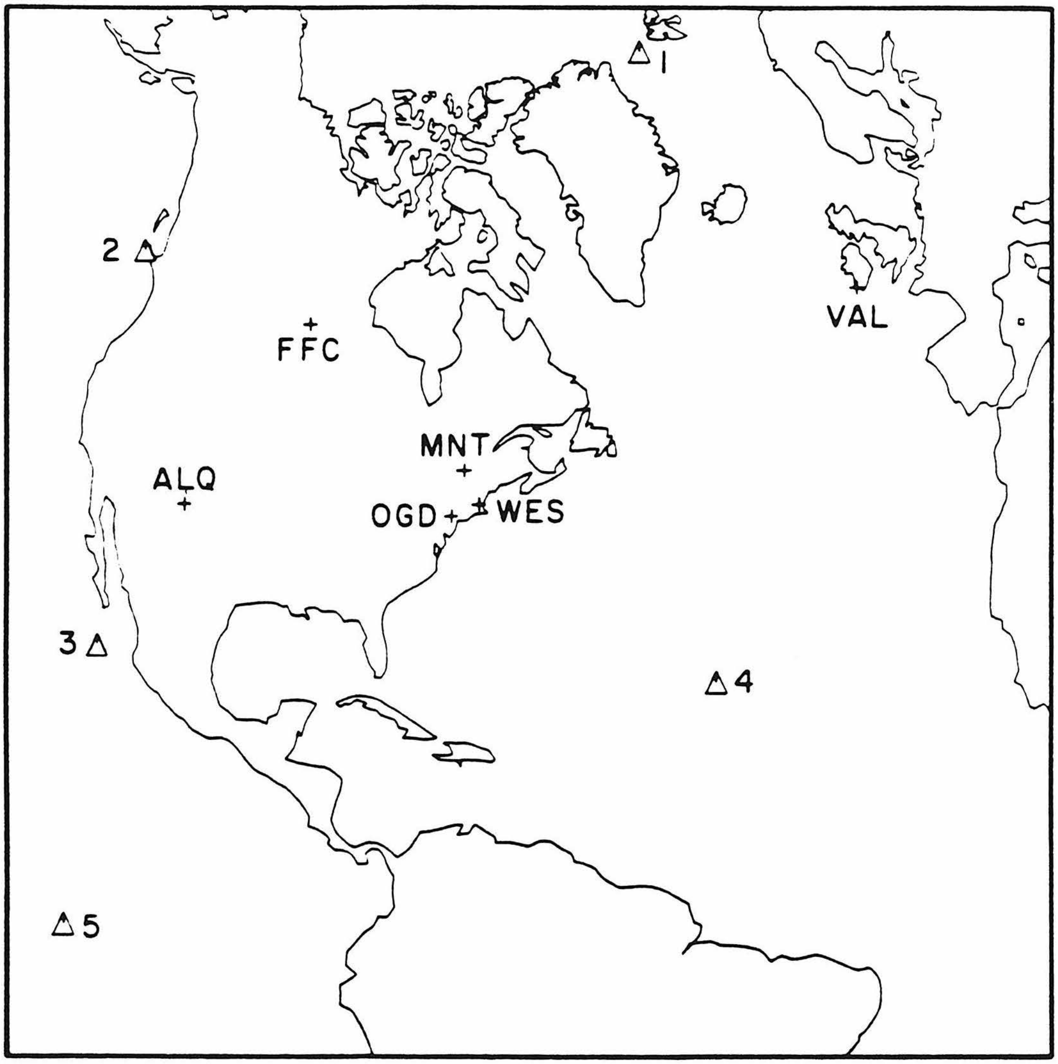

Figure 3.5 Location of stations and events used in the previous figure.

the SS bounce point is taken into account, the SS phase would be shifted about 5 sec later relative to S. No separate lid and tunnelled arrivals are apparent in these seismograms and both show very late amplified SS signals relative to the continental records above them. From our modeling experience, it appears, in both cases, that the diving ray near 300 km depth is arriving at nearly the same time as the 405 km reflection as predicted by the TNA model. The Atlantic path, though, appears to be significantly faster than the Pacific path. Comparing ALQ to OGD we see about a 36 sec difference in time, relative to S, for the ray sampling near 300 km depth and about a 27 sec difference for the reflection from the 405 km discontinuity. This data sample is typical of the large variations seen for many paths beneath the North American plate. Seismograms following similar paths are generally consistent, though rapid lateral variations, such as between the paths to MNT and WES are not uncommon.

It should be apparent that the choice of a good starting model is critical to this study. It was decided to use a laterally heterogeneous starting structure to take into account the drastically different modes of propagation in the East Pacific and the shield areas. To simplify the problem, two different vertical shear profiles were chosen to represent areas where there is a well developed lithosphere and where there is not. The starting model assumes the two structures are connected by a discontinuous jump from one to the other. The boundary chosen to separate the two models is shown in Fig. 3.6. The boundary follows the line of recent tectonic activity in North and South America (Sclater and Parsons, 1981) with the provision that the boundary be at the edge of one of the cells the model is divided into. The cell division is discussed later. The vertical structures within the two areas are shown in Fig. 3.7 along

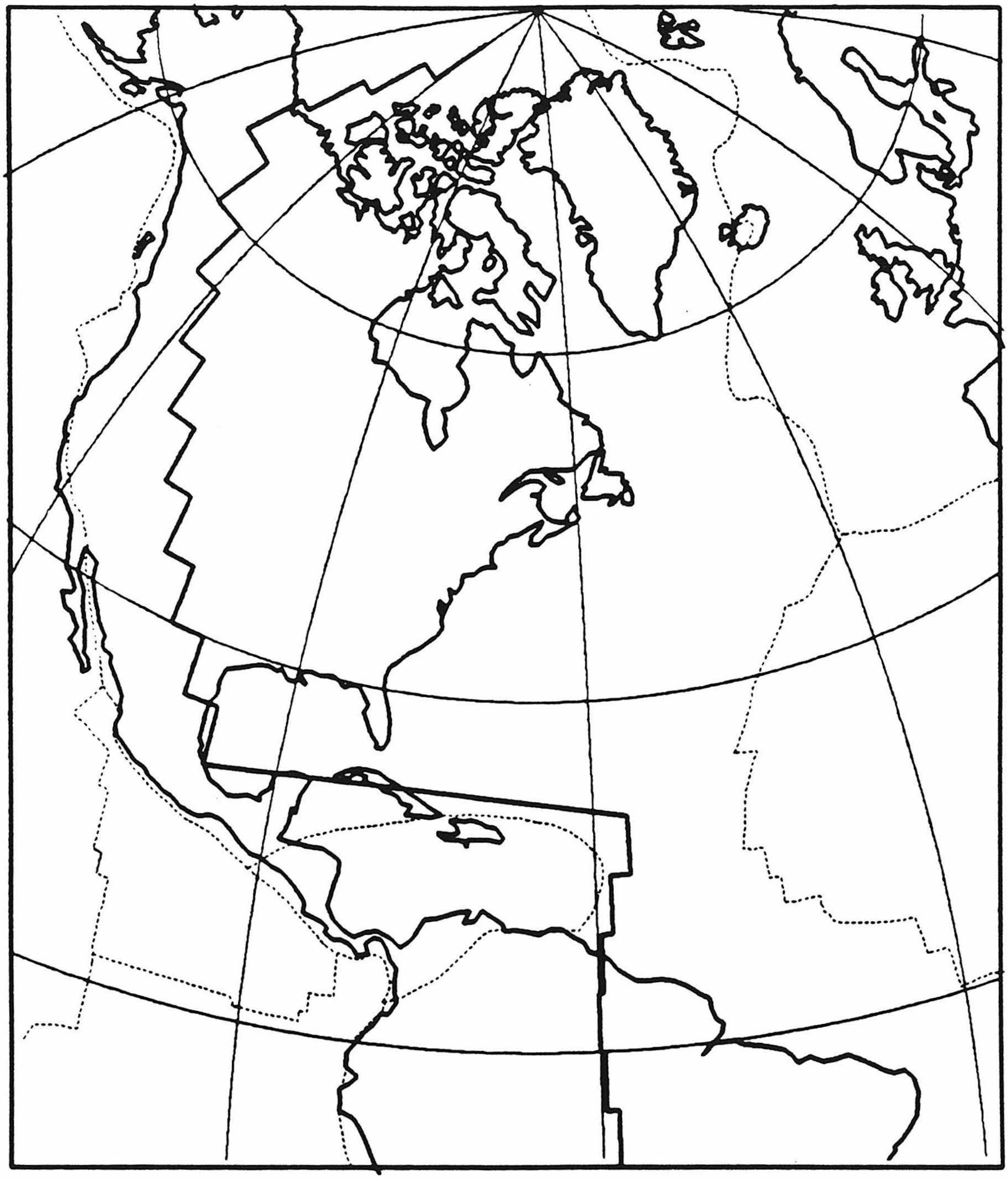

Figure 3.6 The heavy solid line indicates the boundary in the starting model between the tectonic (west) and stable regions.

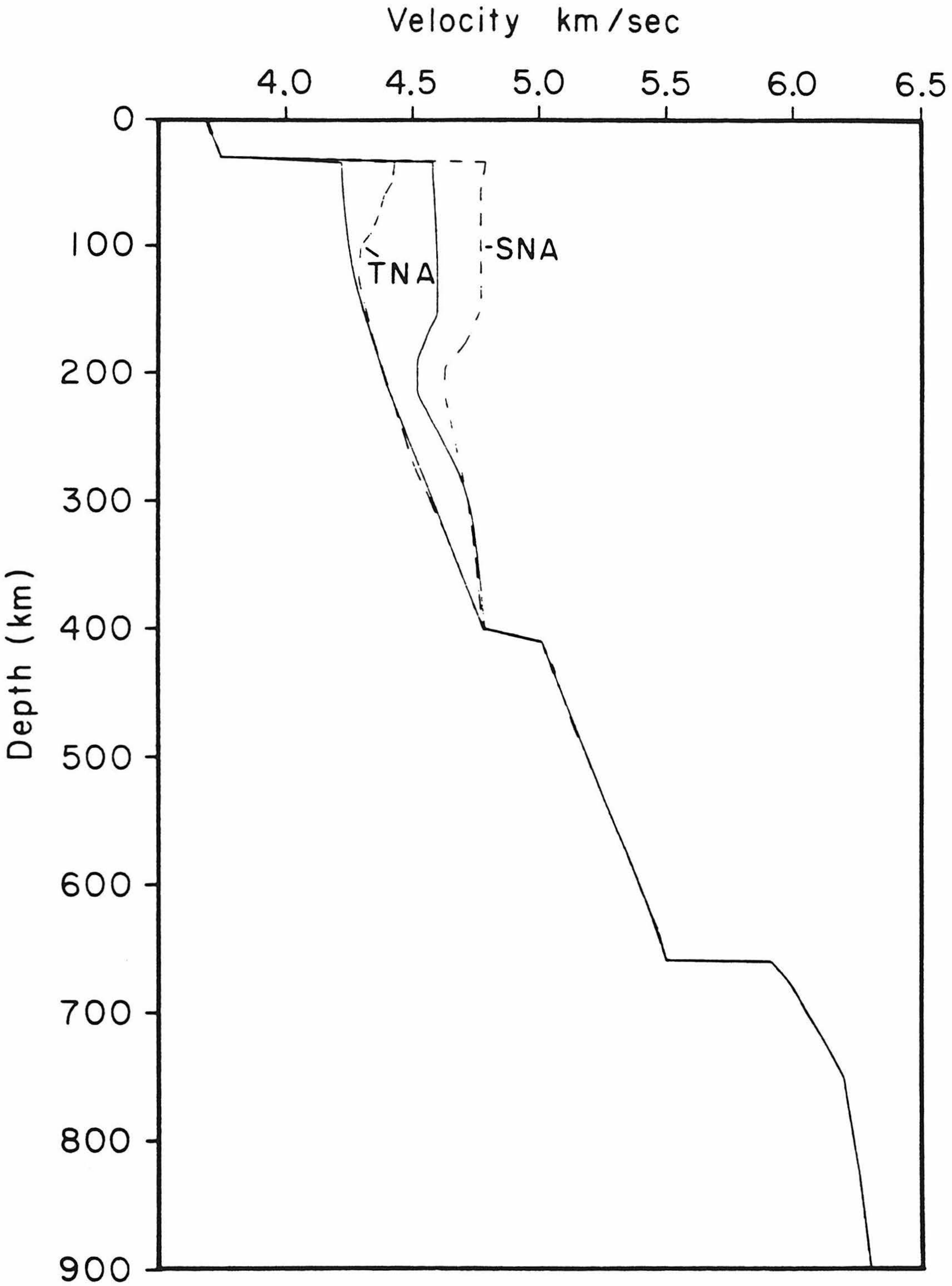

Figure 3.7 The starting tectonic and stable starting models (solid lines) relative to models TNA and SNA.

with models TNA and SNA. The dashed lines are SNA and TNA and the starting stable and tectonic models are drawn with solid lines. All the models are identical below 400 km depth. The starting tectonic model is the same as TNA except for the absence of a thin lid above 75 km depth. This is to remove the raytracing problems associated with the lid at distances less than 15°. The starting stable model is different from SNA to about 300 km depth. The reason for this is the desire to have geometric raypaths for the tunnelled arrivals observed in the data. The model selected has lid arrivals out to 20°, as does SNA. However, due to the lower velocity in the lid and the high gradient from 200 to 280 km depth, there are also turning rays beginning at 19° (38° for SS) which bottom below the lid. Fig. 3.8 shows the rays in the upper 400 km produced by the tomographic starting model (solid) and by SNA (dashed) at 19° distance. The lid and 405 km reflection rays match very well but the tomographic starting model also has a turning ray from about 250 km depth. The stable area starting model also predicts the extended B branch seen in shield and old ocean data (discussed in Chapters 1 and 2) to beyond 30°. It should be noted that the starting models were chosen to predict raypaths which correspond to observed arrivals but the travel-times and rayparameters may be very different than the observed ones.

Measuring residuals for the SS data shown in Figs. 3.3 and 3.4 is not as easy as for teleseismic S data. There are no clear breaks in the data indicating the onset of the arrivals nor are there clear onsets for later S arrivals such as shown in Chapters 1 and 2. To compute residuals, associated with the arrivals discussed above, synthetic seismograms and a simple visual correlation technique were used. The WKBJ technique was used as it is the most time efficient available and it is a ray method. The

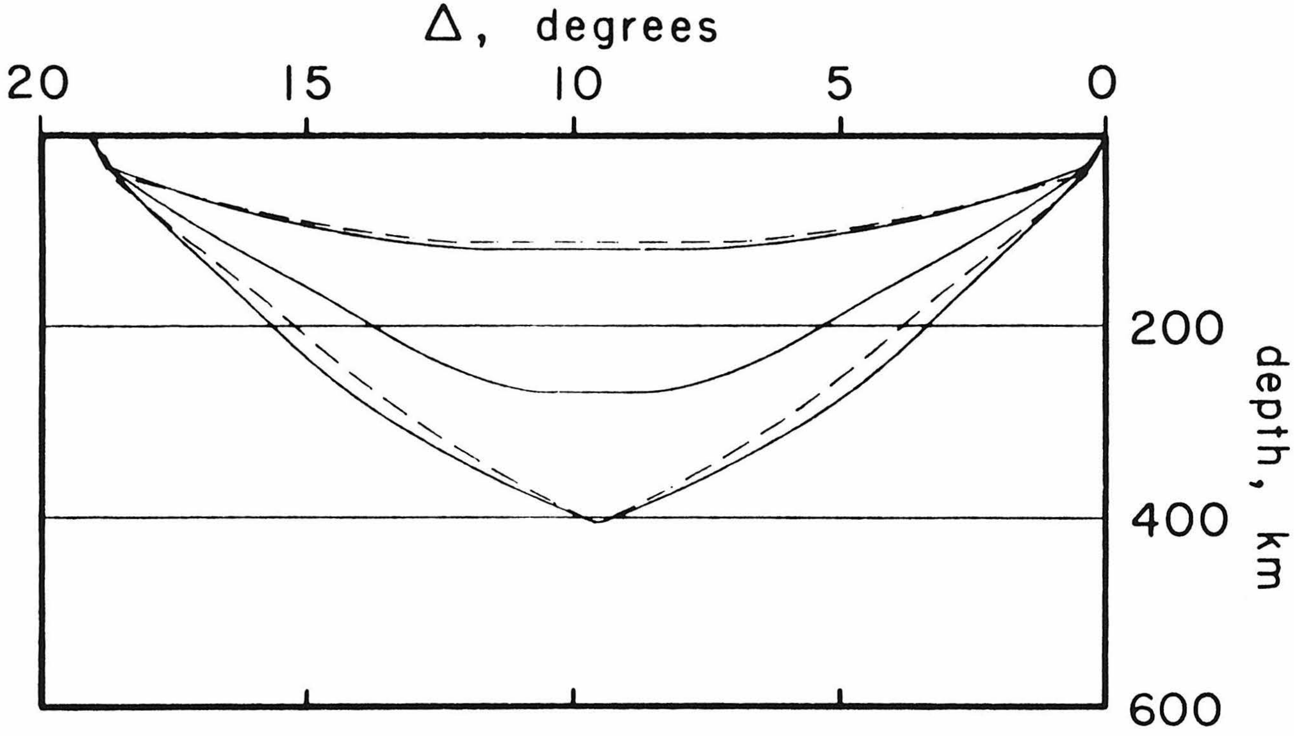

Figure 3.8 Raypaths at 19° for the starting stable model (solid lines) and those predicted by model SNA. Note the extra arrival from near 270 km depth for the starting stable model.

technique is explained in detail by Chapman (1978) and we will only make some minor points about it here. The technique involves tracing a suite of rays and computing their travel-times and distances. From the travel-times and distances for all rays arriving around a particular observation point, a synthetic seismogram of the motion at that point can be computed. Thus, in the synthetic computation the information about the rayparameter of a particular arrival is already at hand.

The WKBJ theory assumes a laterally homogeneous structure so that some modification must be made for paths which cross the stable-tectonic boundary of the starting model. We make several simplifying assumptions in the computation of synthetics through the boundary. First of all, we assume the boundary is always perpendicular to the great circle connecting the station and receiver. This reduces the problem to two dimensions and does not account for any raypaths outside the great circle plane. Next, we take the approach of Helmberger et al. (1985b) and assume the WKBJ technique can be used with any distance-travel-time curve regardless of whether or not the rays propagated through laterally homogeneous structure. Helmberger et al. (1985b) discuss this approach extensively and show comparisons with more formally correct synthetic codes. Applying the WKBJ technique in this way produces arrivals at the correct time but the amplitudes can be in error. However, in this study we only use travel-time and path information and the amplitude errors are unimportant. Finally, in calculating the suite of ray distances and travel-times we reduce the effect of the boundary to a minimum. Rays with starting rayparameters associated with bottoming depths below 400 km are traced to the boundary with the same algorithm used in chapter 1. At the boundary, the rays are traced using the new structure in the same way with no change in ray parameter. Rays with bottoming depths above 400 km cannot be traced through the boundary from slow to fast without changing the rayparameter. The rayparameter is changed at the boundary by

$$P_{new} = \frac{R\sin(\theta_2)}{V_2} = R\sqrt{\frac{1}{V_2^{\,2}} - \frac{\cos^2(\theta_1)}{V_1^{\,2}}}, \qquad (3.6)$$

where P_{new} is the new rayparameter, R is the radius at which the boundary is encountered, V1 is the velocity on the side of the impinging ray at radius R, V2 is the velocity on the other side of the boundary and θ_1 is the angle of incidence of the impinging ray. Fig. 3.9 shows a schematic of the situation at the boundary. Equation (3.5) is just Snell's law at the boundary ignoring the vertical gradients. Rays that cross the boundary at the depth of the low velocity zone in the stable area model and which are then trapped within the low velocity zone are terminated and dropped from the travel-time-distance curve. The output of the synthetic code contains a file of initial rayparameters and the travel-times and distances associated with each rayparameter. The rayparameter for each arrival at a station can be found by a simple linear interpolation from the computed suite of rays. It should be emphasized that the synthetic code is not attempting to compute the exact response for a model with two separate vertical structures. It is only an attempt to find raypaths which are similar to those of actual arrivals and to compute the predicted arrival times of those arrivals for a particular model.

To illustrate the synthetic measuring process, we will examine a single seismogram recorded at MNT from Earthquake 2 in Fig. 3.5. The path from Event 2 to MNT begins in the tectonic province and ends in the stable region (Fig. 3.6). The source receiver distance is 37.2° and the tectonic portion is 7.05°. For each

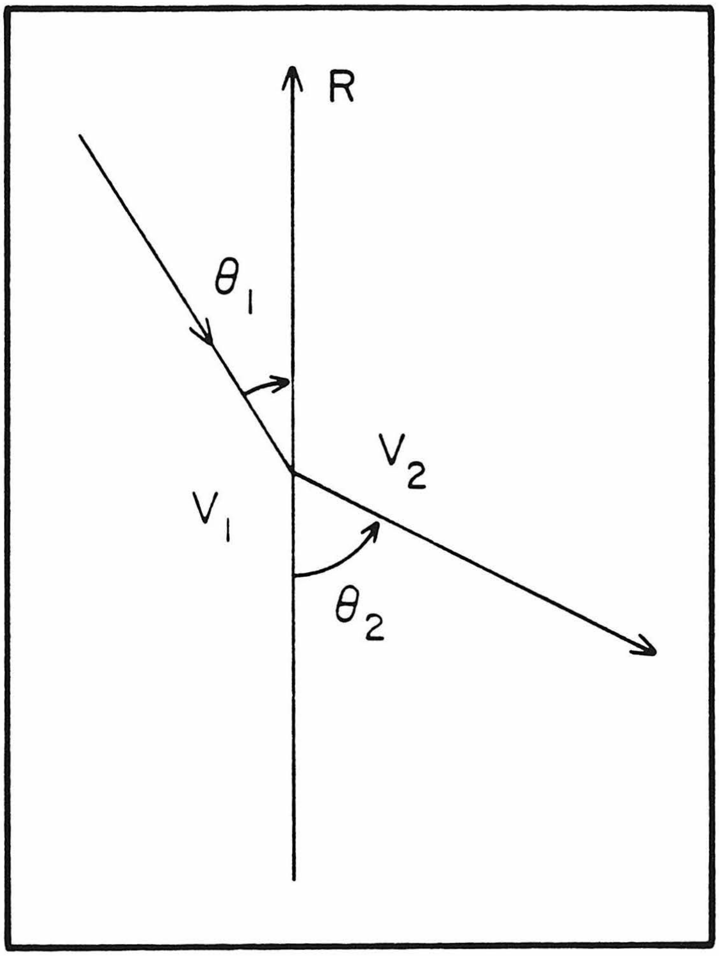

Figure 3.9 Diagram illustrating the interaction of a ray with the boundary dividing the two halves of the starting model.

seismogram crossing the boundary the portion in each province is calculated. Most of the path is within the stable portion of the model and we would expect the heterogeneous synthetic to be similar to a pure stable one. Fig. 3.10 shows a comparison of the actual heterogeneous synthetic and synthetics computed using the stable and tectonic models at the same distance. The absolute S time for the heterogeneous synthetic is about 4.6 sec faster than the tectonic one and 4.6 sec slower than the stable one, but in the figure the S waves are all aligned. The mechanism is almost pure strike-slip (from Chandra, 1974) and the depth is 7 km. The ISC depth is 22 km. The tectonic synthetic is obviously far different from the other two. The stable and heterogeneous synthetics have three similar SS arrivals. In order of arrival time, they are a lid SS phase, a turning ray near 280 km depth and a reflection from the 405 km discontinuity. Note that the 7^o of tectonic path has slowed all the SS arrivals relative to S but that the lid arrival is slowed much more than the deeper arrivals as one would expect. Fig. 3.11 shows the technique used to measure the data residuals. The MNT record is shown below the heterogeneous synthetic three times. The S-wave time is picked off the record at the spot indicated in the figure. The S-wave residual turns out to be -1.0 sec relative to the calculated value using the heterogeneous code. The three pairs of synthetic-datum are aligned to estimate residuals for the three SS arrivals. From top to bottom, the synthetic-datum lid arrivals, tunnelled arrivals and 405 km reflections are aligned. The SS residual, relative to S, is computed by measuring the displacement of the synthetic and real S-wave. The residuals are written on the left of the figure. Since the S-wave is 1 sec fast, the actual residuals for this record are -1.0, -29.2, -12.3 and -8.4 sec. These values are typical for this particular path indicating that the lid should be much faster but that below 200 km, the model is not too different from the actual structure. All the SS and second arrival S

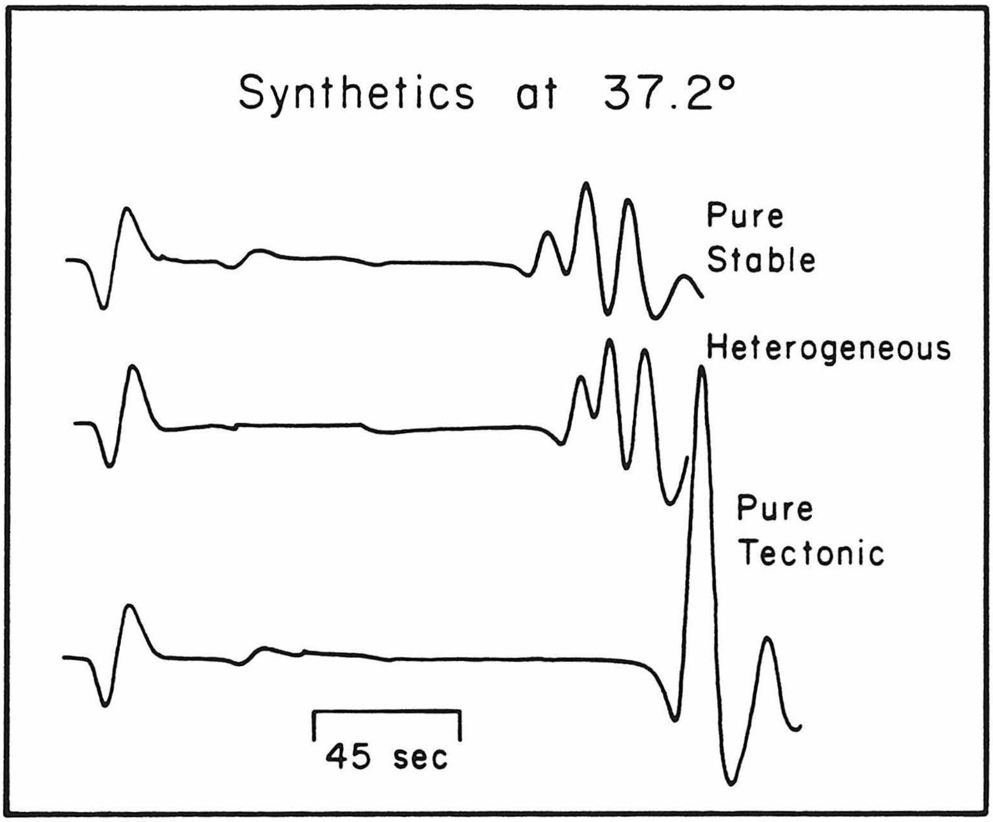

Figure 3.10 Synthetics at 37.2° for the stable and tectonic models with a synthetic computed for a path 7° tectonic and 30° stable.

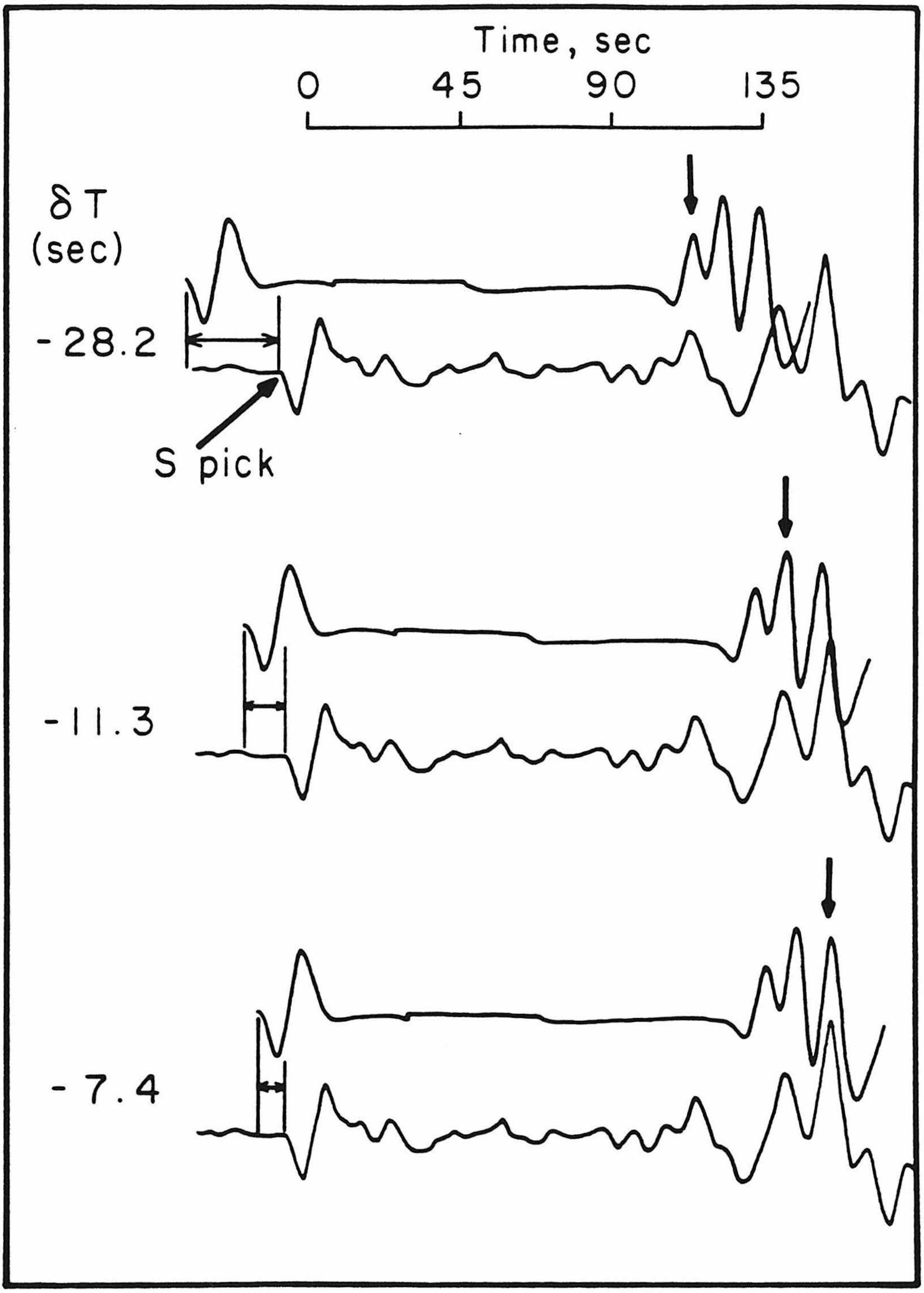

Figure 3.11 An example of the measuring technique applied to a seismogram at 37°. The three SS arrivals are measured relative to the S wave. The arrows indicate the phases being measured.

data were processed with this technique.

Method

This section explains the details of the application of the inversion technique to the data discussed earlier. The measuring technique, discussed in the previous section, yielded a data set of 3923 residuals. Each residual was corrected for ellipticity using the relations given by Dziewonski and Gilbert (1976). It was also decided to correct for crustal thickness and topography. Using S and SS waves beyond 8°, one cannot hope to resolve differences in crustal structure. Particularly when comparing travel-times for oceanic and continental paths, the known crustal and topographic differences would be mapped into the mantle in some way. An SS wave, with a midpoint in an oceanic area, would be about 5 sec faster than one with a continental midpoint assuming the mantle was uniform. The crustal thickness map of Soller et al. (1982) was used to determine the crustal thickness in 5° by 5° areas. Similarly, the topography was estimated for the same areas, to the nearest 100 m, using the Times Atlas of the world. When the raypaths were traced, the SS residuals were modified by subtracting *dt* from the measured values where *dt* is given by equation (3.7)

$$dt = 2dc \left(\sqrt{\frac{1}{V_1^2} - p^2} - \sqrt{\frac{1}{V_2^2} - p^2} \right) + 2dh \sqrt{\frac{1}{V_1^2} - p^2} \qquad (3.7)$$

where *dc* is the variation in crustal thickness relative to the starting model, V_1 is the crustal velocity (3.7 km/sec), V_2 is the mantle velocity below the crust, *p* is the ray-parameter and *dh* is the topography relative to sea level. Both S and SS residuals were modified using half the *dt* given above and using the station elevation for *dh* and the crustal thickness below the station for *dc* .

The division of the model, into cells, is a fairly arbitrary procedure. We chose the area of the cells to be approximately 500 by 500 km in lateral extent, similar in size to those used by Clayton and Comer (1983). This gave roughly the same number of blocks sampled as rays. The vertical division of the blocks varied. A list of the vertical boundaries of the cells is given in Table 3.1. The top layer is rather thick relative to the layers just below. This is due to the ray distribution. With the data used here, there would be very few rays bottoming above 70 km depth so that dividing the top layer in two would be pointless. All the lid arrivals and short-period Sn arrivals were assumed to travel in this layer. These arrivals are conspicuous by their fast arrival times, low amplitudes and wavetrain nature. Our goal is to find the average velocity in the lithosphere with the thickness fixed. Below the first layer, layer thicknesses are less than the top layer and the lower mantle layers. We felt this to be necessary due to the large changes in gradient seen in the upper mantle. Also, the layers were fixed so that there is a layer boundary near the two discontinuities at 400 and 660 km depth. Inverting for constant slowness anomalies within blocks is an artificial way of looking at the mantle and, especially in the upper mantle, this may cause some blurring of the image in depth.

From an inspection of the residuals and from the experience developed in Chapters 1 and 2, it is obvious that variations in shear velocity are much larger in the shallow mantle than in the deeper mantle. Rays sampling the lower mantle are strongly influenced by the upper few hundred kilometers of structure with respect to their travel-times. Clayton and Comer (1983) and Dziewonski (1984) use station statics to account for upper mantle heterogeneity in their inversions for lower mantle

Table 3.1 : Model Layers

Layer	Depth, km
1	0-140
2	140-235
3	235-320
4	320-405
5	405-490
6	490-575
7	575-670
8	670-770
9	770-870
10	870-1000
11	1000-1150
12	1150-1300
13	1300-1450
14	1450-1600
15	1600-1750
16	1750-1900

structure. This study, however, is an attempt to find both lower and upper mantle structure. We make the assumption that most variations in the data are due to uppermantle structure. This was done by doing a preliminary inversion for lateral variations in the upper three layers of the model only. In other words, the ray segments l and the total raylengths L in equation (3.4) are computed only for the part of the paths in the upper 320 km. Eight iterations were performed with this data set, this was enough for the model to approach the velocities given by TNA and SNA near the East Pacific Rise and the Canadian shield respectively. At this point, station statics and event statics were computed. They are just the average delay associated with each station and event relative to the inverted model. Most of the statics were less than .5 sec in magnitude but there were a few stations with statics larger than 1 sec. The station statics are given in Table 3.2. The event statics could be due to mislocation errors. The station statics are possibly from errors in the crustal thickness estimation or the existence of large sediment piles, with low velocities, below the station. These generally small statics, relative to typical S-wave station delays (Lay, 1983), were subtracted from the original data to form a new data set. The new data set was inverted for the top three layers, again with eight iterations. This solution was then used as the starting model to invert for structure in the entire mantle sampled by rays.

Using the heterogeneous solution derived above as the starting model, the entire mantle was allowed to vary for the next 25 iterations. To allow for finer scale variations where the data had resolution, the blocks were then divided into four, with dimensions of roughly 250 by 250 km. We then iterated 25 more times with the smaller blocks allowed to vary independantly. The final results were then smoothed

Table 3.2 : Average Station Residuals (sec)

Stat	Res	Stat	Res	Stat	Res	Stat	Res
AAM	.3	AKU	1.7	ALE	.0	ALQ	-.2
ARE	-.1	ATL	-.2	BEC	.7	BHP	-1.1
BKS	.6	BLA	-.2	BLC	-.4	BOG	.8
BOZ	1.1	CAR	-.8	CMC	.1	COL	-.5
COP	.4	COR	.5	DAG	-.3	DAL	-.1
DUG	.2	EDM	1.1	ESK	.0	FBC	.0
FCC	-.5	FFC	.0	FLO	-.2	FSJ	.2
FVM	.1	GDH	.4	GEO	.8	GIE	1.4
GOL	.5	GSC	.4	GWC	-.2	HAL	.6
JCT	.3	KBS	1.5	KEV	.3	KON	.8
KRK	-.5	KTG	.0	LHC	-.2	LND	-.2
LON	.6	LOR	.3	LPB	-.2	LPS	1.1
LUB	.6	MAL	-.2	MBC	.1	MDS	.4
MNN	.0	MNT	.4	MSO	-.1	NNA	.0
NOR	.9	NUR	-.3	OGD	.1	OTT	-.1
OXF	-.6	PDA	.7	PHC	.3	PNT	.3
PTO	.0	QUI	.4	RCD	.5	RES	.2
SCB	.1	SCH	-.1	SCP	-.2	SES	.0
SFA	.3	SHA	1.3	SJG	-.8	STJ	.5
STU	.1	TOL	.4	TRN	.0	TUC	.0
UME	.5	UNM	.5	VAL	.4	VIC	-1.0
WES	.2	YKC	.0				

by a weighted average of adjacent blocks giving the slowness variation s in block b as

$$s_b = \frac{8w_b\, s + \sum_i 4w_i\, s_i + \sum_j 2w_j\, s_j + \sum_k w_k\, s_k}{8w_b + \sum_i 4w_i + \sum_j 2w_j + \sum_k w_k} \tag{3.8}$$

where b is the block of interest, i represents all adjacent blocks, j represents all blocks with a common line with b and k represents all blocks with a common point with b. The factor w_x is the total weight for a particular block x. This is given by the sum over all rays of $w_r\, l_r$ for the block. See equation (3.4) and the discussion there.

Resolution and Errors

Before presenting the results of the inversion it is necessary to consider the resolution possible with the data set. Wiggins (1972) discusses the problem of model resolution and shows that generally the value of a particular model parameter is not resolvable but that one can compute a combination of model parameters which can be resolved with a particular data set. The computation involves a singular value decomposition of the $L^T L$ matrix (equation 3.3) which is something we have avoided by using the SIRT iteration technique. In place of a formal resolution kernal for each block, we will follow Humphreys (1985) and perform inversions of data derived from known input structures. A comparison of the input model and the inversion result will enable one to estimate the resolving power of the data rayset.

Fig. 3.12 shows an input structure for which residuals were computed using the data ray paths. The heavy black areas are regions of fast velocity. All other areas have zero variation from the starting model. The anomalous fast regions extend to all depths in the mantle. The upper two layers were given a 3% variation, the third

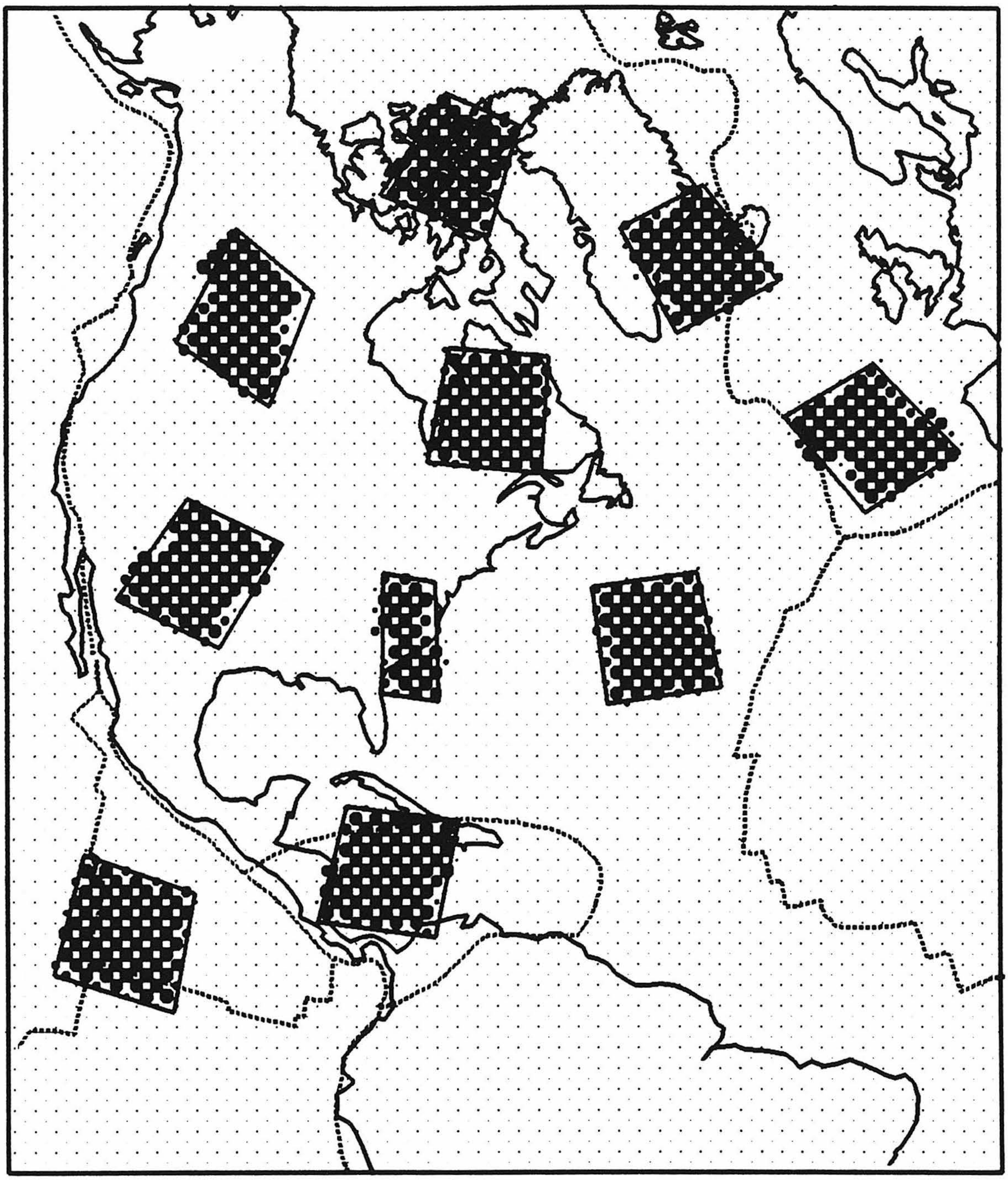

Figure 3.12 The input structure for a synthetic inversion using the data raypaths. The input anomalies are enclosed by boxes. They contain 4 blocks per layer except for the anomaly just north of Florida which contains only 2 blocks. The anomalies extend vertically throughout the model space.

layer a 2% variation and all the layers below have 1% variations. The location of the anomalies is such as to give an idea of the resolution for most of the model space without putting anomalies so close as to cause mixing from one anomaly to another in the inversion. The synthetic residuals were processed with the technique applied to the real data (discussed above). This includes inverting for just the upper three layers first and also the smoothing of the final solution as given by equation (3.8). The final results of the inversion are displayed in Figs. 3.13a-g as planar sections of every second layer in the model. The boxes containing the input anomalies in Fig. 3.12 are reproduced on the inversion result maps. The scale for the velocity variations are given below the maps. Notice that the scale only reaches 80% of the input structure in the upper 4 layers and 70% of the input in the lower layers. The stipled regions are blocks which have a total weight of less than 400 km. That is, if the denominater in equation (3.8) for a block b is less than 400 km the block is considered completely unresolved. For an average weight w_r of 3, this means blocks need 1600 km of raylength in their immediate vicinity to be included in the maps. The same masking is used in all the following figures.

The results of the synthetic inversion show large variability in the resolving power from location to location. The top two layers show excellent reconstructions of the input structures up to 80% of the amplitude with the exception of the two Atlantic anomalies. The southern Atlantic anomaly shows clear east-west streaking with only about 50% of the correct amplitude within the input area. Similarly, the northern Atlantic block shows streaking in a northwest-southeast direction. This result is not surprising due to the event-station distribution. Most of the Atlantic events are on the Mid Atlantic Ridge with paths westward to North America. The north

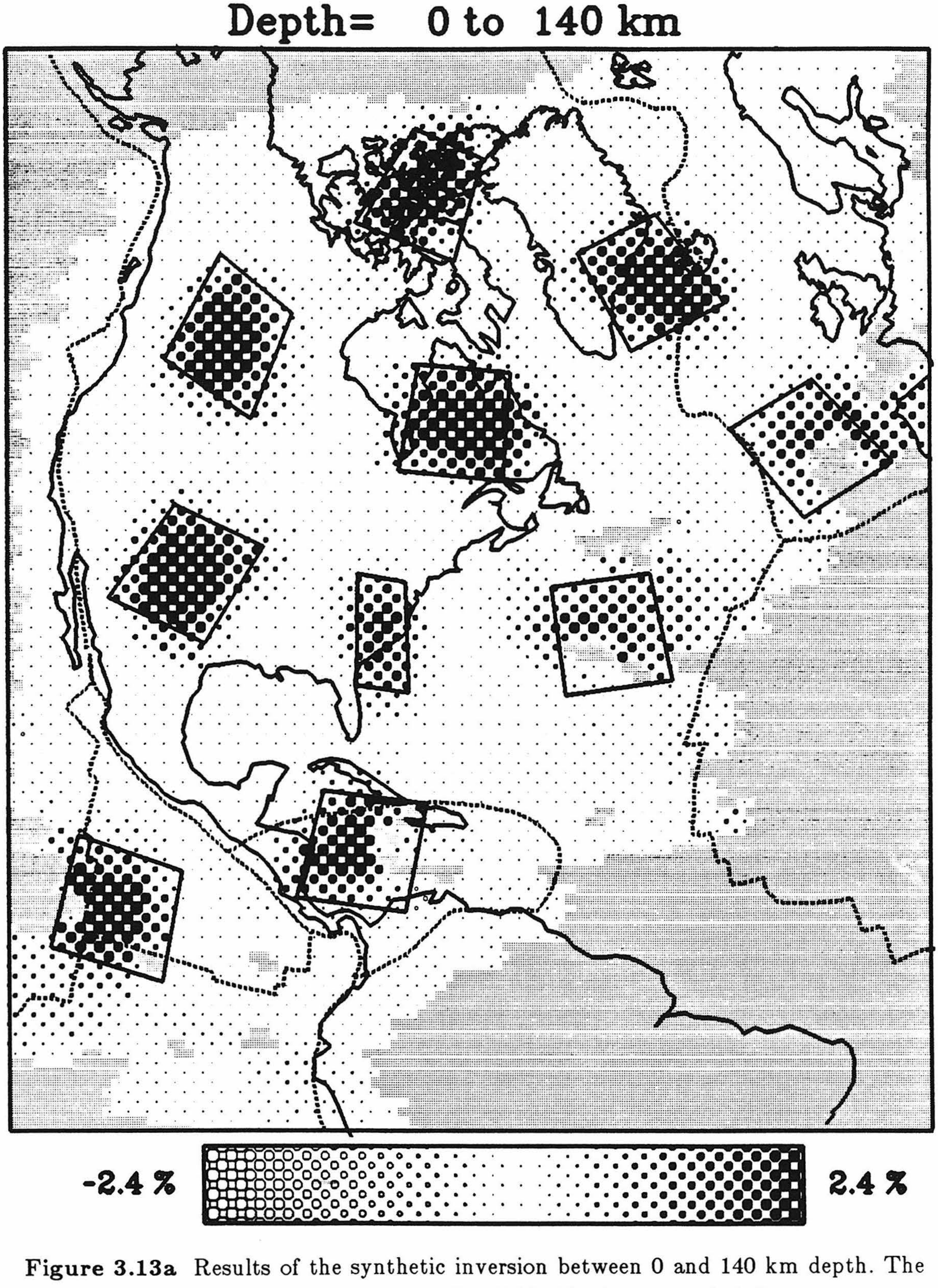

Figure 3.13a Results of the synthetic inversion between 0 and 140 km depth. The input structure is shown in Fig. 3.12. The boxes in that figure are reproduced here. The scale, in percentage velocity variation, is shown above.

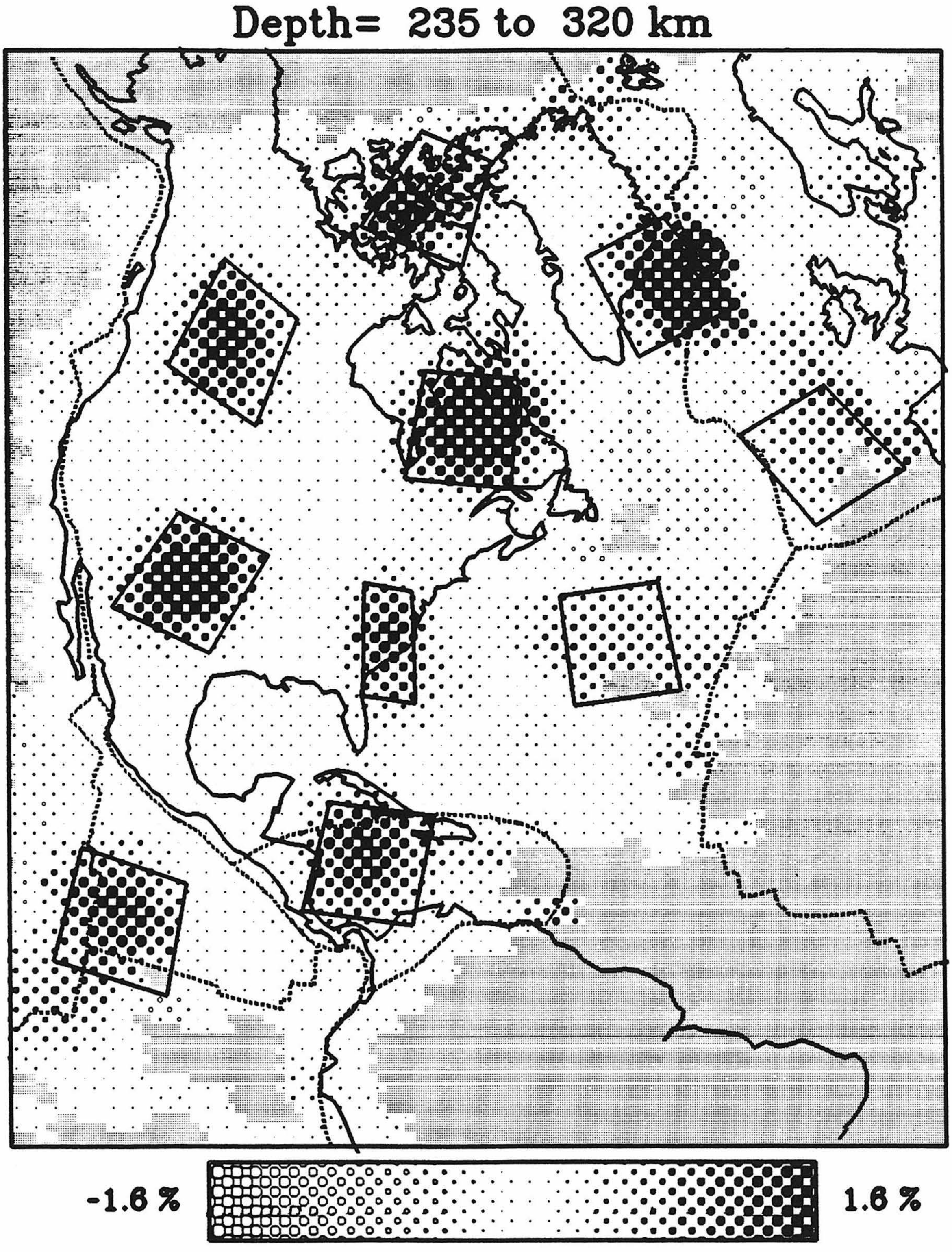

Figure 3.13b Results of synthetic inversion from 235 to 320 km depth.

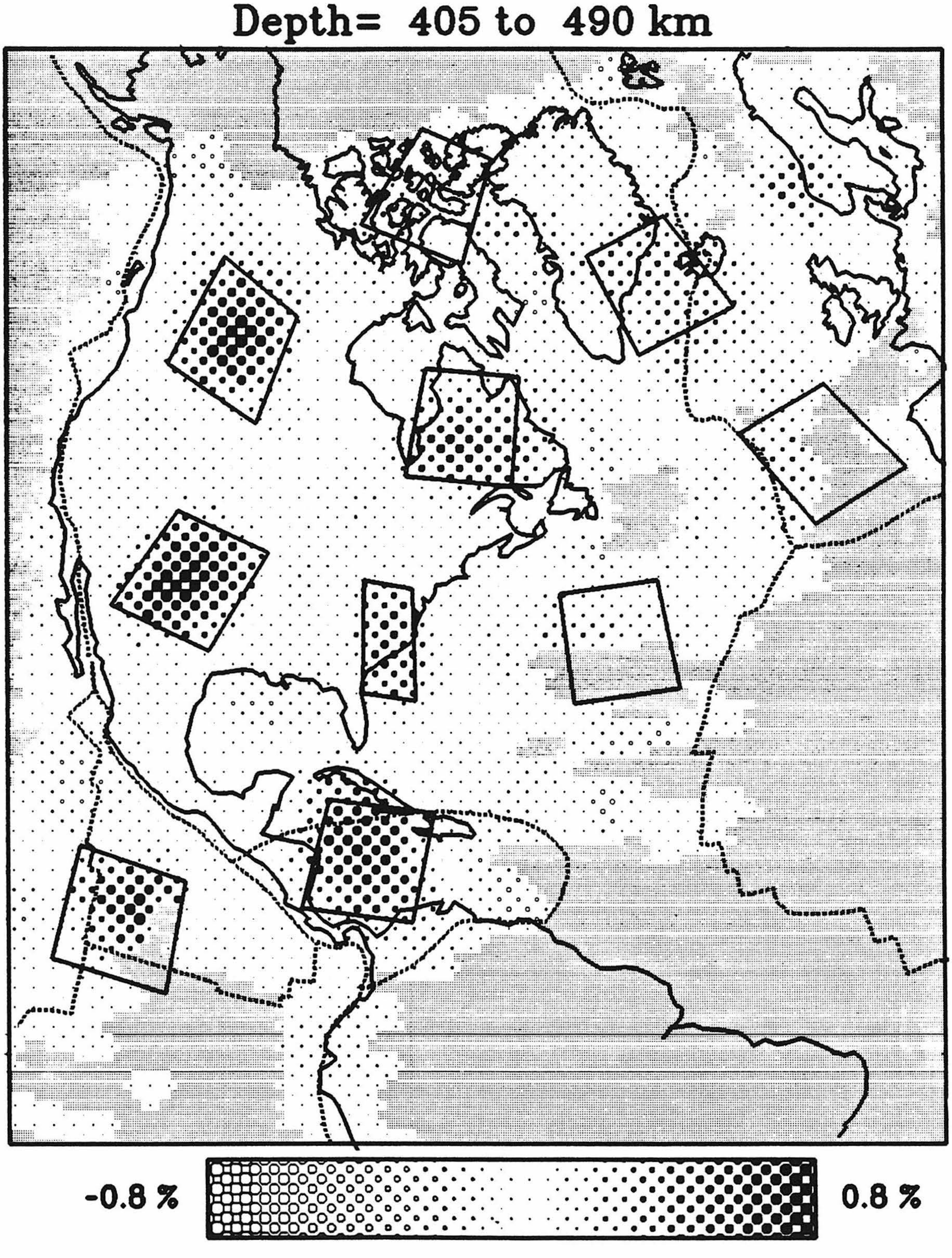

Figure 3.13c Results of synthetic inversion from 405 to 490 km depth.

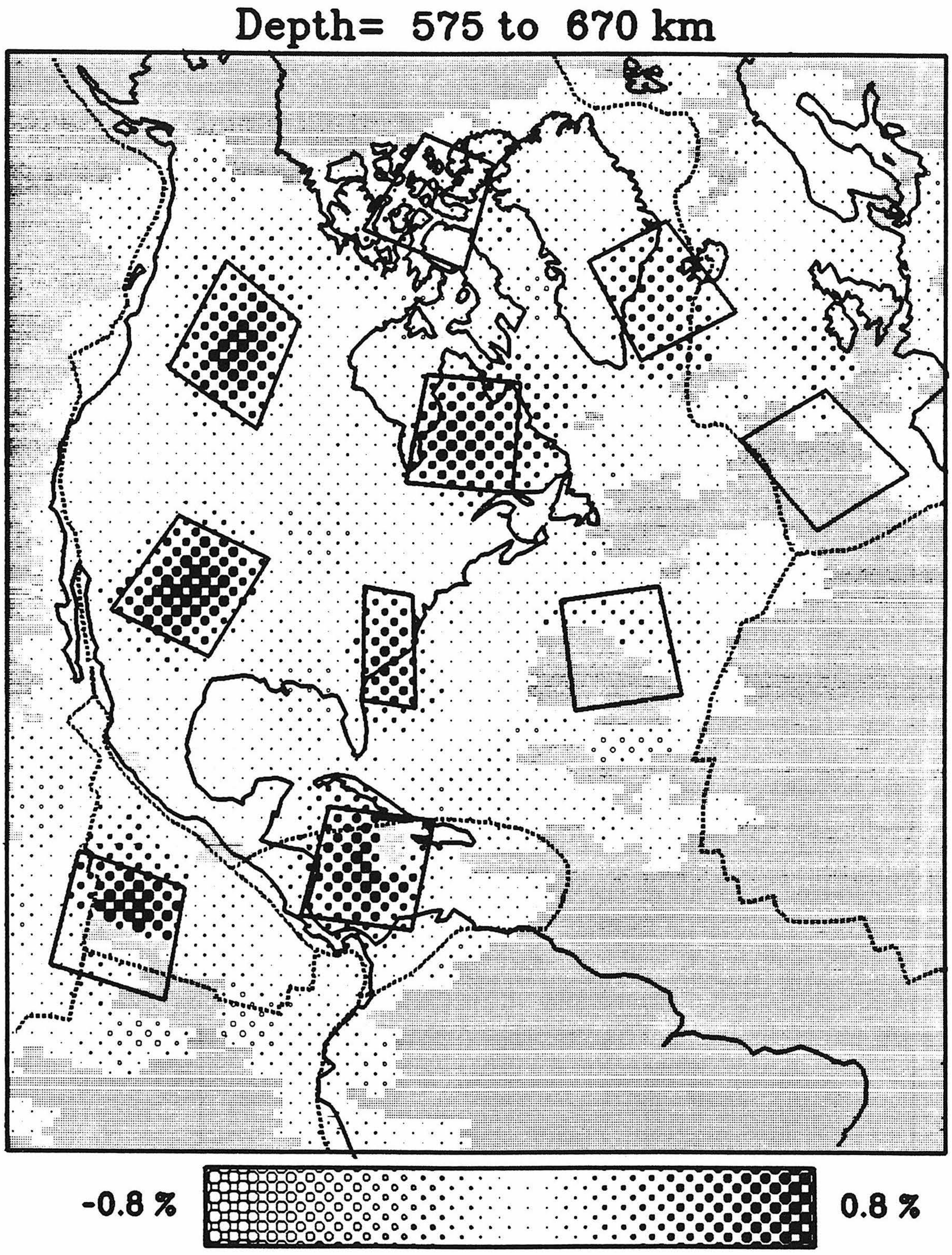

Figure 3.13d Results of synthetic inversion from 575 to 670 km depth.

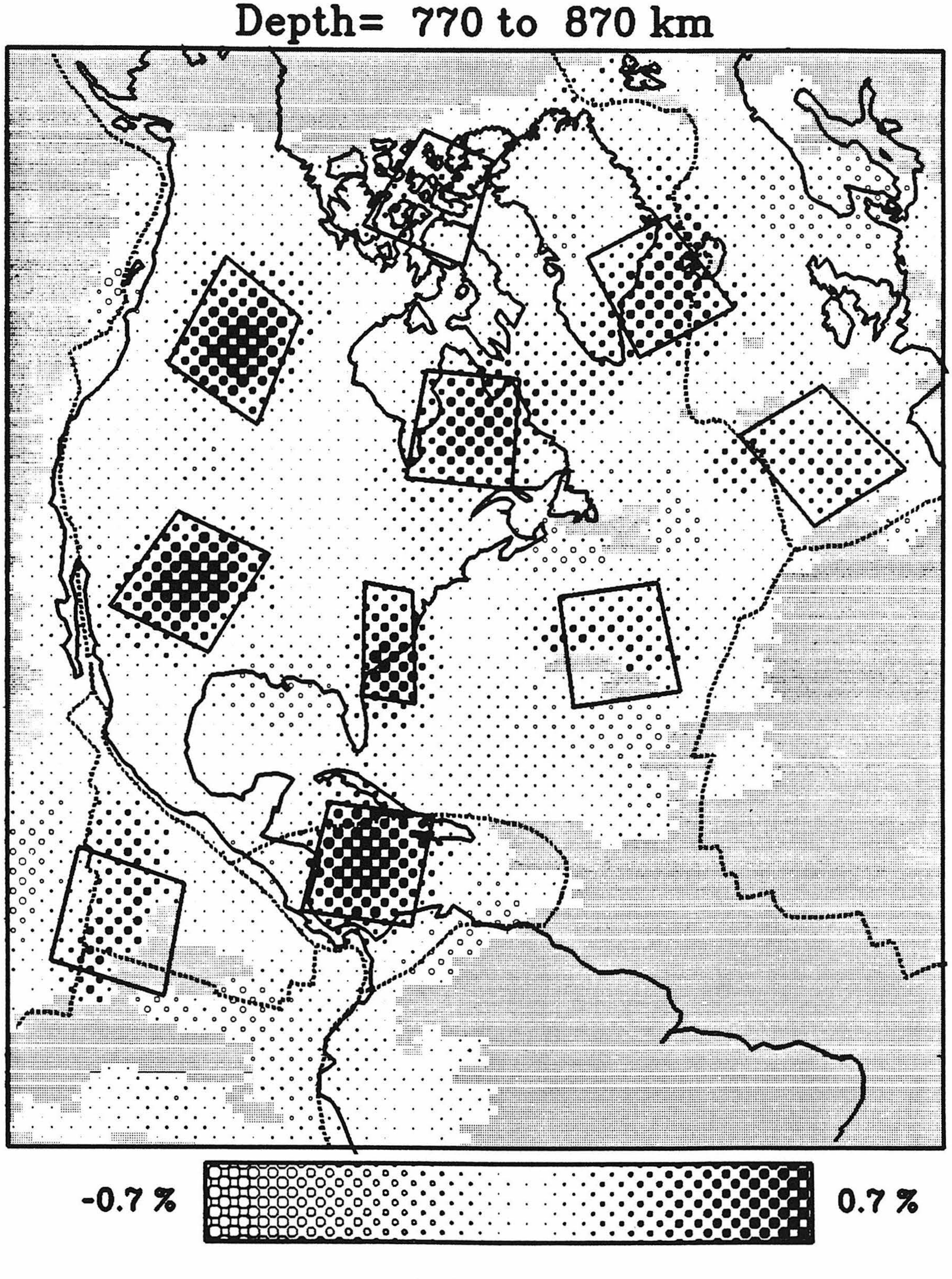

Figure 3.13e Results of synthetic inversion from 770 to 870 km depth.

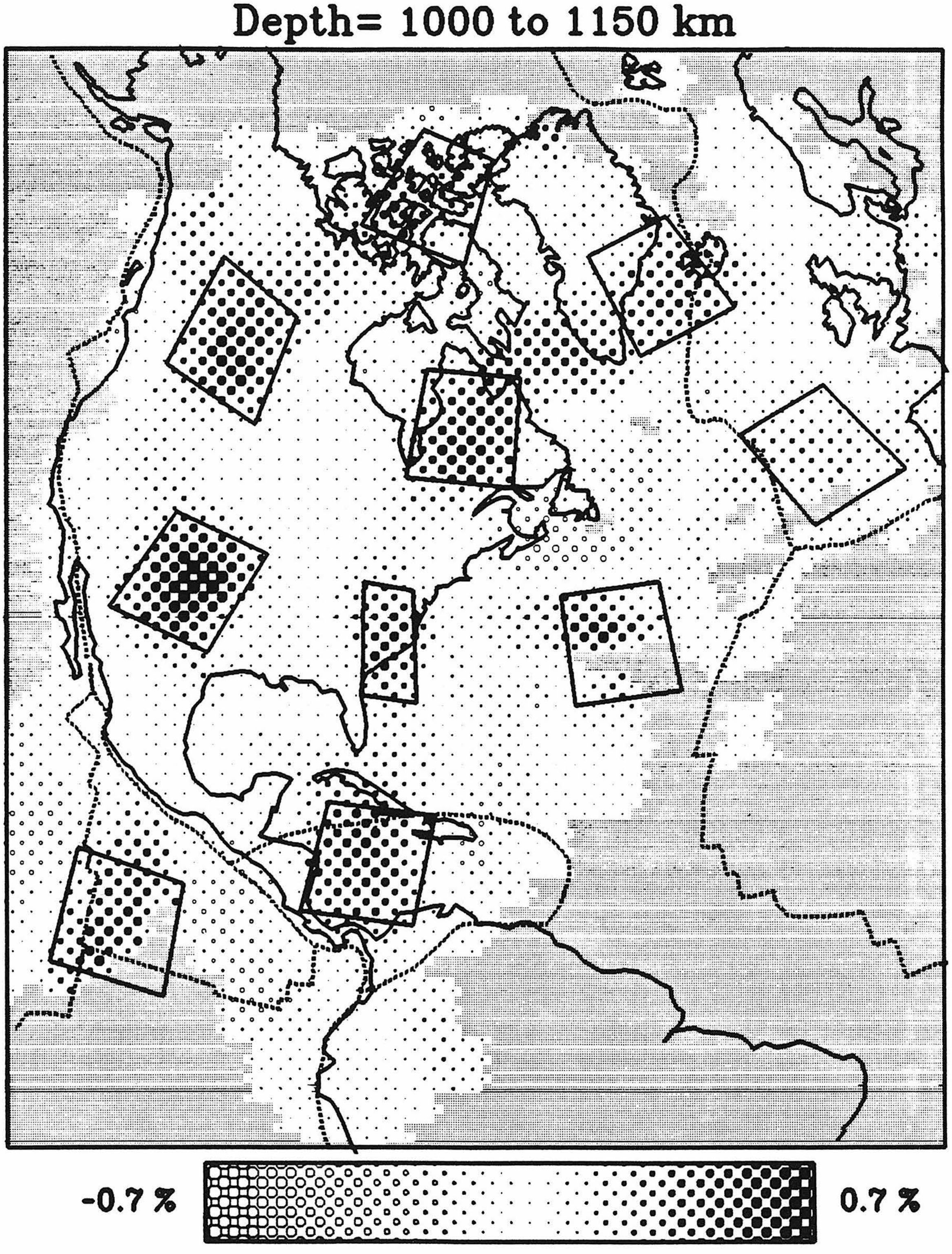

Figure 3.13f Results of synthetic inversion from 1000 to 1150 km depth.

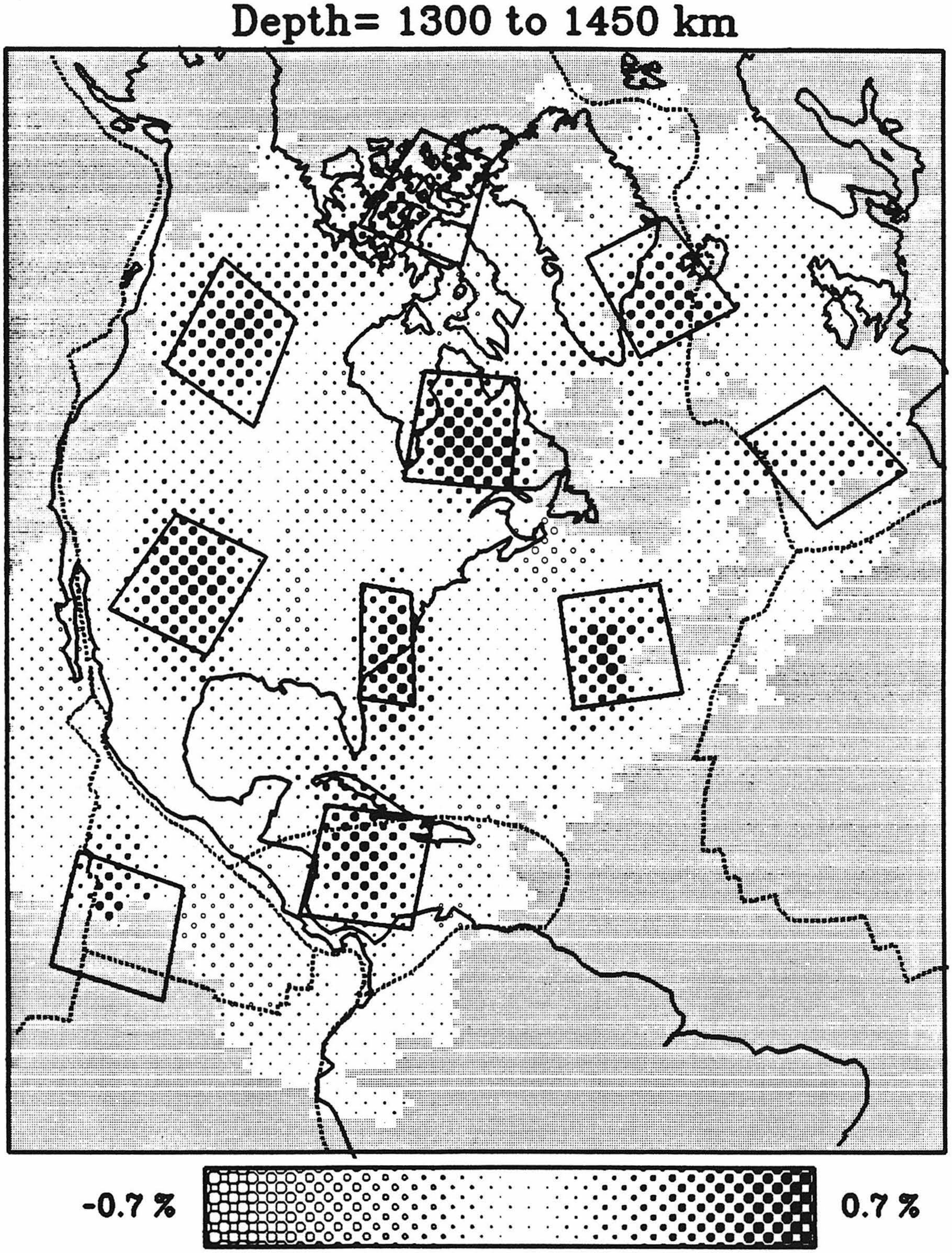

Figure 3.13g Results of synthetic inversion from 1300 to 1400 km depth.

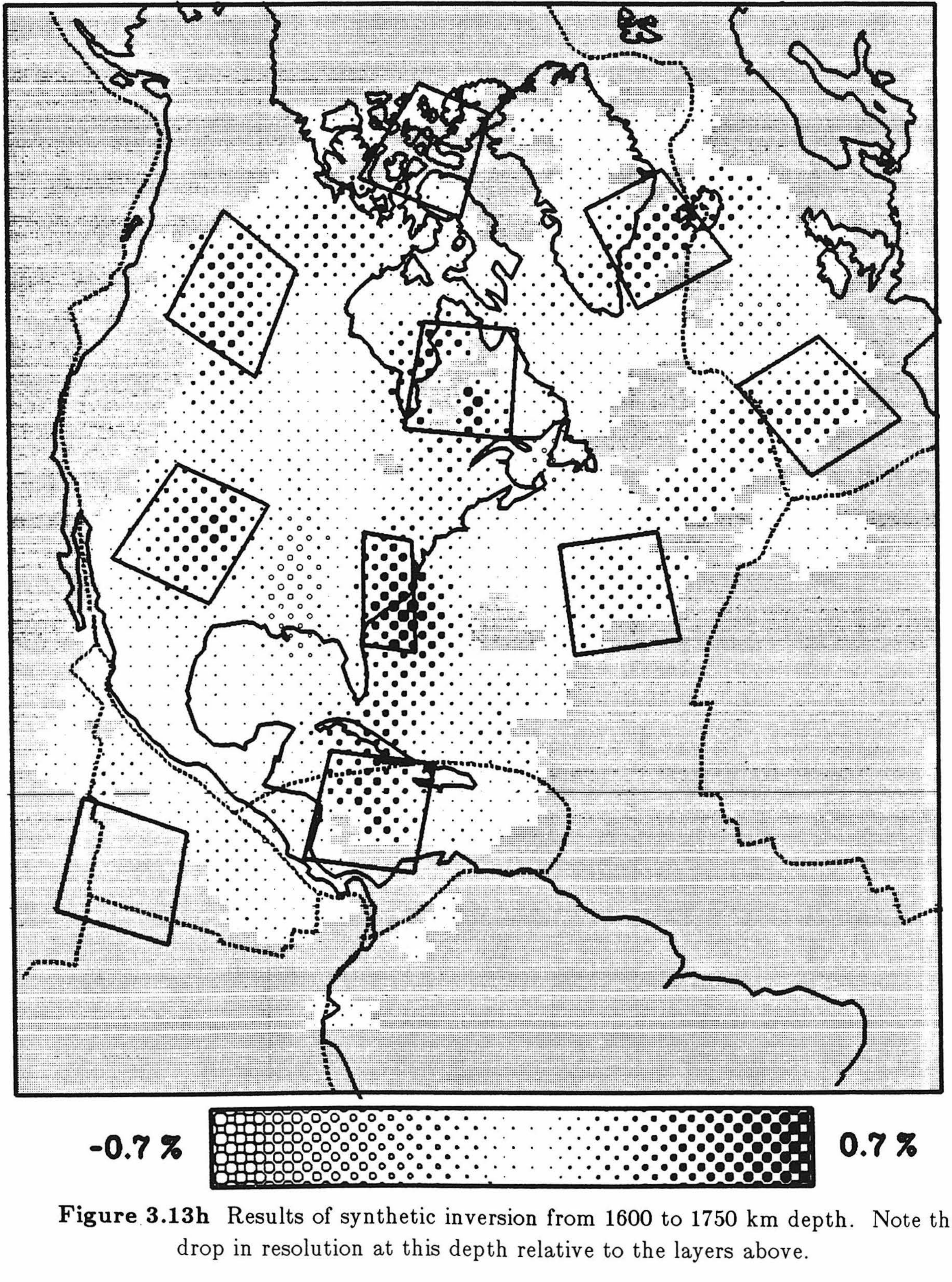

Depth= 1600 to 1750 km

Figure 3.13h Results of synthetic inversion from 1600 to 1750 km depth. Note the drop in resolution at this depth relative to the layers above.

Atlantic is sampled mostly by events from north of Iceland to stations in Europe. Below 320 km, Figs. 3.13c-g, the reconstructions are not as good as for the shallow mantle. This is probably due to the longer raypaths needed to sample deeper and the initial inversion allowing only the upper three layers to vary. Streaking of the solution is evident from 770 km to 1150 km depth between the eastern Canadian block and the block near Iceland. The block near Portugal is the worst location at all depths. Note, however, that above 1600 km depth and within North America and the Carribean, every anomaly is reproduced to within 50% amplitude and that areas outside the anomalous blocks have smaller amplitude variations than within them. Below 1600 km the anomalies become more spread out and it is only possible to discern large scale regional variations. When examining the results of inverting real data, in the next section, these synthetic examples should be kept in mind.

The vertical resolution was not addressed in the above discussion. Turning rays in the mantle generally spend more than 50% of their time in the layer in which they bottom. Thus, the vertical resolution is generally much better than the horizontal resolution.

A second experiment was done to investigate the effect of noise on the inversion. Due to uncertainties in the position of the minute mark on the seismograms and the difficulty in finding the exact onset of an S-wave, the teleseismic travel-time picks are uncertain to within ± 1 sec. The upper mantle arrivals have greater uncertainty due to interference from several phases arriving at the same time. We estimate the uncertainty of those picks to be about ± 2.5 sec. These estimates are probably conservative and many picks are probably more accurate than stated above. Random mislocation of earthquakes by about 10 km will also add about 1 sec to the uncertainties.

To test the effect of random errors, an inversion was run on the data rayset with random travel-time anomalies. The rays were given an anomaly from -2.5 sec to 2.5 sec with an equal probability of having any value between the extremes. This is not a realistic experiment but is done only to make an estimate of what errors in the times can produce in the inversion. Figs. 3.14a-d show planar sections through 4 layers of the model derived from inverting random numbers. The scales for velocity variations are given below the maps. Note that the top layer ranges from 3% to -3% and the lower layers vary from .9% to -.9%. These ranges are those used in the next section showing the inversion of the real data. We use the same scales for this test so that these results can be compared directly to the final model. Note that the inversion rarely gives blocks with near maximum amplitude and that when it does, the anomalies are very localized. The largest variations are found where the resolution runs shown previously were worst, i.e., the Atlantic region. Fig. 3.15 shows the position of three cross sections through the model. Figs. 3.16a-c show the cross sections along the labeled lines with a vertical exaggeration of about 3 to 1. The scale varies with depth as it will in the final model figures. From 0 to 320 km depth, the scale is 3% to -3%, from 320 to 405 km it is 1.5% to -1.5% and below 405 km the maximum variations are .9% to -.9%. As in the planar sections, the largest amplitude anomalies are very localized. There are no large amplitude structures continuous over more than 400 km depth. As with the resolution test runs, these figures should be kept in mind when interpreting the results shown next.

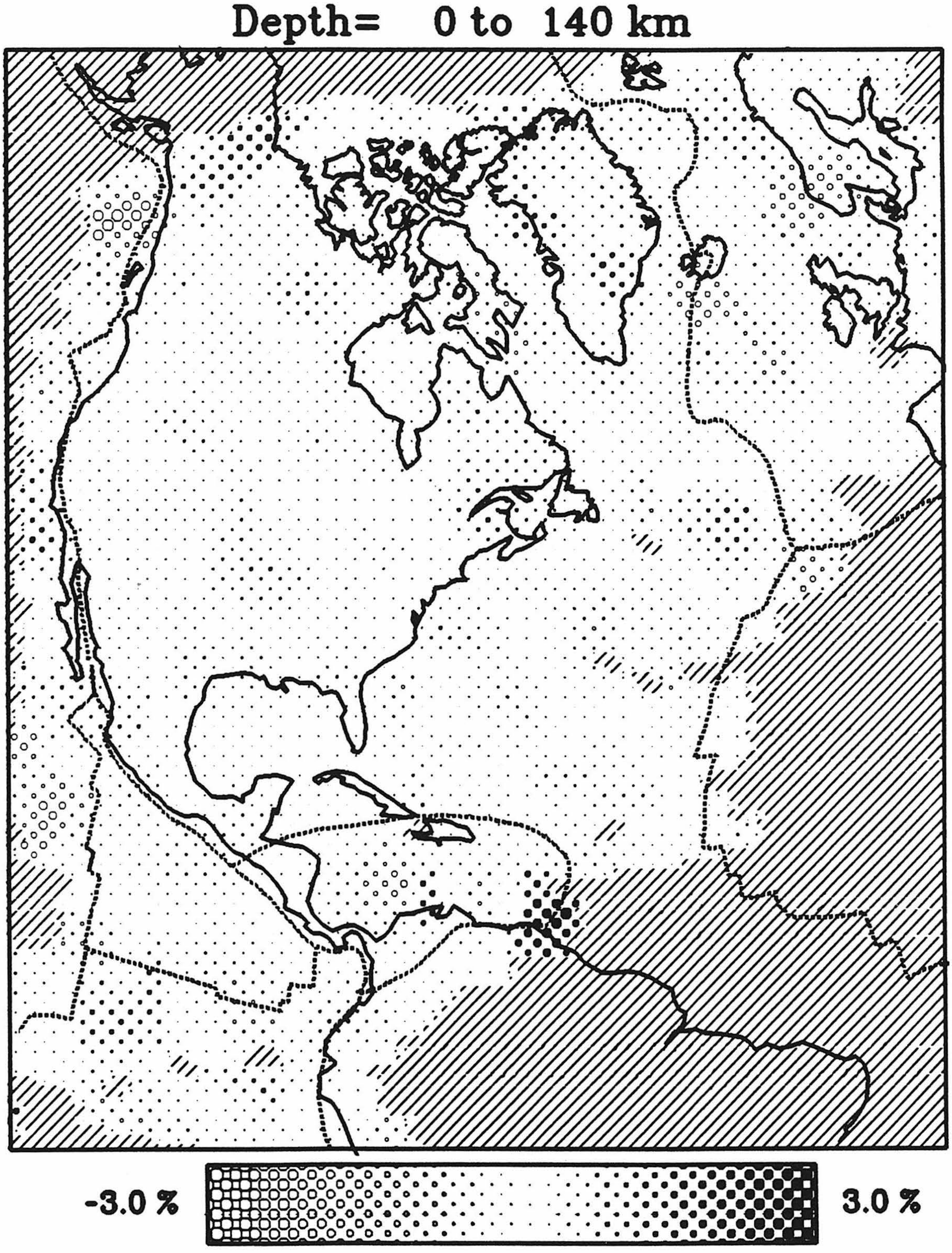

Figure 3.14a Results of inverting random time residuals from 0 to 140 kmdepth.

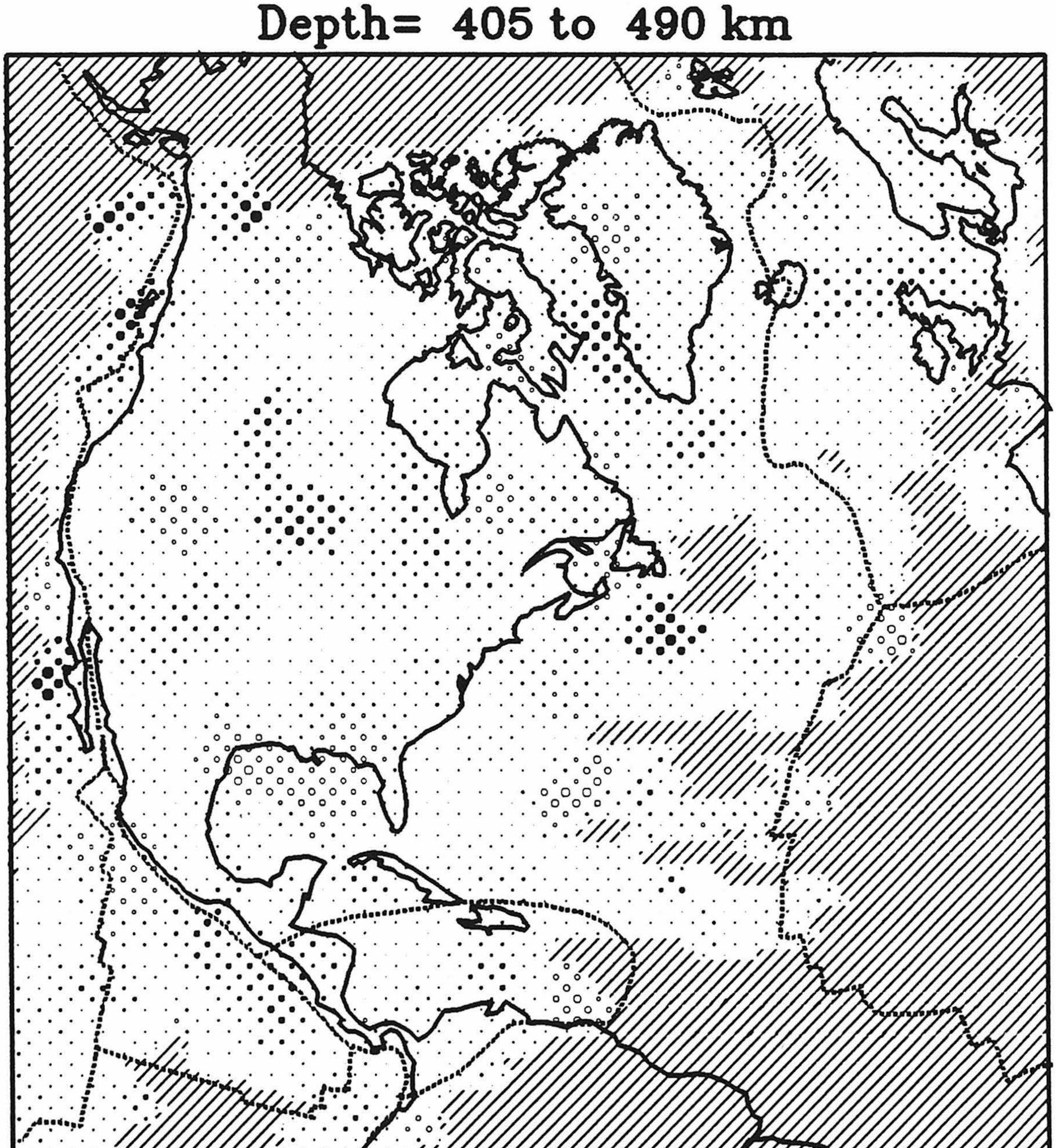

Figure 3.14b Results of inverting random time residuals from 405 to 490 km depth.

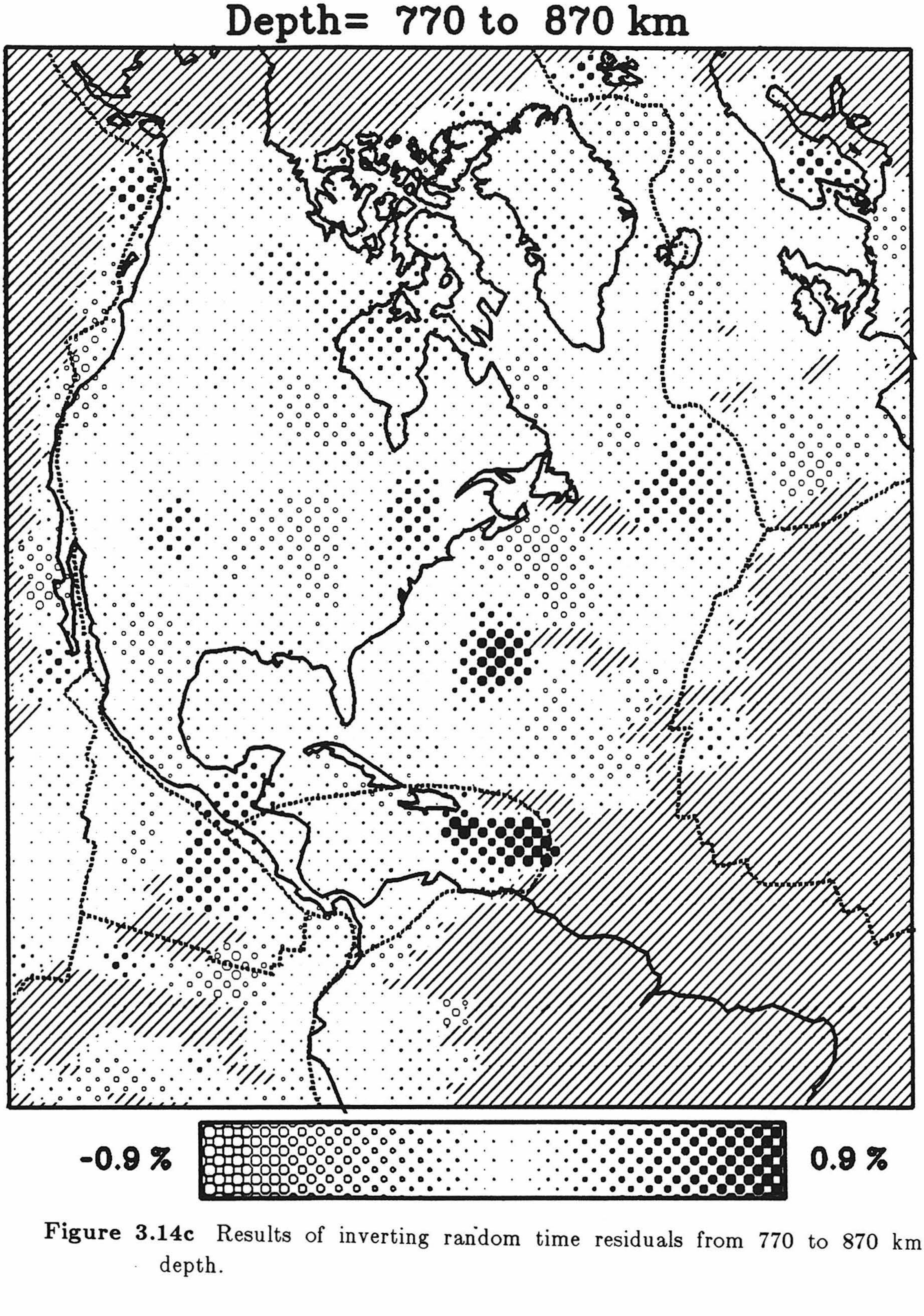

Depth= 770 to 870 km

Figure 3.14c Results of inverting random time residuals from 770 to 870 km depth.

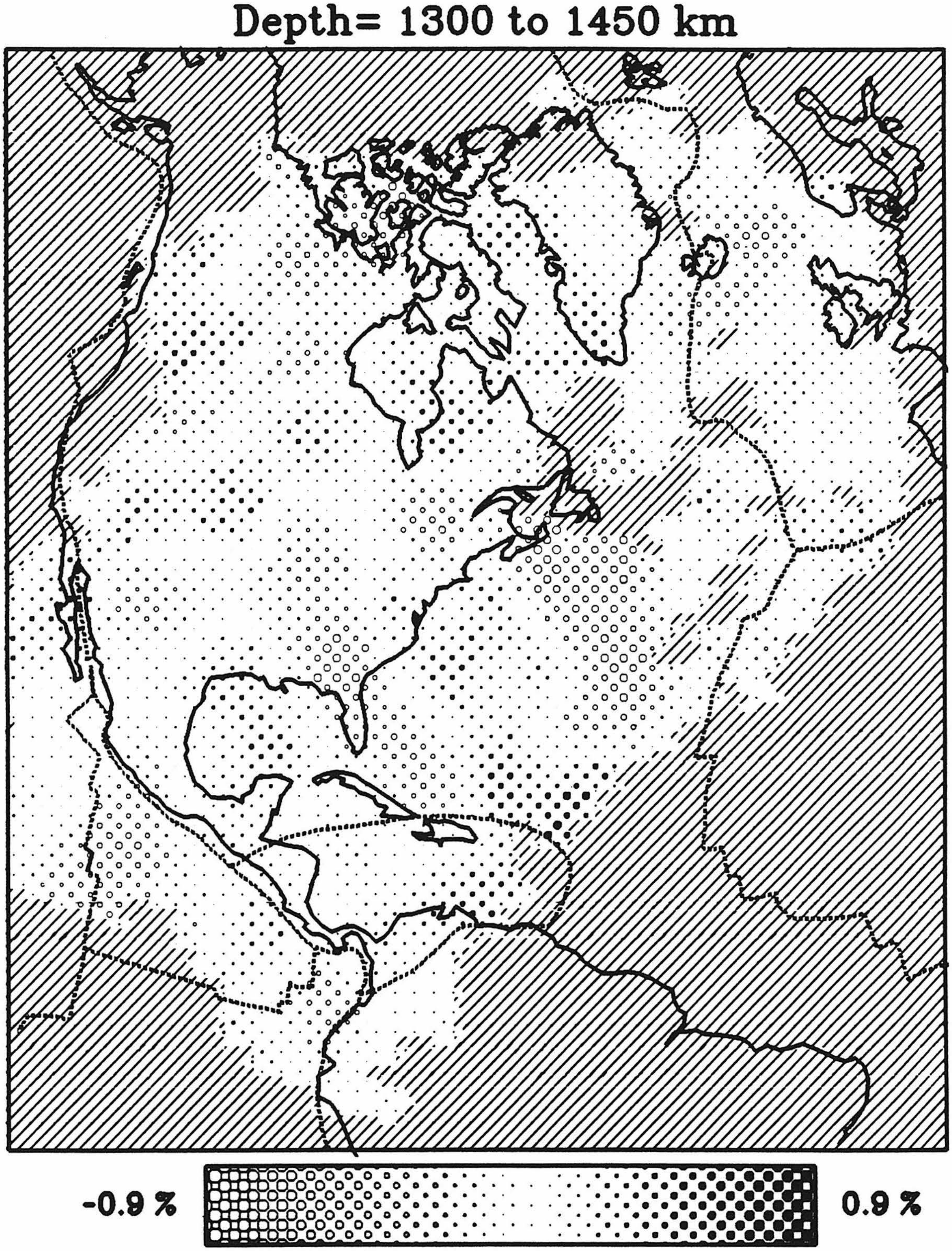

Figure 3.14d Results of inverting random time residuals from 1300 to 1450 km depth.

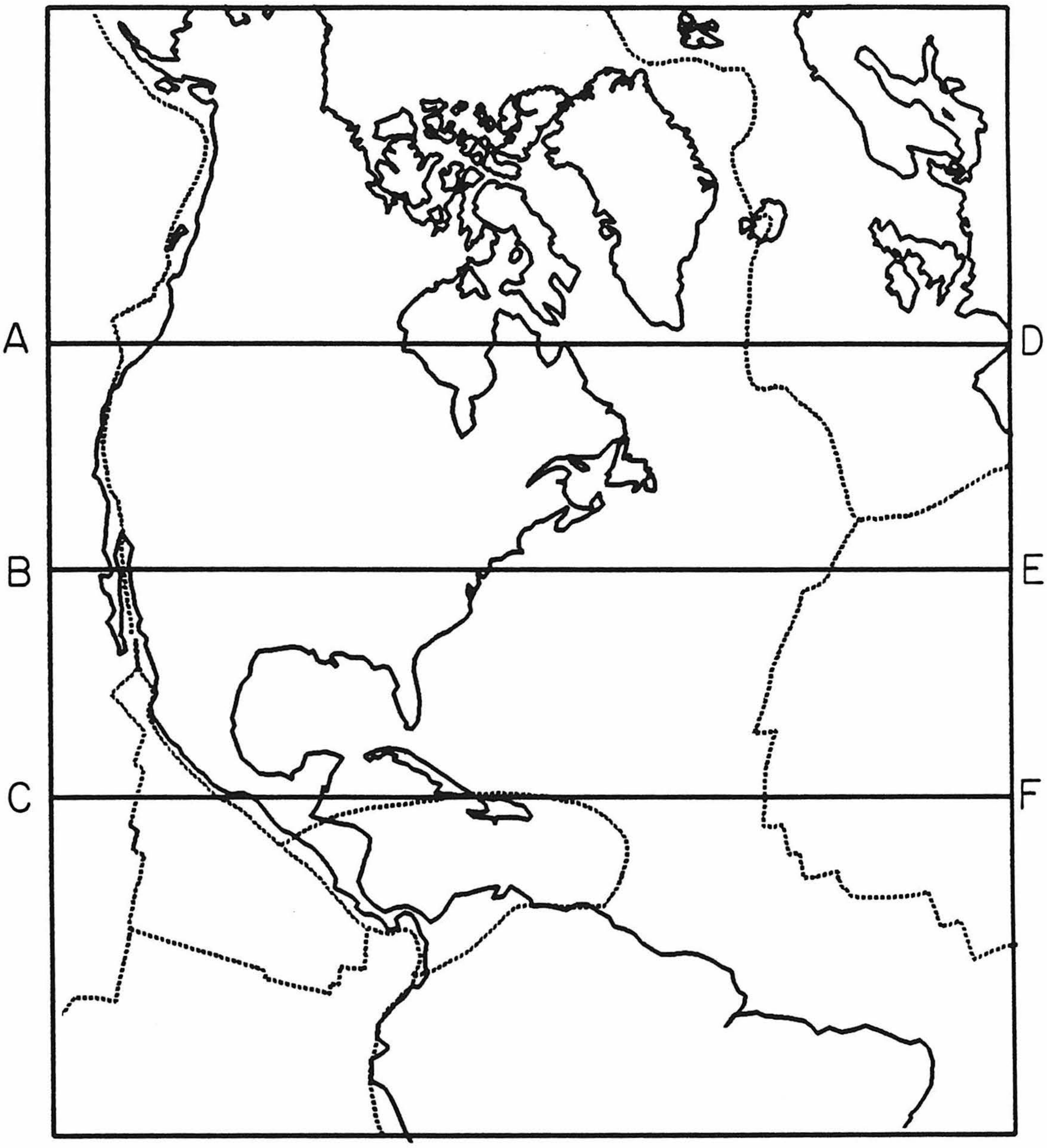

Figure 3.15 Position of three cross sections through the random residual inversion model.

Figure 3.16a Cross section of the results from inverting random data along profile A-D in the previous figure. The scale varies with depth from +3% to -3% above 320 km, +1.5% to -1.5% from 320 km to 405 km and +.9% to -.9% below 405 km depth.

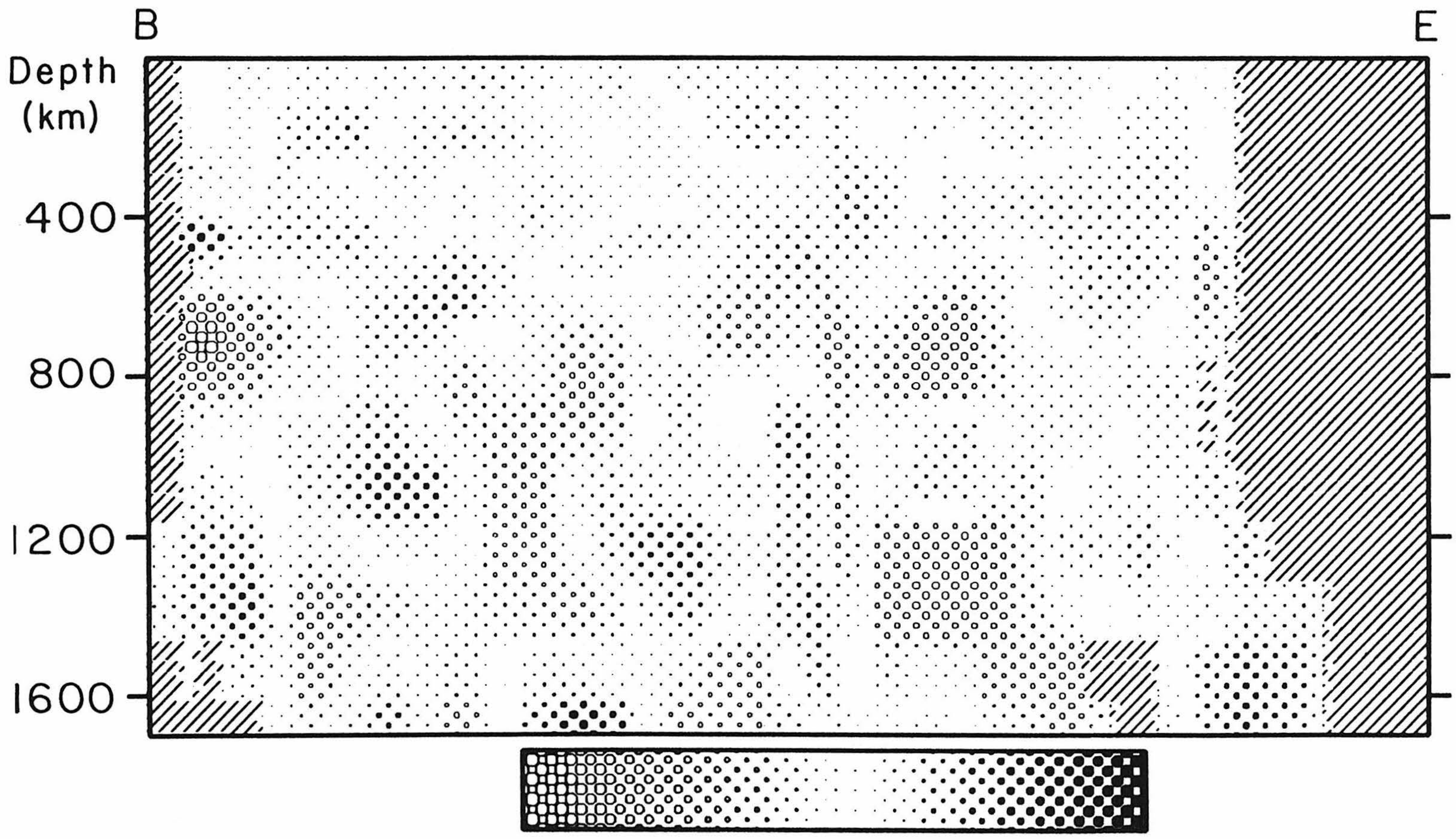

Figure 3.16b Cross section of the results from inverting random data along profile B-E of Fig. 3.15.

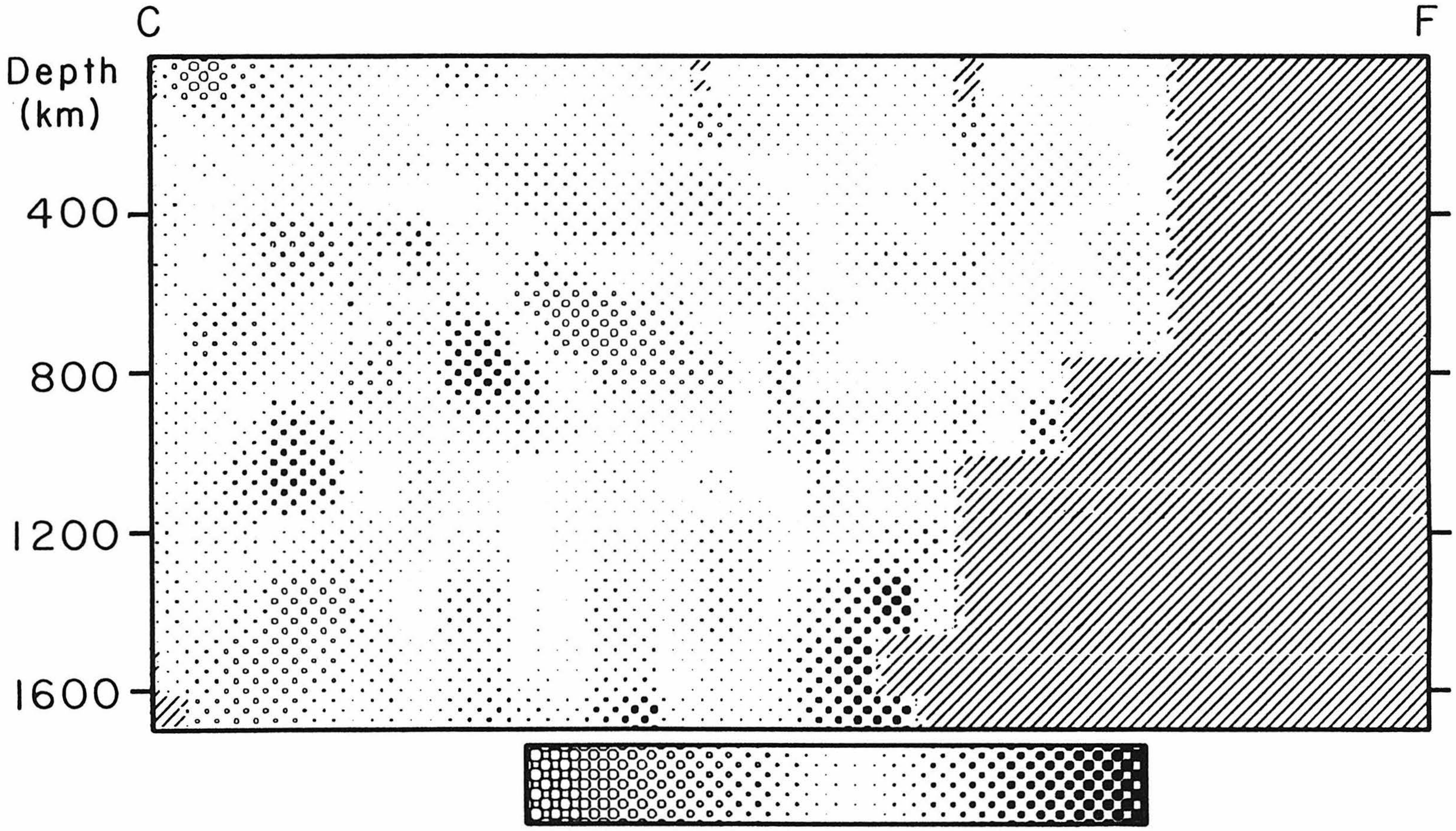

Figure 3.16c Cross section of the results from inverting random data along profile C-F of Fig. 3.15.

Results and Discussion

The results of the inversion are presented as planar sections for each layer in Figs. 3.17a-p. Lines of constant latitude are drawn every 10^o and lines of constant longitude every 30^o for reference. The projection is such that great circles through the center of the map are straight lines. The worst distortion is around the edges of the map. The most obvious feature of the inversion was the large lateral variations found in the upper 320 km relative to the deeper mantle. For this reason, the scales vary from +3% to -3% in the upper three layers, +1.5% to -1.5% in the fourth layer and +.9% to -.9% in the mantle below 405km depth.

The top layer, from 0 to 140 km depth, shows the largest and most rapid variations in velocity. The range in velocities shown is from about 4.7 km/sec to 4.4 km/sec. Some regions of the shield have velocities up to 4.8 km/sec. Notice that all stable continental areas and oceanic areas with crustal ages greater than about 80 Ma have velocities greater than 4.7 km/sec (see Sclater and Parsons, 1981, for a map of crustal ages). Oceanic regions with crust between 20 and 80 Ma have velocities between 4.55 km/sec and 4.7 km/sec except for the western Carribean. Note that between Greenland and Canada there is a decrease in velocity to about 4.55 km/sec consistent with the map of Sclater and Parsons showing this area to be oceanic crust less than 60 Ma. The intermediate age regions of the Atlantic do not vary in velocity in direct proportion to the age; however, this region had the worst resolution at this depth in the test case shown in Fig. 3.13a and thus this may not be a real phenomena. The Atlantic results agree in general with work by Hart and Press (1973) who found an average Sn velocity of 4.71 km/sec in portions of the Atlantic older than 50 Ma and an average Sn velocity of 4.58 km/sec in the Atlantic with

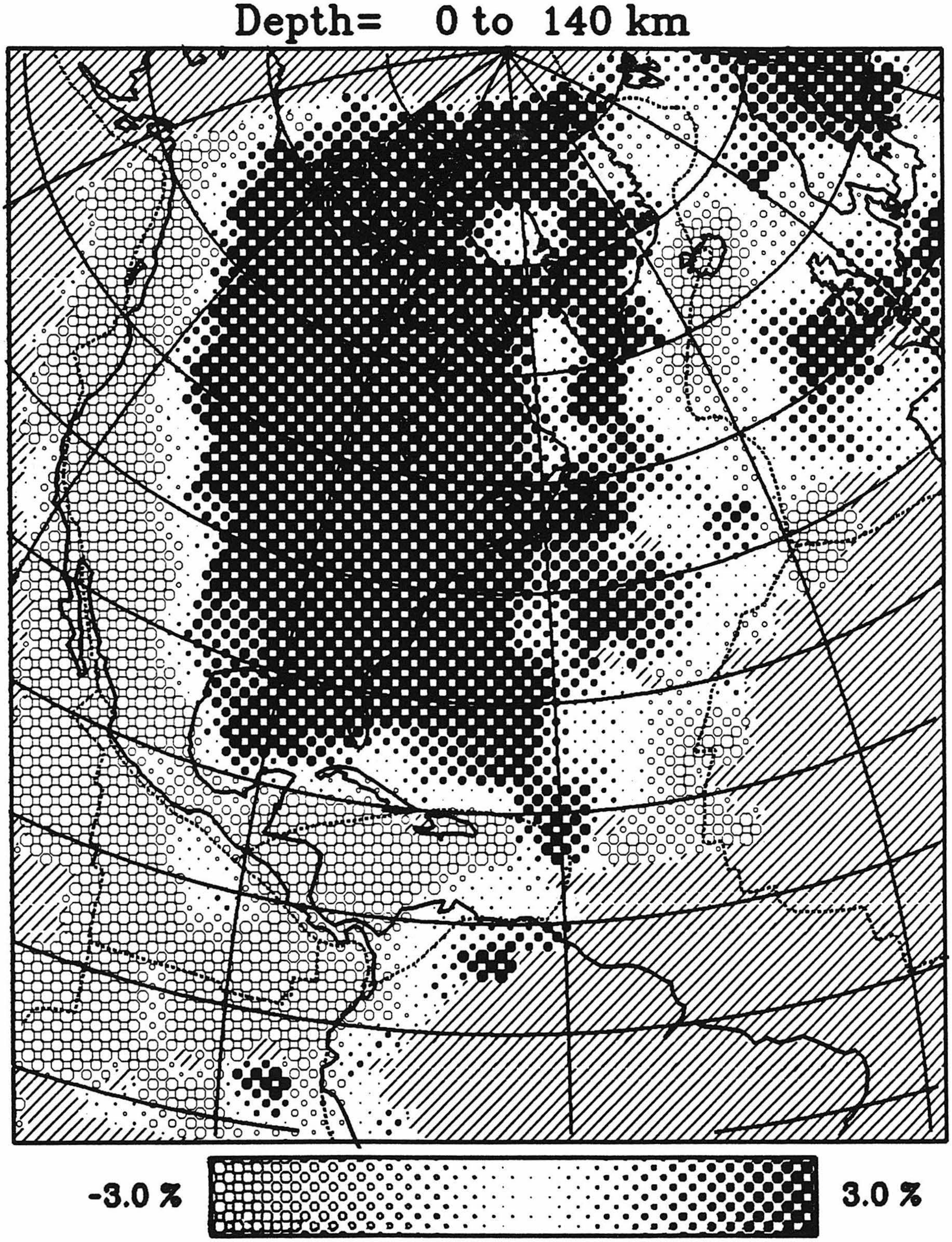

Figure 3.17a Results of the inversion for a planar section from 0 to 140 km depth. The dotted lines mark plate boundaries. Unresolved areas have a slanted line pattern through them.

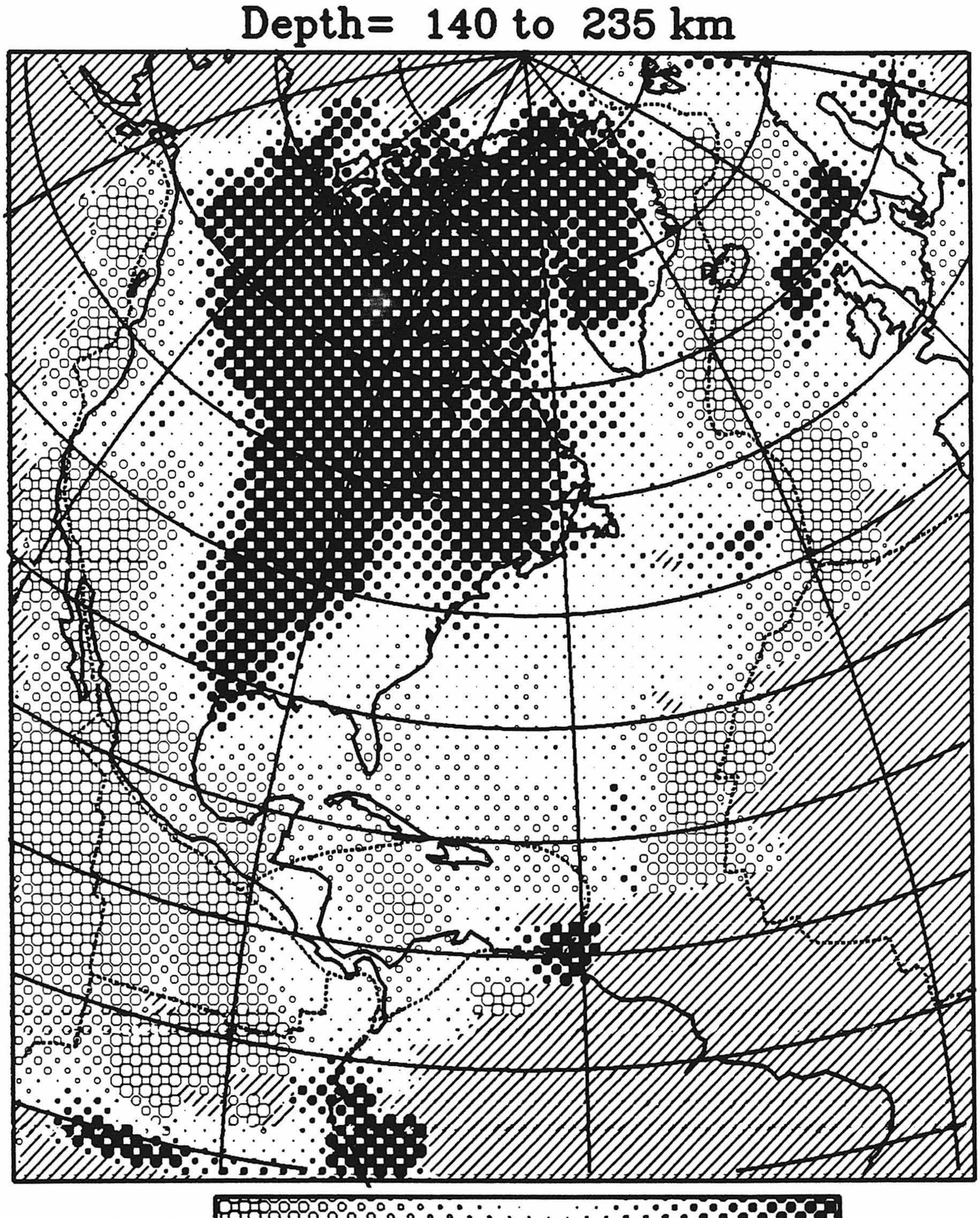

Figure 3.17b Inversion results from 140 to 235 km depth.

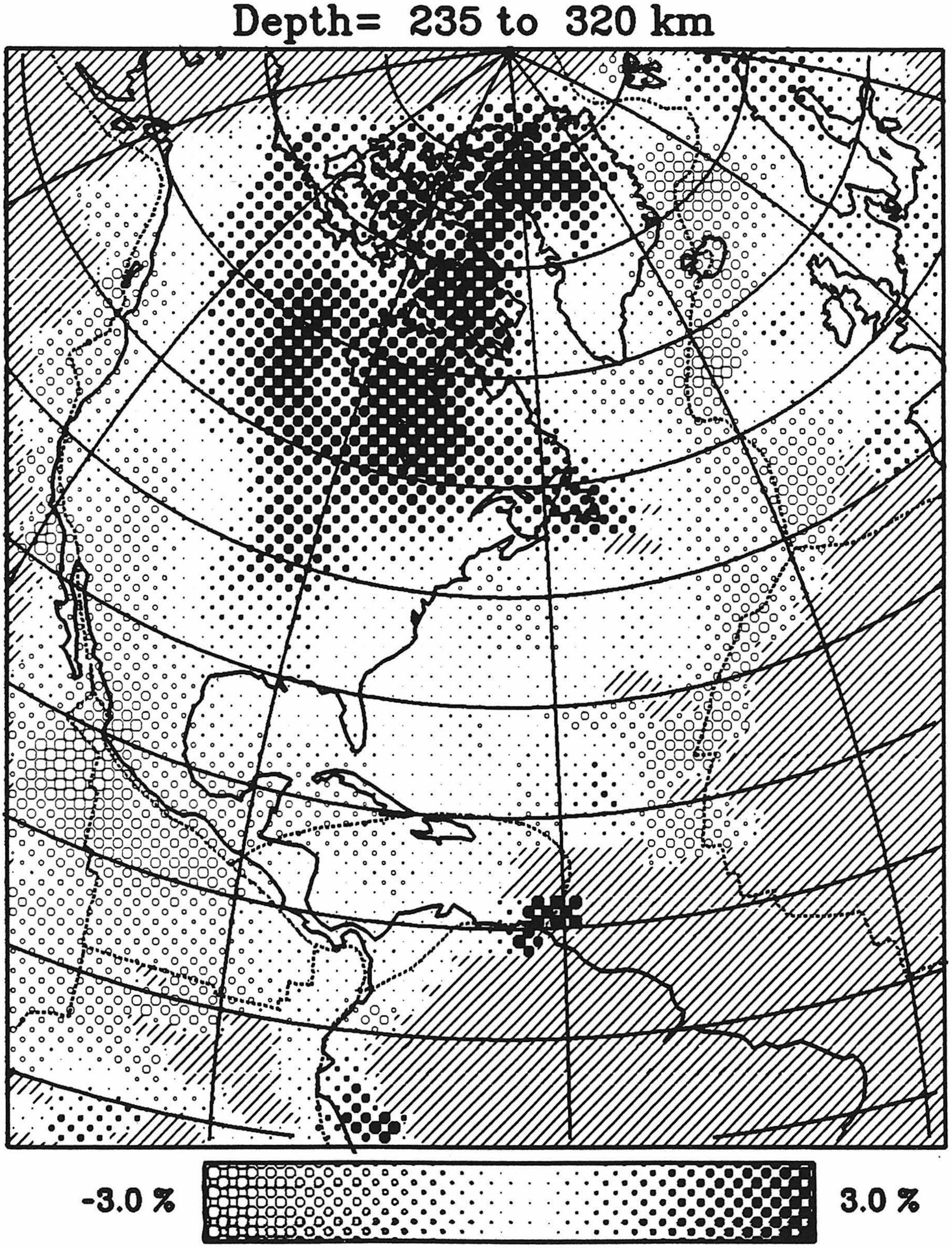

Figure 3.17c Inversion results from 235 to 320 km depth.

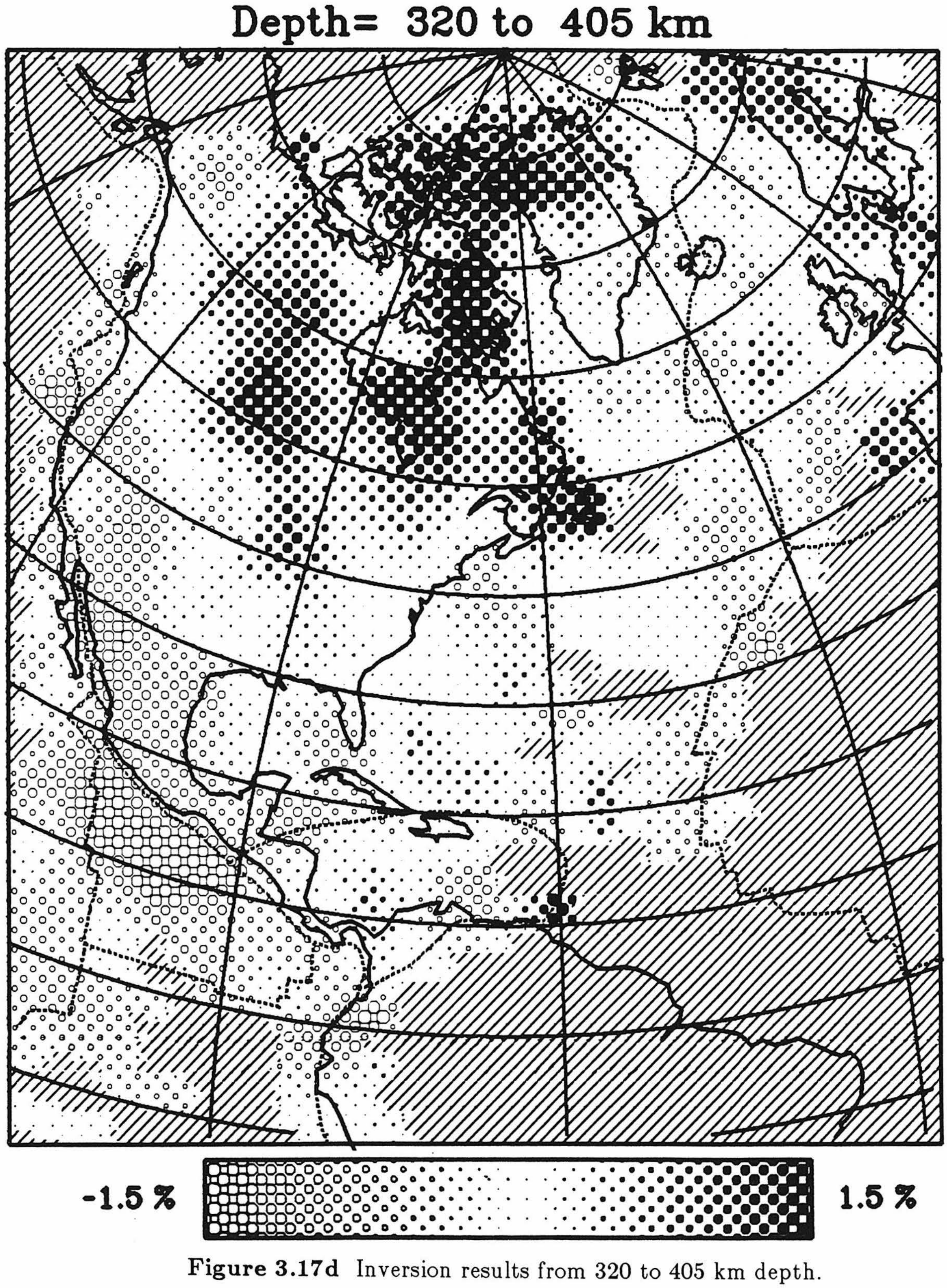

Figure 3.17d Inversion results from 320 to 405 km depth.

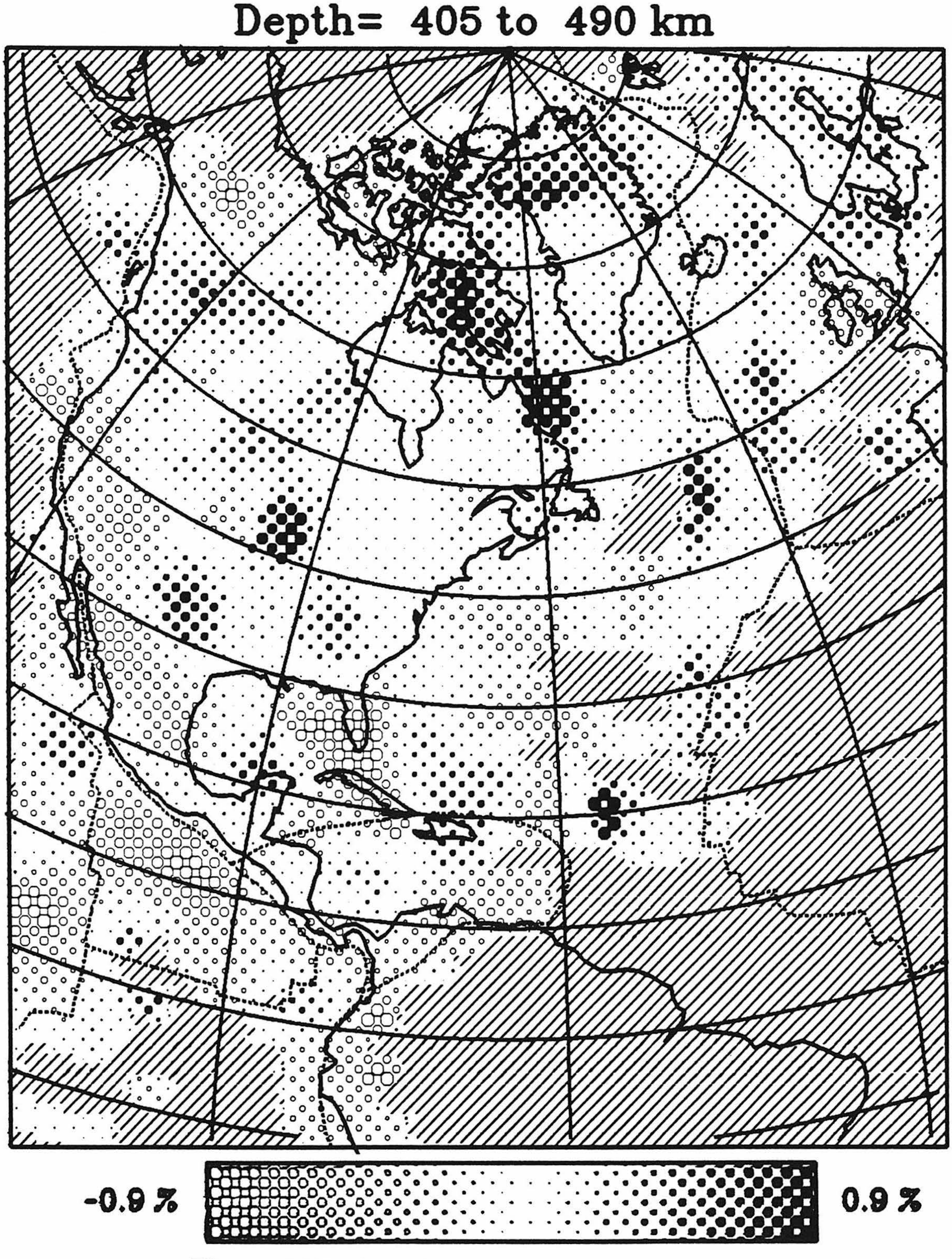

Figure 3.17e Inversion results from 405 to 490 km depth.

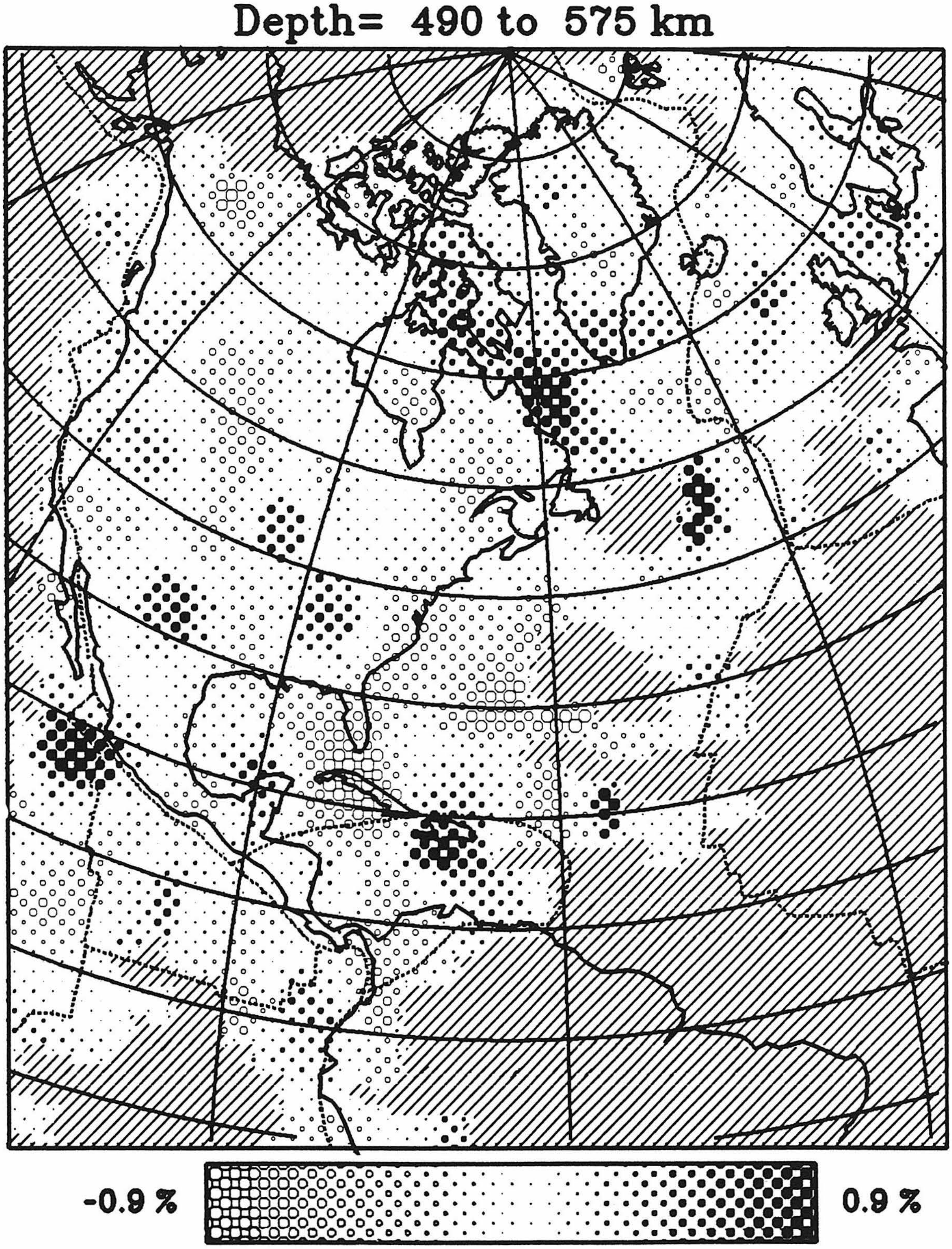

Figure 3.17f Inversion results from 490 to 575 km depth.

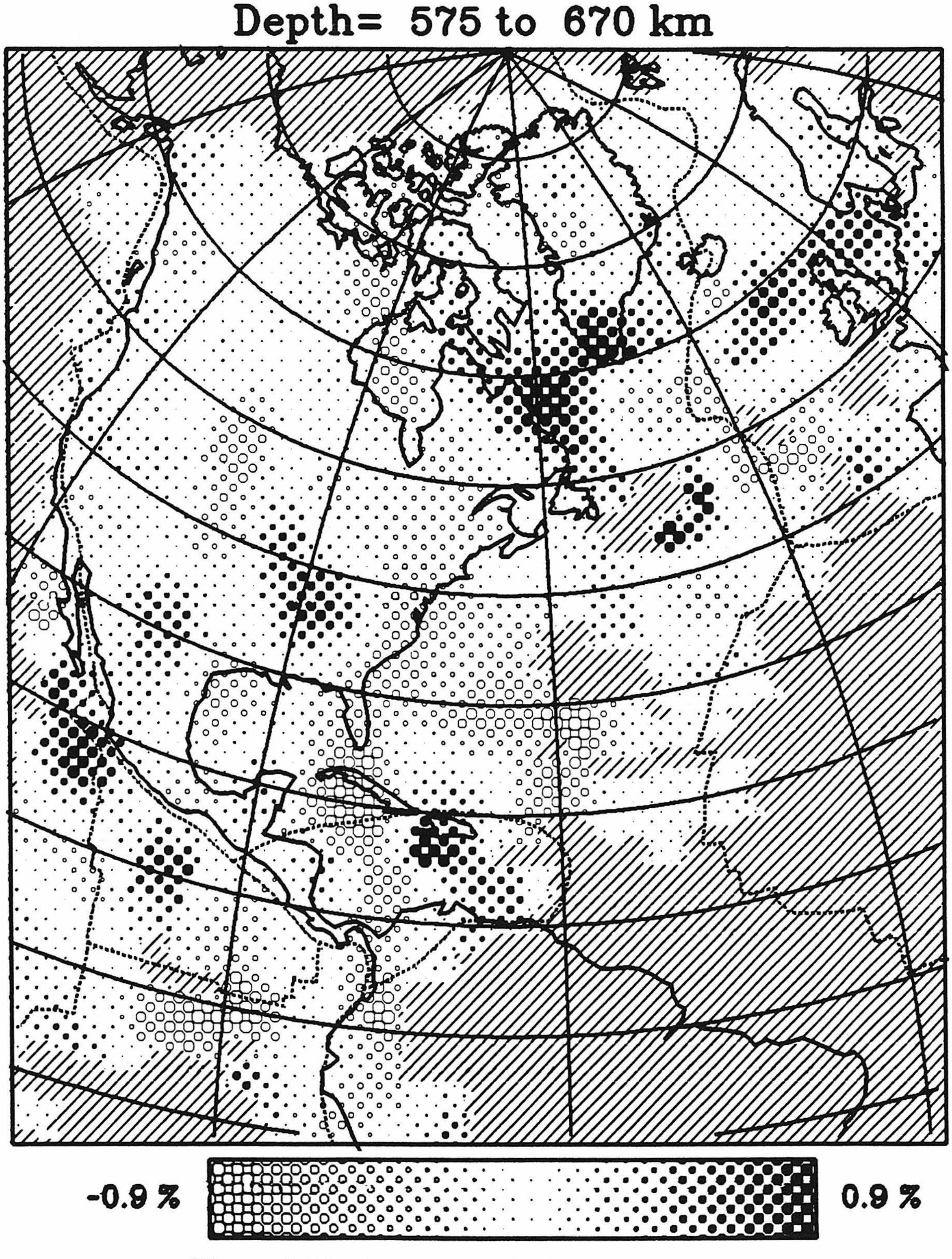

Figure 3.17g Inversion results from 575 to 670 km depth.

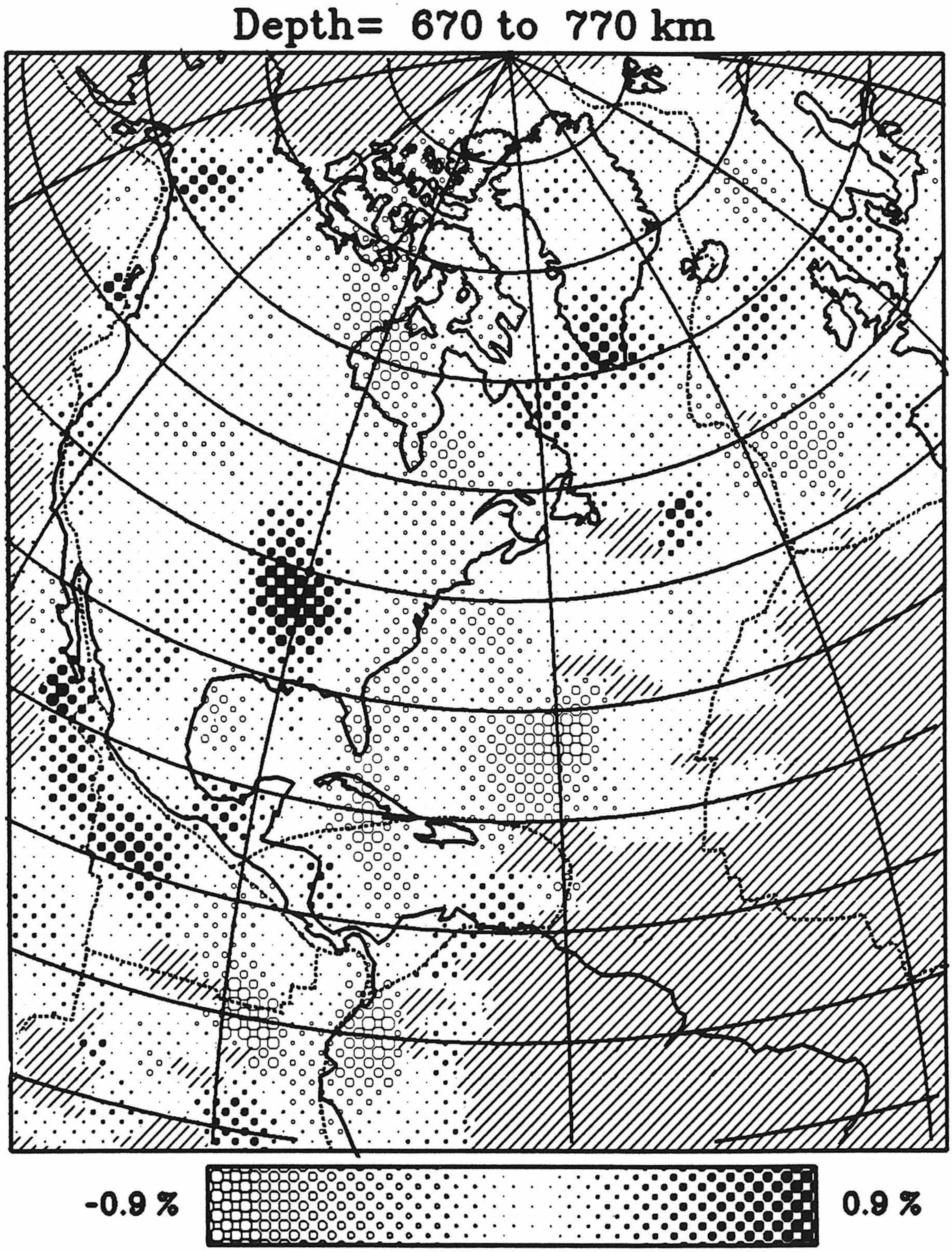

Figure 3.17h Inversion results from 670 to 770 km depth.

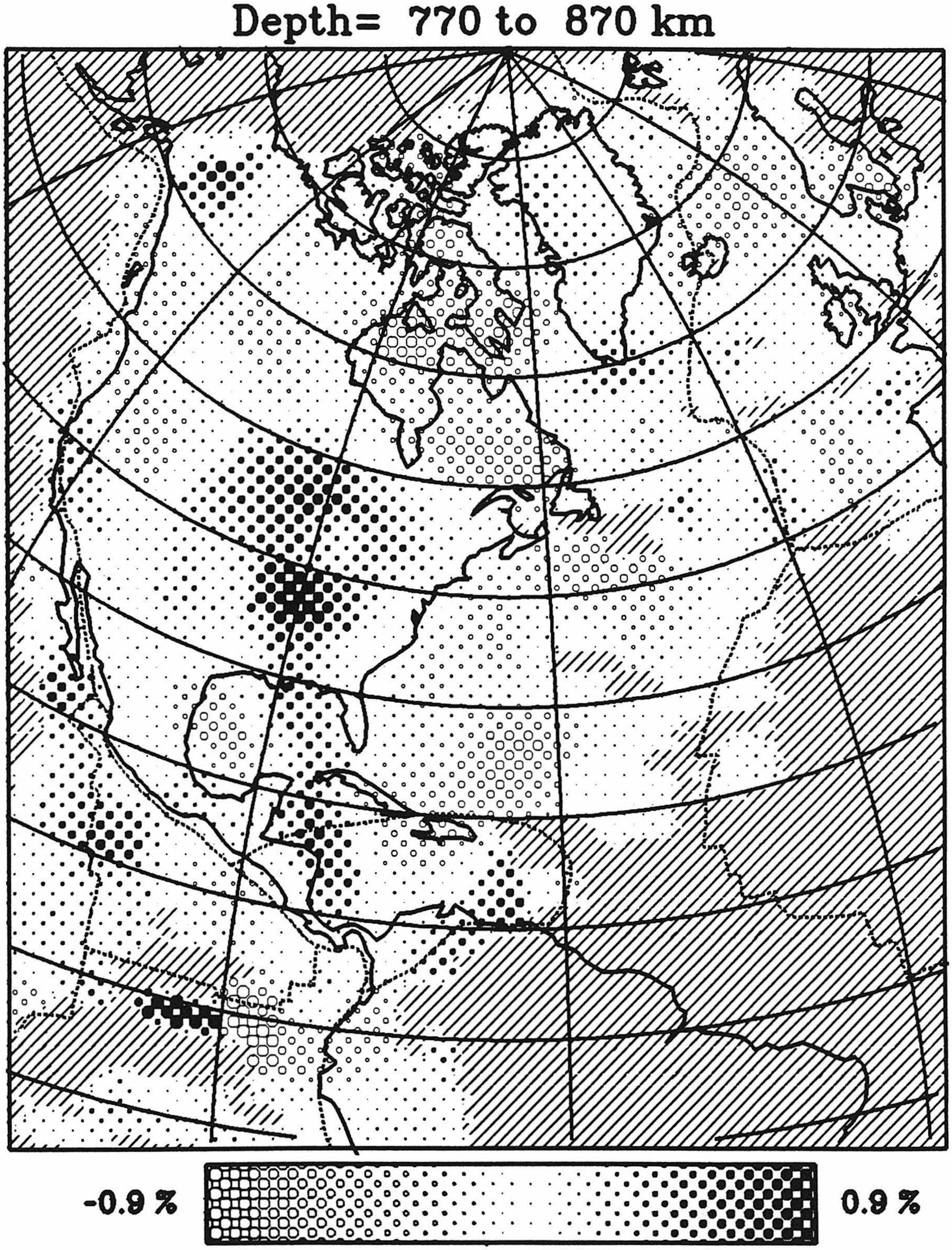

Figure 3.17i Inversion results from 770 to 870 km depth.

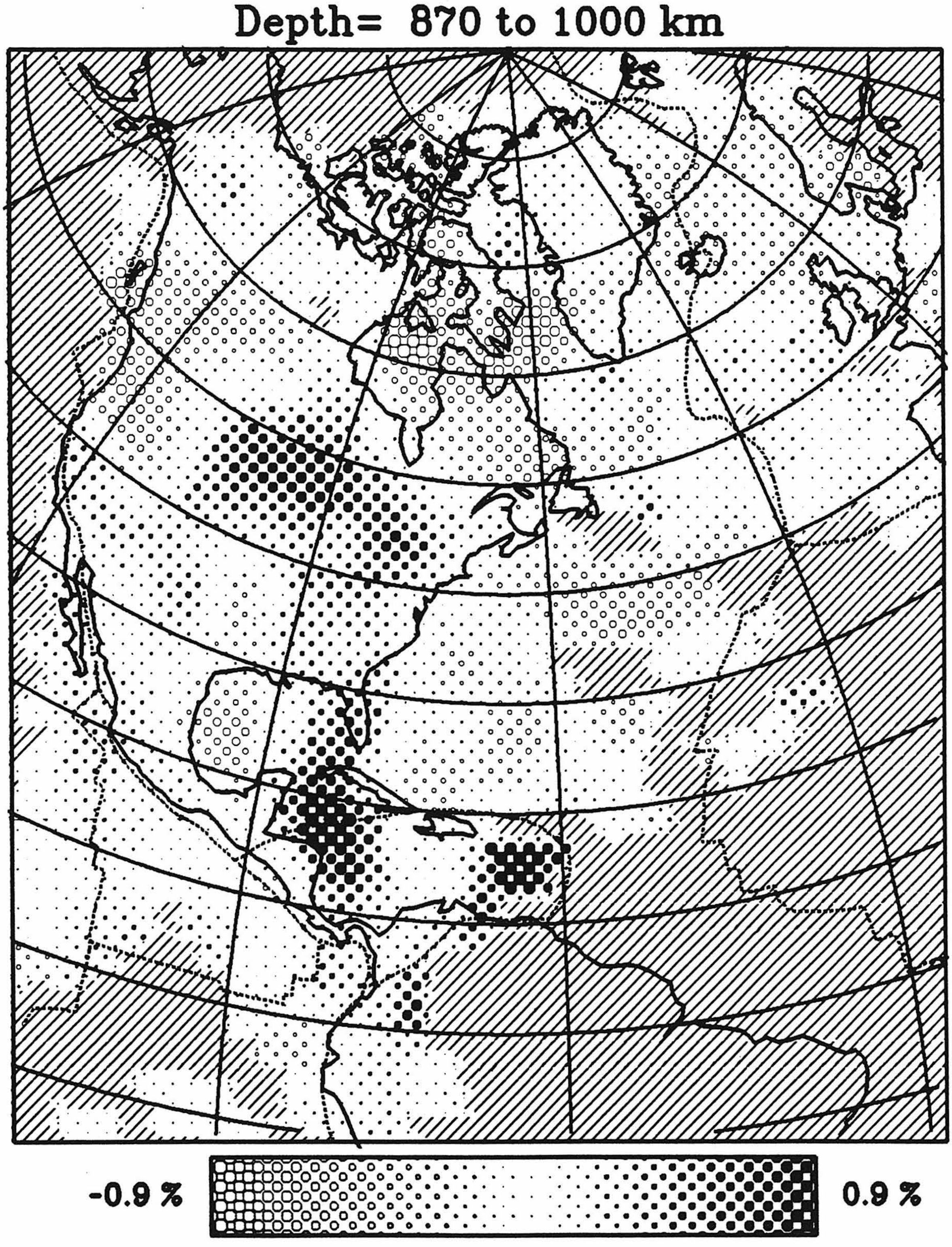

Figure 3.17j Inversion results from 870 to 1000 km depth.

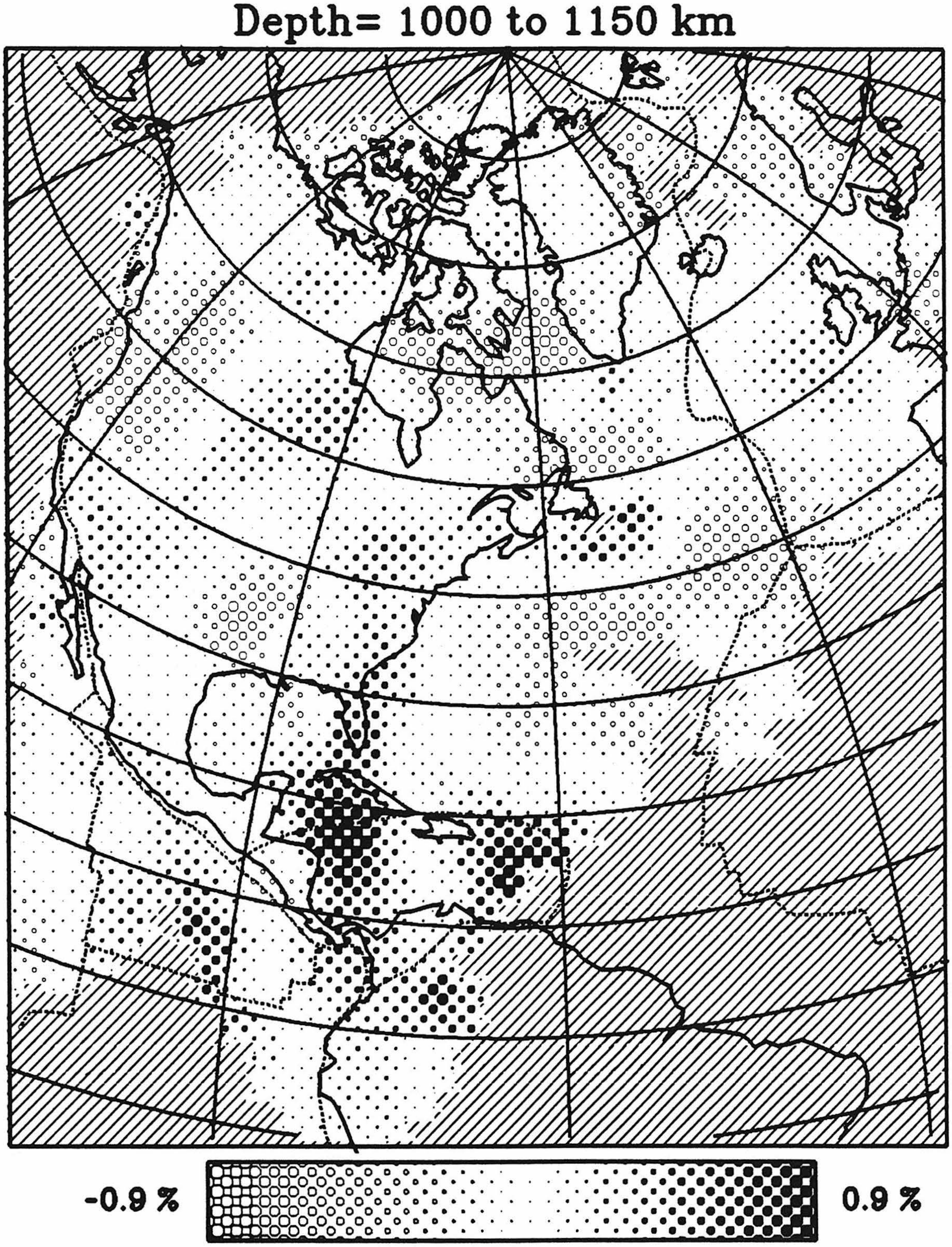

Figure 3.17k Inversion results from 1000 to 1150 km depth.

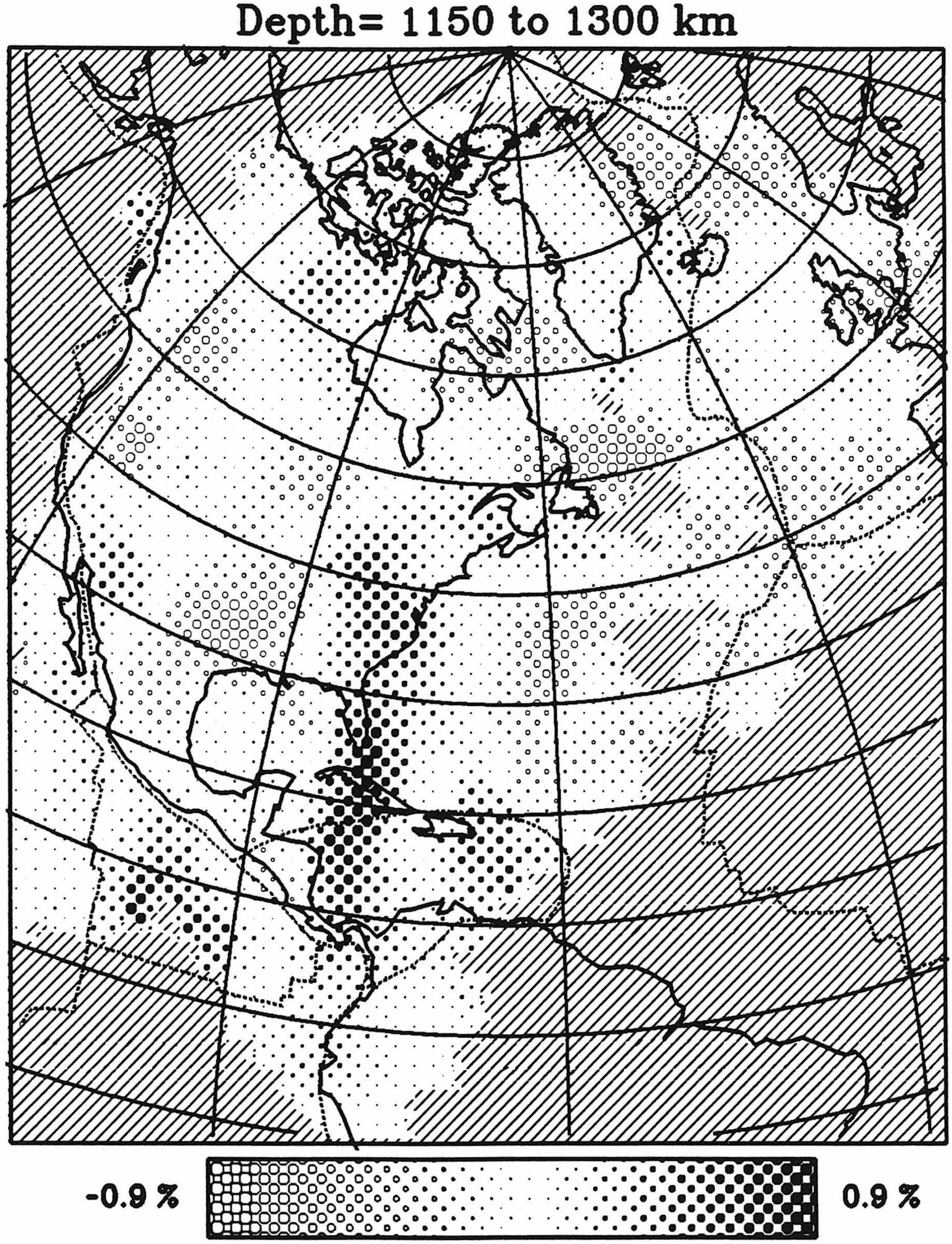

Figure 3.171 Inversion results from 1150 to 1300 km depth.

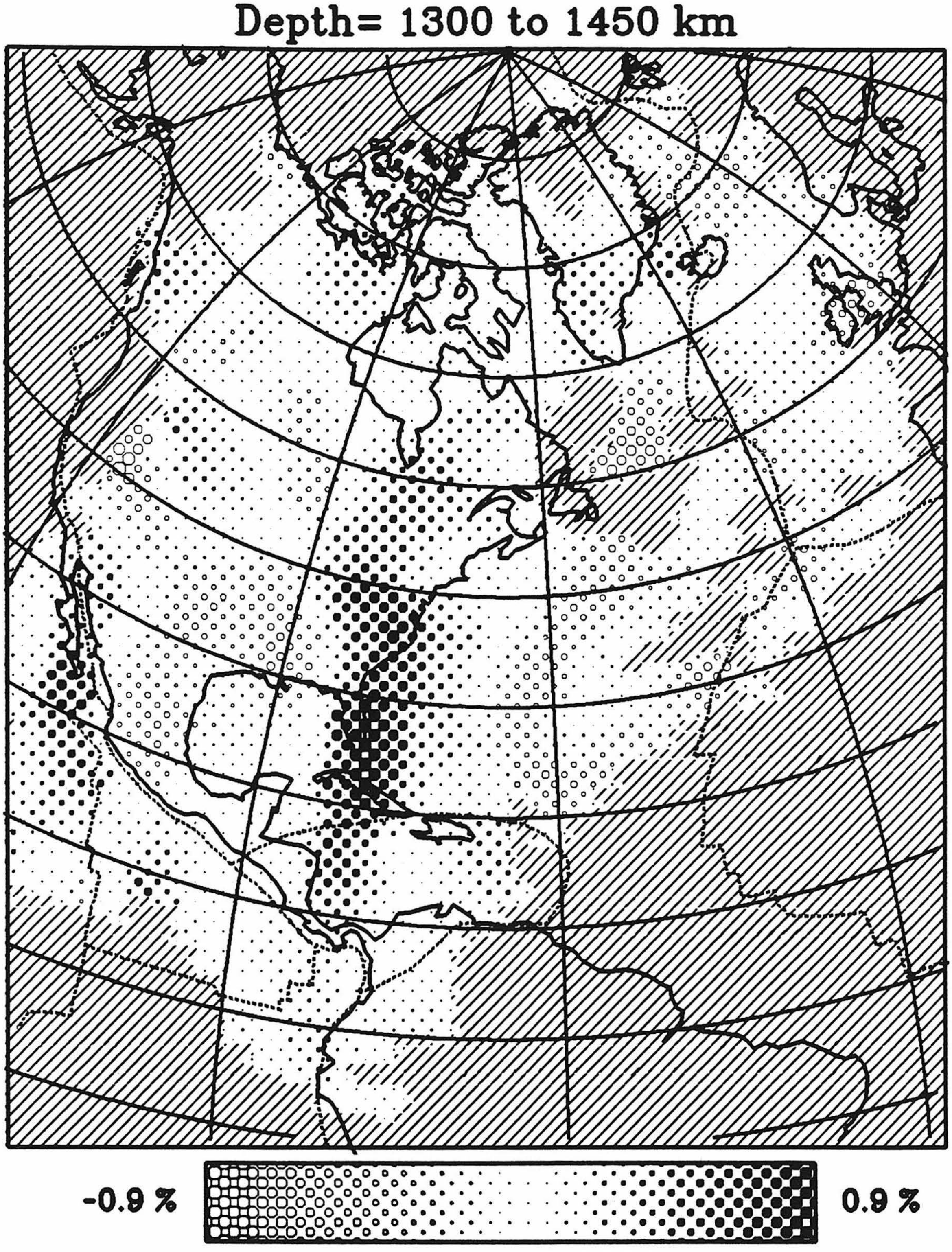

Figure 3.17m Inversion results from 1300 to 1450 km depth.

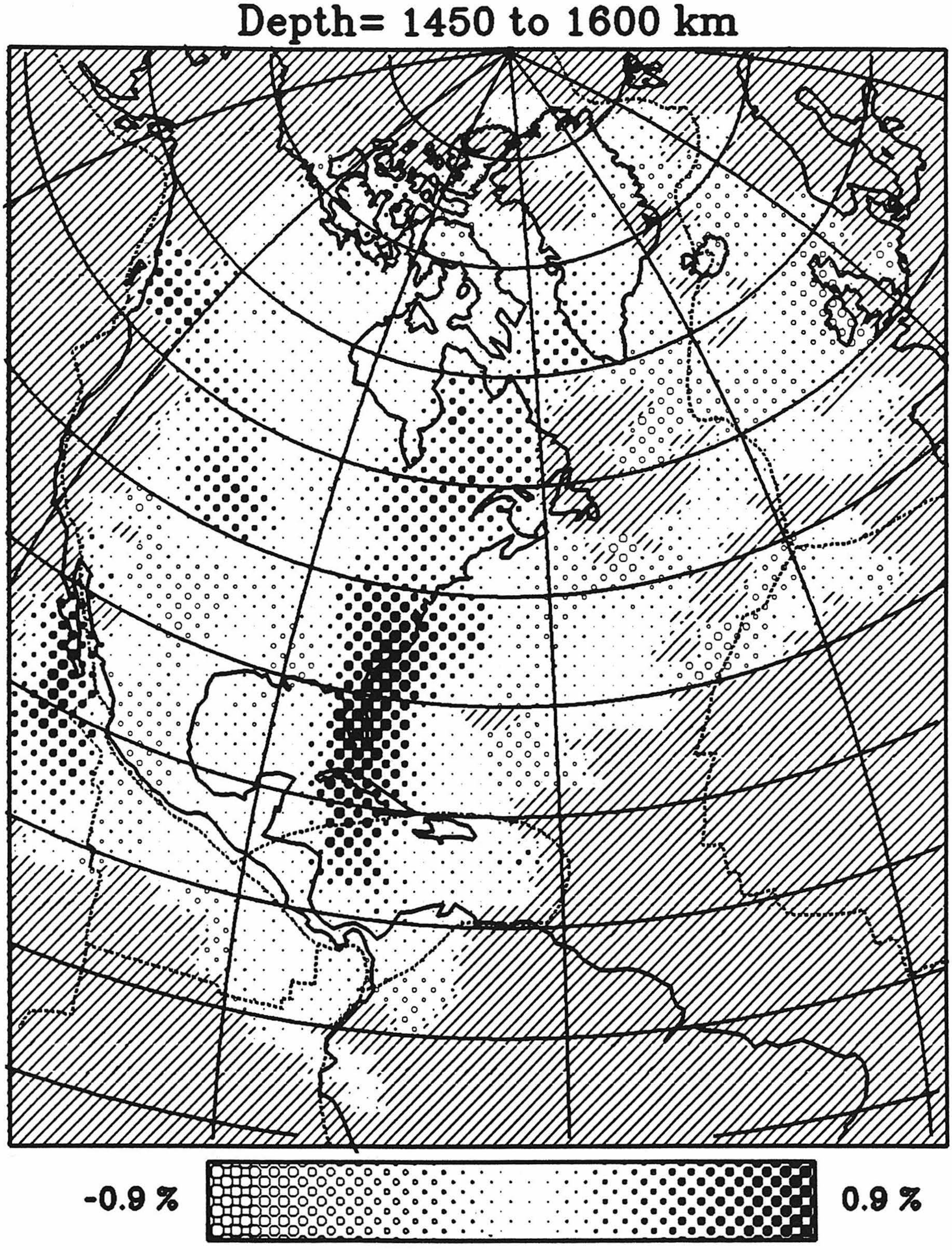

Figure 3.17n Inversion results from 1450 to 1600 km depth.

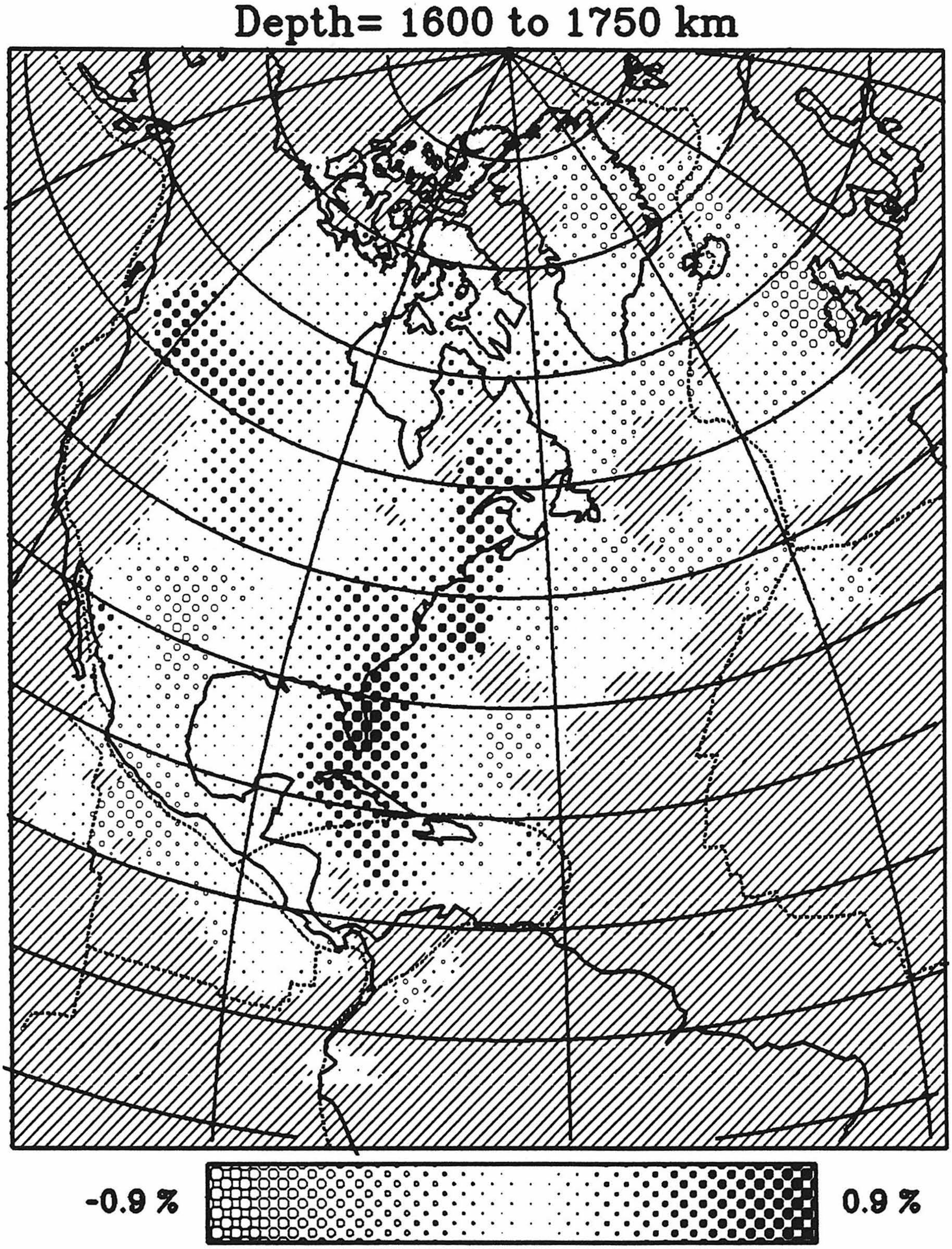

Figure 3.17o Inversion results from 1600 to 1750 km depth.

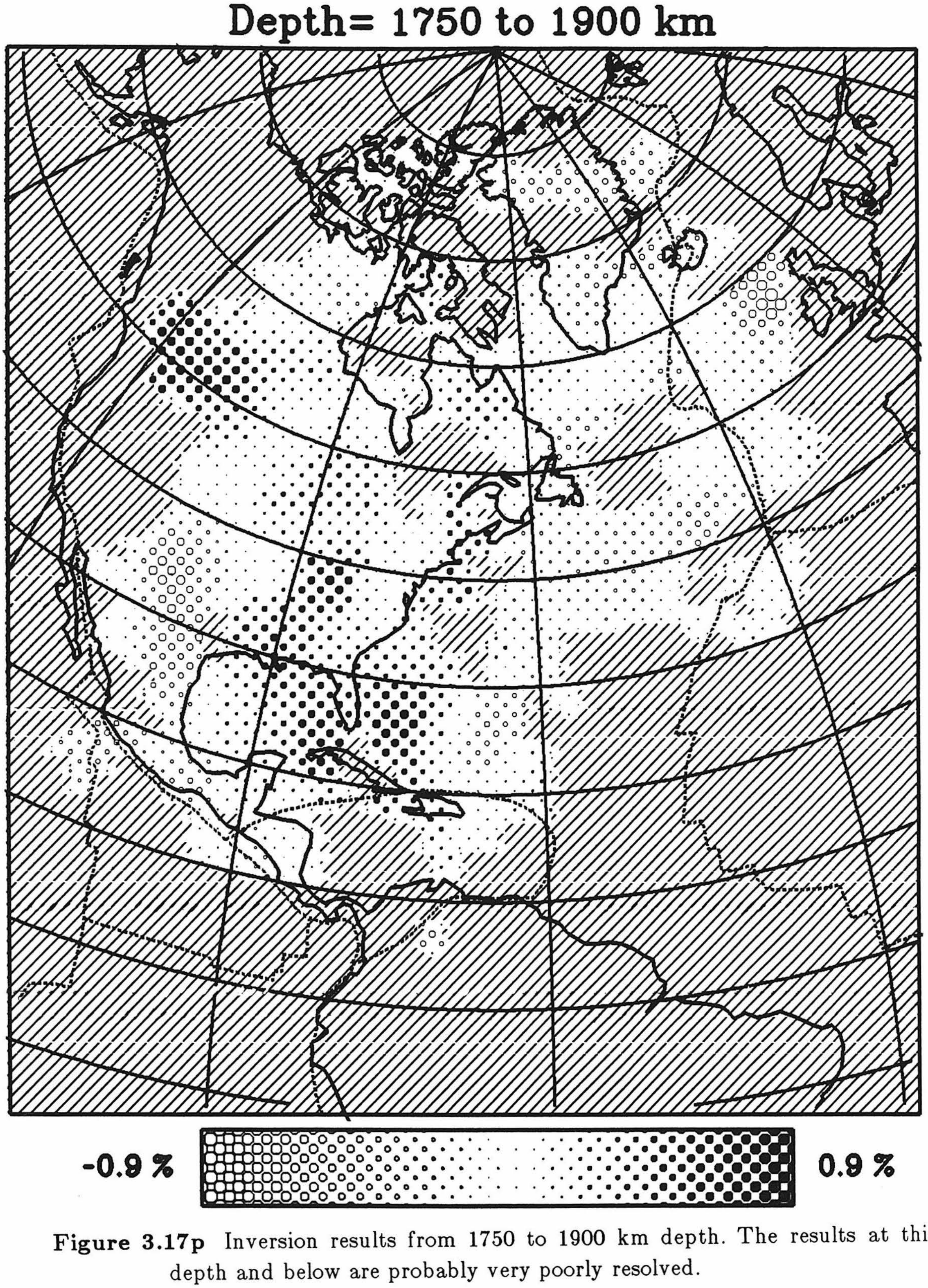

Figure 3.17p Inversion results from 1750 to 1900 km depth. The results at this depth and below are probably very poorly resolved.

crustal ages younger than 50 Ma. Finally, note that all the oceanic regions with crust less than 20 Ma have velocities of 4.4 km/sec or less, including most of the Mid Atlantic Ridge. The recently active continental regions, such as the basin and range, also have very slow shallow mantle velocities. The transition from slow to fast shallow mantle velocities seems to be extremely sharp with the intermediate transition zone between the two probably due to the smoothing applied to the model. The top layer has a thickness of 140 km and obviously the velocity could vary considerably within that depth range, particularly in intermediate to young oceanic areas. The estimated velocity within this layer was derived mostly from Sn measurements and regional S phases and thus probably represents the highest velocities within the depth range. Thus, regions with thinner lids may have slightly lower velocities on average in the upper 140 km. This may cause some compensating decrease in velocity in the layers just below the top one.

The next three layers, from 140 to 405 km depth, show a fairly consistent correlation with the surface tectonics. From 140 to 235 km, very high velocities are seen in all regions of North America which have not undergone deformation since the beginning of the Paleozoic. The east coast of the United States and Greenland, which underwent deformation in the Appalachian orogeny, show about 3% lower velocities at these depths. All old ocean basins, including the Gulf of Mexico, also show velocities 3 to 4% slower than beneath stable continent. Note how slow the Mid Atlantic Ridge is and how similar it is to the East Pacific Rise and basin and range provinces. The velocities are about 6% slower beneath these active regions than beneath the stable continent. It is also interesting to see higher velocities east of the subduction zone off the coast of Oregon and Washington at these depths. Below 235 km the lateral variations decrease though the pattern remains similar to the pattern at shallow depths. From 235 to 405 km, the Superior and Churchill provinces of the Canadian shield are clearly still very fast relative to every other location. See Fig. 3.18, taken from Stearn et al., 1979, for the location of the provinces and their ages. The Superior and Churchill provinces have not undergone deformation for 1800 Ma. The Grenville and Central provinces are also fast to about 400 km but are between 1 and 2% slower than the older provinces. Throughout these depths, the young East Pacific, the basin and range and the youngest portions of the Atlantic are all very slow. The older oceanic basins seem to be 1 to 2% faster than the youngest ocean from 235 to 400 km, implying hotter than normal mantle to 400 km depth beneath active spreading zones. This contradicts the results of Chapter 2 in that we found similar velocities from 250 to 350 km beneath the Atlantic and East Pacific. The 1 to 2% variations found in this chapter may be within the uncertainty of the resolution in the Atlantic where the coverage is weakest.

The transition zone, from 405 to 670 km depth, shows a completely different pattern than the upper 400 km of the model. Generally, the lateral heterogeneity has decreased by about a factor of 5. Also, the anomalies present are very localized, in many cases representing single blocks. The largest feature seems to be a slighltly slow region throughout the western Atlantic. It should be kept in mind that rays bottoming in the transition zone are almost never first arrivals and at many distances are interfering with other arrivals. Thus, these rays probably have the largest uncertainties associated with them. The random noise inversion results shown in Figs. 3.14b-d resemble somewhat the type of lateral variations observed in the transition zone and it is felt that perhaps most of the patterns visible here are not real. What is

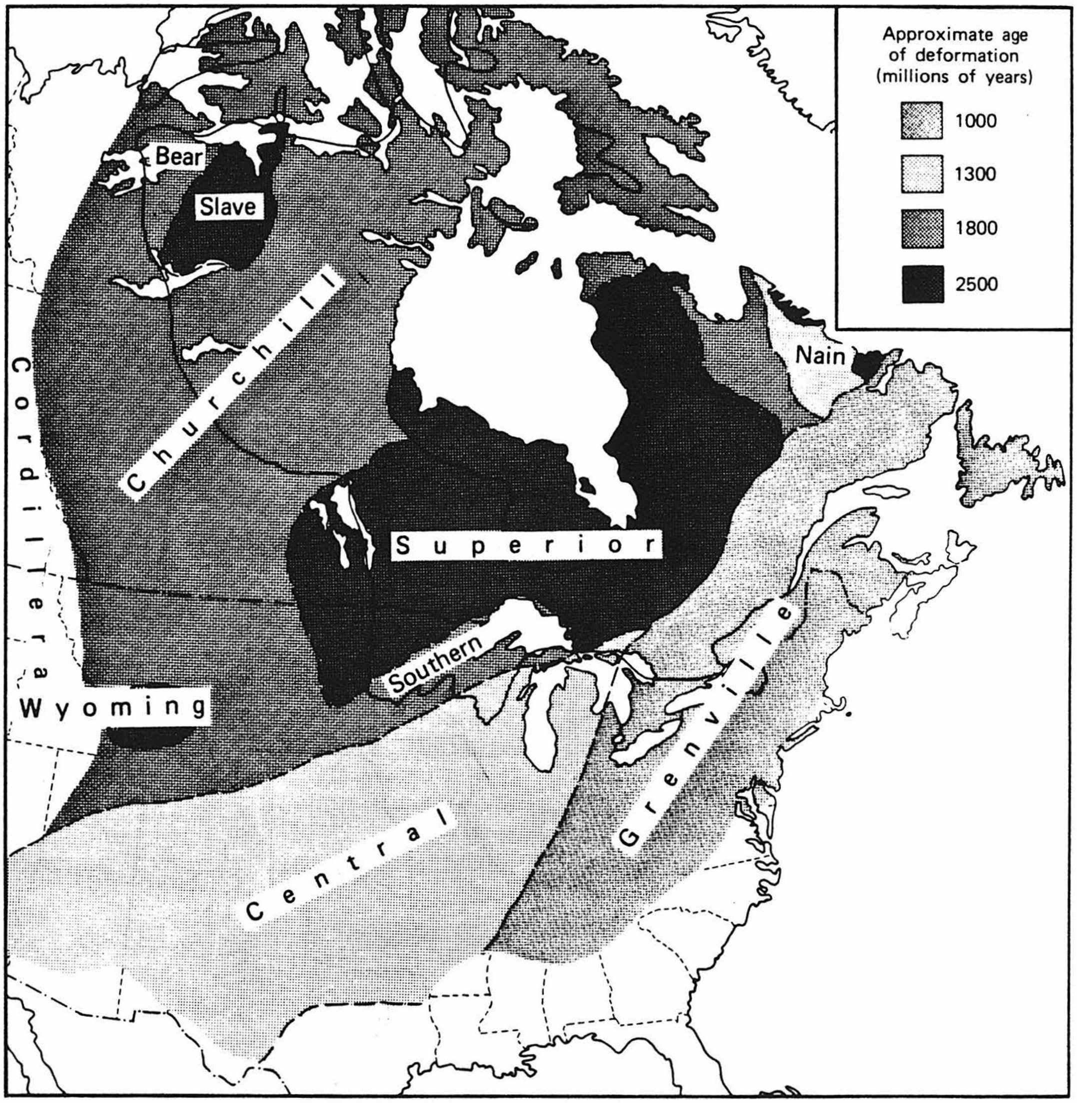

Figure 3.18 Tectonic provinces of precambrian North America with the approximate age of the last deformation episode for each province, taken from Stearn et al., 1979.

important is that the lateral heterogeneity drops considerably below 400 km depth and that the heterogeneity observed is not correlated with any particular tectonic province. Also, there is no large scale anomaly with an amplitude larger than 1% throughout the transition zone anywhere in the model space. In spite of the noise present, such a feature would be detectable.

The lower mantle should be better constrained than the transition zone since arrivals from below 700 km depth are generally uncontaminated by other phases. Still, the eight horizontal slices of the lower mantle (Figs. 3.17h-p) show considerable heterogeneity. As in the transition zone, many localized volumes (in depth as well as laterally) with anomalous velocities are apparent. For example, the high velocities under the East Pacific Rise from 670 to 870 km are gone from 870 to 1300 km depth. Also, though the anomaly is visible, it is only about .5% in amplitude and its dimensions are such that it would produce a maximum of .7 sec travel-time difference for a ray traveling directly through it. Thus, as with the transition zone, many of the localized anomalies seen in the lower mantle panels are probably not real. Unlike the transition zone, however, there is a large scale feature continuous laterally over 3000 km and vertically over about 1000 km with a large amplitude. Notice in the western Caribbean a thin high velocity zone from 670 to 870 km depth. Increasing in depth, the anomaly is present with a slight eastward drift to 1700 km depth. This anomaly is present north of the Caribbean as well with an increasing eastward drift with depth. From 20° to 30° latitude, the high velocity goes from about 85° W at 800 km depth to east of Florida at 1600 km depth. Between 30° and 40° latitude the anomaly extends from about 95° W at 800 km depth to about 75° W at greater depths. From 40° to 50°, the high velocity region is very broad in the north central United

States from about 700 to 1000 km depth. At the same latitude a deep extension from 1000 to 1600 km can be seen beneath the north eastern states, though with lower amplitude than to the south. It should be pointed out that this region was well resolved in the resolution test runs (Figs. 3.13a-g). Another feature of the lower mantle seems to be generally slow velocities to 1700 km depth throughout the Atlantic and eastern Canada.

The results of the inversion discussed above can also be seen in cross sections. Fig. 3.19 shows the location of 5 cross sections through the model space and Figs. 3.20a-e show those sections. The sections have 3 to 1 vertical exaggeration and the velocity scale varies with depth in the same way as the planar sections did. The first cross section, Fig. 3.20a, is through the Canadian shield and Iceland. The high velocity deep root beneath the Superior and Churchill provinces of the shield is obvious. Iceland is seen to be very slow to about 300 km depth with no obvious root deeper in the mantle. The section through Europe is fast on average in the upper mantle but shows no distinct pattern. The resolution there is very poor and perhaps some shallow high velocities in the region are being spread throughout the upper mantle. Notice the lower mantle has no distinct large scale features but is on average slow throughout the section, particularly beneath eastern Canada.

The next four sections are meant primarily to illustrate the high velocity anomaly seen in the lower mantle. Fig. 3.20b shows a large flat anomaly from about 770 to 1000 km depth beneath central North America with a vertical extension at the eastern end of it to the bottom of the model. Note also the growth of a continental root towards the center of North America. This crosses the central province and is not as large as the root beneath the northern shield provinces. A thinner high

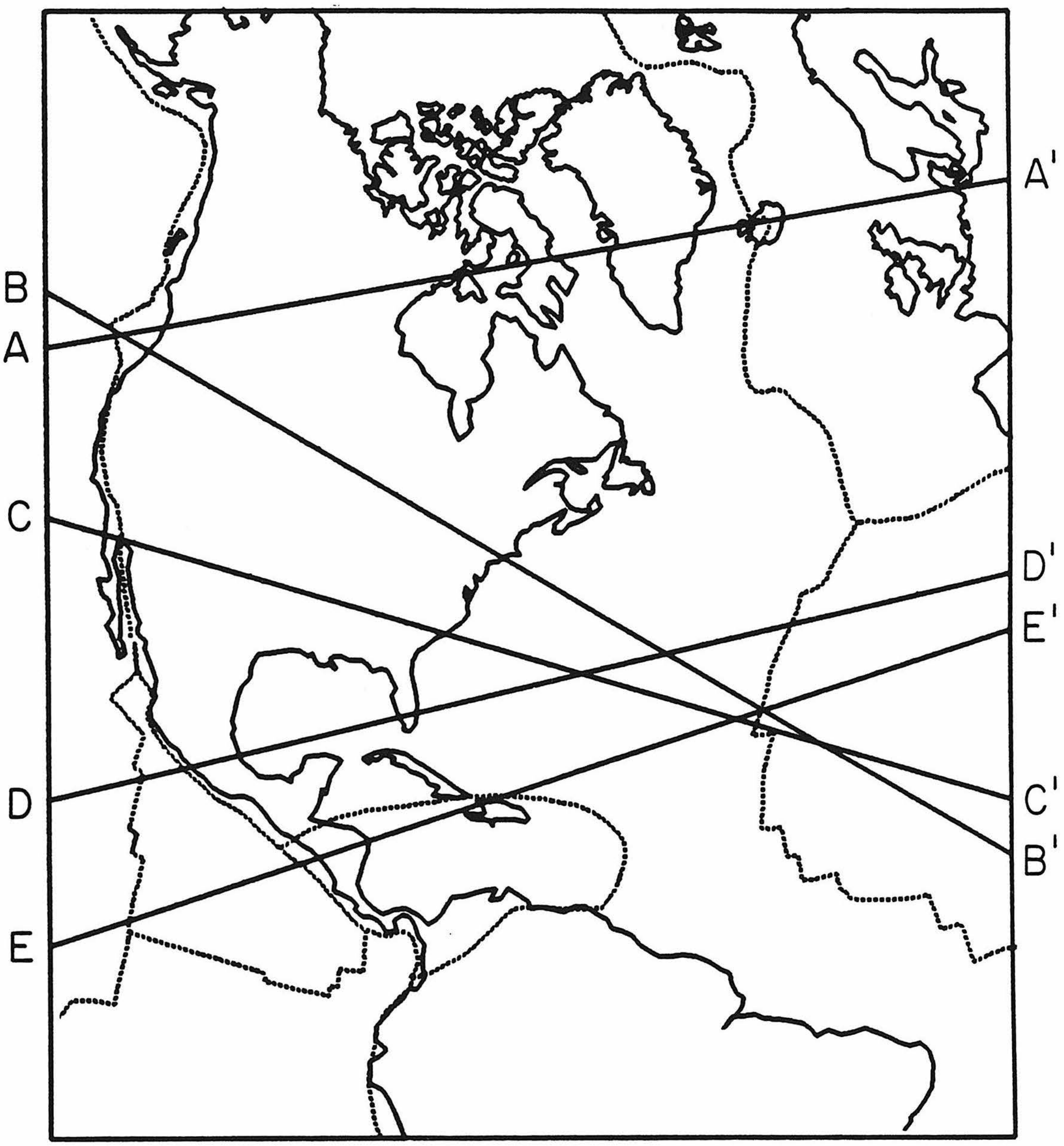

Figure 3.19 Location of five cross sections through the final model. The profiles along these sections are shown in the next figures.

Figure 3.20a Cross section A-A' from the previous figure. The scale varies with depth from +3% to -3% above 320 km, +1.5% to -1.5% from 320 to 405 km and from +.9% to -.9% below 405 km. The lateral location can be found by comparing the shallow variations in this figure with the planar section shown in Fig. 3.17a. For example, the very slow shallow velocities to the right of this figure are directly beneath Iceland.

Figure 3.20b Cross section B-B' of Fig. 3.19.

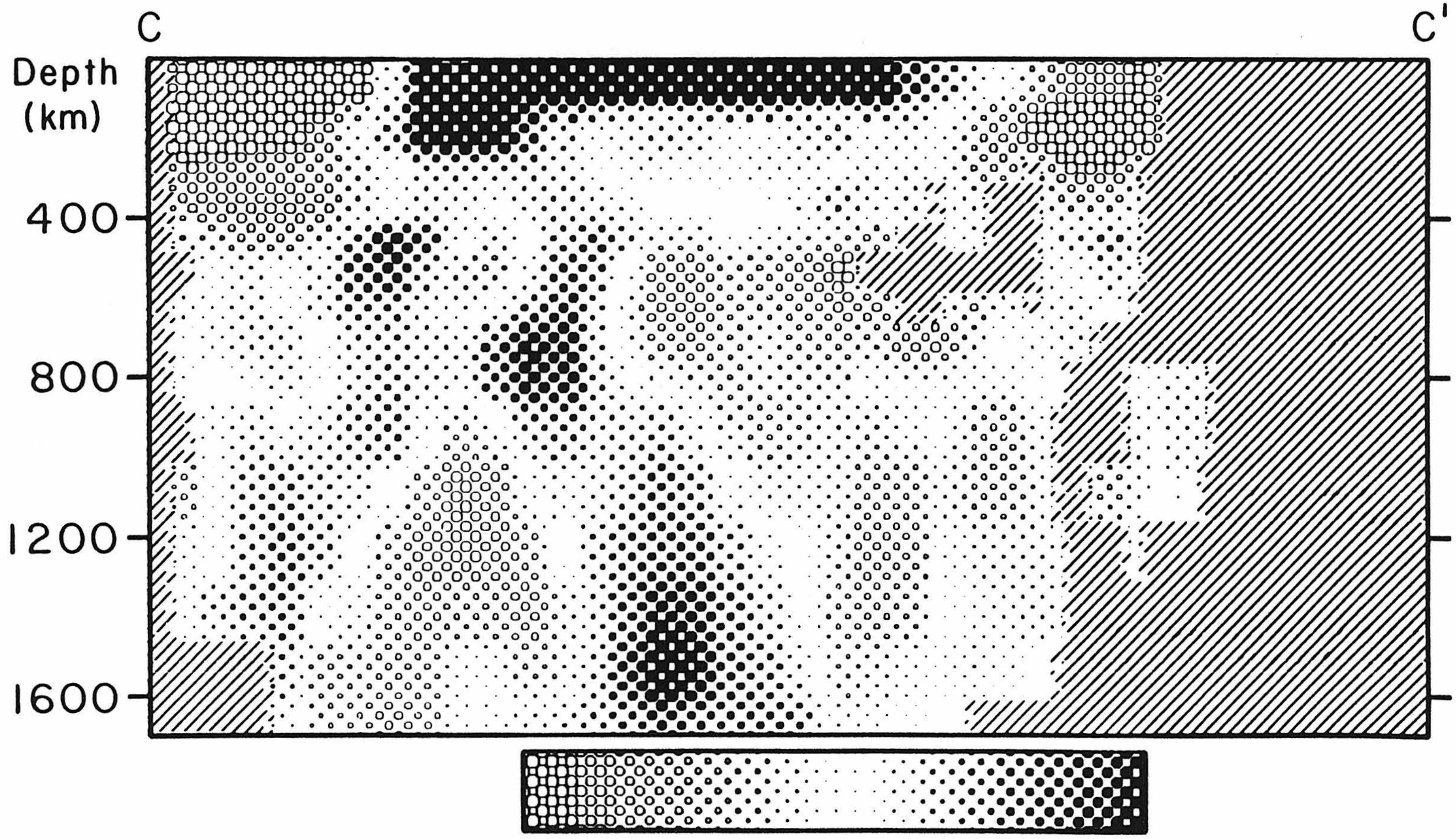

Figure 3.20c Cross section C-C' of Fig. 3.19.

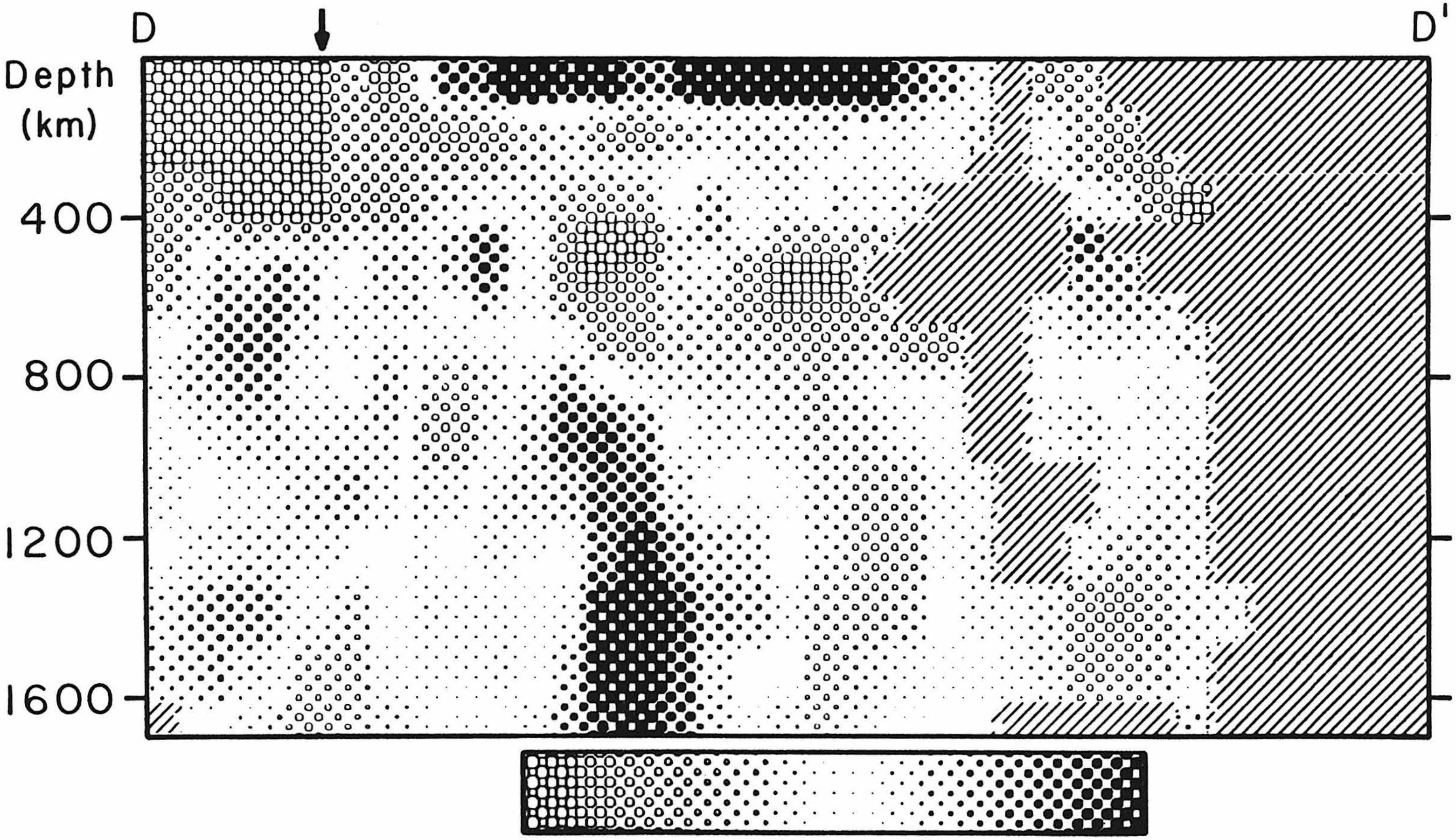

Figure 3.20d Cross section D-D' of Fig. 3.19. The arrow indicates the position of the trench off Mexico.

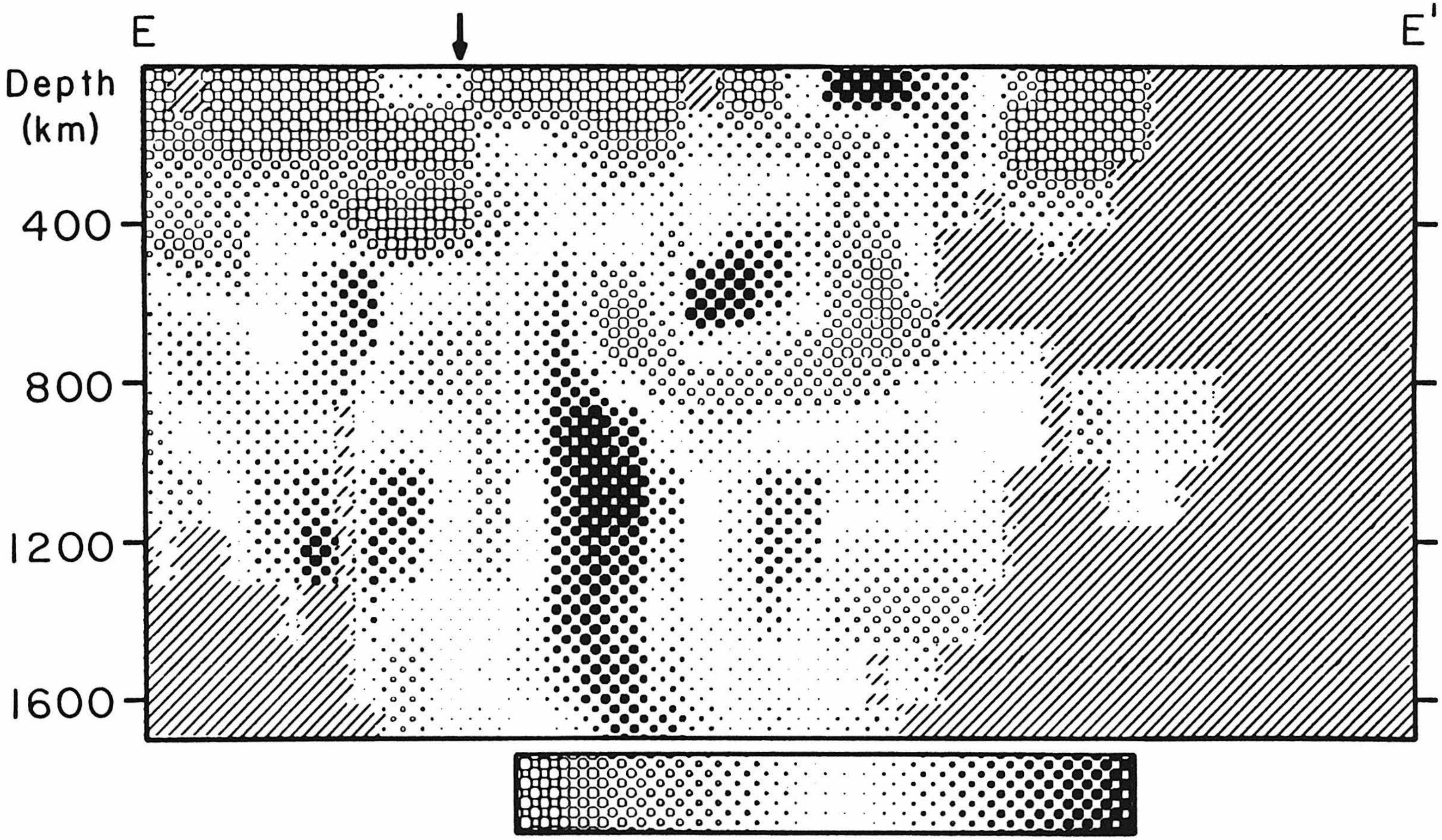

Figure 3.20e Cross section E-E' of Fig. 3.19. The arrow indicates the position of the trench near Central America.

velocity lithosphere can be seen extending over the east coast of North America into the Atlantic. The next section south, Fig. 3.20c, shows the same lower mantle anomaly but it descends more rapidly into the mantle than the previous figure showed. It is also very diffuse, especially near 1700 km depth, but it must be kept in mind that even the synthetic inversion tended to blur input images, particularly at the deeper levels. Note that this section through the southern United States shows no real continental root below 200 km depth. The following section, Fig. 3.20d, passes through the southern part of the Gulf of Mexico. A thin high velocity layer near the surface is present from the Gulf through the Atlantic but there is generally slow mantle from 140 km to 400 km depth along the whole profile. The location of the present day subduction zone is indicated by an arrow on the section. There is slightly faster velocity material dipping beneath the subduction zone, relative to the surrounding mantle, but there is no clear indication of the subducting plate. The subducted oceanic lithosphere is very young here and therefore thin and hot. This may be the reason nothing obvious is present in the inversion. Below 400 km depth, the high velocity lower mantle anomaly is very clear. Note how it is far more vertical than in the sections to the north. Finally, the last section, Fig. 3.20e, is through Central America and the Carribean. Again, the position of the trench is indicated by an arrow at the top of the figure. From the trench to 1700 km depth, faster than normal mantle can be traced easily. From below 600 km depth, the anomaly is almost vertical.

From the experience gained in doing the synthetic inversion, Figs. 3.13a-g, it is felt that the lower mantle anomaly discussed above is real. No structure in the inversion of noise was as continuous or of such large amplitude as this feature. The amplitude of the anomaly is found to be .7 to 1% but due to the known blurring found in this region (Figs. 3.13e-g), the real structure could well be more narrow and of larger contrast, probably about 2%. Unlike any other structure seen in the lower mantle, this anomaly can cause very large travel-time differences for certain raypaths. Particularly from events south of the Carribean to stations in eastern Canada, 5 to 7 sec travel-time anomalies can be produced. In fact, these very fast times are observed in the data consistently for such paths. Most of the events there are on fracture zones and should be free of any contamination due to near source heterogeneities. It is especially reassuring that independant investigators have observed at least part of this structure in the past. Jordan and Lynn (1974) found high velocities below the western Carribean from 600 to 1400 km depth using P and PcP as well as S and ScS waves from deep events beneath Peru. Lay (1983) found clear evidence for the same anomaly using S and ScS times from deep events beneath Bolivia and Argentina. Except for about 20 S times from a deep event beneath Peru, none of the data used in the above mentioned studies were used in this study. The extension of the anomaly northward would be undetectable in the previous studies due to the event-station geometries. Dziewonski's (1984) study of lower mantle P velocity does not show this feature of our model but he presents only a very long wavelength model. A narrow feature, such as described above, would probably not be apparent in a spherical harmonic expansion of mantle velocities to only l=6.

The interpretation of the results of this experiment is difficult, especially when it is not known exactly what features are due to noise and error and which are real. There seem to be two structures in the model which are robust, i.e., they are large scale with significant amplitude such as to cause large travel-time anomalies. First, the velocity of the upper 400 km of the mantle seems to correlate well with the tectonic history at the surface. There is a progression even within the shield from very deep, high velocity roots beneath the oldest shield provinces to less deep, slower roots beneath the younger provinces. The parts of North America affected by the Appalachian folding events have significantly lower velocities from 200 to 400 km depth than the more stable continental parts of North America. All oceanic areas appear much slower from 150 to 400 km depth than any of the stable parts of the continent. The low velocities found from 150 to 320 km depth imply that there must be very high gradients in this depth range similar to those seen in models SNA and TNA. Anderson and Bass (1984) have shown that such high gradients can only be produced by a nonelastic process. Either partial melting (Spetzler and Anderson, 1968; Anderson and Spetzler, 1970) or a dislocation relaxation process (Minster and Anderson, 1980) must be causing the low velocities at these depths. Both processes are temperature controlled and thus we conclude the thermal gradients below the Canadian shield must be lower to about 350 km depth than beneath the surrounding oceanic and active continental regions. Chapman and Pollack (1977) derived mantle thermal models from heat flow data for continents and oceans. They conclude that stable continental regions are cooler than oceanic regions and continental orogenic zones to below 300 km depth. The North America model developed here tends to support their conclusions. Jordan (1981a) has suggested that shields have chemically distinct roots to great depths in the mantle. Our results for North America certainly do not contradict his model but do not prove it either.

The second large feature in the results seems unconnected to the upper mantle. The high velocity ridge from about 10° N to 50° N is probably a real phenomena. It crosses several tectonic provinces and does not seem to be related to any present day processes at the surface of the earth. A possible explanation for the anomaly is that it is related to the past subduction of the Farallon plate. Fig. 3.21 shows the position of the subduction zones off the coast of North America 120 Ma relative to the hotspot reference frame. The present day geoid and continents are also shown. The figure is a modification of one given by Chase and Sprowl (1983) in which they find a correlation of present day geoid lows and the position of subduction zones about 120 Ma. Notice that the position of the fast anomaly below 1500 km depth (Figs. 3.17n-p) lies at the western edge of the subduction zones shown in Fig. 3.21. Notice also, that at Carribean latitudes there must have been subduction at about the same location for the last 120 Ma as the present day subduction zone is not far from the subduction zone at those latitudes shown in Fig. 3.21. Further to the north, the subduction zones must have migrated far to the west in the last 120 Ma as the coast line is now over 3000 km from the ancient subduction zone shown above.

Engebretson et al. (1984) discuss in more detail the relative and absolute plate motions of the Farallon and North American plates. They show a similar position for the subduction zones about 120 Ma and give a further description of the changes from then to present. They show a shift in the coast line westward of about 700 km at 10° N from about 120 Ma to 50 Ma. At 40° N the shift was about 2600 km over the same time period. Furthermore, they state that the Farallon plate was older than 100 m.y. prior to 75 Ma and dropped in age to about 40 m.y. old about 50 Ma at 40° latitude. Further to the south, the subducting plate was probably older than to the north during that period. The decrease in age of the subducting plate may be the reason the anomaly we see seems stronger at greater depths than it does above 800 km. It is also interesting to note that the Laramide thrusting (from 75 Ma to 40 Ma)

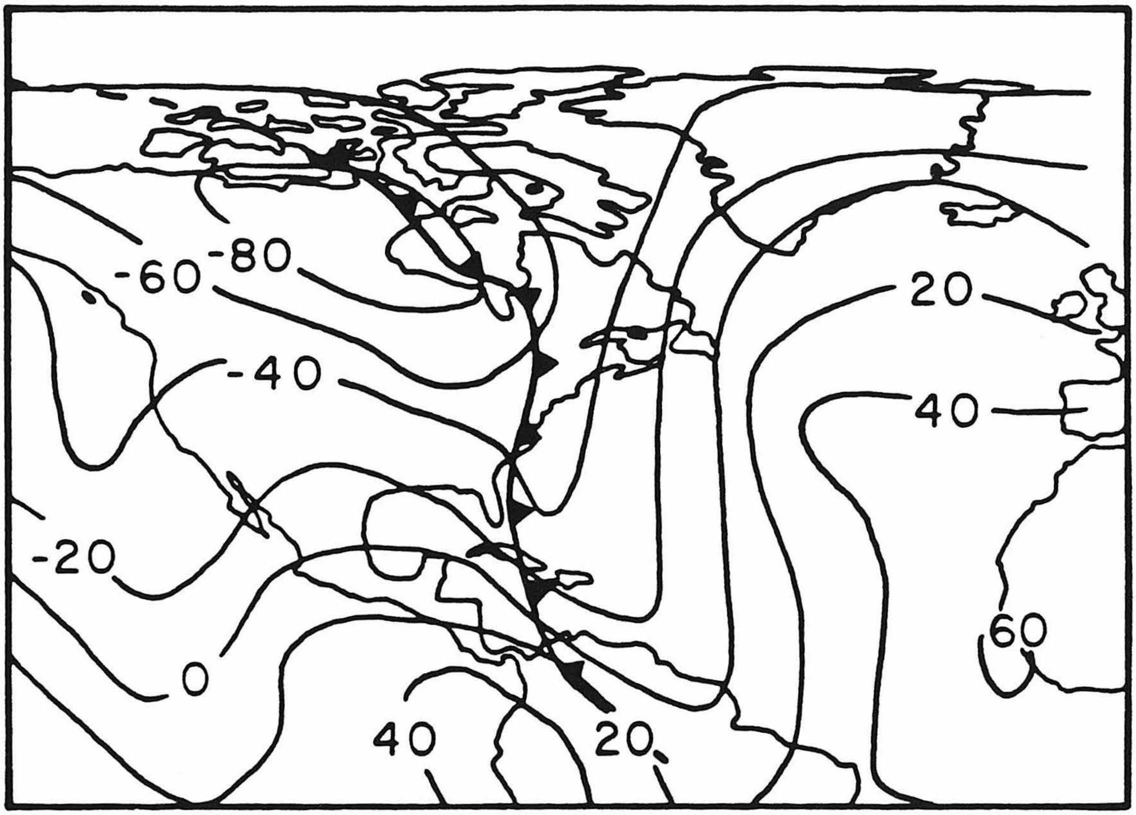

Figure 3.21 Position of subduction zones (heavy line with back arrows) 120 Ma in the hotspot reference frame relative to the present continental configuration (taken from Chase and Sprowl, 1983). Note that the position of the old subduction zone is at the eastern edge of the high velocity anomaly below 1500 km depth, Figs. 3.17n-o.

is thought to be due to the slab flattening and underthrusting the western United States to about the state of Wyoming (Dickenson and Snyder, 1978). Engebretson et al. (1984) attribute this to an increase in the convergence rate of the Farallon and North American plates during this time. Bird (1984) shows how the hingeline, where the slab dips steeply, advanced eastward during the Laramide but then rapidly retreated from 55 Ma to 35 Ma back to the coastline. He also states that the flat slab probably sank rapidly at some point, possibly during the rapid regression of the hingeline. The posulated position of the flat slab during the Laramide in the hotspot reference frame, agrees well with the position of the broad flat zone of high velocity between 750 to 1000 km depth beneath the north central United States (see Figs. 3.17i-k and Fig. 3.20b).

Thus, a possible explanation for the deep high velocity structure from the Carribean to the northern United States, is that this structure represents a cold thermal anomaly due to a remnant of the subducted Farallon plate. The approximate velocity contrast of 2% implies a $200^o C$ to $300^o C$ thermal anomaly. This assumes the ratio of velocity change to temperature change is -.0005 km/sec/C^o as derived by Creager and Jordan (1984). Their value is for P velocity but Jordan and Lynn (1974) found the velocity anomaly beneath the Carribean to be the same for both P and S. Schubert et al. (1975) predict temperature anomalies of about $500^o C$ over a 100 km width for slabs penetrating to 800 km depth. The anomaly described above implies a smaller contrast in temperature over a larger region. The integrated thermal anomaly observed, however, is of the same order as Schubert et al. (1975) predict and Creager and Jordan (1984) have measured. If one assumes the slab becomes anchored to the lower mantle upon contact with it (as suggested by Uyeda and Kanamori, 1979) the lower mantle high velocity regions can be associated with past periods of subduction. The deeper part of the anomaly, from 1150 to 1600 km depth, coincides with subduction processes from about 80 to 120 Ma. From 40 to 80 Ma, there was increased convergence and flattening of the slab occuring in the western United States north of about 30° N. The broad high velocity area in the north central United States may be the remains of the slab subducted during that time period. Further to the south, where subduction was more regular, the lower mantle anomaly is also more uniform with a slight westward drift with decreasing depth. From 40 Ma to present, the subduction along the western margin of North America has been of oceanic lithosphere younger than 40 Ma. The subducting plate was therefore thinner and hotter and perhaps has not left a large thermal anomaly in the mantle. There is very little high velocity material in the lower mantle north of 50° N. At these latitudes , the convergence after 80 Ma was between North America and the Kula plate (Engebretson et al. 1986). The Kula plate had a more northward trajectory than the Farallon plate and its age to the north of 50° N was less than that of the Farallon plate further to the south (Engebretson et al. 1986). For this reason, perhaps, there was much less consumption of old oceanic lithosphere beneath Canada in the hotspot reference frame during the last 100 Ma.

The above discussion is of course highly speculative and much more work needs to be done on the seismic structure of the mantle as well as a more detailed description of past subduction histories. If the arguments are qualitatively correct, however, they have important consequences for mantle dynamics. The most important implication is that old oceanic lithosphere is circulating in the lower mantle. Whether this is so has been a subject of great debate, see for example O'Connell (1977) and Richter

(1979). Recently, however, Creager and Jordan (1984) have presented strong evidence for penetration of the slab to about 1000 km depth beneath the Kuriles. They also claim the slab, even in the lower mantle, has about a 5% velocity anomaly associated with it. On the other hand, Giardini and Woodhouse (1984) have presented evidence for a shortening and thickening of slabs near the 660 km discontinuity beneath the Tonga subduction zone. They suggest this indicates a resistance to penetration of the slab below 670 km depth. In another recent work, Hager (1984) showed that the geoid highs over subduction zones can best be modeled by a continuous flow through the boundary near 670 km depth but with an increase in viscosity of the mantle at that depth of about a factor of 30. He also notes that if slabs are not penetrating the lower mantle, they must be piling up above the 670 km boundary to a height of 350 km over 2000 km horizontal lengths in order to statisfy the observed geoid. Certainly no evidence is seen for this anywhere beneath the North American plate in this study. The above studies qualitatively agree with the results presented here for the lower mantle. The convergence rate of the Farallon and North American plates is given by Engebretson et al. (1984) as 70 to 150 km/m.y. from 120 Ma to 30 Ma. At these rates, if the slabs fell through the whole mantle at a constant velocity, all slabs subducted before 23 Ma would now be below 1600 km depth and would not be seen in our model. If the high velocity anomalies near 1600 km depth are actually slabs subducted 100 Ma, then assuming the velocity in the upper 600 km is as given by Engebretson et al. (1984), the velocity of the slab below 600 km depth must be an order of magnitude less, about 10 km/m.y.. It is also interesting that the lower mantle anomaly observed here has a significant width, probably over 500 km, assuming spreading in the inversion similar to what the synthetic inversion showed. This is far wider than typical slabs in the upper mantle where most studies find slab velocity anomalies to be about 100 km thick (see Roecker, 1985, for a recent study of slab structure in the upper mantle). What happened beneath North America may be similar to the observations of Giardini and Woodhouse (1984) in the Tonga subduction zone. The deep slabs encounter a large resistance near 670 km depth due to a large increase in viscosity. At that depth the slabs tend to thicken and shorten by horizontal shearing as described by Giardini and Woodhouse but also, they continue to sink through the mantle though at a much slower rate due to the higher viscosity. Broadening of the thermal anomaly in the lower mantle could also be caused partially by the conductive cooling of the surrounding mantle. Further study is obviously needed to confirm or deny these speculations.

Conclusion

In this chapter we have used the tomographic inversion technique to derive a three dimensional model of shear velocity beneath the North American plate to about 1700 km depth. The large variations in observed S and SS travel-times were found to be explainable by large lateral variations in the upper 400 km of the mantle. These variations are directly correlated, in general, with the surface tectonic history above the mantle. The Superior and Churchill shield provinces were found to have a very high velocity root to about 400 km depth. All oceanic regions in the model had velocities much lower than beneath the shield from 150 to 400 km.

Below 400 km depth, the variations in shear velocity are much lower. Little heterogeneity was found in the transition zone; however, a slab shaped high velocity anomaly continuous from the Carribean to the southern Canadian border was found from 700 to 1700 km depth. The anomaly may be up to 2% in amplitude. The northern part of the anomaly is spread out over about 30^o in longitude while to the south it is more vertical. The entire high velocity structure shows some eastward dip. It is hypothesized that the lower mantle anomaly may be the remnant of the subducted Farallon plate from about 40 Ma to 100Ma.

Conclusion

The work in this thesis found a consistent correlation of shear wave velocity in the upper 400 km of the mantle and the tectonic history of the surface of the North American plate. We have found that the larger the time interval since the last orogenic event, the higher the velocities are in the upper 400 km. For most areas with little Cenozoic deformation, high velocities are found at depths above 100 km and the tectonic history - shear velocity correlation is particularly strong from about 150 to 300 km depth. Sipkin and Jordan (1975, 1976, 1980), on the basis of ScS and multiple ScS travel-times, have claimed that a similar correlation of shear velocity and continental age exists on a world-wide scale. Their estimate of the depth of the correlation was uncertain due to the vertical travel paths of their data. When comparing the results of mantle structure studies of different areas, it is difficult to draw conclusions due to the different assumptions and techniques used. For instance, comparisons of typical body-wave and surface wave studies must take into account the dispersion due to anelasticity present in the mantle. Also, long-period models usually do not contain discontinuities due to the lack of resolving power over short length scales whereas body-wave models are usually parameterized with several sharp jumps in velocity. In this section we will compare the results found here with published results from other areas which used the same parameterization of the mantle as was used in this thesis. An attempt will then be made to make some generalizations for the earth as a whole.

Rial et al. (1984) studied the upper mantle shear structure beneath the Russian platform, Baltic shield and the Alpine fold belt from about 75°E to 20°E using S and SS phases. The starting models used in that study were just SNA and TNA presented in Chapter 1 of this thesis. They found the SNA model was adequate to fit all the seismograms which propogated through the Russian platform and the Baltic shield. The distance range of the data used was from 40° to 56° and thus the SS arrivals included triplication branches bottoming from about 250 to 800 km depth. Most of this area has been stable for about 1700 Ma (Sclater and Parsons, 1981) and these results indicate the Russian platform and Baltic shield have a shear structure throughout the upper mantle very similar to the shear structure beneath provinces of Canada which have been stable for a similar time period. In contrast, the Alpine front to the south was found to have far lower velocities in the upper 400 km. Model TNA was too slow to satisfy the data and Rial et al. (1984) present a new structure for this area. A thin, higher velocity lid and higher velocities below 225 km depth, relative to TNA, fit the Alpine data. From 70 to 225 km the Alpine model has velocities about 8% slower than SNA. The data were sparce for this region and the slower velocities could easily extend to below 300 km depth. The Alpine front, of course, is a region of very recent orogenic activity.

Grand and Helmberger (1985) studied other paths using SSS waves as well as S and SS phases. Essentially the same technique was used as in the first chapters of this thesis. They found similar results for the Russian platform as Rial et al. (1984) but found the fold belts of Central Asia to have about 5% slower shear velocities from 50 to 250 km depth relative to the SNA model. Again, the data were not sufficient to determine the exact depth of the relatively slow mantle and the low velocities could easily extend to 350 km depth if the the upper 100 km were faster. These slow regions were deformed in the Asia-India collision event about 35 Ma (Molnar and Tapponnier, 1975). Lyon-Caen (1985) studied S and SS upper mantle propagation beneath the Indian shield and the Tibetan plateau. She found a minimum of 4%

slower shear velocities beneath Tibet than beneath India from 70 to 250 km depth. The Indian shield model had slightly lower velocities than SNA but was essentially the same as that model.

Burdick et al. (1983) and Grand et al. (1985) studied the upper mantle beneath northern Africa using S, SS and SSS waves at upper mantle distances. Both studies found that the upper mantle shear waveforms which propagated through the northwest African shield were very similar to those observed in the Canadian shield at similar distances. However, relative to S the upper mantle SS phases were 2 to 3 seconds faster than those in Canada. The conclusion reached was that the lithosphere is slightly thicker and the low velocity zone less pronounced beneath the northwest African shield relative to the Canadian shield. Otherwise, the SNA model is a good estimate of the upper mantle shear structure beneath that region. The higher velocities beneath this province agree well with a heat flow study by Chapman and Pollack (1975). They found very low heat flow in this region and postulated an extremely cold upper mantle to 400 km depth beneath this part of Africa. They also suggest that a deep root beneath Africa may be impeding the motion of the African plate. It is also interesting that Hager et al. (1985) model the anomalous geoid high over West Africa by the presence of hot lower mantle beneath Africa and not hot upper mantle. To the east of the shield, Grand et al. (1985) found lower upper mantle velocities. East of 10° E, in northern Africa, there has been abundant Cenozoic volcanism. This seems to be reflected in the change in shear structure from west to east. A model which fit the sparce data from northeastern Africa showed a high velocity lid with a well developed low velocity zone near 200 km depth. The structure is similar to that found beneath the eastern United States and the old Atlantic (Chapters 2 and 3).

No other continental studies have been performed using the technique discussed in this thesis. However, many studies have been conducted to find the average travel-time delays beneath seismic stations on a world-wide scale. Dziewonski and Anderson (1983) present perhaps the most complete set of station delays for P travel-times. Their results are for azimuthally averaged P time delays using only teleseismic arrivals. The raypaths for teleseisms are very steep in the upper 400 km of the mantle and the results of the Dziewonski and Anderson study should give an estimate of the average variation in P velocity in the upper 400 km beneath the stations studied. They find average P times in the western Australian, the Siberian and the central African shield regions to be consistently fast, similar to the pattern they find for the Canadian shield. Also, station BDF, located in the Brazilian shield, records fast arrivals similar to the values measured at Canadian stations like FBC, FCC and GWC (see Fig. 3.1 for the station locations). Finally, the station SPA at the south pole, is also found to be fast. Of the stable shield regions, only the South African shield province is found to have stations with consistently slower P times than the Canadian shield. In contrast, most stations in recently tectonic areas are slow (for example, the Alpine front, southeast Asia, eastern Australia and western North America). The distribution of P travel-time delays in the Dziewonski and Anderson (1983) paper indicate that almost all stable cratonic areas on the earth have very fast upper mantle beneath them. From the Asian, African and North American studies discussed above, it seems likely that most shields have shear velocity structures similar to that found beneath Canada.

There has only been one other multiple S upper mantle study of an oceanic region. Graves et al. (1985) looked at multiple S data for a profile from Tonga to North America, deriving a cross section of mantle shear velocity for a Pacific path.

They found a structure beneath the old Pacific similar to that found beneath the old Atlantic in Chapter 2. The absolute velocities, however, were about 1% slower throughout the upper 450 km in the Pacific model. This is supported by the slow multiple ScS times measured by Sipkin and Jordan (1980) for the old Pacific and also may explain why the Rayleigh wave phase velocities measured by Nakanishi and Anderson (1983) for old ocean are less than those predicted by the Atlantic model (see Fig. 2.14).

To further generalize the oceanic-continental differences found in this thesis, the results of the many oceanic surface wave experiments must be discussed. To study the upper mantle to depths below 150 km using surface waves, one must use very long-period fundamental modes or look at overtones at shorter periods. Early global studies using very long-period data (up to 350 sec periods) indicated clear differences in structure beneath different tectonic provinces. Toksoz and Anderson (1966) and Kanamori (1970) both found slower velocities beneath tectonically active areas as compared with shield areas to at least 400 km depth. Kanamori (1970) found no major difference between oceanic and shield structure below 200 km depth. Anderson (1967), however, presented shield and oceanic models with slower oceanic velocities to 400 km depth based on data from Toksoz and Anderson (1966). One problem comparing the results of this thesis with the above studies is the definition of shield. In the Kanamori study all continental areas not tectonically active at present were considered shield. Thus, significantly different structures may be included in the single shield province.

Knopoff (1983) reviews a large number of more regional fundamental mode surface wave studies. He concludes, from many studies, that oceanic and tectonic areas have significantly slower shear velocities than Precambrian shields to 300 km depth.

The works he discusses have little resolution below 300 km depth and no conclusion is drawn for systematic differences in structure below that depth.

More recently, Lerner-Lam and Jordan (1983) used overtone data as well as fundamental mode data to compare upper mantle structure beneath Eurasia and the Pacific. They conclude that Eurasia has higher velocities to 400 km depth than the central Pacific. However, the models derived in their paper are quite different from those derived in this thesis. In particular, they find far slower velocities in the upper 150 km for both the Pacific and Eurasia relative to those found here for Canada and the Atlantic.

Finally, Woodhouse and Dziewonski (1984) have presented maps of upper mantle shear velocity for the whole earth. Their study sought a model which would predict entire seismograms and thus the study included both fundamental as well as overtone data. Above 350 km depth, every stable continental region has higher than average shear velocity. Most oceanic areas from 150 to 350 km depth have slower than average shear velocities. Exceptions to this are the oceanic regions between Australia and Antartica and between southern Africa and Antartica. The south-central Atlantic ocean is also fast at these depths in their maps. Whether these exceptions to the general trend are artifacts of the inversion or represent real earth structure is certainly an important area for further research. Little correlation of tectonic province and shear velocity is seen below 450 km depth.

The surface wave studies discussed above have little information on the detailed structure of the earth as a whole. However, they are compatible with the conclusions of this thesis with respect to lateral heterogeneity. Precambrian shields appear to have high velocity roots to about 350 km depth relative to all other tectonic provinces. From the studies using S, SS and SSS waveform modeling discussed above, it also appears that Precambrian shields have similar shear velocity structures with a thick high velocity lid, a decrease in velocity between 150 and 200 km depth and a lower than average gradient below. The oceanic models found in this thesis are also qualitatively compatible with the surface wave results. The main structural feature beneath oceanic provinces is a high velocity lid whose thickness and velocity increases with the age of the overlying crust reaching a maximum of 100 km thickness and a velocity over 4.7 km/sec. Below the lid are very low shear velocities to about 200 km depth followed by a region of high gradient to about 350 km depth. Little heterogeneity was found below 350 km depth in this thesis. The agreement, in Fig. 2.14, of Rayleigh wave phase velocities for periods greater than 250 sec with those predicted by SNA, TNA and ATL indicates that the structure found in this thesis below 350 km is probably a good average for the earth though some details may be in error.

It is interesting to speculate on the meaning of the seismic results discussed above. The growth of a high velocity lithosphere away from oceanic spreading centers has been known for some time. There is also a corresponding increase in depth of the ocean and a decrease in the heat flow with age for oceanic crust. This has been modeled as simple cooling of the hot mantle at ridges with time (see Kono and Yoshii, 1975). As discussed in Chapter 3, the very low velocities beneath the lid and the high gradient from 200 to 350 km depth indicate a nonelastic process such as partial melting is occuring. Anderson and Bass (1984) have shown that gradients as high as in models ATL and TNA can not be produced by the temperature derivative of elastic constants and reasonable thermal gradients. It is interesting that Oldenburg (1981) found conductivity maxima at 70 km depth beneath young ocean and 180 km depth beneath oceanic crust of 70 Ma. These depths are close to the depths of minimum shear velocity in models TNA and ATL respectively. Oldenburg (1981) concludes that the conductivity highs represent the depths of maximum partial melting beneath the respective oceanic areas. An oceanic model of a thickening thermal boundary layer above a partially melted asthenosphere appears to be compatible with the results found in this thesis for oceanic provinces. As no sharp increase in velocity was found near 200 km depth it appears unlikely that there is a chemical boundary near this depth as suggested by Anderson (1979).

Continental shear structure, particularly beneath old shield areas, is more difficult to explain. The deep roots found here beneath cratons, the existence of which was suggested by Jordan (1975), probably indicate lower than average temperatures beneath old stable continental crust to about 400 km depth. Support for this also comes from Chapman and Pollack (1977) who suggested that the heat flow measurements from stable continents imply cooler than average geotherms to at least 300 km depth. They suggest the same process occurs beneath continents as occurs beneath oceans. That is, from the last thermal (orogenic) event, cooling has continued downward to the present time. For old cratons which have been stable for up to 3000 Ma, they predict the thermal boundary layer has grown to about 350 km depth. Oxburgh and Parmentier (1978) and Jordan (1978) have shown, however, that if this were the case, up to 10 km of subsidence would have occured in the cratons due to the increase in density of the cooling mantle rock. This does not appear to have occured. Also, this model does not explain the decrease in velocity at about 175 km depth observed beneath shields in the studies discussed previously. Evidence for a rather sharp decrease in velocity at these depths has been presented by Jordan and Fraser (1975) and Sacks et al. (1977). These authors have found converted S to P arrivals from 150 to 200 km depth beneath the Canadian and Baltic shields respectively. The polarity of the converted phases indicates a slow to fast transition from depth. Also, Given and Helmberger's (1981) P-velocity model for northwest Eurasia shows a decrease of 2.5% in velocity over 10 km depth at about 150 km depth. Their study had particularly good data sampling this depth range.

The above discussion supports the idea that there is some chemical difference between cratons and elsewhere. This concept is not new. Jordan (1975, 1978, 1981a) has suggested that there are deep chemical roots beneath continents. Oxburgh and Parmentier (1978) have given a scenario whereby the continental lithosphere is formed by the addition of basalt depleted mantle rising from descending slabs. Anderson and Bass (1984) also suggest a difference in chemistry between the continental lithosphere and the mantle below the lithosphere with an olivine rich lithosphere and a garnet-pyroxene rich mantle below. The olivine rich depleted mantle would be intrinsically less dense than a more garnet-pyroxene rich assemblage and thus a lithosphere of depleted mantle would not sink even if it were cooler than the surrounding mantle (see Oxburgh and Parmentier, 1978 and Jordan, 1981a for a discussion of stability, and Boyd and McCallister, 1976 for a discussion of the relative densities of depleted and undepleted mantle). The solidus temperature is also higher for the depleted rocks. The high velocity layer to about 175 km depth in model SNA is possibly formed of olivine rich depleted mantle. The rapid decrease in velocity between the depths of 150 to 200 km observed beneath shields would then mark a change in chemistry from olivine rich to a more basalt rich composition. This also agrees with work by Boyd and Nixon (1975) who find that kimberlite nodules originating between 100 to 150 km depth are more basalt depleted and thus less dense than the nodules originating from 150 to 200 km depth. The shear velocity studies presented in this thesis and elsewhere show that there are lower temperatures beneath stable cratons well below 200 km depth. The correlation of high velocities to 350 km depth and the position of old shields implies that the roots are not coincidentally situated beneath shields. Though the chemical roots may be only 150 to 200 km thick, it appears that the thermal boundary layer beneath shields extends to near 400 km depth. This idea also agrees with the Chapman and Pollack (1977) geotherms. A thermal boundary layer extending below a chemical boundary has been proposed by Jordan (1981a) and we feel the seismic studies given here and elsewhere support this. This implies that the 'tectosphere', the vertical section of mantle which moves as a single unit over the earth, is about 400 km thick beneath stable cratonic regions. However, many continental regions, such as northeastern Africa and the eastern United States, have either had their thermal boundary layer disrupted or they never cooled to great depth. The existence of a deep root seems to be directly related to the tectonic processes which occur at the surface (for instance volcanism in northeast Africa and folding in eastern United States and central Asia).

The composition of the surrounding upper mantle has, of course, been debated for years. Ringwood (1975) has postulated a model with mostly olivine and minor amounts of pyroxene and garnet. Ito (1974) found that olivine-eclogite with about 63% pyroxene, 30% garnet and 7% olivine best fits the available data for the lower oceanic lithosphere. Recently, Bass and Anderson (1984) have used the seismic results presented in Chapters 1 and 2 as well as many other studies, to conclude that a picritic eclogite composition best fits the seismic results for the upper mantle. This assemblage contains 47% pyroxene, 37% garnet and 16% olivine. Deciding among these models is beyond the scope of this thesis. However, Anderson (1982) has concluded that if the upper mantle is eclogitic, subducted slabs would not be able to penetrate the lower mantle. This would contradict the interpretation of the lower mantle results found in Chapter 3 as indicating that former slabs are now at depths of 700 to 1700 km. Other explanations of the high velocity anomalies found in Chapter 3 are certainly possible but the work of Hager (1984) and Creager and Jordan (1984) seems to indicate there is mixing of upper and lower mantle material. Determining the composition of the upper mantle and its relation to the lower mantle, then, remains an important problem in geophysics.

References

Adams, R. D., 1971. Reflections from discontinuities beneath Antarctica, *Bull. Seism. Soc. Am.*, **61**, pp. 1441-1451.

Aki, K., A. Christofferson and E. S. Husebye, 1977. Determination of the three-dimensional seismic structure of the lithosphere, *J. Geophys. Res.*, **82**, pp. 277-296.

Anderson, D. L., 1967. Latest information from seismic observations, in *The Earth's Mantle,* Academic Press Inc., London.

Anderson, D. L., 1979. The deep structure of continents, *J. Geophys. Res.*, **84**, pp. 7555-7560.

Anderson, D. L., 1982. Chemical composition and evolution of the mantle, *Adv. Earth Planet. Sci.*, **12**, pp. 301-318.

Anderson, D. L. and B. R. Julian, 1969. Shear velocities and elastic parameters of the mantle, *J. Geophys. Res.*, **74**, pp. 3281-3286.

Anderson, D. L. and H. Spetzler, 1970. Partial melting and the low velocity zone, *Phys. Earth Planet. Int.*, **4**, pp. 62-64.

Anderson, D. L. and J. Regan, 1983. Upper mantle anisotropy and the oceanic lithosphere, *Geophys. Res. Lett.*, **10**, pp. 841-844.

Anderson, D. L. and J. D. Bass, 1984. Mineralogy and composition of the upper mantle, *Geophys. Res. Lett.*, **11**, pp. 637-640.

Anderson, R. N., D. W. Forsyth, P. Molnar and J. Mammerickx, 1974. Fault plane solutions of earthquakes on the Nazca plate boundaries and the Easter plate, *Earth Planet. Sci. Lett.*, **24**, pp. 188-202.

Baag, C. and C. A. Langston, 1985. Shear-coupled PL, *Geophys. J. R. astr. Soc.*, **80**, pp. 363-387.

Bass, J. D. and D. L. Anderson, 1984. Composition of the upper mantle: geophysical tests of two petrological models, *Geophys. Res. Lett.*, **11**, pp. 237-240.

Bath, M., 1966. Propagation of Sn and Pn to teleseismic distances, *Pure appl. Geophys.*, **64**, pp. 19-30.

Berry, M. J., 1973. Structure of the crust and upper mantle in Canada, *Tectonophys.*, **20**, pp. 183-201.

Bird, P., 1984. Laramide crustal thickening event in the rocky mountain foreland and great plains, *Tectonics*, **3**, pp. 741-758.

Birch, F., 1952. Elasticity and composition of the earth, *J. Geophys. Res.*, **57**, pp. 227-286.

Boyd, F. R. and P. H. Nixon, 1975. Origins of the ultramafic nodules from some kimberlites of northern Lesotho and the Monastery Mine, South Africa, *Phys. Chem. Earth*, **9**, pp. 431-454.

Boyd, F. R. and R. H. McCallister, 1976. Densities of fertile and sterile garnet peridotites, *Geophys. Res. Lett.*, **9**, pp. 509-512.

Brune, J. and J. Dorman, 1963. Seismic waves and earth structure in the Canadian shield, *Bull. Seism. Soc. Am.*, **53**, pp. 167-200.

Bungum, H., 1977. Two focal-mechanism solutions for earthquakes from Iceland and Svalbard, *Tectonophys.*, **41**, pp. 15-18.

Bungum, H. and E. S. Husebye, 1977. Seismicity of the Norwegian Sea: The Jan Mayan fracture zone, *Tectonophys.*, **40**, pp. 351-360.

Burdick, L. J., 1981. A comparison of the upper mantle structure beneath North

America and Europe, *J. Geophys. Res.*, **86**, pp. 5926-5936.

Burdick, L. J. and G. R. Mellman, 1976. Inversion of the body waves from the Borrego Mountain earthquake to the source mechanism, *Bull. Seism. Soc. Am.*, **66**, pp. 1485-1499.

Burdick, L. J. and D. V. Helmberger, 1978. The upper mantle P velocity structure of the western United States, *J. Geophys. Res.*, **83**, pp. 1699-1712.

Burdick, L. J. and J. A. Orcutt, 1978. A comparison of the generalized ray and reflectivity methods of waveform synthesis, *Geophys. J. R. astr. Soc.*, **58**, pp. 261-278.

Burdick, L. J., S. P. Grand, D. V. Helmberger, T. Lay, J. A. Rial, 1983. Remote sensing of attenuation bias using SS, *Woodward-Clyde Consultants Technical Report, WCCP-R-83-01.*

Butler, R., 1979. Shear-wave travel times from SS, *Bull. Seism. Soc. Am.*, **69**, pp. 1715-1732.

Cara, M., 1979. Lateral variations of S velocity in the upper mantle from higher Rayleigh modes, *Geophys. J. R. astr. Soc.*, **57**, pp. 649-670.

Carpenter, E. W., 1966. Absorption of elastic waves - an operator for a constant Q mechanism, *A. W. R. E. Rep. 0-43/66*, 16 pp..

Chandra, U., 1974. Seismicity, earthquake mechanisms and tectonics along the western coast of North America, from 42° N to 61° N, *Bull. Seism. Soc. Am.*, **64**, pp. 1529-1549.

Chapman, C. H., 1976. A first-motion alternative to geometrical ray theory, *Geophys. Res. Lett.*, **3**, pp. 153-156.

Chapman, C. H., 1978. A new method for computing synthetic seismograms, *Geophys. J. R. astr. Soc.*, **54**, pp. 481-518.

Chapman, D. S. and H. N. Pollack, 1975. Cold spot in west Africa: anchoring the African plate, *Nature*, **250**, pp. 477-478.

Chapman, D. S. and H. N. Pollack, 1977. Regional geotherms and lithospheric thickness, *Geology*, **5**, pp. 265-268.

Chase, C. G. and D. R. Sprowl, 1983. The modern geoid and ancient plate boundaries , *Earth Planet. Sci. Lett.*, **62**, pp. 314-320.

Choy, G. L. and P. G. Richards, 1975. Pulse distortion and Hilbert transformation in multiply reflected and refracted bodywaves, *Bull. Seism. Soc. Am.*, **65**, pp. 55-70.

Clayton, R. W. and R. P. Comer, 1983. A tomographic analysis of mantle heterogeneities from body wave travel time data, *EOS Trans. AGU*, **64**, pp. 776.

Comer, R. P. and R. W. Clayton, 1986. Reconstruction of mantle heterogeneity by iterative back-projection of travel-times 1. theory and reliability, submitted to *J. Geophys. Res.*.

Creager, K. C. and T. H. Jordan, 1984. Slab penetration into the lower mantle, *J. Geophys. Res.*, **89**, pp. 3031-3049.

Dey-Sarkar, S. K. and C. H. Chapman, 1978. A simple method for the computation of body-wave seismograms, *Bull. Seism. Soc. Am.*, **68**, pp. 1577 -1593.

Dickinson, W. R. and W. S. Snyder, 1978. Plate tectonics of the Laramide orogeny, *Mem. Geol. Soc. Am.*, **151**, pp. 355-366.

Doyle, H. A. and A. L. Hales, 1967. An analysis of the travel times of S waves to North America in the distance range 28° to 82°, *Bull. Seism. Soc. Am.*, **57**, pp. 761-771.

Dziewonski, A. M., 1984. Mapping the lower mantle : Determination of lateral heterogeneity in P velocity up to degree and order 6. *J. Geophys. Res.*, **89**, pp. 5929-5952.

Dziewonski, A. M. and F. Gilbert, 1976. The effect of small, aspherical perturbations on travel times and a re-examination of the corrections for ellipticity, *Geophys. J. R. astr. Soc.*, **44**, pp. 7-17.

Dziewonski, A. M., B. H. Hager and R. J. O'Connell, 1977. Large-scale heterogeneities in the lower-mantle, *J. Geophys. Res.*, **85**, pp. 239-255.

Dziewonski, A. M. and D. L. Anderson, 1981. Preliminary reference earth model, *Phys. Earth Planet. Int.*, **25**, pp. 297-356.

Dziewonski, A. M. and D. L. Anderson, 1983. Travel times and station corrections for P waves at teleseismic distances, *J. Geophys. Res.*, **88**, pp. 3295-3314.

Ebel, J. E., L. J. Burdick and G. S. Stewart, 1978. The source mechanism of the August 7, 1966, El Golfo earthquake, *Bull. Seism. Soc. Am.*, **68**, pp. 1281-1292.

Eissler, H. K. and K. C. McNally, 1984. Seismicity and tectonics of the Rivera plate and implications for the 1932 Jalisco, Mexico, earthquake, *J. Geophys. Res.*, **89**, pp. 4520-4530.

England, P. C., B. L. N. Kennett and M. H. Worthington, 1977. A comparison of the upper mantle structure beneath Eurasia, *Geophys. J. R. astr. Soc.*, **54**, pp. 575-585.

Engebretson, D. C., A. Cox and G. A. Thompson, 1984. Correlation of plate motions with continental tectonics : Laramide to basin-range, *Tectonics*, **3**, pp. 115-119.

Engebretson, D. C., A. Cox and R. G. Gordan, 1986. Relative motions between oceanic and continental plates in the Pacific basin, *Geol. Soc. Am. Special Paper*, **206**, pp. 1-59.

Forsyth, D. W., 1975. A new method for the analysis of multi-mode surface-wave dispersion : application to Love-wave propagation in the East Pacific, *Bull. Seism. Soc. Am.*, **65**, pp. 323-342.

Fukao, Y., T. Nagahashi and S. Mori, 1982. Shear velocity in the mantle transition zone, in *High Pressure Research in Geophysics*, eds. Akimoto, S. and M. H. Manghnani, Center for Academic Publications, Tokyo.

Futterman, W. I., 1962. Dispersive body waves, *J. Geophys. Res.*, **67**, pp. 5279-5291.

Giardini, D. and J. H. Woodhouse, 1984. Deep seismicity and modes of deformation in Tonga subduction zone, *Nature*, **307**, pp. 505-509.

Given, J. W., 1984. Inversion of body-wave seismograms for upper mantle structure, *PhD. Thesis*, 154pp., Caltech, Pasadena.

Given, J. W. and D. V. Helmberger, 1981. Upper mantle structure of northwestern Eurasia, *J. Geophys. Res.*, **85**, pp. 7183-7194.

Grand, S. P. and D. V. Helmberger, 1984a. Upper mantle shear structure of North America, *Geophys. J. R. astr. Soc.*, **76**, pp. 399-438.

Grand, S. P. and D. V. Helmberger, 1984b. Upper mantle shear structure beneath the northwest Atlantic ocean, *J. Geophys. Res.*, **89**, pp. 11465-11475.

Grand, S. P. and D. V. Helmberger, 1985. Uppermantle shear structure beneath Asia from multi-bounce S waves, *Phys. Earth Planet. Int.*, **41**, pp. 154-169.

Grand, S. P., D. V. Helmberger and L. J. Burdick, 1985. Attenuation bias measurements of the Semipalatinsk and North African test sites, *Woodward-Clyde Consultants Technical Report, WCCP-R-85-01.*

Graves, R., S. P. Grand and D. V. Helmberger, 1985. Upper mantle cross-section from Tonga to California, *EOS trans. AGU*, **66**, pp. 975.

Gutenburg, B., 1948. On the layer of relatively low wave velocity at a depth of about 80 km, *Bull. Seism. Soc. Am.*, **38**, pp. 121-148.

Hager, B. H., 1984. Subducted slabs and the geoid: constraints on mantle rheology and flow, *J. Geophys. Res.*, **89**, pp. 6003-6015.

Hager, B. H., R. W. Clayton, M. A. Richards, R. P. Comer and A. M. Dziewonski, 1985. Lower mantle heterogeneity, dynamic topography and the geoid, *Nature*, **313**, pp. 541-545.

Hart, R. S. and F. Press, 1973. Sn velocities and the composition of the lithosphere in the regionalized Atlantic, *J. Geophys. Res.*, **78**, pp. 407-411.

Helmberger, D. V., 1973. Numerical seismograms of long period body waves from seventeen to forty degrees, *Bull. Seism. Soc. Am.*, **63**, pp. 633-646.

Helmberger, D. V. and R. A. Wiggins, 1971. Upper mantle structure of the midwestern United States, *J. Geophys. Res.*, **76**, pp. 3229-3245.

Helmberger, D. V. and G. R. Engen, 1974. Upper mantle shear structure, *J. Geophys. Res.*, **79**, pp. 4017-4028.

Helmberger, D. V. and L. J. Burdick, 1979. Synthetic seismograms, *Ann. Rev. Earth Planet. Sci.*, **7**, pp. 417-442.

Helmberger, D. V., G. R. Engen and S. P. Grand, 1985a. Upper-mantle cross section from California to Greenland, *J. Geophys.*, **58**, pp. 92-100.

Helmberger, D. V., G. R. Engen and S. P. Grand, 1985b. Long period wave propagation in laterally varying structure, *J. Geophys.*, **58**, pp. 82-91.

Humphreys, E. D., 1985. Studies of the crust-mantle system beneath Southern California, *PhD. Thesis*, 189pp., Caltech, Pasadena.

Husebye, E. S., H. Gjoystdal, H. Bungam and D. Eldholm, 1975. The seismicity of the

Norwegian and Greenland seas and adjacent continental shelf areas, *Tectonophys.*, **26**, pp. 55-70.

Ibrahim, A. K. and O. W. Nuttli, 1967. Travel-time curves and upper mantle structure from long period S waves, *Bull. Seism. Soc. Am.*, **57**, pp. 1063-1092.

Ito, K., 1974. Petrological models of the oceanic lithosphere: geophysical and geochemical tests, *Earth Planet. Sci. Lett.*, **21**, pp. 169-180.

Jeffreys, H., 1939. The times of P, S, and SKS, and the velocities of P and S, *Mon. Not. R. astr. Soc.*, **4**, pp. 498-533.

Johnson, L. R., 1967. Array measurements of P-velocities in the upper mantle, *J. Geophys. Res.*, **72**, pp. 6309-6325.

Jordan, T. H., 1975. The continental tectosphere, *Rev. Geophys. Space Phys.*, **13**, pp. 1-12.

Jordan, T. H., 1978. Composition and development of the continental tectosphere, *Nature*, **274**, pp. 544-548.

Jordan, T. H., 1981a. Continents as a chemical boundary layer, *Philos. Trans. R. Soc. London*, **301**, pp. 359-373.

Jordan, T. H., 1981b. Global tectonic regionalization for seismological data analysis, *Bull. Seism. Soc. Am.*, **71**, pp. 1131-1141.

Jordan, T. H. and W. S. Lynn, 1974. A velocity anomaly in the lower mantle, *J. Geophys. Res.*, **79**, pp. 2679-2685.

Jordan, T. H. and L. N. Frazer, 1975. Crustal and upper mantle structure from Sp phases, *J. Geophys. Res.*, **80**, pp. 1504-1518.

Kanamori, H., 1967. Upper mantle structure from apparent velocities of P waves recorded at Wakayama Micro-earthquake Observatory, *Bull. Earthq. Res. Inst.*,

45, pp. 657-678.

Kanamori, H., 1970. Velocity and Q of mantle waves, *Phys. Earth Planet. Int.*, **2**, pp. 259-275.

Knopoff, L., 1983. The thickness of the lithosphere from the dispersion of surface waves, *Geophys. J. R. astr. Soc.*, **74**, pp. 55-81.

Kono, Y. and T. Yoshii, 1975. Numerical experiments on the thickening plate model, *J. Phys. Earth.*, **23**, pp. 63-75.

Langston, C. A. and D. V. Helmberger, 1975. A procedure for modeling shallow dislocation sources, *Geophys. J. R. astr. Soc.*, **42**, pp. 117-130.

Lay, T., 1983. Localized velocity anomalies in the lower mantle, *Geophys. J. R. astr. Soc.*, **72**, pp. 483-516.

Lerner-Lam, A. L. and T. H. Jordan, 1983. Earth structure from fundamental and higher-mode waveform analysis, *Geophys. J. R. astr. Soc.*, **75**, pp. 759-797.

Lyon-Caen, H., 1985. Comparison of the upper mantle shear velocity structure of the Indian shield and the Tibetan plateau and tectonic implications, *EOS trans. AGU*, **66**, pp. 988.

Minster, J. B. and D. L. Anderson, 1980. Dislocations and nonelastic processes in the mantle, *J. Geophys. Res.*, **85**, pp. 6347-6352.

Mitchell, B. J. and G. Yu, 1980. Surface wave dispersion, regionalized velocity models, and anisotropy of the Pacific crust and upper mantle, *Geophys. J. R. astr. Soc.*, **63**, pp. 117-130.

Molnar, P. and L. R. Sykes, 1969. Tectonics of the Carribbean and middle America region from seismicity and focal mechanisms, *Geol. Soc. Am. Bull.*, **80**, pp. 1639-1684.

Molnar, P. and P. Tapponnier, 1975. Cenozoic tectonics of Asia: effects of a continental collision, *Science,* **189**, pp. 419-426.

Nakanishi, I., 1981. Shear velocity and shear attenuation models inverted from world-wide and pure-path average data of mantle Rayleigh waves ${}_0S_{25}$ to ${}_0S_{80}$ and fundamental spheroidal modes ${}_0S_2$ to ${}_0S_{24}$, *Geophys. J. R. astr. Soc.*, **66**, pp. 83-130.

Nakanishi, I. and D. L. Anderson, 1983. Mesurements of mantle wave velocities and inversion for lateral heterogeneity and anisotropy, 1. analysis of great circle phase velocities, *J. Geophys. Res.*, **88**, pp. 10267-10284.

Nataf, H. C., I. Nakanishi and D. L. Anderson, 1984. Anisotropy and shear-velocity heterogeneities in the upper mantle, *Geophys. Res. Lett.*, **11**, pp. 109-112.

Niazi, M. and D. L. Anderson, 1965. Upper mantle structure of western North America from apparent velocities of P waves, *J. Geophys. Res.*, **70**, pp. 4633-4640.

O'Connell, R. J., 1977. On the scale of mantle convection, *Tectonophys.*, **38**, pp. 119-136.

Officer, C. B., M. Ewing and P. C. Whenschel, 1952. Seismic refraction measurements in the Atlantic ocean, 4. Bermuda Rise and Nares Basin, *Geol. Soc. Am. Bull.*, **63**, pp. 777-808.

Okal, E. A. and D. L. Anderson, 1975. A study of lateral heterogeneities in the upper mantle by multiple ScS travel-time residuals, *Geophys. Res. Lett.*, **2**, pp. 313-316.

Oldenburg, D. W., 1981. Conductivity structure of oceanic upper mantle beneath the Pacific plate, *Geophys. J. R. astr. Soc.*, **65**, pp. 359-394.

Oxburgh, E. R. and E. M. Parmentier, 1978. Thermal processes in the formation of continental lithosphere, *Phil. Trans. R. Soc. Lond.*, **288**, pp. 415-429.

Priestly, K., J. A. Orcutt and J. N. Brune, 1979. Higher mode surface waves and structure of the great basin of Nevada and western Utah, *J. Geophys. Res.*, **85**, pp. 7166-7174.

Ram, D., 1981. Seismic velocity structure using array data, *Phys. Earth Planet. Int.*, **24**, pp. 33-52.

Rial, J. A., S. P. Grand and D. V. Helmberger, 1984. A note on the lateral variation in upper-mantle shear structure across the Alpine front, *Geophys. J. R. astr. Soc.*, **77**, pp. 639-655.

Richter, F. M., 1979. Focal mechanisms and seismic energy release of deep and intermediate earthquakes in the Tonga-Kermadec region and their bearing on the depth extent of mantle flow, *J. Geophys. Res.*, **84**, pp. 6783-6795.

Ringwood, A. E., 1975. *Composition and petrology of the Earth's mantle*, McGraw-Hill, New York.

Roecker, S. W., 1985. Velocity structure in the Izu-Bonin seismic zone and the depth of the olivine-spinel phase transition in the slab, *J. Geophys. Res.*, **90**, pp. 7771-7794.

Sacks, I. S., J. A. Snoke and E. S. Husebye, 1977. Lithosphere thickness beneath the Baltic shield, *Carnegie Inst. Yearb.*, **76**, pp. 805-822.

Schubert, G., D. A. Yuen and D. L. Turcotte, 1975. Role of phase transitions in a dynamic mantle, *Geophys. J. R. astr. Soc.*, **42**, pp. 705-735.

Sclater, J. G. and B. Parsons, 1981. Oceans and continents : similarities and differences in the mechanisms of heat loss, *J. Geophys. Res.*, **86**, pp. 11535-11552.

Sengupta, M. K. and M. N. Toksoz, 1976. Three dimensional model of seismic velocity variation in the earth's mantle, *Geophys. Res. Lett.*, **3**, pp. 84-86.

Sipkin, S. A. and T. H. Jordan, 1975. Lateral heterogeneity of the upper mantle determined from the travel times of ScS, *J. Geophys. Res.*, **80**, pp. 1474-1484.

Sipkin, S. A. and T. H. Jordan, 1976. Lateral heterogeneity of the upper mantle determined from the travel times of multiple ScS, *J. Geophys. Res.*, **81**, pp. 6307-6320.

Sipkin, S. A. and T. H. Jordan, 1980. Multiple ScS travel times in the western Pacific : implications for mantle heterogeneity, *J. Geophys. Res.*, **85**, pp. 853-861.

Soller, D. R., R. D. Ray and R. D. Brown, 1982. A global crustal thickness map, *Tectonics*, **1**, pp. 125-151.

Spetzler, H. and D. L. Anderson, 1968. The effect of temperature and partial melting on velocity and attenuation in a simple binary system, *J. Geophys. Res.*, **73**, pp. 6051-6060.

Stauder, W., 1975. Subduction of the Nazca plate under Peru as evidenced by focal mechanisms and by seismicity, *J. Geophys. Res.*, **80**, pp. 1053-1064.

Stearn, C. W., R. L. Carroll and T. H. Clark, 1979. *Geological evolution of North America*, 556pp., John Wiley and Sons.

Stewart, G. S. and D. V. Helmberger, 1981. The Bermuda earthquake of March 24, 1978 : a significant oceanic intraplate event, *J. Geophys. Res.*, **86**, pp. 7027-7036.

Stewart, S. W. and L. C. Pakiser, 1962. Crustal structure in eastern New Mexico interpreted from the Gnome explosion, *Bull. Seism. Soc. Am.*, **52**, pp. 1017-1030.

Sykes, L. R., 1970. Focal mechanism solutions for earthquakes along the world rift system, *Bull. Seism. Soc. Am.*, **60**, pp. 1749-1752.

Tanimoto, T. and D. L. Anderson, 1985. Lateral heterogeneity and azimuthal anisotropy of the upper mantle : Love and Rayleigh waves 100 - 250 s, *J. Geophys.*

Res., **90**, pp. 1842-1858.

Thatcher, W. and J. N. Brune, 1969. Higher mode interference and observed anomalous Love wave phase velocities, *J. Geophys. Res.*, **74**, pp. 6603-6611.

Toksoz, M. N. and D. L. Anderson, 1966. Phase velocities of long-period surface waves and structure of the upper mantle, *J. Geophys. Res.*, **71**, pp. 1649-1658.

Uyeda, S. and H. Kanamori, 1979. Back-arc opening and the mode of subduction, *J. Geophys. Res.*, **84**, pp. 1049-1061.

Walck, M. C., 1984. The P-wave upper mantle structure beneath an active spreading center : the Gulf of California, *Geophys. J. R. astr. Soc.*, **76**, pp. 697-723.

Weidner, D. J., 1974. Rayleigh wave phase velocities in the Atlantic ocean, *Geophys. J. R. astr. Soc.*, **36**, pp. 105-139.

Whitcomb, J. and D. L. Anderson, 1970. Reflection of P'P' seismic waves from discontinuities in the mantle, *J. Geophys. Res.*, **29**, pp. 5713-5728.

Wickens, A. J. and G. G. R. Buchbinder, 1980. S-wave residuals in Canada, *Bull. Seism. Soc. Am.*, **70**, pp. 809-822.

Wielandt, E. and L. Knopoff, 1982. Dispersion of very long-period Rayleigh waves along the East Pacific Rise : Evidence for S wave anomalies to 450 km depth. *J. Geophys. Res.*, **87**, pp. 8631-8641.

Wiggins, R. A., 1972. The general linear inverse problem: implication of surface waves and free oscillations for earth structure, *Rev. Geophys. Space Phys.*, **10**, pp. 251-285.

Wiggins, R. A., 1976. Body wave amplitude calculations-2, *Geophys. J. R. astr. Soc.*, **46**, pp. 1-10.

Wiggins, R. A. and D. V. Helmberger, 1973. Upper mantle structure of the western

United States, *J. Geophys. Res.*, **78**, pp. 1870-1880.

Woodhouse, J. H. and A. M. Dziewonski, 1984. Mapping the upper mantle : three dimensional modeling of earth structure by inversion of seismic waveforms, *J. Geophys. Res.*, **89**, pp. 5953-5986.